Development and Application of Photon Counting Techniques for Fluorescence Microscopy

Zanda, Gianmarco

Awarding institution:
King's College London

Development and Application of Photon Counting Techniques for Fluorescence Microscopy

Gianmarco Zanda

Department of Physics

King's College London

A thesis submitted for the degree of

Doctor of Philosophy

August 2015

To Eleonora and to my loving family

Acknowledgements

First of all, I would like to thank Klaus, my supervisor, who patiently guided me in this project, and who supported me during the difficult times of this PhD.

A special thanks to Greg, for his help and all the valuable advices he gave me; to Liisa, for the discussions and suggestions on this work; to Alix, for her practical and moral help; to Mike and Dan fro proof-reading it; and to James and Pei-Hua for teaching me how not to kill my cells.

I am grateful to the Master & Back Program for funding my PhD.

If I achieved this, it is thanks to the constant support and relentless love of my whole family: I could have not make it without them.

I am very grateful to all the people I met in my years at King's and in London: some of them left, some are still around, but everyone contributed in his own way to make my PhD a time to be remembered. Among them, a little thanks goes to Giorgia, Stefano and Luciano that in different ways contributed to the start of all this. And to Frix, Ela, Moto, Giovanni and Chiara for their attempts to cheer me up during the hard times (and for the innumerable coffees).

A special thanks goes to gli Amichevoli, to "I miei ragazzi" and to my friends back in Italy: a part of me is always with them.

Finally, I can never thank Eleonora enough for all she gave and is giving to me. She changed my life for good. *Grazie, Amore mio.*

Thank you all!

Declaration

This dissertation is the result of my own work, except where explicit reference is made to the work of others, and has not been submitted for another qualification to this or any other university.

Gianmarco Zanda

Publications

1. G Zanda, N Sergent, M Green, JA Levitt, Z Petrasek, and K Suhling; Wide-field single photon counting imaging with an ultrafast camera and an image intensifier;
   Nuclear Instruments & Methods Section A - Accelerators Spectrometers Detectors and Associated Equipment, **695**: 306-308, 2012.
   doi: `http://dx.doi.org/10.1016/j.nima.2011.11.087`

2. LM Hirvonen, S Jiggins, N Sergent, G Zanda, and K Suhling; Photon counting imaging with an electron-bombarded CCD: Towards a parallel-processing photoelectronic time-to-amplitude converter;
   Review of Scientific Instruments, **85**, 12, 2014.
   doi: `http://dx.doi.org/10.1063/1.4901935`

3. LM Hirvonen, S Jiggins, N Sergent, G Zanda, and K Suhling; Photon counting imaging with an electron-bombarded CCD: Towards wide-field time-correlated single photon counting (TCSPC);
   Nuclear Instruments & Methods Section A - Accelerators Spectrometers Detectors and Associated Equipment, **787**, 323-327, 2015.
   doi: `http://dx.doi.org/10.1016/j.nima.2015.01.031`

Abstract

Fluorescence lifetime imaging microscopy (FLIM) is a key technique to image cells as, in addition to the advantages of standard fluorescence microscopy, it allows to study the environment and probe interaction in living specimens. Implementing FLIM via Single Photon Counting (SPC) proved to be the most effective technique considering the fluorophores limited photon budget before being irreversibly bleached.

This thesis focuses on the development and application of Single Photon Counting techniques to imaging systems and to spectroscopy. Firstly, the BODIPY-C_{12} molecular rotor was used to determine dye-concentrations between 3 and 16 μM for living cells and lipid droplets via FLIM and intensity measurements

A novel compound, named ET, was tested for the first time on living cells and its possible applications as a molecular rotor discussed.

The use of an Electron Bombarded Charge-Coupled Device (EBCCD) camera as a parallel-processing Time to Amplitude Converter device for SPC Imaging with sub-frame exposure time resolution was investigated and, although not implemented, the results supports the proposed method.

In order to design a wide field time-correlated single photon counting system, a Complementary Metal-Oxide Semiconductor (CMOS) Fast-Camera was coupled with an 3-stage image intensifier. This proved to be suitable for luminescence lifetime measurements of a Ruthenium complex, with results of 1.7μs comparable with confocal scanning Time-Correlated SPC (TCSPC). Finally, conclusions and future work are discussed.

Contents

List of Figures

List of Tables

Nomenclature

Chemical Compounds

$[Ru(dpp)_3]^{2+}$ Tris(4,7-dyphenyl-1,10-phenanthronline)ruthenium(II) dichloride

BODIPY Boron-dipyrromethene

Eu-POM Europium-polyoxometalate

Acronyms

AIDS Acquired Immune Deficiency Syndrome

APD Avalanche Photo Diode

APS Active Pixel Sensor

CFD Constant Fraction Discriminator

CHO Chinese Hamster Ovary

CMOS Complementary Metal Oxide Semiconductor

DLPC Dilauroylphosphatidylcholine

DPPC Dipalmitoylphosphatidylcholine

DSE Debye-Stokes-Einstein

ER Endoplasmatic Reticulum

FCS Fluorescence Correlation Spectroscopy

$FLIM$ Fluorescence Lifetime Imaging

$FPALM$ Fluorescent PhotoActivatable Localization Microscopy

$FRAP$ Fluorescence Recovery After Photobleaching

$HeLa$ Henrietta Lacks, the name of the patient the HeLa cells have been harvested

HPD Hybrid PhotoDetectors

IR InfraRed

$LMCT$ Ligand-to-Metal Charge Transfer

MCA MicroChannel Analyser

MCP Microchannel Plate

$MLCT$ Metal-to-Ligand Charge Transfer

MLE Maximum Likelihood Estimation

NA Numerical Aperture

OPE One Photon Excitation

$PALM$ PhotoActivated Localisation Microscopy

PHD Pulse Height Distribution

$PLIM$ Phosphorescence Lifetime Imaging Microscopy

PMT PhotoMultiplier Tubes

PSF Point Spread Function

QE Quantum Efficiency

RBC Red blood cell

ROI Region of interest

SIM Structured Illumination Microscopy

$SK-OV-3$ Human ovary adenocarcinoma

$SPAD$ Single Photon Avalanche Diode

$SSIM$ Saturated Structured Illumination Microscopy

$STED$ Stimulated Emission Depletion

$STORM$ Stochastic Optical Reconstruction Microscopy

$SWFM$ Standing Wave Fluorescence Microscopy

TAC Time to Amplitude Converter

$TCSPC$ Time Correlated Single-Photon Counting

RBC Twisted Intramolecular Charge Transfer

$TIRFM$ Total Internal Reflection Fluorescence Microscopy

TPE Two Photon Excitation

UV Ultra Violet

Chapter 1

Introduction

Biology, medicine, and the other life sciences pursue the study of living organisms at all levels. The scope of their research fields has expanded over time both in scale and in complexity, ranging from microscopic organism such as bacteria, to complex biological systems such as plants, animals, and entire ecosystems. Research for understanding the biological processes of these organisms has been supported by the continuous development of new techniques and instrumentation, aiming to solve the questions posed by the scientific progress in these fields. The innovations and the development of novel methods in other fields of study such as mathematics, chemistry, and engineering, enriched the pool of research techniques available to the life sciences.

Among the several subjects of study, cells are still the basis for biological research, while in-deep study of more complex pluricellular organisms still requires challenging technological advancements. Hence, the investigation of these cellular model systems represents a fundamental step to the understanding of biological phenomena and structures.

With the aim of studying living samples, high resolution techniques allowing the investigation of cells and their internal processes are necessary. Electron microscopy and atomic force microscopy (AFM) are non-optical microscopy techniques and achieve resolutions in the nanometer scale, however, the former is not suitable for living cell measurements (it normally requires coating and in vacuum imaging), while the latter is limited to the study of surfaces.

Optical microscopy, on the other hand, permits a resolution of hundreds of

nanometers and it is suitable for imaging living specimens. In recent years, technological advancements in localisation microscopy achieved resolutions below the optical diffraction limit and enabled the development of the so called super-resolution techniques, allowing single-molecule localisation. These achievements were publicly recognised in 2014 by the Nobel Prize in chemistry awarded to Moerner[3], for the imaging of the first single fluorophore, and to Betzig and Hell[4; 5] for the development of super-resolution techniques.

Alongside these technological advancements, fluorescence played a pivotal role: in optical microscopy and spectroscopy techniques, fluorescence provides a powerful multi-parameter tool (spectrum, intensity, lifetime, polarisation can be measured) with a wide range of biological and medical applications. Imaging of fluorescent-labeled molecules (fluorophores) is an established technique both for *in vivo* and *ex vivo* investigations, especially in live cell cultures or disease models. However, the quantitative measurement of fluorescent intensity in heterogeneous biological specimen is not straightforward, due to the high optical scattering of light. Fluorescence lifetime measurements proved to be a useful means to overcome this difficulty, and over the past decades time-resolved techniques affirmed themself for the significant contribution to biology and biomedical studies.

Fluorescence lifetime allows contrasting between different fluorophores in tissues and its measurements (on the assumption that the sample does not change) are independent of the fluorophore concentration and to variation of the fluorescent signal due to the instrumentation or the sample[6]. Therefore, this approach provides more robust quantitative information, compared to intensity measurements, in heterogeneous samples such as biological tissues.

In fluorescence microscopy in particular, single photon counting (SPC) techniques prove to be the most effective in regards of the Signal to Noise Ratio (SNR)[7; 8; 9]. Especially in the cases where the amount of emitted light is limited, the development of techniques exploiting all the available photon budget, before the fluorophore is irreversibly bleached, is fundamental[8; 10]. Thus, the development, investigation, and selection of new dyes and imaging approaches is of great interest, and the work in this thesis focuses on improvements in Photon Counting techniques.

In this chapter, the motivation for this project along with a literature review will

be given, fluorescence principles and fluorescence applications in microscopy described, then super-resolution techniques and the theory of molecular rotors will be introduced. Chapter 2 introduces the instrumentation and the methods that have been used in this project; the following two chapters (Chapter 3, Chapter 4) describe the application of two compounds, ET and BODIPY-C_{12}, and discuss possible improvements from the use of these dyes in nanoseconds Photon Counting imaging for living cells applications. Chapters 5 and 6 focus on the imaging techniques: in particular by using a Electron Bombarded Charge-Coupled Device (EBCCD) camera and a Complementary Metal-Oxide Semiconductor (CMOS) FastCamera for μseconds Photon Counting. At the end of each chapter, a brief summary of the section is presented. The last section, Chapter 7, summarises the findings and the results of this project; in addition to the conclusions, the future work possibilities are discussed.

1.1 Motivation

The work of this thesis focuses on the optimisation of techniques and applications using the single photon counting approach in microscopy and spectroscopy. The possibility of achieving single photon sensitivity is a great advantage but requires a tradeoff with the other parameters involved: the choice of the appropriate fluorescent dye is fundamental and the availability and limitations of electronics play a determinant role.

Among fluorescence-based techniques, fluorescence lifetime imaging microscopy has been demonstrated to be a powerful and reliable technique as it allows one to discriminate between different emitting components otherwise indistinguishable using intensity/quantum yields measurements alone[11; 12]. The application of FLIM can be performed either in time or frequency domain. While each technique presents advantages, the choice of a time correlated single photon counting approach (time domain) is often preferred to the frequency domain techniques due to the better signal to noise ratio, especially for low light illumination measurements[7].

Optical microscopy can be broadly divided into point-like and wide-field illumination and detection. The first configuration can take advantage of the SPC

approach, but suffers from the long processing time required and the low rate of data acquisition. On the other hand, wide-field approaches suffer from relatively low frame rates and are normally unable to achieve single-photon sensitivity. In general, techniques using single-point detectors, such as scanning in confocal microscopy, result in a high sensitivity but normally require long acquisition times in order to collect reliable statistics. However, when using living samples and/or investigating dynamic processes, reactions with short timescales cannot be studied with this approach, and in practice only long timescale reactions (i.e. longer than the duration of the measurement) can be easily analysed[13]. Furthermore, the fluorescent dyes commonly available for FLIM have lifetimes in the nanosecond range, and point-like electronics and instrumentation have been developed to achieve measurements in the same timescale. With the ever increasing achievable speed of modern electronics, such as delay lines, wide-field approaches can capitalise on these improvements, but a tradeoff between acquisition rate and sensitivity is still necessary. In order to overcome these limitations, detectors attempt to increase the signal-to-noise-ratio by intensifying or adding a gain to the collected signal (i.e. intensified CCD and EMCCD), in exchange for a loss in spatial resolution. Thus, the development of photon-sensitive techniques and detectors expanding these time and sensitivity boundaries can be beneficial to several fields, especially to the study of living cell dynamics where different intracellular signalling and processes can range from sub-second timescales to hours or even days[14]. This project presents the investigation on using a FastCamera as a widefield imaging system, and sets the theoretical framework for using an EBCCD camera as a parallel TAC device.

The study on the molecular rotors (compounds whose fluorescence intensity or lifetime are sensible to their environment viscosity) presented in this work is relevant for several fields such as biology, chemistry and engineering. In fact, reactions dependent on diffusion often set the rate of mass transport of reagents, thus deeming them greatly important for these scientific fields. Viscosity is one of the main factors that determines the mass transfer rate, so it is important to measure it in a reliable and precise way. Whereas mechanical methods for viscosity measurements have been developed[15], it is of interest to develop methods to measure microviscosity: for many complex systems at the microscopic level,

the viscosity is heterogeneous and the measured macroviscosity is an averaged value. For example, for biological systems like cells, the membranes and organelles are expected to have different viscosities and their correct measurement is of fundamental importance for both understanding and controlling the processes within the cell. In fact, several diseases like diabetes, atherosclerosis and Alzheimer have been linked to interactions at the membrane, and these events can be triggered by changes in viscosity[16; 17; 18; 19]. Furthermore, the use of macroscopic viscosity measurements of biological fluids (blood, blood plasma, etc.) has been suggested to monitor diseases such as polycythemia, multiple myeloma, and leukemia[16; 19; 20; 21; 22]. The possibility to map the viscosity at microscopic level is then even more important in the aspect of understanding the intracellular reactions taking place within the different regions of the cell. In order to achieve measurements at molecular level, several methods emerged, including both microscopic and spectroscopic techniques, such as fluorescence correlation spectroscopy (FCS)[23; 24; 25], fluorescence recovery after photobleaching (FRAP)[26], fluorescence anisotropy (steady-state or time resolved)[27; 28; 29], single particle tracking[30], and the observation of viscosity-dependent photochemical reactions[31; 32; 33]. Mechanical methods have also been applied, such as measuring the change in morphology due to an applied force: for example these methods have been applied to measure cell membranes viscosity[15; 34] but they do not allow the investigation of the intracellular behaviour and submorphology of the cell. However, when intensity measurements are involved, it is important to consider the difficulties in decoupling changes in intensity arising from different sources. These changes, in fact, may result from viscosity or spatial variations of dye concentration within a complex system (i.e. a cell). In these cases, viscosity measurements based on fluorescence lifetime are considered more reliable compared to the intensity ones. Within this framework, this thesis presents the investigations on two molecular rotors and on two novel imaging approaches, aiming to enrich the pool of available techniques for the life science.

1.2 Fluorescence

Fluorescence is a phenomenon known since ancient times, but only during the 19th century a scientific explanation of it was given by Stokes[35]. Fluorescence is a particular form of photoluminescence: it consists of the emission of light of a certain colour (wavelength) due to an excitation with a higher energy light (shorter wavelength). This behaviour is described by the Jablonski diagram[36] in Figure 1.1.

The part of a molecule responsible for its colour is called chromophore: this region absorbs only specific wavelengths and reflect or transmit others. If the absorbed light is then re-emitted, this phenomenon is known as luminescence. The irradiated light excites one weakly bound electron of the luminescent probe from its lower electronic level (singlet state S_0) to a higher singlet level (e.g. S_1) and the electron in the excited state has the spin paired (opposite spin) to the electron in the ground state, so a transition is permitted. The decay of such excited electron to the lower energy state can be non radiative (vibrational relaxation) with a rate constant k_{nr} or radiative (luminescence) with rate constant k_r. The latter, in particular, can be divided in two kinds of emission according to the route of the electron: if it moves from a singlet level to a lower energy one (from S_1 to S_0) the phenomenon is called "fluorescence"; if during its relaxation it moves instead to a triplet level (T_1), the spin of the excited electron is reverted and the transition to ground level is formally forbidden (as the electrons have the same spin), this leading to a lower emission rate: this phenomenon is known as "phosphorescence". At macroscopic level, these two phenomena differ in the time between excitation and emission: typical fluorescence lifetime is in the order of several nanoseconds[6], although some fluorophores have lifetimes less than one nanosecond[37] and others about one hundred (depending on their environment[38; 39]), and phosphorescence in the order of μs[6], due to the forbidden transition and thus the lower probability of the electron to move from excited state to ground state.

1.2.1 Fluorescence Lifetime

Fluorophore is the term commonly used to define the group of compounds in which fluorescence can occur following excitation. They are often conjugated to a macromolecule (e.g. lipid, protein, etc) and can be used as fluorescent dyes. Fluorescence lifetime is defined as the average time spent by a fluorophore in the excited state and depends on the radiative and non radiative emission rate, thus it can be expressed as

$$\tau = \frac{1}{k_r + k_{nr}}. \tag{1.1}$$

For a single exponential decay, the lifetime τ is also defined as the decay constant of the exponential:

$$I = e^{-\frac{1}{\tau}t} \tag{1.2}$$

being I the emitted light intensity and t the time. By using this definition, the emission will decrease about 63% by the time $t = \tau$. In fact, when the time is equal to the lifetime, the emission is $1/e \approx 0.37$. Due to the independence of fluorescence lifetime measurements from the concentration of fluorophores and the increasing information available from its analysis, time-resolved fluorescence is largely used nowadays in fluorescence spectroscopy, imaging, and biology[40]. The main advantages of fluorescence-related techniques are the high sensitivity (possible to image single molecule), the possibility to label specific structures (e.g. organelles inside a cell), the low phototoxicity and the sub-micron resolution; in addition, fluorescence microscopy can be applied to living specimens as optical techniques do not damage the sample.

Each energetic state of a fluorophore comprise several vibrational levels and the transitions between the states have different degree of probability: due to this, by exciting a sample along a range of wavelengths it is possible to plot its absorption spectrum, as shown in Figure 1.2. Absorbance measurements will reveal more information about the sample behaviour, in accordance with the Beer-Lambert

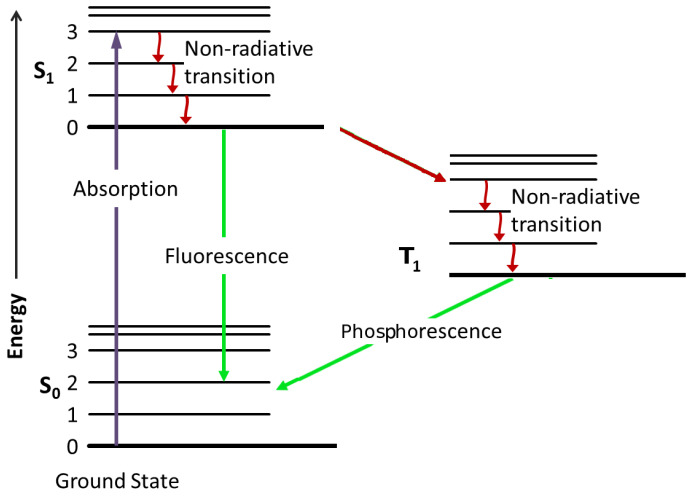

Figure 1.1: Jablonski diagram: the absorbed photon excites a weakly bound electron in the molecule from the ground state (lower electronic level, S_0) to a higher energy level (excited singlet level, S_1). The return to the ground state may happen in a radiative or non-radiative way. If the radiative decay happens from states having paired spin electrons (from excited singlet level S_1 to ground level S_0), the emission is called fluorescence. If the electron reverts its spin, instead, a "forbidden" triplet level (T_1) is formed and the radiative decay from T_1 to S_0 is called phosphorescence.

law[6]:

$$A = \epsilon[c]d \tag{1.3}$$

where A is the optical density of absorbance of the sample, ϵ is the coefficient of molecular extinction, $[c]$ the concentration of the absorbing substance and d the length of the path. By assuming to have negligible scattering, we can rewrite the previous equation in respect of the absorbed light:

$$A = -\log_{10} \frac{I_0}{I(d)} \tag{1.4}$$

with I_0 the intensity of the incident light and $I(d)$ the intensity at the length d. Due to the different vibrational levels of the ground state, the radiative transitions from the excited state will produce different energies for the emitted photons. Because of that, instead of at a single frequency, emission can be observed over a range of frequencies, thus producing its emission spectrum. By remembering the relationship between the wavelength λ and the frequency ν:

$$\lambda = \frac{c}{\nu} \tag{1.5}$$

with c being the speed of light, the terms wavelength and frequency can be freely exchanged. The spectra for emission and absorption are usually separated for most fluorophores, but they can partially overlap. The separation between the peaks of each spectrum is called *Stokes shift*: the excitation energy is higher than the emission energy and this results in the emitted light spectrum to be shifted to higher wavelengths (lower frequencies). In addition, this shift is independent from the excitation wavelength; in fact, even if an electron can reach a higher excited state and a radiative transition is possible, in most cases it will reach the lowest vibrational level (e.g. from S_2 to the lowest level of S_1) before emitting, thus making the spectrum independent of the excitation frequency. Since the spacing of the vibrational levels among excited and ground states are similar and so are the respective transition probabilities, the emission spectrum often recalls the absorption one as in a mirror (mirror image rule). In the particular case of the electron reaching a further excited state (e.g. S_2) but emitting just during

the decay from S_1 to S_0, this rule is broken as the emission spectrum mirrors only the part of the absorption spectrum corresponding to the $S_1 - S_0$ transition.

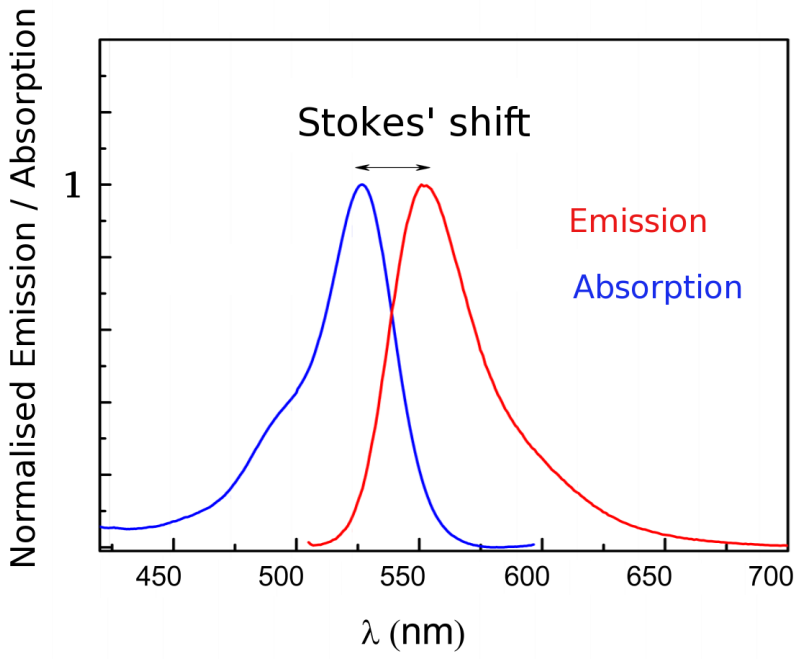

Figure 1.2: Stokes shift: normalised absorption and emission spectra example for the Rhodamine 6G fluorescent dye (redrawn from [41]). The absorption peak is at 530 nm, the emission peak at 560 nm, and the resulting Stokes'shift is ∼30 nm. Since the spacing of the vibrational levels among excited and ground states are similar and so are the respective transition probabilities, the emission spectrum often recalls the absorption one as in a mirror.

1.2.2 Quantum Yield

Along with the lifetime, the quantum yield is one of the fundamental characteristics of a fluorophore. Fluorescence quantum yield Φ is a value that represents the efficiency of a fluorophore, and it is expressed as the ratio between the amount of photons emitted and absorbed, so its value is between 0 and 1. When a photon event excites a fluorophore, its deactivation may happen via radiative or non-radiative route: the quantum yield express thus the probability of a photon to

be emitted via fluorescence.

$$\Phi = \frac{\text{photons emitted}}{\text{photons absorbed}}. \tag{1.6}$$

The quantum yield is probabilistic which means that it can also be expressed as a function of the rate constants: given k_r and k_{nr} the rate constants related to the radiative and non radiative transitions respectively, Φ can be written as

$$\Phi = \frac{k_r}{k_r + k_{nr}}. \tag{1.7}$$

In different environments or conditions, the same molecules can show different lifetimes and quantum yields, this depending on changes in the rate constants. In general, high quantum yields indicate a high radiative rate k_r (in practice, the majority of electrons return to the ground state via the preferred emissive route), and likewise a short lifetime. Vice versa, longer lifetimes are related to larger non radiative or smaller radiative rates: for example, phosphorescence emission presents a very low radiative rate (due to forbidden transitions) and thus long lifetimes ($\sim \mu s$).

1.2.3 Bleaching

Bleaching is a generic term indicating the processes that set the maximum number of times a fluorophore can undergo an excitation cycle between the ground and the excited states. In principle this number is unlimited, but in practice it is limited to few tens of thousand cycles[12]. The effect of the bleaching is to cause the fluorophore to permanently lose the ability to express fluorescence. On the other hand, when this phenomenon is reversible it is generally termed quenching, this indicating all the processes leading to a temporary loss of the ability to emit due to non-covalent interactions between a fluorophore and its environment (or sometimes between identical fluorophores: self-quenching)[42].
The processes connected to the bleaching are several and different, and the exact photochemistry is not deeply understood but it is evident a correlation with the existence of a triplet state. In fact, the time normally associated to the triplet excited state is longer than the brief permanence in the singlet state, thus

increasing the probability of an excited molecule to losing an electron in the interaction with surrounding molecules or with molecular oxygen[12].
The oxygen, excited to its singlet state due to these interactions, may further chemically react with its environment. Singlet oxygen is particularly dangerous in living samples environments as it may interact with organic molecules leading to phototoxicity for the cells[12].

1.2.4 Autofluorescence

Some biological substance exhibit intrinsic fluorescence, and this phenomenon is normally indicated as autofluorescence. The research on autofluorescence mechanisms is relevant in particular for the study on living cells and tissues, both as diagnostic tool and for the better understanding of molecular interactions and signalling processes in living specimens. The main autofluorescent fluorophores in cells are amino acids, necessary to build enzymes and proteins, redox cofactors regulating the metabolism, porphyrins, proteins, and fluorescent-pigments (often used as markers of ageing-related diseases[42]). On the other hand, autofluorescence signal is often considered noise by fluorescence techniques as its spectral emission and lifetime may overlap the ones of the fluorophores normally used in these measurements.

1.2.5 Fluorescence Anisotropy

When a fluorescent solution is excited by polarised light, a subset of the fluorophores population is preferentially excited by this light, and the final emission may also be partly polarised. The fluorescence anisotropy (r) represents the amount of emission that shows polarisation. This phenomenon depends on the fluorophore structure and the existence of preferred directions for absorption and emission. In example, in a homogeneous solution the fluorophores are in the ground-state and randomly oriented; when excited by a polarised light, the emitters whose absorption transition moments are oriented parallel to the electrical vector of incident light are preferentially excited[6, chapter 10] (the excitation probability is expressed by eq. 1.16). Thus, a fraction of emitted light is polarised according to the polarisation of the excitation source, although not all of the stim-

ulated molecules are oriented in the same direction. This is due to the rotational diffusion of the excited fluorophores occurring during their excited state lifetime. Hence, information about the local viscosity of fluorophore's environment and the size and mobility of the rotating unit can be obtained from anisotropy measurements. In order to calculate anisotropy value, both parallel and perpendicular (to the excitation light polarisation) light intensities have to be measured, indicated as $I_{||}$ and $I_{\perp}$ respectively. This task can be performed either repeating the same experiment in the two polarisations or by using a beamsplitter to simultaneously[1] measure the signals. Fluorescence anisotropy measurement depends on the size, the mobility, the shape of molecules and on their environment[6; 41]. Furthermore, the fluorescence lifetime of a fluorophore is not affected by its rotational diffusion. Anisotropy measurements are normally performed using two methods: L-format or T-format configurations[6]: the former uses a single emission channel, whilst the latter observes the parallel and perpendicular components using two different channels. The L-format is frequently used because most detectors have only a single channel. A schematic diagram of L-format anisotropy measurements using a cuvette (like the ones performed in this work) is shown in Figure 1.3. Fluorescence anisotropy can be subdivided in steady-state anisotropy and time-resolved anisotropy. The temporal resolution achievable for the rotational correlation time is normally between 0.1 and 10 times the fluorescence lifetime[44; 45]. The general equation defining the fluorescence anisotropy r is:

$$r = \frac{I_{\parallel} - G \times I_{\perp}}{I_{\parallel} + 2G \times I_{\perp}} \tag{1.8}$$

and the time-resolved anisotropy can be then defined as:

$$r(t) = \frac{I_{\parallel}(t) - G \times I_{\perp}(t)}{I_{\parallel}(t) + 2G \times I_{\perp}(t)} \tag{1.9}$$

[1]The simultaneous acquisition of the two signals requires two independent acquisition boards. In fact, after each photon is detected the resetting of the capacitor on the board generates a *dead time*, when no other photon can be detected. In general, when only a board is available, the collection is alternated between the two detectors, further reducing the amount of collected light[43].

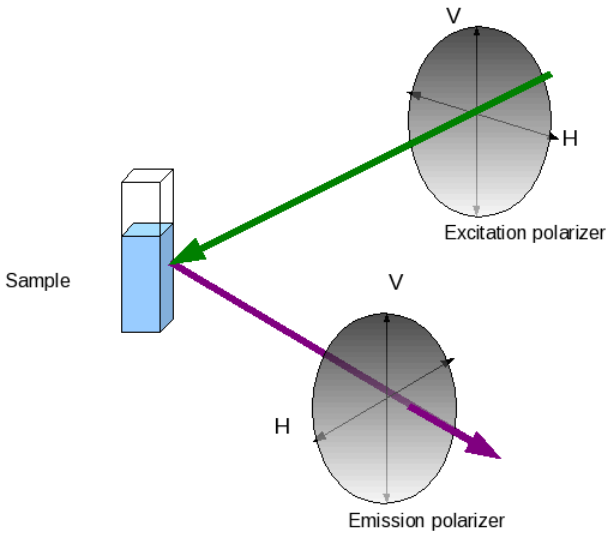

Figure 1.3: Schematic of L-format anisotropy measurement

where r is the anisotropy, and $I_{\parallel}$ and $I_{\perp}$ the parallel and perpendicular polarisation components of the emission in respect to the incident light. The numerator represents the intensity difference between the two directions, whether the denominator is the total fluorescence emission. The factor 2 at the denominator depends on the way the measurement is performed: the total emission is the sum of the parallel component $I_{\parallel}$ and the two perpendicular components (see Fig. 1.3) but, since only one of them is measured, the value $I_{\perp}$ is multiplied by 2[46]. In case of different transmission and detection efficiency, the correction factor G is present in the equations 1.8 and 1.9; otherwise, its value is 1. This factor represents the detection efficiency at a given wavelength and it can be expressed as the ratio between perpendicular and parallel intensities $I_{0\perp}$ and $I_{0\parallel}$ for a sample of known polarisation (normally $\sim$ 0, having equal components in the two polarisation directions)[46]:

$$G = \frac{I^0_{\perp}}{I^0_{\parallel}}. \tag{1.10}$$

For spectrophotometer measurements, the G factor can be calculated due to symmetry: for the configuration in Figure 1.3, by polarising horizontally (H) the input signal, the polarised emission vertical (V) and horizontal (H) components are both perpendicular to the excitation signal and so should be equal. The ratio of these two components is the G factor[6; 46]:

$$G = \frac{I_{HV}}{I_{HH}}, \tag{1.11}$$

where I_{HH} and I_{HV} are the measured emission intensity detected horizontally and vertically respectively, having the excitation signal polarised horizontally.In particular, by identifying the vertical and horizontal polarisation as in Fig. 1.3, equation 1.8 can be written as[11]:

$$r = \frac{I_{\parallel} - G \times I_{\perp}}{I_{\parallel} + 2G \times I_{\perp}} \tag{1.12}$$

with the G factor being:

$$G = \frac{I_{\perp}}{I_{\parallel}}. \tag{1.13}$$

In the hypothesis of a freely rotating and spherical molecule, the time-resolved fluorescence anisotropy decay can be expressed as:

$$r(t) = r_0 e^{-\frac{t}{\theta}} \tag{1.14}$$

where r_0 is the initial anisotropy $r_0 = r(t)|_{t=0}$, and θ is the rotational correlation time. In case of a hindered molecule (e.g. in an anisotropic environment such as a cell membrane), the previous equation is modified as follows:

$$r(t) = (r_0 - r_\infty)e^{-\frac{t}{\theta}} + r_\infty \tag{1.15}$$

where r_∞ is defined as the anisotropy at a time $t = \infty$. If this value is not zero, it indicates the presence of a barrier to free isotropic rotation. If a dipole absorption moment is parallel to the incident light polarisation, the molecule excitation occurs. Thus, the fluorescence anisotropy and in particular r_0 depend on the ex-

citation probability. For vertically polarised excitation light and $z-$symmetrical molecule, this probability p can be written as[47]:

$$p_i \quad = \quad \cos^{2i}\alpha \cdot \sin\alpha \tag{1.16}$$

where α is the angle between the absorption dipole moment and the vertical excitation light, and i indicating the type of $i-$photon excitation (in this work, only one-photon excitation has been used, so $i = 1$). If a confocal microscope is used to perform the polarised fluorescence measurements, additional depolarisation has to be taken into account for large Numerical Aperture objective lens[48; 49; 50; 51; 52; 53]. Without taking into account the instrumental depolarisation, it is possible to define[6; 27; 47; 54] the fundamental anisotropy in the following way[54]:

$$r_0 \quad = \quad \frac{2i}{2i+3}\left(\frac{3}{2}\cos^2\beta - \frac{1}{2}\right), \tag{1.17}$$

given β the angle between the absorption transition dipole moment and the emission transition moment, and again i indicating the excitation type. From eq. 1.17 we can then define the maximum values for r_0 as 0.4 in case of one-photon excitation and 0.57 for two-photons. The equation for one-photon excitation can be expressed:

$$r_0 \quad = \quad \frac{2}{5}\left(\frac{3}{2}\cos^2\beta - \frac{1}{2}\right), \tag{1.18}$$

In order to describe the depolarisation depending on the rotational diffusion (in case of spherical molecules), the Perrin equation[6] can be used:

$$\frac{r_0}{r} \quad = 1 + \frac{\tau_f}{\theta} = \quad 1 + 6\tau_f D_{rot} \tag{1.19}$$

where τ_f is the fluorescence lifetime, θ the rotational correlation time, r the steady-state anisotropy, and D_{rot} the rotational diffusion coefficient (equal to $\frac{1}{6\theta}$). When the lifetime is much larger than θ ($\theta \ll \tau_f$), the value of r tends to zero. On the other hand, when the rotational correlation time is much larger than

the lifetime ($\theta \gg \tau_f$), the ratio τ/θ is small, thus the values of initial anisotropy r_0 and of steady-state anisotropy are very close. The rotational correlation time can be described by the Debye-Stokes-Einstein (DSE) equation:

$$\theta = \frac{\eta V}{\kappa_B T} \tag{1.20}$$

where η is the medium viscosity, V the molecule's volume, κ_B the Boltzmann constant, and T is the temperature expressed in Kelvin. By combining equations 1.20 and 1.19, the relationship between viscosity and anisotropy can be described as shown in Equation 1.21 and in Figure 1.4, the former being a different form of the Perrin equation and the latter being named Perrin plot.

$$\frac{1}{r} = \frac{1}{r_0} + \frac{\tau_f \kappa_B T}{r_0 \eta V} \tag{1.21}$$

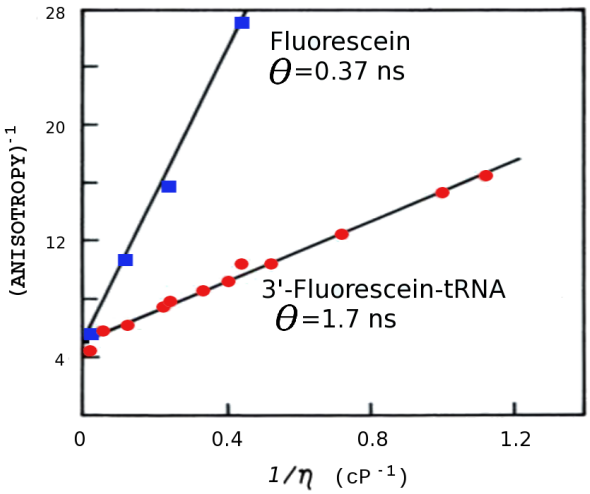

Figure 1.4: Example of Perrin plot for Fluorescein (blue squares) and Fluorescein-labelled tRNA (red circles). From the intercept with the y axis is possible to extrapolate $1/r_0$, this giving an apparent value of r_0 =0.2 for the Fluorescein samples. The temperature was constant at 20°C (293 K); excitation at 480 nm and emission at 520 nm. Graph adapted and redrawn from [6, page 370].

1.3 Fluorescence microscopy and SPC imaging

Fluorescence microscopy is widely used in biology and medicine: although it does not reach the high resolution of electron microscopy, it allows to study live cells and their environment, making this technique useful in all the fields where it is important to preserve the health of the sample. Sensors for pH, oxygen, ions, glucose, chloride, calcium and other mediums have been developed exploiting the fluorescent properties of several fluorophores[6, chapter 19].
Fluorescence microscopy is based on the optical microscopy techniques, where sample images are acquired through visible light. The development of the first microscope dates back to the 16th century, when Hans and Zacharias Jansen, a spectacle maker and his son, realised a magnifying device consisting in two lenses in a tube[55]. The scientific community focused then on using the microscopes[56] to understand the principles of imaging formation and on developing a theory for diffraction and interference[57].
The diffraction pattern generated by point-shape object on the image plane of a microscope is called *Airy pattern*, and its central, brightest region is named *Airy disk*. The Airy disk represents the best focused spot for a circular aperture imaging system. When a pinhole is placed in front of the detector, and its diameter is set to the size of the Airy disk, it only allows the first order of the Airy pattern and this diameter correspond to 1 *Airy* unit. Firstly developed by Abbe[2; 57] in the 19th century, the theory of image formation and optical resolution describes the relationship between the incident light wavelength, the microscope objective, and the diffraction-limit:

$$d = \frac{1.22\lambda}{NA} = \frac{1.22\lambda}{n \sin \Theta} \tag{1.22}$$

where d is the diameter of the resulting spot in the image plane for a point-like light source, λ the illumination light wavelength and NA, the numerical aperture of the microscope objective. The NA depends on the angular aperture of the microscope (2Θ) and the refractive index n of the medium between the objective and the diffracting object. The point spread function (PSF) is the response of an imaging system to a point-like light source in a focused optical system, and

its ideal form can be considered as the fundamental unit in imaging theory: the Airy disk corresponds in fact to the PSF in the image plane for an axially-aligned, single lens optical system.

Fluorescence microscopes can be divided in two main groups: wide-field and

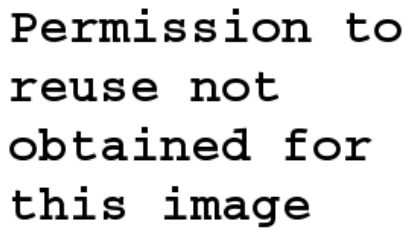

Figure 1.5: Airy pattern example: the figure shows the different cases of resolved and unresolved patterns. The resolution limit is shown and is defined as the smallest distance at which two pattern can still be resolved. The first order of the Airy pattern is termed Airy disk.[58].

confocal. In a wide-field microscope, the sample is illuminated and all the light emitted from the sample contributes to the formation of the image, regardless of the focal plane that originates it. A confocal microscope instead collects light from the focal volume only. A schematic for a confocal microscope is presented in Figure 1.6: the insertion of a pinhole in the excitation path allows to scan the sample point by point and the fluorescence signal collected comes only from the focal spot, generating a smaller PSF in respect to an equivalent wide-field system. The light is collected through the same objective lenses and routed to one (or more) photomultiplier tube (PMT) through a dichromatic mirror and the 2D image reconstructed using a dedicated software. The excitation source can use either one or two photons: one-photon excitation (OPE) consists in exciting the fluorophore at a single wavelength corresponding to its absorption

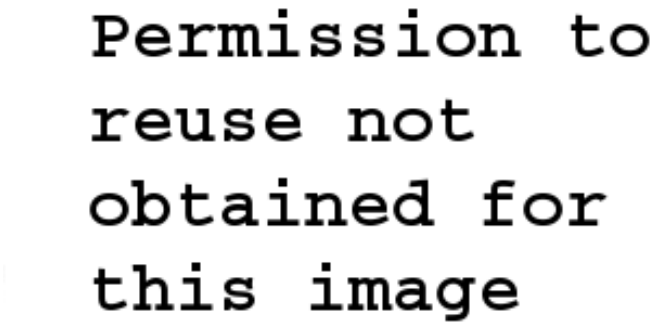

Figure 1.6: Confocal microscope working principle: the illumination is provided by a focused light beam (normally a laser) scanning the specimen (green). The fluorescence emission (red) is then routed through a dichromatic mirrorand a pinhole to the detector. The pinhole allows only the on-focus fluorescence from the focal plane to reach the detector[58].

peak; two photon excitation (TPE) instead uses two photons of lower energy than the required excitation wavelength to reach the excitation state of the molecule (if more photons are used, it is referred as multi-photon excitation). Since the size of the Point Spread Function depends on the wavelength, using OPE is preferred when higher resolution is needed. On the other hand, TPE allows to focus and collect light from the focal spot only, then excluding fluorescence coming from out-of-focus areas and reducing photobleaching. In OPE only the out-of focus effect can be reduced, usually by inserting a pinhole in the image plane in front of the detector. OPE normally uses light in the visible or ultra violet (UV) range, whereas TPE uses light in the near Infrared spectrum. TPE is especially preferred when a higher penetration depth is required or when the Stokes shift of the fluorophore is small. In fact, although the light scattered from biological tissues or materials limits the thickness of the sample to be imaged (typical $80\mu m$[59] for OPE), for TPE it is possible to locate the origin of the multiple scattered signal allowing penetration depths of 100s microns[59]. In addition, when the absorption and excitation spectra are quite close to each other, TPE allows a better wavelength-separation of the excitation beam and emitted fluorescence[60].
In Figure 1.7 it is possible to see the difference between the PSF of a confocal and of a wide-field microscope, and Table 1.1 shows a comparison for axial and lateral resolution of the two type of microscopes: the out-of-focus background fluorescence in the widefield microscope prevents the possibility to resolve in the z direction. The typical resolutions for conventional light microscopes are $200 - 300$ nm in x,y directions and $500 - 700$ nm in z[61].

1.3.1 Fluorescence Lifetime Imaging (FLIM)

Fluorescence Lifetime Imaging (FLIM) is a microscopy technique that maps the lifetime of fluorophores on the sample. The fluorescence decay of the fluorescent probes is collected in each pixel of the digital image and the lifetime can be estimated by fitting these decays to an appropriate function. In most of the applications we describe, this fitting is performed using single, double or triple exponential functions: the choice of which matching function to use depends

Figure 1.7: Point spread function for *a)* widefield and *b)* confocal microscope using a 63× NA 1.4 objective and aperture size 0.7 Airy units[62]. The lateral (x,y) and axial (z) sizes of the PSF are smaller for the confocal microscope in respect to the wide-field by circa 30%. In the picture, the optical axis is vertical, the radial axis is horizontal. The false colour bar represents the square root of the intensity, the scale bar length is 1μm.

	Confocal	Wide Field
Lateral	$R_{xy} = \frac{0.4\lambda}{NA}$	$R_{xy} = \frac{0.6\lambda}{NA}$
Axial	$R_z = \frac{1.4n\lambda}{NA^2}$	-

Table 1.1: Resolutions for confocal and widefield microscopes, where r is the radius of the Airy disk for a point source in image plane, λ is the wavelength of the excitation light, n the refractive index, and NA the numerical aperture of the microscope objective[2].

on the studied fluorophore(s), as its decay may be single or multiexponential; in live samples, it is common to find multiple exponential effects due to the different environment affecting the fluorophore lifetimes. By integrating the collected light for each pixel, it is also possible to form an intensity image of the sample. From the combination of the intensities and the lifetimes is then possible to obtain information and resolve details impossible with the fluorescence intensity alone. An example of data acquired with a confocal microscope and processed with SPC-Image software (Becker&Hickl) is presented in Figure (1.8). The colouring scale shows the different lifetimes in specific areas of the FLIM image of the sample and the bottom area shows the exponential fitting for lifetime calculation in the pixel identified by the blue lines.

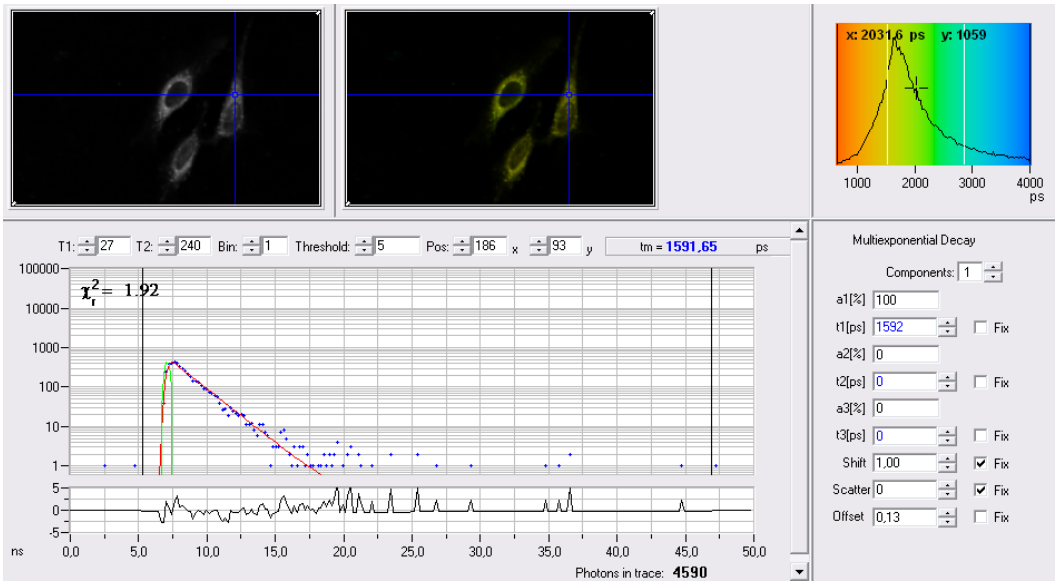

Figure 1.8: FLIM image example with SPCImage B&H software: BODIPY-stained HeLa cells. The pictures shows the intensity (top left) and lifetime (top) images for human cervix cancer cells (HeLa) imaged at 37°C with a 5% CO_2. The graph at the centre shows the fluorescence decay (blue dots) for a pixel in the image and its fitting (red line). The false colour histogram (top right) shows the distribution of the lifetimes in the image, ranging from 800 to 4000 ps.

1.3.2 Super-resolution Microscopy

In recent years, microscopy has been developed to surpass the optical diffraction limit as defined previously in this thesis, and achieve the so called super-resolution imaging. The recent chemistry Nobel prize awarded in 2014 to Moerner (for the first detection of a single fluorophore[3]), Betzig (Photoactivated localisation microscopy[4]), and Hell (Stimulated emission depletion[5], 4Pi[63]) further shows that the achievements in this field have been of fundamental importance for the scientific community. In particular, PhotoActivated Localisation Microscopy (PALM) and Stochastic Optical Reconstruction Microscopy (STORM) techniques and data processing will be discussed in Section 5.4: the approach for these methods is based on the localisation of emitting samples. It was independently developed by three different research groups[64; 65; 66] and named STORM[67], PALM[4], and Fluorescent PALM[68] (FPALM). For simplicity, in this work we will refer to this technique as STORM or PALM.

Stimulated Emission Depletion (STED) employs two pulsed lasers, one having a toroidal shape: the first laser excites the fluorophores in the focal spot, while the second depopulate a "ring" of fluorophores around it, from excited to ground states, via stimulated emission. The second laser has a zero value at its centre and a non-zero value in a circle around it: this particular pattern is also limited by the diffraction limit and as a consequence, STED alone can not achieve super resolution. This limitation is surpassed by the saturation of the depletion level: above a certain intensity of the laser, all the excited electrons are depleted and the spontaneous fluorescent emission is suppressed. As a result, the fluorescing area is only a small region around the focal point and its size is limited by the power of the laser and not by the diffraction of light. The resulting PSF is then far smaller than conventional light microscopy, achieving lateral resolution of generally $\sim$ 20 nm [69], but the measurement of a nitrogen-vacancy PSF of 5.8 nm in crystals[70] have been reported.

The 4Pi technique is based on an attempt to collect all the light emitted from the sample, not only from one side as normally happens with a single objective configuration. It uses two opposing objectives to excite the sample and collect the emission. Exploiting this approach, the PSF elongated in z assumes a

more symmetrical shape and an axial resolution of ∼100 nm can be obtained[63]. Among the several other techniques developed and emerging we can cite in example, Structured Illumination Microscopy (SIM)[71; 72] and Standing Wave Fluorescence Microscopy (SWFM)[73]. Along with these techniques, also Total Internal Reflection Fluorescence Microscopy (TIRFM)[74] can be mentioned as it achieve resolution improvements, but only in the z direction. SIM is a widefield technique that achieves resolution improvements by employing a structured illumination pattern: a grid structure, generated through interference, is superimposed on the sample during the images acquisition. This pattern is shifted or rotated between each image set collection and the results processed with specific algorithms, these allowing to resolve high-frequency features normally not detectable with the microscope. This technique can be applied in axial, lateral, or both directions. Since the diffraction limit affects the illumination pattern itself, the achievable resolution for SIM is about double of a standard widefield microscope[71; 75; 76]. By saturating the excitation pattern (Saturated SIM) lateral resolutions of 50 nm have been achieved [77]. SWFM technique[78; 79] exploits the standing waves formed by the interference of two laser beams in order to generate an excitation pattern along the axial direction, thus allowing optical sectioning of the imaged sample. TIRFM has been extensively used in fluorescence microscopy and spectroscopy. It exploits the different refractive indices at the interface of two adjacent materials: the incident light above a critical angle at the glass-probe interface creates an evanescent wave inside the sample. This wave can be used to excite fluorescent molecules within a small thickness ($\sim$ 100 nm [80; 81]) of the sample, thus TIRFM applications are limited to the near-surface region. The $PALM$ technique consists in the combination of single fluorophore imaging capability with selective activation of several distributed fractions of these luminescent probes in time, in addition to the data processing to generate sub-diffraction-limited images. The studies on single-molecule imaging in the last decades[84; 85] demonstrate the possibility to calculate the centre of a molecule with great precision (further the diffraction limit). The resolved distance is inversely proportional to the square root of the number of photons detected[86]: for example, in order to achieve a resolution of $\sim$ 10 nm the technique requires about 1000 photons (in low light level background conditions).

	Optical microscopy		
Wide field	Lateral resolution:	200-300 nm	[81]
Confocal	Lateral resolution:	150-200 nm	[81]
	Axial resolution:	500-700 nm	[61]
TIRF	Lateral resolution:	200-300 nm	
	Axial resolution:	100 nm	[81]
STED	Lateral resolution:	∼20 nm	[69]
PALM	Lateral resolution:	20-50 nm	[81]
STORM	Lateral resolution:	∼30 nm	
	Axial resolution:	∼50 nm	[82]
SIM	Lateral resolution:	∼100 nm	
	Axial resolution:	∼300 nm	[65; 83]
4Π	Lateral resolution:	∼200 nm	
	Axial resolution:	∼100 nm	[66]
	Electron microscopy		
TEM		0.05 nm	
SEM		< 1 nm	
	Scanning Probe microscopy		
AFM	Lateral resolution:	∼1 nm	
	Axial resolution:	∼0.1 nm	
NSOM	Lateral resolution:	20-50 nm	[66]

Table 1.2: Resolution comparison for different imaging techniques. The first part of the table shows the optical microscopy resolutions, whereas the second and third part briefly states the resolutions for electron and scanning probe microscopy.

However, this localisation method is not suitable in biological systems for a large amount of proteins. In fact, instead of only a single emitter below the diffraction limit, the minimum resolution volume presents a high density of fluorescent proteins, and thus the overlapping intensities prevent from using single-molecule-localisation. More complex algorithms can be used to resolve multiple PSFs, but this increases the complexity and the computational cost. In order to circumvent this limitation, it is possible to activate and localise a sparsely distributed subset of molecules: in this way even if each diffraction-limit volume will contain several fluorophores, it will be possible to resolve their centres as long as they are wavelength-separated. In practice, in a low-density situation, each subset emits at different wavelengths and individual molecules can be resolved, so their centres can be located, recorded, and a super-resolution image created. The application of this technique became possible along with the development of photoactivatable fluorescent labels[64; 71; 73; 75; 83; 87; 88]. The operating principle of PALM assumes a starting situation where most of the molecules are not active, and only a small fraction of them (in the order of 1%) is then activated, yielding fluorescence. This emitting state is usually obtained via UV or near-UV excitation; the fluorescent subset is then imaged, and each contributing molecule localised with a precision beyond the diffraction limit. These fluorescent labels are then deactivated or somehow removed (e.g. by photobleaching), and a new fraction of probes can be activated and imaged, generating a new set of centres' coordinates for the final image reconstruction. By repeating this acquisition routine for thousands of cycles, and obtaining even millions of molecule localisations, a reconstructed super-resolution image of the labelled structure can be created. Another main feature of this method is its simplicity: in fact, the microscope's setting are the same as for a common wide-field microscope, making it a quite economical super-resolution technique. The main advances in this field depend on the fluorophores, though. The number of newly developed photoactivatable labels is growing[71; 73; 75; 83; 88] and in addition to it, a large amount of existing fluorophores have been discovered to photoswitch under certain conditions [69; 75; 83; 89; 90; 90; 91; 92].

1.4 Molecular Rotors and Viscosity

Viscosity is a primary feature of fluids and it affects diffusion, mobility and other characteristics of the fluids. Viscosity is defined as the resistance of a fluid to flowing. It can be described in different ways, according to field of study: in this work we will focus on the absolute (or dynamic) viscosity. This viscosity η is expressed as the ratio between the shearing stress and the fluid gradient of velocity:

$$\eta = \frac{F \cdot d}{\Delta v \cdot A}, \tag{1.23}$$

where F is the shearing force, A the area where the force is acting, Δv is the velocity variation, and d the distance between the flowing layers of fluid.
While there are established techniques to measure macroscopic viscosity, measuring microscopic viscosity is still a debated topic. Microviscosity is the measure of the viscosity effect at a μm scale and involves single particle interaction with its environment rather than ideally infinite homogeneous fluids (bulk viscosity). The microscopic behaviour of fluids is very important, for example, in biology in order to understand the diffusion of chemicals and molecular processes of cells. The main problems in the definition of the microviscosity are that the size of the probes is comparable with the molecules forming the environment to be studied, and that several biological systems (i.e. membranes) feature an organised structure, hence the environment is not isotropic.
The term microviscosity is then often used as "equivalent viscosity", that is the viscosity of an homogeneous environment in which the probe yields the same response. Molecules in solution tend to move according to two main routes: Stokes diffusion and free-volume diffusion. The former is a viscous process of displacement of the molecules of the solvent, while the latter is associated with movement into "holes" of the solvent (free-volume). A relationship between viscosity and free volume was proposed by Dolittle[41]:

$$\eta = \eta_0 * (V_0/V_f), \tag{1.24}$$

where η_0 is a constant , and V_0 and V_f are the Van Der Waals volume and the free volume of the solvent, respectively.

One proposed method to measure the viscosity is the use of a particular kind of fluorescent dyes, termed molecular rotors[93; 94; 95; 96; 97], that vary their fluorescence features depending on the environment free volume.The structure of the most common molecular rotors has a chemical bond they can twist across in the excited state, named Twisted Intramolecular Charge Transfer (TICT) excited state: after the excitation, this twist tends to set the system back to a lower energy state, preventing fluorescent emission. The change in the viscosity affects the possibility of the rotor to twist, then allowing it to maintain an excited state for longer and increasing the probability of luminescence emission[98].

In particular, if a fluorophore shows a dependence on viscosity that agrees with

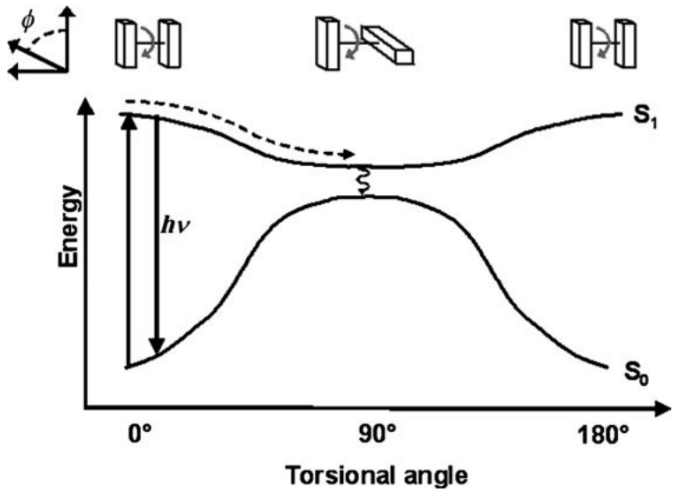

Figure 1.9: Schematic of Molecular Rotor behaviour as a function of the intramolecular torsion angle between 0° and 90°: the potential energies of ground- (S_0) and excited-state (S_1) varies according with the angle. A non radiative decay is more likely to occur when the energy gap is smaller ($\phi = 90°$) and a radiative decay when it is larger ($\phi = 0°$). Thus, viscosity of the environment affects the rotational mobility of the molecule, making the emission more or less favourable. Image reproduced with permission from [98].

Förster-Hoffmann theory [99] (see eq. 1.25), it may be defined as a fluorescent molecular rotor. These molecules comprise two main sub-unit (electron donor and acceptor) linked by a single bond between them and their quantum yield can be expressed by the equation:

$$\Phi = z\eta^{\alpha} \tag{1.25}$$

where Φ is the quantum yield, z and α two constants depending on the fluorescent molecule and its environment[98; 100; 101; 102; 103; 104], η again the viscosity of the environment. The value of α is solvent dependent even for the same fluorophore[101; 104]. Molecular rotors have been used as labels to estimate viscosity of their environment, even in high-pressure conditions[105; 106; 107], to study interaction with proteins in blood plasma[108], and for microviscosity measurements in pharmaceutical systems[109], as well as ionic liquids and microbubbles[110]. For some rotors, the dependence of the emission spectrum on the concentration[111] makes interpretation of intensity-based results a difficult task. Quenching and concentration effects can be separated using fluorescence lifetime measurements, since they are unaffected by concentration. One of the main limitations of the available molecular rotors is that many of them features peak excitation wavelengths in the UV spectrum, as well as blue shifted emission, making these dyes highly unsuitable for use in a biological environments and in other materials with absorption bands in the UV[112].
In Figure 1.9 it is possible to see the behaviour of a rotor (e.g. DCVJ[98]) as a function of the intramolecular torsion angle between 0° and 90°: the potential energies of ground- ($S0$) and excited-state ($S1$) varies according with the angle. It can be observed that the ground state energy surface increases with the rotation of the bond, whether the excited one decreases, being then the respective maximum and minimum very close to each other ($\phi = 90°$). A non radiative decay is more likely to occur when the energy gap is smaller (curly arrow, $\phi = 90°$) and a radiative decay when it is larger (solid, arrow, $\phi = 0°$). Thus, viscosity of the environment affects the rotational mobility of the molecule, making the emission more or less favourable. The geometry of the energy surfaces and the precise effect of viscosity vary greatly for different rotors, so the choice of the

appropriate dye for a specific application is crucial.

1.4.1 Living Cells

Of great interest for biology and medical studies is the viscosity of a cell. This feature affects several processes in biological systems, and also metabolism and protein-protein interaction within the cell. Viscosity has been reported to be correlated to Alzheimer's disease[16; 113; 114; 115] (membrane viscosity), and to influence the shape and elasticity of red blood cells (RBCs) (blood vessel viscosity), this associated with many disease such as Acquired Immune Deficiency Syndrome (AIDS), diabetes mellitus, deep venous thrombosis and myeloma [116]. Measurement of viscosity can be achieved via mechanical or fluorescence methods. The mechanical one consists in the application of a physical force on a fluid and uses a rheometer to measure its morphological changes. Measurement of apparent viscosity of cell membrane has been reported [15; 34], but it represents the average response of the whole cell, and the intracellular viscosity could not be investigated. On the other hand, several fluorescence-based techniques have been used: Fluorescence Recovery After Photobleaching (FRAP), Fluorescence Correlation Spectroscopy (FCS), fluorescence anisotropy and particle tracking. Measurements via FRAP yield an average viscosity for the bleaching area, so the maximum achievable resolution with this method is the size of the bleaching spot. By using fluorescence anisotropy measurements, the rotational correlation time can be exploited to calculate viscosity of areas up to the optical resolution limit [117].

1.5 Literature Review

In this section the last achievements in the study of microviscosity, concentration estimation, and luminescent probes are presented, as well as a review of advancements in detecting devices for photon counting applications.

1.5.1 Viscosity Measurements in Cells

Although several methods have been applied to measure the cell substructure viscosity, there is not a uniform agreement in the results. In particular, different areas of the cell exhibit different viscosities depending on the measuring technique.

The cytoplasm is the thick solution filling each cell and comprised within the cell membrane. It comprises a gel-like aqueous part (cytosol) and the organelles forming the internal structure of the cell. The possibility to measure the macroscopic and microscopic viscosity is influenced by the size of the probes used, and it has been suggested that diffusion-based measurements are dependent on the probe size[118]. Although the results vary with the different cell species[28; 119; 120] used, at microscopic level the viscosity is similar to that of water (1.0 cP), ranging from 0.94 to 2 cP. These results have been obtained using fluorescence spectroscopy[28], ratiometry[119], lifetime imaging[120], or a combination of ratiometry and lifetime imaging using molecular rotors (indocyanine-based rotor "cy3")[121]. The macroscopic viscosity of cytoplasm instead, has been measured to be 44 cP for cervical cancer HeLa cells and 24 cP for Embryonic Swiss Mouse Fibroblast (3T3) cells[118].

Several investigations on biological models have been undertaken about the viscosity of cell membrane. The cell membranes consist notably of lipids and proteins; the former tend to aggregate in a lipid bi-layer chain, whereas the latter fill the bi-layer and contribute to the membrane structure. A liposome (an artificial lipid bi-layer structure) has been used by Nipper *et al.*[122] to model the cell membrane structure; the viscosity changes were measured via fluorescent molecular rotors and the obtained results compared with FRAP measurements: the obtained value showed a strong correlation. Similarly, the viscosity for the dipalmitoylphosphatidylcholine (DPPC) liposome was found[123] to be 94 cP at the experimental temperature of 25°C. Nevertheless, a large range of viscosity, ranging from 30 to 1000 cP, has been reported[123]. A different liposome, dilauroylphosphatidylcholine (DLPC), has also been used as a membrane model using ratiometric molecular rotors[124] with a resulting viscosity of 61 cP.

As for the intracellular vesicles, such as the endoplasmatic reticulum (ER), of

a Human ovary adenocarcinoma (SK-OV-3) cell, Levitt, Kuimova and their collaborators measured a value of 160 cP using a molecular rotor (BODIPY-C_{12}) approach via FLIM[95], whilst they reported 60 cP via time-resolved fluorescence anisotropy measurements[125]. Results in the same order of magnitude have been published for Chinese hamster ovary (CHO) (50 cP)[126] and for HeLa cells (30-70 cP)[98].

1.5.2 Concentration Measurements

The correct concentration measurement of ions or other elements within living specimens is of great interest for biology, chemistry and physiology. The concentration of ions like Calcium (Ca^{2+}) has been linked to the triggering and regulation of several processes within the cell[127], amongst other effects.
One of the common ways to measure concentration is to use a ratiometric approach: this method is based on the calculation of the ratio between two fluorescence intensities, one directly dependent on a certain condition (i.e. the bonding of the dye with some cellular structure) and one depending on the dye concentration only.
This approach has been extended to molecular rotors, thus termed ratiometric molecular rotors, allowing the relative measurements of viscosity and concentration. In its simple form, a ratiometric rotor includes two independent chromophores: the one independent on viscosity is used to determine the concentration, whilst the other is used as a molecular rotor thus giving information on the viscosity. Haidekker and his group reported using one of these rotors for measuring viscosity in bulk liquids[128] and in synthetic membranes[124].

1.5.3 Transition Metal Luminescent Complexes

Several transition metal complexes have been studied for their exhibition of strong luminescence properties. In the last decades Ruthenium-based complexes in particular have been investigated for their unique properties: the main advantages include a high photostability, a lack of dye to dye interaction, good water solubility, and large Stokes' shifts, allowing a greater spectral separation in comparison to standard fluorophores[42]. In addition, the use of the transient metals rhenium

by Hueholt *et al.*[129] have been reported and iridium complexes by Flamigni and her group reviewed[130].
The emission cycle mechanism of these dyes consist in a metal-to-ligand charge transfer (MLCT): it involves the absorption of a photon by the metal part of the complex and then the transfer of the excited state energy to the ligand part[131]. The excited state of the complex undergoes a transition to a stable triplet state and thus leading to phosphorescence emission, accounting for the typical long lifetime of this class of compounds.
The engineering of the ligand bonding to the metal core (e.g. Ru) allows to manipulate the complex properties such as the lifetime, as reported by Medlycott and Hanan in their review for Ru-based probes[132].
The Ruthenium complex Ru(bpy) in particular has been proved to be a useful oxygen sensor: Sasso and his collaborators demonstrated its use to monitor mitochondrial respiration[133], whereas Gerritsen and his group, and Sud and his co-workers reported its use for cell imaging[134; 135]. Furthermore, the application of this sensor to detect cancerous cells[136] and tissues[137; 138] has been reported by Sud and Mycek and by Lochmann and his group respectively. More recently, an optimisation of the measurements based on FLIM has been proposed by Hosny and her collaborators[139], and a 3D imaging approach based on Ruthenium has been reported by Choi's group[140]. Other transition metal complexes are expected to exhibit similar capabilities.

1.5.4 Lanthanide Complexes

Opposite to the emission mechanism of transient metals, Lanthanide-based trivalent complexes (such as Europium, Terbium, Ytterbium, Neodymium, Dysprosium, and Samarium) emit light via a ligand-to-metal charge transfer (LMCT) route[42]. For this class of compounds, the ligands act like an antenna by capturing the excitation photons, then undergoing an intersystem crossing to the triplet state, followed by an intramolecular energy transfer from the triplet state to the metal. Their unique orbital structure limits the capability of free lanthanides to capture photons, but on the other hand it reduces quenching effects[141]. This particular feature leads to long lifetimes (μs-ms range) for

these complexes, and generally to insensitivity to changes in the environment. However, a notable sensitivity of the lifetime to coordinated water molecules is known, and exploiting this effect for cell imaging applications has been investigated by Thibon and Pierre, and by Moore *et al.*, and reviewed by Bünzli and his collaborators[142; 143; 144; 145]. The lifetime can also be tuned by changing the structure of the antenna-ligand, as described by Parker[146], and investigated by Hynes *et al.*[147], and by Song and his group[148], who designed an oxygen sensor based on the variation of Europium lifetime due to the oxidation of the aromatic antenna. The use of lanthanide complexes has found large application in time-gated techniques, as reviewed by Bünzli[145], and as FRET probes[149] with the metal as donor. Although the use of lanthanide dyes for microscopy and in-vivo imaging, and in cancer research[149; 150; 151] has been reported by Charbonnier and Aita, their application to a biological sample is limited by the weak stability in water and their potential toxicity. Furthermore, the long lifetime of these dyes make them less attractive for high-speed scanning techniques, as it may increase the required acquisition time[42].

1.5.5 Photon Counting Detectors

For wide-field and point-like approaches aiming to detect single photons, the fundamental parameter to consider is the Signal to Noise Ratio (SNR). From the detector point of view, this parameter is the sensitivity, usually quantified as the Quantum Efficiency (QE) of the device at a given wavelength[13]. Recent point-detectors QE ranges from 40 to over 70% in the 400-700 nm wavelengths interval, whereas the efficiency for wide field devices varies between 90%, for recent CCD detectors, and a few per cent for old class devices.
Historically, photomultiplier tubes (PMTs)[152; 153] had a dominant position among the point-detectors, but in the last years single-photon-counting avalanche diodes (SPADs)[154], and recently introduced hybrid photodetectors (HPDs)[155; 156] became common tools in fluorescence experiments. The efficiency of the hybrid devices is dependent on the coupled photocathode, and peaks at 45% in the visible spectrum for GaAsP photocathodes, while the efficiency of SPAD detectors ranges from 50 to 70% at the same wavelengths, depending on the

production technology considered[157; 158; 159]. PMTs and HPDs in general operate at high-voltage, while SPADs require lower voltages, making them less affected by ambient-light. In addition to the sensitivity, the timing capabilities of the devices have to be considered. For the SPAD devices, the thick reach-through detectors present an instrumental response function having a full width half maximum (FWHM) between 100 ps[159] and 200-600 ps[153], while the thin technology developed by "Politecnico di Milano" achieves an IRF of tens of picoseconds[160; 161] at the expense of a lower quantum efficiency. More recently, the Politecnico di Milano group improved this design and introduced a red-enhanced epitaxial SPAD[162], manufactured by Micro Photon Device, with high QE and better time response.

PMTs and HPDs have comparable quantum efficiency (lower than SPADs), both feature a large sensitive area, and require high voltages. PMTs have temporal resolution comparable with thick SPADs[153], while HPDs achieve a resolution of about 100 ps[155], but artifacts arising from ionisation of residual atoms in the vacuum tube have been reported[163].

These detectors usually achieve high sensitivities, but inherently require a longer acquisition time for sufficient statistics to be collected. This factor influences the temporal scales that can be studied with these devices: normally, only timescales far longer than a single measurement can be investigated[13].

Wide field based detectors consist mainly in cameras, featuring several sensor technologies and readout methods. The best sensitivity for this class of detectors is achieved by back-thinned CCD-based devices (QE 80-90% at 500-700 nm)[13] but they are generally limited by a low frame rate. Intensified CCD (ICCD) cameras[164], instead, can be used for time-resolved experiments (through gating or frequency modulation), but suffer from a few drawbacks. This device is constituted by an image intensifier, that converts each incoming photon into thousands of photons, and a standard CCD that detects the intensified photon cloud. This amplification of the signal reduces the readout noise and increases the SNR but, due to the low QE of the photocathode stage ($\sim$ 45% for GaAsP) of the intensifier, this effect is appreciable for low-light levels only. In addition, due to the high voltage required by the intensifier, excessively high illumination levels can actually damage the device. Finally, the exact signal quantification is difficult

due to the additional variance introduced by the gain mechanism.
The same approach, based on the coupling of an intensifier to a complementary metal oxide semiconductor (CMOS) camera, instead of a CCD, has been proposed[165; 166] to exploit the high frame rate of this class of cameras. Similarly, Electron-bombarded (EB) cameras use an amplification mechanism before the detection on the sensitive area of the device. The amplification stage converts incoming photons into electrons via a photocathode, and these photoelectrons are accelerated to generate thousands of secondary electrons due to the impact with the detector (a CCD or a CMOS), usually achieving a better spatial resolution than ICCDs[167; 168; 169]. A different amplification method is the electron multiplication (EM) before the analog-to-digital conversion (ADC). EMCCD cameras[170] use a high sensitivity back-thinned CCD detector, but the photoelectrons are amplified hundreds of times inside each pixel before the digitisation, and this design greatly reduces the readout noise.
Wide field approaches require further considerations compared to point-like detectors. While the QE is still important, the fill factor (the ratio of the pixel sensitive area to the pixel size) plays a determinant role and it may result in a reduction of the total efficiency of the detector. These low fill factor effects are normally compensated with microlens arrays[13]. Moreover, the frame rate of the cameras is a critical factor for time resolved measurements: while advancements in the electronics allow frame rates of hundreds of kilohertz[171; 172], the number of pixel read in each frame determines the maximum temporal resolution. However, for very high frame rates the signal collected in each frame drastically decreases, and the weight of the readout noise lead to very low SNR, requiring a tradeoff between the the temporal resolution and the efficiency of the system.

Chapter 2

Instrumentation & Methods

All of the experiments in this project were performed using the instruments and techniques described in this chapter. Two different microscopes were used: a confocal Leica TCS SP2 and a widefield inverted Nikon Eclipse 2000 TE; the imaging detectors were either an EBCCD camera (Hamamatsu, C7190-13), and different models of CMOS cameras (Phantom, V7.3; Photron, SA1) coupled with an image intensifier (P20; or analog Photek, MCP140-P47). The light sources were a pulsed diode laser (Hamamatsu, PLP470), a low-power UV laser (Picoquant PDL800-B with PLS-340 head), as described in the following sections. The software used for the data processing were QuickPALM, RapidSTORM and an in house code developed by our group. Tri2 and SPCImage software were used for lifetime calculation and mapping. For the living samples experiments, HeLa cells were used: they were cultured at 37°C and 5% CO_2, and during the imaging experiments the same conditions were maintained.

2.1 Spectrometers

For the spectrographic part of this project, two spectrometers were used: one luminescence emission spectrometer (Perkin Elmer, LS-50B) and a UV/VIS spectrophotometer (Hitachi, U-4100) for absorption measurements. The sample was placed in a 10 mm optical path Quartz cuvette, with clear faces. As can be seen in the schematic for the LS-50B (see Fig. 2.1), the excitation light is reflected,

then passes through a slit and a grating in order to obtain a single wavelength. This light hits the sample and the emission is collected at a 90° angle (in order to separate excitation and emitted light) again through a slit and the moving grating, allowing a single wavelength at the time to be detected. As the grating moves, the light is collected on the detector and an emission spectrum produced. In this instrument, the excitation wavelength is normally kept constant and only the emission is collected. In contrast to this, the UV/Vis spectrophotometer (Fig. 2.2) excites the sample at the selected wavelengths by slowly moving the grating and calculates the amount of light absorbed in respect to the light collected at the other end of the sample (linear configuration); this instrument allows to measure a reference sample at the same time and to calculate the absorbance in respect to it. For the polarisation measurements, two polarizers where inserted along the path of the light as shown in Figure 2.1, and their orientation changed (vertical/horizontal) for each set of measurements.

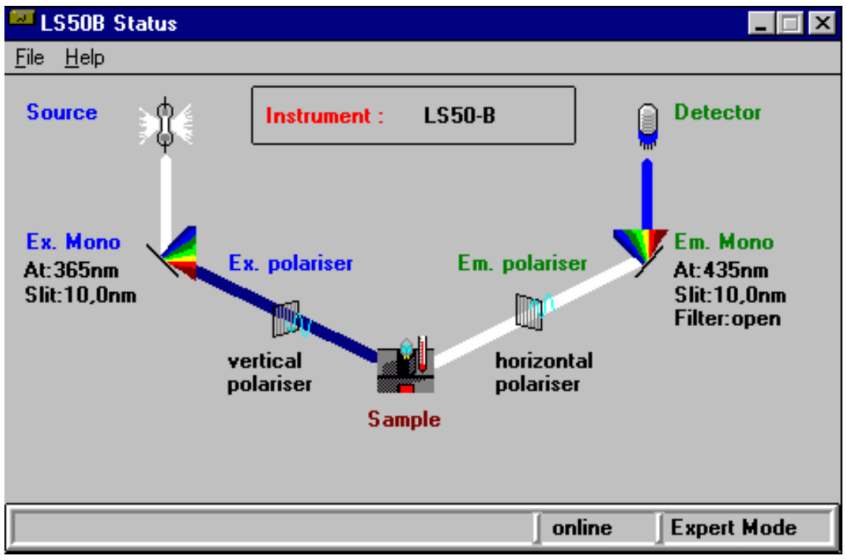

Figure 2.1: A screenshot from FWLAB controlling software shows the schematic of Perkin Elmer LS-50B spectrometer: the 90° angle (L-shape configuration) between the source and the detector insures the separation of incident and emitted light.

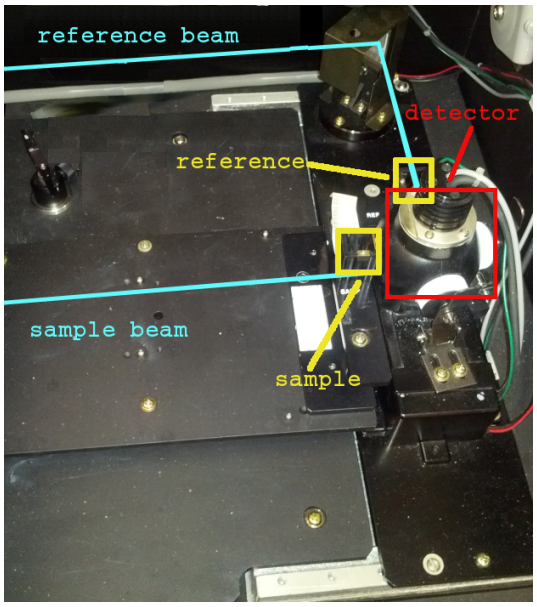

Figure 2.2: Schematic of the Hitachi, U4100 spectrophotometer: the excitation beam changes its wavelength along the measurement and the amount of light absorbed at each frequency is measured at the other end of the sample. This measurements can also be performed in respect to a reference sample placed along a path at 90°.

2.2 Microscopes

2.2.1 Confocal microscope

During this project an inverted confocal microscope was used, a Leica TCS SP2 (Leica Microsystems, Wetzlar, Germany). The set of objectives at our disposal for this microscope, manufactured by Leica, were the followings. Air objectives: 10× (HC PL FLUOTAR, NA 0.3), 20× (HC PL FLUOTAR, NA 0.5) and 40× (HCX PL FLUOTAR, NA 0.75). Immersion objectives: 63× (HCX PL APO CS, NA 1.2) water, and 63× (HCX PL APO CS, NA 1.4) and 100× (HCX PL APO, NA 1.4) oil immersion.
The internal detectors were two analogue Photomultiplier Tubes (PMT). The Leica Control Software[173] is suited with the standard imaging routines and microscope controls, along with Fluorescence Recovery After Photobleaching (FRAP) and with 3D reconstruction options. The light sources used were the following, depending on the particular experiment:
• a mercury vapour lamp ;
• an Argon laser (providing excitation lines at 458, 476, 488 and 514 nm);
• a Hamamatsu PLP470 pulsed diode laser (Hamamatsu Photonics K.K., Hamamatsu City, Japan), emitting 88 ps pulses at 467 nm, with a variable repetition rate between 2 Hz and 100 MHz, and a maximum average power of 1 mW;
• a PicoQuant pulsed diode laser, wavelength in the UV (342 nm), with a variable repetition rate from 2.5 to 40 MHz, and a average and peak power of 1.0 μW and 277 μW respectively, at 10 MHz repetition rate.

As integrated detectors, this microscope comes fitted with two analogue PMTs. In order to select the emission wavelengths to be detected, adjustable slits are located between the PMTs and a light splitting prism. In addition to that, an extra PMT is fitted to the microscope port above the sample, thus allowing transmitted light images to be obtained, and with the possibility to do phase contrast imaging with an optional phase or dark-field stage.

2.2.2 Wide-field microscope

For the wide-field experiments, with the EBCCD and FastCamera, a Nikon Eclipse TE 2000-U inverted microscope was used. This presents four output ports and was equipped with a halogen bulb above the sample and a mercury vapour lamp on the side as light sources. A pulsed laser was used through the side port in place of the mercury lamp. The microscope turret was fitted with a set of objectives as follows: 4× (NA 0.13), 10× (NA 0.3), 40× (NA 0.6) Nikon Plan Fluor air objectives, and a 60× (NA 1.2) Nikon Plan Apo water immersion one.

2.3 Time Correlated Single Photon Counting

For fluorescence lifetime measurements, the commonly used technique in case of short lifetimes is the single-photon counting method. This technique exploits the photon emission probability dependence to the time after excitation. The statistical distribution of photons arrival time is the total fluorescence decay. A pulsed laser is normally used as a source, and when a photon is detected, the event time of arrival after the excitation is recorded. Many events are then collected in order to obtain the arrival times histogram. Photomultiplier tubes (PMTs) and microchannel plates detectors are commonly used as single-photon detectors[13; 174; 175; 176; 177; 178]. Time Correlated Single-Photon Counting (TCSPC) is a well-established technique that allows detection and precise timing of every photon arriving at the detector[179]. The first use of this technique was proposed by Bollinger in 1961 to study scintillator emission[180]. TCSPC is very important in all the low-light measurements due to a number of benefits it provides:

• Very high signal-to-noise ratio (SNR) due to digitisation of signal.

• Theoretically infinite dynamic range: the more the counts, the more reliable the measurements.

• If combined with a fast scanning technique in confocal and two-photon laser scanning microscopes can be used as a high temporal and spatial resolution and high efficiency FLIM technique.

• The resolution in time achievable by TCSPC, in particular, is limited by the detector time response, not by the width of its output pulse[179].
• Poisson statistics.
• Easy visualisation of decays.

Detectors used for photon counting have characteristic features that can differ from those of other photodetectors. We can briefly indicate the most important properties[179; 181]:
• The dark count rate is the average rate of counts that are detected without the application of any excitation light. These detected events are mostly due to thermal causes and are largely reduced (almost suppressed) by using a detector with a cooling system.
• The maximum count rate is mostly dependent on the electronics speed and can then be limited (e.g. dead time).
• The timing jitter term is a source of timing uncertainty for the registered photon events. For example, for a PMT the amplitude of the single electron pulses at the output may be variable and it can arise a variation in the electronics delay.

2.3.1 Time to Amplitude Converter (TAC)

Invented by Bruno Benedetto Rossi in his attempt to measure cosmic rays in 1942[182], this device produce a voltage output proportional to the time interlapse between two pulses (start and stop). The working principle is illustrated in Figure 2.3: the system consists in a capacitor sourced by a constant current, and the capacitor charging is started and stopped by some input pulse signals. When the first pulse starts the charging, since the current is constant, the voltage increases linearly with time. When the stop signal is received, the final voltage measured at the output will be proportional to the time difference between the pulses. Historically PMTs have been used as time to amplitude converters: the charging of the capacitor was started by the PMT receiving the excitation pulse and stopped by it detecting the emitted signal. Thus, the arrival time (proportional to the recorded voltage) of each event can be used to construct a histogram

of the times.

Figure 2.3: Working principle of Time to Amplitude Converter (TAC): when the initial pulse (START) is received, the capacitor starts to accumulate charge until a second pulse (STOP) is received and the accumulation on the capacitor ends. The voltage V then, measured at the capacitor, is proportional to the time interlapse between START and STOP [picture from `https://www.inkling.com/read/physics-nuclear-medicine-cherry-4th/chapter-8/d--time-to-amplitude-converters`].

2.3.2 TCSPC Instrumentation and Working Principle

TCSPC counting is normally performed by using a confocal scanning microscope associated with a single channel detector, such as an Avalanche PhotoDiode (APD) or a PhotoMultiplier Tube (PMT). In order to obtain an image, and in case of single point detectors, the scanning of the excitation beam on the sample is required; this affects the total acquisition time: its value is typically in the order of minutes for a cell sample image; longer or shorter times depends on the scanning ROI's area and on the emitting dye. To overcome this drawback, the use of multiple excitation beams and detectors was proposed[183].
The TCSPC system we used consisted in an external PMT (PCM 100, Hamamatsu), connected to a TCSPC acquisition card (SPC 830, Becker & Hickl GmbH, Berlin, Germany) and fitted to the output port of the confocal microscope. The

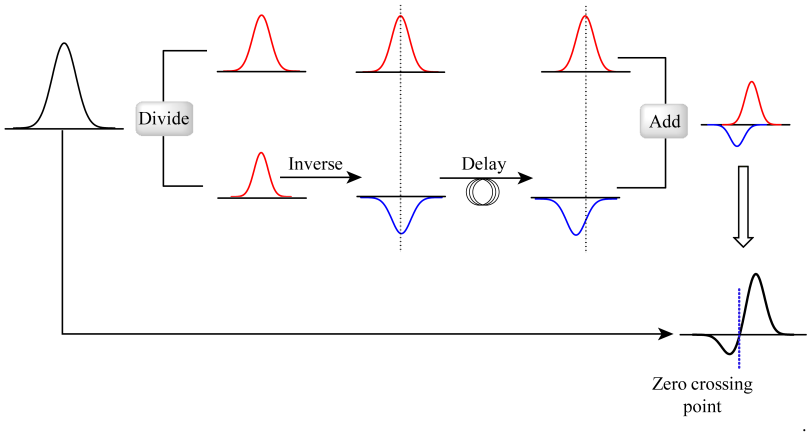

Figure 2.4: CFD operation principle. The original input is split in two identical signals, the first is kept constant whether the other is processed. The second signal is inverted and delayed, then added again to the first one. The resulting output will have a precise zero crossing point independent of the varying heights of the input signals. [Image of Public Domain from `http://upload.wikimedia.org/wikipedia/commons/5/52/Operation_of_a_CFD.png`].

PMT generates an electric pulse every time a photon is detected, and this signal is sent to the TCSPC card. Due to the varying intensity and shape of every pulse detected, applying a direct timing method produces inaccurate temporal results. For example, using a leading edge discriminator with a given threshold would lead to a timing jitter due to the different pulse height of each input signal. Instead, a reference pulse and a Constant Fraction Discriminator (CFD) are used to achieve precise measurement of each photon arrival time. The CFD divides the incoming electrical signal in two different signals: one is inverted, attenuated, delayed, and then added to the other one. The resulting output will show a zero crossing point (see Fig. 2.4), and this value will be independent of the pulse height, if the delay is constant for each processed signal. This output is then used to start a Time-to-Amplitude Converter (TAC) capacitor. The TAC is stopped by the reference signal sent from the laser control unit, denoting the following laser pulse emission and the start of a new acquisition cycle. The accumulated charge on the capacitor is then proportional to the time between the two

signals. In practice, instead of measuring the time between the laser pulse and the emitted photon, this inverted configuration approach uses the photon event as a trigger and the next laser pulse as the stop signal[43]. This method leads to better results than the direct configuration approach (using the laser pulse as trigger and the detected photon to stop the charging of the capacitor) because it reduces the system dead time. In fact, the resetting of the capacitor ramp is done only when a photon is actually detected, and thus its associated dead time does not occur for every laser pulse like in the conventional configuration.
The output of the TAC is then converted into temporal information in the MicroChannel Analyser (MCA) by an Analogue-to-Digital Converter (ADC). A histogram representing the fluorescence decay in each pixel is obtained by the photons arrival times along many cycles[179]. The fitting of the fluorescence decay (see Sec. 1.3.1) is then performed by software: the B&H SPCImage software or the Tri2 program (Dr Paul Barber, Gray Institute for Radiation Oncology & Biology, University of Oxford)[184; 185]. These software read the decay data associated to each pixel, fit it to a single, bi- or tri-exponential function, and produce a greyscale and a false-colour lifetime image.For applications such as time-resolved anisotropy measurements, to measure emission at two different wavelengths, or in general when two acquisition channels are required, the detection configuration can be modified in order to simultaneously collect photons on two PMTs. This modification consists in the insertion of a beamsplitter cube at the descanned output port of the confocal microscope, dividing the light signal to two PMTs placed at the sides of the cube. The collected signals are then routed and sent to the first and second acquisition channel of the TCSPC card[179, chapter 3][43]. These signals are then allocated by the board electronics in a memory area associated to each detector, this allowing to measure decays for different wavelengths[186; 187; 188] or polarisations[189; 190] in one single experiment. The limitations of the electronics do not allow to *simultaneously* measure two signals using a single acquisition board, but rather the collection is alternated between the two PMTs, thus further reducing the acquired signal on each detector. This limitation depends on the dead time associated with the system: that is the time after each detected photon the board cannot collect any new photon. This effect depends on the time required by the TAC to reset the capacitor and

by the electronics for ADC processing[43].

2.4 Detectors

2.4.1 PMTs

The first demonstrations of the modern PMT were in 1934 by Iams and Salzberg[191] and 1946 by Engstrom[192], and since then a great increase in the multiplication effect has been achieved[177; 193; 194]. A PMT is basically a vacuum tube with the following structure[195]:

• an input window through which the light can enter the tube;

• a photocathode, which emits photo-electrons when illuminated by the incoming light;

• depending on the geometry of the PMT, a focusing electrode that focuses the photoelectrons on the first dynode is present;

• a sequence of dynodes set at increasing voltage in order to accelerate the electrons; the electrons hitting the surface are multiplied at each step due to secondary electron emission effect;

• an anode that collects the multiplied electrons from the last dynode and outputs the resulting current.

When the PMT is operated in pulsed mode, the output shows an average low current and each input signal generates an easily measurable pulse in the output. The structure of a photomultiplier tube (shown in Figure 2.5) is designed to optimise the multiplication of photoelectrons emitted from the photocathode. These electrons pass through all the multiplicative stages of the dynodes and eventually reach the anode. This effect arises from a secondary emission phenomenon: when an electron generated from the photocathode (photoemission) and energy E_P hits the surface of a dynode, a certain amount σ of electrons (secondary emission) are generated and accelerated to the next dynode from the applied voltage. The number of secondary electrons emitted for a single striking primary electron (generated at the photocathode) is σ and it is termed secondary emission coefficient. Alkali antimonide, beryllium oxide (BeO), magnesium oxide (MgO), gallium phosphide (GaP) and gallium arsenide phosphide (GaAsP)

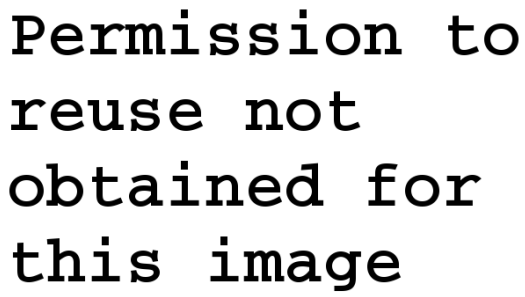

Figure 2.5: Structure of a Photomultiplier Tube and working principle. When a photon passes through the entrance window and hits the photocathode, a photoelectron is created (photoemission). This photoelectron is then forced through a series of dynodes by an applied high voltage: at each dynode stage the electrons are multiplied (secondary emission) and finally read out as a current at the anode. [from `https://wiki.engr.illinois.edu/pages/viewpage.action?pageId=49747077`]

are common secondary emissive materials[193; 195; 196]; these are normally deposited onto a substrate electrode to create a dynode as shown in Figure 2.6. In theory, for a given secondary emission coefficient σ, the amplification of the current generated by the electrons is σ^n , with n equal to the number of dynodes in the tube. Besides, there are variations in dynode structures, each with specific gain, time response and configuration. Because of it, the best design and optimal performance should be obtained in accordance with the desired application for the PMT.

Figure 2.6: Structure of a dynode and secondary emission working principle. The primary electron, generated at the photocathode stage or at a previous dynode step, hits the electrode and is multiplied by secondary emissive material at the surface[195].

2.4.2 Image Intensifier and Microchannel Plate (MCP)

Image intensifiers are a category of devices designed to intensify the collected light especially in low light conditions. This result is obtained by converting the collected photons into photo-electrons through a photocathode and then by increasing the number of electrons through the multiplication effect of one or more microchannel plate (MCP) stages. These electrons are then converted back into photons from the phosphor screen. The screen can then be imaged in order to

obtain intensified pictures[13; 197].
The MCP is a device designed to amplify input electrons and it takes advantage of secondary emission working principle. An MCP is formed of millions of individual channels (also termed "pores"), each acting as a secondary electron multiplier, assembled together in a periodic structure. A primary particle (e.g. electron, ion), by hitting the plate surface, accesses a pore and frees electrons. These secondary emitted electrons are then accelerated, due to a voltage applied across the plate, and travel along the channel striking its walls and producing new electrons. This cascade phenomenon happens several times and generates a huge number of electrons at the back of the plate. It is possible to increase further this quantity using a series of MCPs (e.g. 3 for the used intensifier) and yielding an output of more than 10^7 electrons. Furthermore, the transit time for any MCP stack is very small (in the order of 10s of ps) compared to PMTs due to the shorter distance the electrons have to travel inside the channels respect to the distance between dynodes[198; 199]. The input pattern at front of the MCP (at the photocathode side) is preserved also at the output (phosphor side): this is because the incident particles are confined into individual pores. Thus, it is possible to obtain an intensified image directly at the rear of the plate (proximity-focusing); this is very important in all low-light imaging techniques. In general, the output is acquired at the back of the last plate (for MCPs series) by an anode (it may vary in design and number) or imaged on a phosphor screen (as in this project). As mentioned above, the high gain and high spatial and temporal resolution make the MCP a valuable device for imaging applications, and it is also largely used in electron spectroscopy, astronomy, molecular studies etc.
Typically, each MCP-based detector is designed for a specific application but they all share the same schematic structure: firstly, a system or a device to convert the input particles in photons or electrons; secondly, an array of MCPs to multiply the incoming electrons or photons; finally, a readout device for collecting the image. Photocathodes are generally used as converter for wavelength in the visible or Infra Red (IR). The MCP can directly detect UV- and X-rays and because of this, a converter stage is not always required. Different solutions are then used depending on the particle energy[198]. The intensifier consists of one or more

(typically between 1 and 3) microchannel plates, in accordance with the chosen application. For single photon counting and imaging, for example, two or three MCPs are normally used.
For application where no arrival timing is needed (e.g. mass spectroscopy), MCPs are commonly used as detectors and the readout device is normally a single metal anode. Besides, for imaging where no high temporal resolution is required, a phosphor screen can be used and combined with a CCD camera or similar detector. For imaging application requiring high temporal resolution other solution may be used (e.g. resistive anodes; Delay-Line-Readout; Cross-strip anodes)[198; 200], and in this thesis a method is proposed to exploit the phosphor afterglow for increasing temporal resolution.
The Image Intensifier used in this project consists of a BiAlkali photocathode, 3 MCPs and a P20 phosphor screen. The configuration is similar to the example shown in Figure 2.7, where only a single microchannel plate is presented. The operating voltages between the different stages were set as reported by Suhling *et al.*[201]: 150V between the photocathode and the first stage, 800V between the first and second MCP, 2.35kV between the second and the third, and 4.50kV between the last stage and the phosphor screen. The multiplication phase increases the intensity of the input light, but has the drawback of reducing the resolution of each photon events: the repulsion among multiplied electrons enlarge the cloud that hit the phosphor. In fact, the electronic cloud spread among several pixels on the camera forms a photon event[202]. In order to overcome this effect, the use of a centroiding algorithm is proposed: this technique helps in the recovering of resolution lost in the multiplication process[200; 201; 203].

2.4.3 EBCCD

An electron-bombarded charge-coupled device (EBCCD) is a special CCD camera largely used for low light conditions measurements, specially in fluorescence microscopy. It was firstly developed by Philips in 1990[204] and made available for commercial use by Hamamatsu in 2000. EBCCDs were originally designed for applications in astronomy, especially due to their high signal-to-noise ratio in low light levels conditions[205]. At present, this class of devices and the emerging

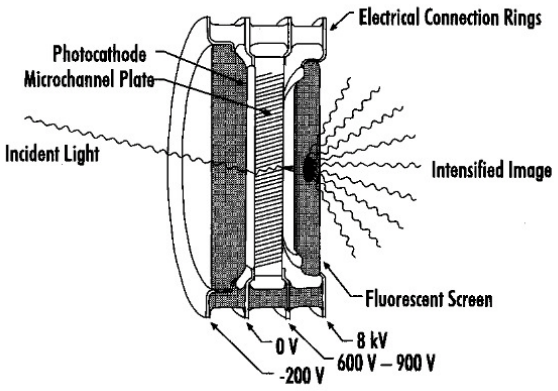

Figure 2.7: The structure of an image intensifier. Each photon event collected in the photocathode is converted to a photo-electron and multiplied (10^6) through the MCP stage. The electron cloud is then converted back to light by a phosphor screen and can then be imaged. Image reused with permission from [198].

EBCMOS are finding applications in microscopy, medicine and biological low-light imaging as well as in high-energy physics[206; 207; 208; 209; 210]. This device is constituted by a photocathode, similar to that in an image intensifier, and a back-thinned CCD. The photons detected on the photocathode generate photo-electrons that are then accelerated in a vacuum tube, due to an applied high voltage (in the order of kV), across the path towards the rear-side of the back-thinned CCD covered by a layer of aluminium. This approach is based on the direct detection of the photoelectrons on the CCD array, hence it avoids the loss of positional information associated with the conversion of the photoelectron in an electric pulse (like PMTs), or the introduction of a blur in the image by using a phosphor screen (like an image intensifier). The mean energy needed to create an electron-hole pair in Silicon depends on several factors such as the temperature, and the energy of the incident photons[211; 212; 213; 214; 215; 216; 217]: this value normally ranges between 3.6 and 3.7 eV. The resulting gain due to one electron impacting the CCD is normally about a thousand. The higher gain and the improvement in the read-out are the main advantages of an EBCCD compared to a normal CCD. Also, a relatively low noise and the good suppression

of geometrical distortion, in addition to binning and subsampling possibility, are relevant features of EBCCD. On the other hand, the main disadvantage of this device is the quantum efficiency of the photocathode: its efficiency is about 30% (about 50% for GaAsP cathode) and it is lower than the 80 to 90 percent of a standard back-thinned CCD[218]. Also, there is the unwanted occurrence of ion events in the detection process. From the increasing of the gain arises also a reduction of EBCCD dynamic range. In fact, each accelerated photoelectron causes the formation of $\sim$ 1300 electron-hole pairs circa (at 8 kV acceleration voltage) and this resulting in the CCD wells getting filled faster than usual. To compensate this effect, the pixel size for this device is larger than standard CCD[219].
In our work, the camera used for the experiments is a Dual-Mode Cooled EB-CCD camera, model C7190-13W, produced by Hamamatsu. According to the device specifications[220]: it has a GaAsP photocathode with a Quantum Efficiency of about 50% at 520nm; the distance between the photocathode and the CCD is about 1.3 mm; the pixel size is 24 μm x 24 μm, for 512(H) $\times$ 512(V) pixels; the readout noise is 15 electrons (r.m.s.); the CCD dark current is 50 electrons/pixel/s at -15°C, and 8 electrons/pixel/s at -25°C; the frame rate varies depending on the selected readout: 2.95 Hz for the High-precision (capable to detect single photon events), 4.8 Hz for the High-speed readout; the voltage across the photocathode and the CCD can be varied between 4 and 8 kV, in 16 discrete steps.
The camera uses an acquisition software named HiPic3. This program allows to collect single frames and sequences, it can perform analogue integration and can be set to Single Photon Counting mode (post-process of the frames). The SPC data analysis in this thesis was performed using the software described in the section(s) 2.5. The results presented in Chapter 5 are tightly related to the novel achievements of EB-CMOS cameras[210; 221]: this class of devices shares the described acceleration method for the photoelectrons but uses a CMOS array instead of a CCD as a detector, and allows acquisition rates of hundreds of thousands of Hertz. Thus, the comments and results in this thesis can be easily extended to such a device.

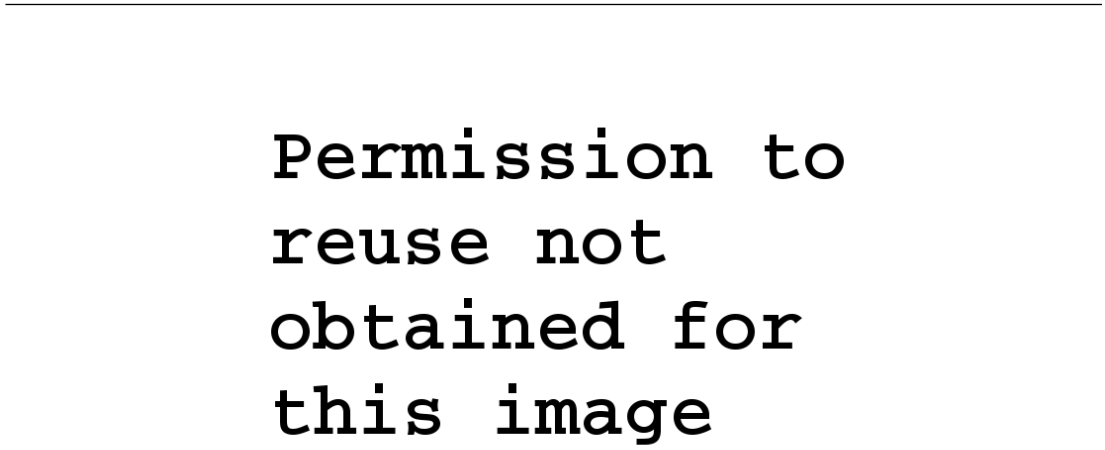

Figure 2.8: The structure of an EBCCD. A photon event collected in the photocathode is converted to a photo-electron and accelerated through the gain stage between the cathode and the back thinned CCD [from `http://micro.magnet.fsu.edu/primer/digitalimaging/concepts/ebccd.html`].

2.4.4 High-Speed Cameras

In this project we focused on the use of two fast cameras: the Phantom V7.3 (Vision Research, Wayne, New Jersey, USA) and the Photron SA 1.1 (monochrome, Photron Ltd, Tokyo, Japan). The cameras were made available for 4 to 8 weeks loans each in different moments along this study by the EPSRC Engineering Instrument Loan Pool. This class of devices uses a Complementary Metal Oxide Semiconductor (CMOS) sensor. In a CCD, the collected charges are sequentially sent to the side of the chip and then amplified, whereas in the high-speed cameras each CMOS sensor corresponds a local amplifier that directly converts the photoelectron into a voltage. This particular configuration allows to individually discriminate each pixel and to access only a reduced portion of the sensor (dynamic windowing), normally at a higher rate as shown in the Table 2.1. Among the advantages of CMOS, also called Active Pixel Sensor (APS), are the possibility to perform electronic shuttering, hardware image processing, and the low cost compared to CCDs[222]. On the other hand, the APS manufacturing tends to create not perfectly uniform chips, and this introduces a fixed pattern noise effect on reconstructed images. In order to reduce this issue, a correcting “dark value”

	Phantom V 7.3	Photron SA 1.1
Frame rate	Maximum resolution	Maximum Resolution
3,000 fps	800×600	1024×1024
5,000 fps	800×600	1024×1024
10,000 fps	640×480	768×768
30,000 fps	256×256	512×352
50,000 fps	128×128	256×256
100,000 fps	128×128	320×128
200,000 fps	128×64	128×128
250,000 fps	64×64	128×80
500,000 fps	32×32	64×32
675,000 fps	-	64×16

Table 2.1: Comparison of fast cameras: the left column shows the available frame rate, whereas the central and right column indicate the maximum resolution at that rate for Phantom V7.3 and Photron SA1.1 respectively.

needs to be subtracted from each pixel value (either using APS's on-chip processing or post acquisition software)[223]. In addition to that, due to the larger number of electronics associated to each pixel, the fill-factor of CMOS is generally lower than CCD. Each camera is shipped with its own software that controls the device operation (frame rate, resolution, triggering, background correction, etc.) and allows some data post processing. This software are particularly useful to set a region of interest in the frame, and thus imaging just the relevant portion of the frame. Furthermore, these cameras have a series of control buttons that allows it to work without being directly connected to a computer. As an alternative, an optional remote can be used for triggering and controlling the device. The acquisition process is basically the same for both cameras considered: the collected frames are stored at high rate on the on-board memory and then downloaded via a Gigabit Ethernet connection to the controlling computer. The main differences between the models are the resolution and maximum acquisition speed combinations, the internal volatile memory, the sensitivity of the sensors and the background correction capabilities (see Table 2.1).

2.5 Centroiding

Centroiding is a technique that converts the intensity distribution of an event, spread over several pixels, into a positional information (pinpointing the centre of the distribution)[201]. It is a typical feature of photon counting techniques and can be performed either in software or in hardware. The application of photon counting techniques for imaging has been widely applied in many different fields as particle detection, astronomy observation, low-level light bioluminescence[224; 225; 226]. In addition, technologies capable of low-level light detection are especially important because they allow precise and sensitive measurements on delicate samples without affecting their properties (unlike other destructive or invasive techniques, e.g. X-rays). For most of the cases, the light is converted into analogue electrical signals by the detector. When the amount of light on the sensor is so low that we can detect incident photons as individual pulses, we can consider this as a yes/no situation: the photon striking the detector (or the single pixel, in case of an array) can be collected or not, giving rise to a digital detection. Thus, there is a direct proportion between the number of collected pulses and the amount of incoming light. Single photon sensitivity is also dependent on the noise in the detection process: while the digital detection is less susceptible to signal fluctuations, the amplitude of the signal must be larger than that of the background. For example in MCPs, before the detection stage each input electron is multiplied within the channels, through secondary emission, and the output signal is a cloud of electrons that can be easily identified. The "digital" photon counting method, as opposed to the measurement of analog signals, can have better signal-to-noise ratio, detection efficiency and stability[227]. The photon emission and detection process follows Poisson statistics[227].
This technique presents great advantages, but the spatial resolution still depends on the optics and electronics being used. In fact, the detected events cover an area of several pixels and, especially in the cases with higher number of collected photons (e.g. more incoming light or longer exposure time), it is possible to have overlapping and then indistinguishable events. In order to improve the resolution, a centroiding algorithm can be applied, in real time (generally with specific electronics)[228] or post-acquisition (software processing)[200; 201]. The cen-

troiding method operating principle is to identify an area (normally on a CCD or similar sensor) of several pixels, roughly equal to the size of the event of interest and due to an algorithm, to find its centre. This leads to a sub-pixel resolution of the image, but introduce also a noise (e.g. Fixed pattern noise) that often is not negligible.

2.5.1 Centroiding algorithms

The algorithms used in practice can vary depending on the application and on the expected shape of the event to be detected. In order to increase the efficiency of the method, reducing the mismatch between the intensity distribution shape and the fitting algorithm is fundamental[201; 229]. Here few algorithms are presented, but many others are available and being researched[175; 201; 230]:

$$x_{cog3} = \frac{c-a}{a+b+c} \tag{2.1}$$

$$x_{lorentzian} = \frac{c-a}{2(a+c-2ac/b)} \tag{2.2}$$

$$x_{parabola} = \frac{c-a}{2(2b-a-c)} \tag{2.3}$$

$$\begin{aligned} x_{gaussian} &= \frac{\ln c/a}{2\ln b^2/ac} \\ &= \frac{\ln c - \ln a}{2\left(2\ln b - \ln a - \ln c\right)} \end{aligned} \tag{2.4}$$

$$\begin{aligned} x_{cosh} &= \frac{\alpha}{\pi}\operatorname{arctanh}\frac{\sqrt{\frac{b}{a}}-\sqrt{\frac{b}{c}}}{2\sinh\frac{\pi}{\alpha}} \\ \alpha &= \frac{\pi}{\operatorname{arcosh} 0.5(\sqrt{\frac{b}{a}}-\sqrt{\frac{b}{c}})} \end{aligned} \tag{2.5}$$

where the letters from a to c represent the values of the considered pixels (on a CCD or similar device) as shown in Figure 2.9, and b is the central pixel (the peak pixel). The presented algorithms use 3 pixels to assess the central position in each direction x and y, pixel values outside these three points are not taken

into account. The $x_{\text{algorithm}}$ is the centroid value, and this corresponds to the shift (equal to ± 0.5) of the calculated event centre from the centre of the peak pixel (equal to 0). The centroiding is performed in x and y direction separately. Since the intensity distribution of each event is in general bell-shaped,the use of an analytic function (e.g. Gaussian) that match this shape is sometimes preferred to the simple centre-of-gravity (COG) algorithm because of the better fitting[229]. Despite this, each function-based algorithm differs from the other depending on the size of the events to be centroided and on the number of pixel necessary to process it. Thus, the choice must be made with regards to the specific application and also evaluated in accordance with the associated Fixed Pattern Noise, described in the following section.

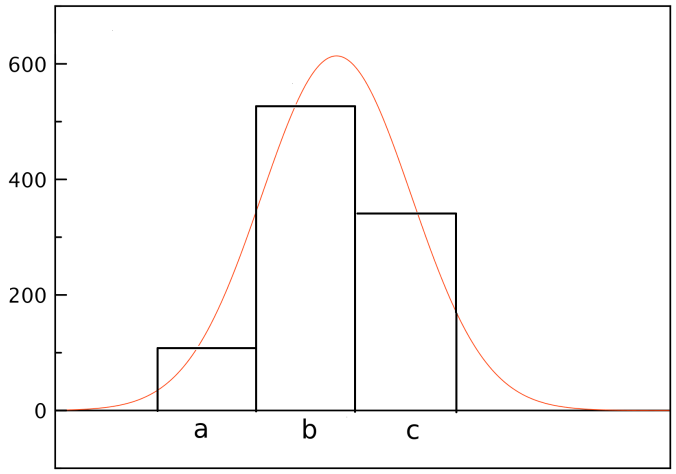

Figure 2.9: Distribution of a single event above several pixels. The a, b and c on the x axis represent the pixel relative position of the event to the peak (being b the position of the peak) and the y axis the indicates the value for each pixel. The distribution is bell-shaped and the mismatch in the fitting with the appropriate function (e.g. Gaussian function in orange in the pictures) generates FPN.

2.5.2 Fixed Pattern Noise

The fixed pattern noise (FPN) is a term that identifies a specific noise typical in digital imaging sensors (e.g. intensified-CCD cameras). It appears as the superimposition of a defined pattern on the images acquired under the same illumination conditions and it is easily observable in case of a uniform illumination of the sensor. The variation on the pixel values often results in the formation of a light (higher value) or dark (lower value) grid over the pixel matrix. Among the several factors that influence FPN, such as dark noise, gain, and incident illumination, the most important one for the photon counting techniques is the centroiding[229]. In fact, since other factors are normally negligible, the mismatch between the centroiding algorithm and the detected event shape is the main reason for FPN. This mismatch can arise from various causes. First of all, the shape of the detected events is in general asymmetric: this can be due to the bias angle (normally between 5° and 15°) introduced by MCPs[198]; the effect can be minimised by searching an optimum alignment of the plate's pores with the CCD pixels. In second instance, despite the fact that the intensity profile has a Gaussian-shape, the fit is not perfect and it results in a mismatch using a Gaussian centroiding algorithm. In addition to it, charge effects can interfere with the event shape: it has been demonstrated[229] that event profile is dependent on event energy. Furthermore, also optical distortion is a source of shape modification during acquisition on a CCD. Finally, the digitisation introduces a loss of information and influences the centroiding[201]. The digitisation in the pixel acquisition process of a CCD takes place as truncation of a real value into integers. This phenomenon results in a noise due to the loss of data and it is more evident for less bit digitisation (i.e. 8 bit). In spite of it, this effect is small in comparison with other noise sources. In fact, the error introduced by digitisation may influence the calculation of the centre of gravity algorithm, but the choice of the appropriate algorithm can make it negligible, demonstrating the main dependence of the FPN on the centroiding[229]. On the other hand, this truncation error can be reduced by increasing the number of bits per pixel, but this leads to a bigger data transfer time. For this reasons the choice of the correct centroiding algorithm is an essential issue. If all pixels are overlaid by a N×N matrix, the

centre of the intensity distribution of each event will be bounded in one of these sub pixels and the occurrences of each position counted. The FPN can then be characterised by an equation that represents the amount of noise[201; 229] introduced:

$$p = \frac{N_{max} - N_{min}}{N_{mean}} \times 100\% \tag{2.6}$$

where p is the noise parameter, N_{max} the maximum number and N_{min} the minimum number of counts in the matrix subpixel positions. N_{mean} is instead the average number of counts on the N×N matrix. The higher the value of p the more fixed pattern noise is affecting the system.

2.5.3 QuickPALM and RapidSTORM

QuickPalm is a plug-in for the widely used ImageJ software[231] and released in 2010 by Henriques and his collaborators[232]; it has been designed to obtain 3D real-time image processing for photoactivated light microscopy (PALM) and stochastic optical resolution microscopy (STORM). These techniques achieve super-resolution imaging by processing an image sequence of photoswitchable molecules at lower resolution. The position of each molecule is then calculated and used to create the super-resolution image(s). Normally this process requires hours or even days in order to obtain the desired reconstruction, practically preventing any possibility of real-time imaging. QuickPALM tries to solve this limitation using fast two-dimensional (2D) processing algorithms (a Högbom 'CLEAN' method[233] to find the emitting spots, and a centre of gravity algorithm for centroiding) and 3D reconstruction.

RapidSTORM, instead, is an open-source programme on its own and was designed by Steve Wolter *et al.*[234] in 2012. The software performs direct stochastic optical reconstruction microscopy exploiting an optimisation of a maximum likelihood estimation (MLE) iterative fitting with a Gaussian curve.
These algorithms working principle does not differ from any other centroiding algorithm, in particular from the SPC techniques commonly used in fluorescence[175; 229].

Group Number										
Element	-2	-1	0	1	2	3	4	5	6	7
1	0.250	0.500	1.00	2.00	4.00	8.00	16.00	32.0	64.0	128.0
2	0.280	0.561	1.12	2.24	4.49	8.98	17.95	36.0	71.8	144.0
3	0.315	0.630	1.26	2.52	5.04	10.10	20.16	40.3	80.6	161.0
4	0.353	0.707	1.41	2.83	5.66	11.30	22.62	45.3	90.5	181.0
5	0.397	0.793	1.59	3.17	6.35	12.70	25.39	50.8	102.0	203.0
6	0.445	0.891	1.78	3.56	7.13	14.30	28.50	57.0	114.0	228.0

Table 2.2: LookUp table for 1951 USAF test pattern. The values represent the number of line pairs (one black and one white) in a millimetre.

2.5.4 USAF test pattern

For the calibration and testing experiments on the imaging devices and systems (e.g. EBCCD, FastCAM) the *1951 USAF target* was used. This is a test pattern set by US Air Force in 1951 and still widely used to test the resolution of optical imaging devices.

The test pattern consists of sets of three lines with different dimensions, and each set is indexed by two values (from 1 to 6, and from -2 to 7); this values can be then used to find the line's size on a look-up table. The largest object that can not be resolved, sets empirically the resolution limit for the tested optical system. In Figure 2.10 is shown the test pattern, and on Table 2.2[235] the look-up table for the dimensions of the different bars groups.

2.6 Cell Culture

During this project, several experiments on living samples were performed, and the cells cultured in the biological laboratory. Cell culture provide a model system for understanding cell physiology and biochemistry, for investigating the effect of drugs, and for studying the genesis of mutations and carcinoma. The possibility to reproduce in a reliable and consistent way the experimental results from a specific line of cells, is the main advantage of using cell culture for these studies. The term "cell culture" indicates the growth in an artificial environment of cells of animal or plant origin.

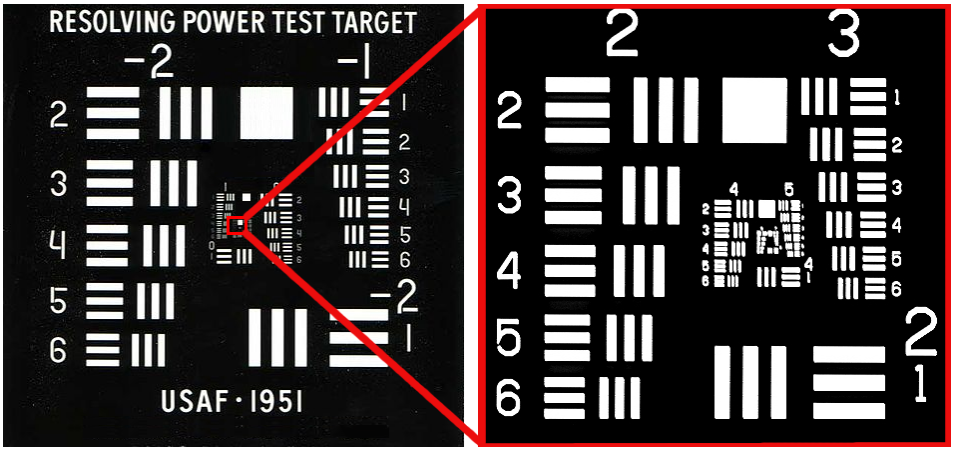

Figure 2.10: 1951 USAF target (left) and a zoomed area of interest (right). The smallest resolved set of bars represent the maximum resolution of the optical device. By comparing the pictures with Table 2.2, it can be seen that for example the position *(4,3)* corresponds to 20.16 line pairs per millimetre (line width 24.8μm), and likewise position *(5,6)* to 57.0 line pairs per millimetre (line width 8.8μm), and so on.

The cells removed from the original subject are grown on a substrate under precise conditions (primary culture), and when they reach a certain size (occupying the substrate available space), they are transferred to a new substrate and fed with a growth medium to further proliferate (sub-culture). Once the subculture process is established, the primary culture is normally defined as a cell line. The cells derived from the original cultures have normally a limited life span and, after several sub-culture passages, the cell population may start to present genetic differences from the primary culture. In addition, the cells usually proliferate for a finite number of times before permanently losing the ability to divide (senescence), and this cell lines are defined as "finite". Some commercially available cells have undergone a transformation to acquire the ability to divide indefinitely, and are named "continuous" or "immortalised" cell lines.
The culture conditions for the cells may vary for each cell type, but in general they are grown on a suitable vessel in an environment including[236]: a medium containing the essential nutrients (vitamins, minerals, amino acids, etc.); some factors favouring the growth; hormones; a controlled gaseous environment (O_2,

CO_2); a specific physico-chemical environment (temperature, pH, etc.). In case the storing of cells is needed for future use, they need to be treated with a protective agent and preserved at temperature below -130°C (cryopreservation).
The cell lines used in this project were HeLa cells, cultured at 37°C in a controlled environment with 5% CO_2. Further details about the preparation of the cells are given in the experimental setup sections of the relevant chapters.

Chapter 3

Molecular Rotors: BODIPY-C_{12}

The aim of this chapter is to determine the concentration of BODIPY-C_{12} in live cells. Firstly, the properties of BODIPY-C_{12}, a fluorescent molecular rotor, in solution are studied by measuring concentration, fluorescence lifetime, emission intensity and absorption. Secondly, the dye is used to label living cells, and their viscosity and dye concentration values estimated from the calibration map.

3.1 Introduction

In recent years, molecular rotors have been exploited to measure the viscosity of their environment[93; 94; 95; 96; 97]. These rotors main property is the dependence of the fluorescence quantum yield and lifetime on the environment viscosity, and this feature is due to the structure of the molecular rotor that can twist along a chemical bond in the excited state. The fluorescent molecular rotor analysed in this chapter is the meso-substituted BODIPY-C_{12} a particular kind of boron-dipyrromethene[237; 238], whose derivatives are commonly used as fluorescent probes and sensors[239; 240]. This rotor was synthesised by Dr. Yahioglu from PhotoBiotics Ltd and the Chemistry Department at Imperial College London. Previous works exploiting this specific dye for viscosity measurements and reporting its uptake and localisation in HeLa cells, SK-OV-3 human ovarian carcinoma cells[95; 125], and in Bacillus spores[241], and encapsulated microbubbles[110] have been published. This is the first investigation of both viscosity and dye

concentration in living cells.
The structure of BODIPY-C_{12} is shown in Figure 3.1. The rotor consists of two parts linked by a single bond: the BODIPY-C_{12} unit and a long carbon chain on top of a phenyl ring. The twisting of the planes is allowed by the single bond. In this chapter we will focus on the possibility to estimate the fluorescent dye concentration in living HeLa cells via intensity and FLIM measurements.

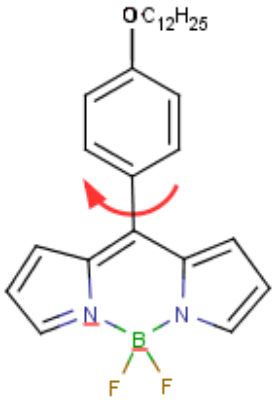

Figure 3.1: Molecular structure of BODIPY-C_{12}. The BODIPY core structure at the bottom is connected via the twisting bond (the red arrow indicating the twist) to a phenyl ring and to a long Carbon chain. **B** - boron, **N** - nitrogen, **F** - fluorine.

3.2 Experiment setup

A stock solution was prepared by dissolving 1 mg of BODIPY-C_{12} (Molecular Weight = 452g/mole) in 2 ml of methanol, resulting in a concentration of 1.1 mM. Four sets of binary solutions of methanol and glycerol (with different volume fraction of glycerol within each set) were made in order to obtain mixtures

with different viscosity: each set consisted of samples with 10% (1.20 cP), 20% (2.59 cP), 40% (11.94 cP), 60% (55.12 cP), and 70% (118.44 cP)volume of glycerol. Each set was then stained with a fixed concentration of BODIPY-C_{12}: the concentration was made constant for each series up to approximately 0.55 μM, 1.1 μM, 3.3 μM and 5.5 μM. The choice of μM concentrations is to prevent a reabsorption effect. In fact, being the absorption peak $\sim$496 nm and the emission peak $\sim$512 nm[242], the Stokes shift for BODIPY is quite small and it is possible that the light emitted by the excited molecules is absorbed by the ground level molecules.

The absorbance for each mixture, proportional to the concentration (see eq. 1.3), was measured by collecting its absorption spectrum using a clear-sides quartz cuvette (Starna, Optical Path 10 mm) with 2 ml of BODIPY-C_{12} solution on a spectrophotometer (Hitachi, U-4100). For the viscosity estimation of each solution, a binary model (see eq. 3.1) was used. The refractive index was measured using a refractometer, equipped with a sodium lamp (589.3 nm) as light source.

An inverted confocal scanning microscope (Leica) was used for the time-resolved fluorescence measurements coupled with an acquisition board for single photon counting (B&H, SPC 830). A multiwell glass-bottom microplate (Whatman) was filled with 20 μl of each solution for fluorescence lifetime measurement. The pulsed diode laser (Hamamatsu, PLP470) with wavelength 467 nm and pulse duration 90 ps used as excitation source was set at a repetition rate of 20 MHz. The emission fluorescence signal passed through a dichroic mirror, a pinhole, and a bandpass filter with wavelength 524 nm (Semrock) and collected by a PMT detector. The setup is shown in Figure 3.2. In the first set of experiments we measured the emission intensity and lifetime for each solution at different concentration and viscosity. In the second part of the experiments the same measurements were repeated on live HeLa cells stained with BODIPY-C_{12}, imaged in a micro-incubator plate and kept at constant temperature and CO_2 conditions. In order to make the results comparable and consistent, the measurements on all the solution samples and on the cells (described in the Section 3.4) were performed on the same day and the same setup was maintained for both experiments.

In order to characterise the different viscosity between the solutions, a model for binary liquids viscosity estimation was used. Specifically, the following equation

was used:

$$\log \eta = x_1 \log \eta_1 + x_2 \log \eta_2 \tag{3.1}$$

with η_1 and η_2 the viscosity for the pure solvents 1 and 2, respectively; x_1 and x_2 the volume fractions for each solvent; η the viscosity of the mixture of the two solvents 1 and 2. The viscosity of 100% glycerol and 100% methanol at 22°C were calculated to be 1182 cP and 0.549 cP respectively, according to a reference viscosity/temperature table[243], in agreement with reported values[95].

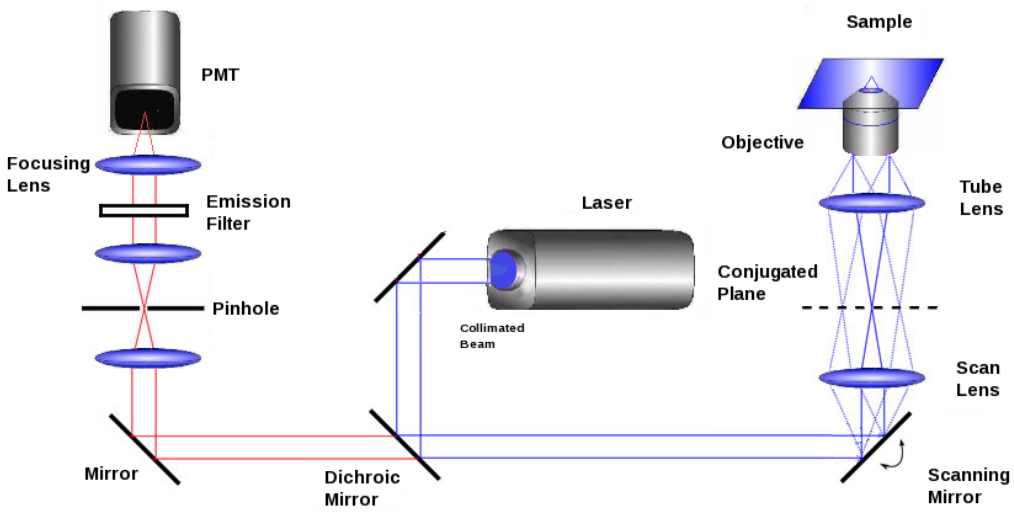

Figure 3.2: Setup for time resolved fluorescence measurements. The pulsed laser source excites the sample: the beam is routed onto the sample through a dichroic and a scanning mirror; the emitted fluorescence travels through the dichroic mirror and is collected on a PMT detector; the photon arrival times are then calculated by the dedicated acquisition board and software.

3.3 BODIPY-C_{12} in Solution

In order to calculate the viscosity of the solutions, a model was used. The measured refractive index for the different methanol and glycerol mixtures is shown in

Glycerol Vol. Fraction	Estimated Viscosity (cP)	Refractive index	Average Lifetime (ns)	σ (ns)
10%	1.20	1.3835	0.43	0.03
20%	2.59	1.3930	0.45	0.03
40%	11.94	1.4170	0.53	0.04
60%	55.12	1.4430	0.88	0.07
70%	118.44	1.4470	1.33	0.07

Table 3.1: The table shows the estimated viscosity of the mixtures, their measured refractive index, and their lifetime. The lifetime for a given volume fraction is calculated as the average of the lifetimes for different concentration samples (0.55 - 5.5 μM). The samples at low viscosity present very close lifetime values of 0.43 and 0.45 ns.

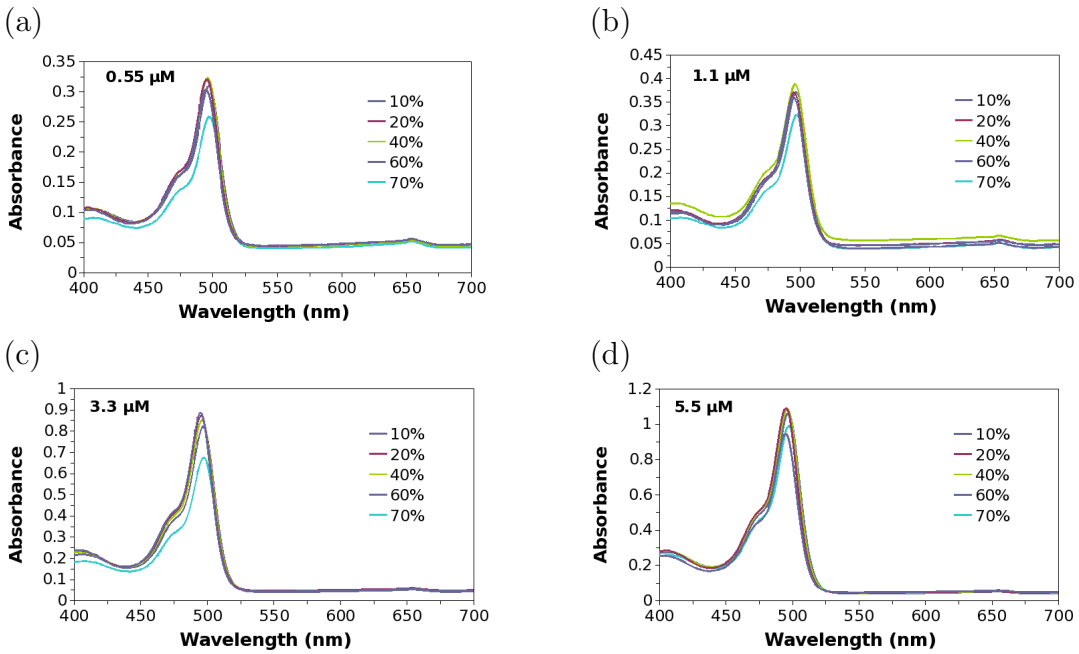

Figure 3.3: The solutions absorbance is proportional to the concentration of the dye. The graphs show that at a given concentration, each dataset presents substantially the same absorbance values.

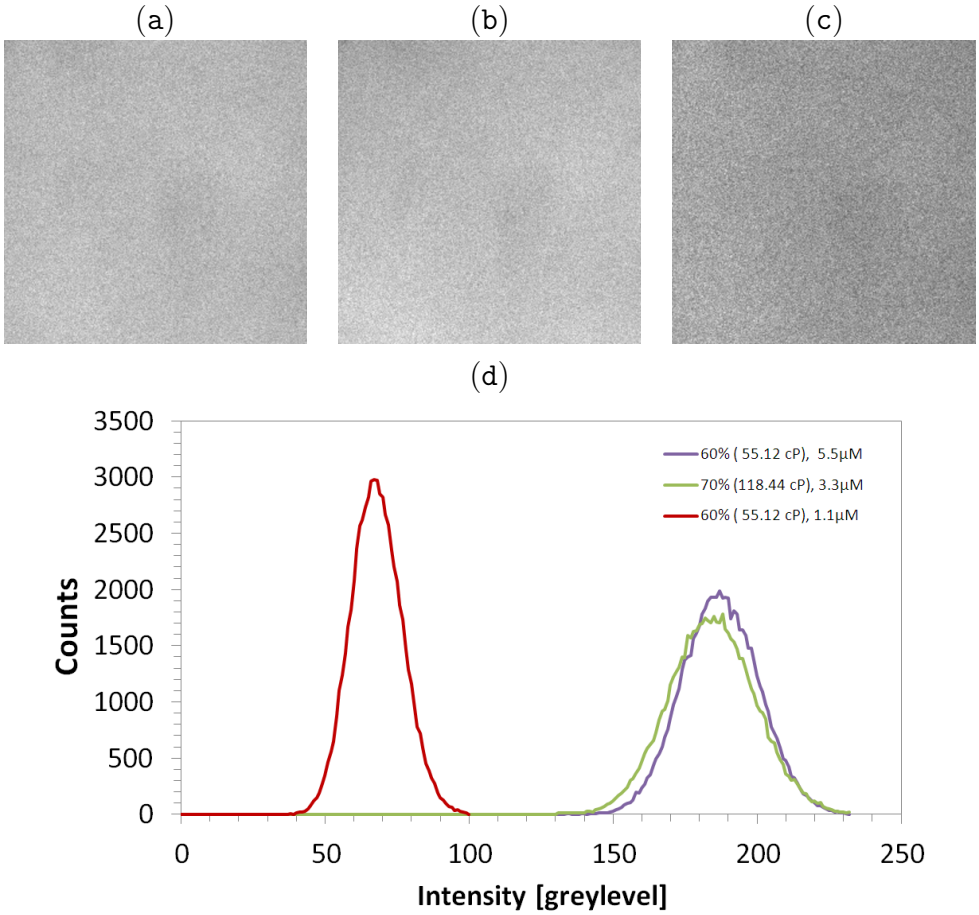

Figure 3.4: Intensity images for solutions with different volume fractions and concentrations (256×256 pixels, 8bit images acquired with the B&H board) (a) 60% glycerol (55.12 cP) and 5.5μM; (b) 70% glycerol (118.44 cP) and 3.3μM; (c) 60% glycerol (55.12 cP) and 1.1μM. Figure (d) shows the intensity histograms for (a), (b) and (c): the histograms of (a) and (b) overlap, making the two solutions identical using an intensity measurement only; from a comparison of the histograms (a) and (c), it can be seen an increase of the mean value of the distribution depending on the concentration of dye, from 67 ±11 to 189 ±16 counts.

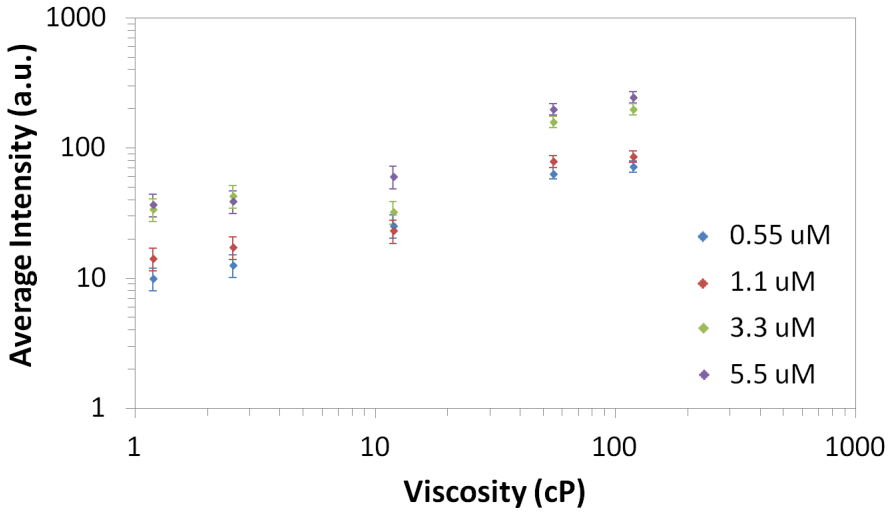

Figure 3.5: Intensity measurements at different viscosities for each concentration dataset. The average intensity was calculated for every image and corrected with respect to the refractive index. The interpolation line on the logarithmic scale for each concentration was calculated and the gradient (equivalent to α) ranged between 0.40 $\pm$0.12 (with R^2=0.77) and 0.46 $\pm$0.03 (R^2=0.98).

table 3.1. The samples concentrations were verified by measuring the absorbance of each solution and exploiting the Beer-Lambert law (eq. 1.3). The results can be seen in Figure 3.3: for each set of mixtures, the concentration was assumed to be constant for each dataset, thus allowing a meaningful comparison in the following part of the experiments. The FLIM images were used to determine both lifetime and emission intensity for each prepared solution. In Figure 3.4 are presented the intensity images for different viscosities and concentrations of BODIPY-C_{12} (`a, b, c`): an increase in the average intensity can be seen (`d`) from the histograms for the samples at 60% glycerol volume fraction corresponding to an increase in the concentration of the dye. By comparing the histograms for Figure 3.4-(`a`) and Figure 3.4-(`b`) it is impossible to differentiate the effect of the dye concentration from the effect of viscosity using the intensity images only, and thus further information like lifetime measurements are needed. In fact, by looking at these almost identical intensity images, one corresponds to a lower dye concentration and higher viscosity sample (70% volume fraction; 3.3 μM), oppo-

site to a lower viscosity and higher concentration one (60% volume fraction; 5.5 μM). The average values measured from the intensity images like in Figures 3.4 were corrected to consider the change in the refractive index of the medium by multiplying them by a correction factor N^2[244], where N is the ratio between the measured refractive index for each solution RI_x and for pure methanol RI_{Methanol}:

$$N = \frac{RI_x}{RI_{\text{Methanol}}}. \tag{3.2}$$

The corrected average intensity for each sample was calculated, plotted versus its viscosity, and the standard deviation of each distribution was used to define the error bars, as shown in the graph in Figure 3.5. It can be seen that the average intensity increases with concentration, and likewise with the viscosity of the solution. From Figure 3.5, it is possible to evaluate the gradient of the relationship between the quantum yield and viscosity (see eq. 1.25): the obtained values for the coefficient α vary between 0.40 $\pm$0.12 ($R^2 = 0.77$) and 0.46 $\pm$0.03 ($R^2 = 0.98$) for the different sets (considering the error on the linear fitting only). The average value for α is 0.43 and $\sigma = \pm 0.04$ (for the σ evaluation, the higher value between the standard deviation of the averaged α, and the uncertainty depending on the propagated error on the linear fittings was used).
It has been mentioned that molecular rotors measure viscosity by sensing the variation of the free volume (see Sec. 1.4 and eq. 1.24), but this effect is not always uniform. It is known[112; 125] in fact, that molecular rotors exhibit a linear relationship on a log-log scale only for specific viscosity intervals. Thus, at very high and very low viscosities the obtained values may be unreliable: considering the high viscosities only (40, 60, 70%) the values for α at different dye concentrations ranged from 0.48 ($R^2 = 0.96$) to 0.82 ($R^2 = 0.95$), with an average value of 0.63 and $\sigma = \pm 0.14$. The reported $\alpha = 0.5$[125] for BODIPY-C_{12} was calculated for viscosity ranging 10-900 cP; the literature value is smaller than α =0.63 calculated at high viscosities from Figure 3.5, but still within its uncertainty range. The differences in the measurement ranges can then be accounted for the different value obtained for α. It is possible to compare the intensity-based value obtained for α with the one obtained via lifetime measurements. It is known[95; 125] that BODIPY-C_{12} in methanol and glycerol solutions shows a monoexponential be-

haviour, as confirmed by its fluorescence decay measurements (Fig. 3.7). The lifetimes were measured as the average of the mean values for the FLIM images at a given viscosity: 0.43 ±0.03 ns for 10%, 0.45 ±0.03 ns for 20%, 0.53 ±0.04 ns for 40%, 0.87 ±0.07 ns for 60%, and 1.33 ±0.07 ns for 70%. A plot of the lifetime dependence on the viscosity on a double logarithmic scale can be seen in Figure 3.6: again it is of interest to verify the gradient for all the points and for the high viscosities only. In fact, previous works[95; 125] show that for BODIPY-C_{12} the gradient (corresponding to the exponent α) is constant for high viscosity. Thus, considering the high viscosity values only, the gradient α is equal to 0.39 ±0.05 ($R^2 = 1.0$) (whilst the gradient for all the datapoints is 0.23±0.08). This value is smaller than the literature[125] one of 0.50 ±0.03 (although obtained at a different measurement range).
The two values obtained for α, 0.39 ±0.05 via the lifetime and 0.63 ±0.14 via the intensity measurements, do not overlap leading to uncertainty in the gradient evaluation. By taking into account the uncertainties in the measurements and the standard deviation on the value of α (±0.05), for a measured lifetime the propagation of the error leads to a final uncertainty on the viscosity of about ±16%. Due to this uncertainty in the value for α, the accepted value 0.5 will be used for the further calculations.

3.3.1 Calibration Graph of Concentration

From the presented results of the BODIPY in solution, it is then possible to produce a reference graph as shown in Figure 3.8: the lifetime uniquely identifies the viscosity for each sample, and the linear increase of the intensity with the concentration (expressed as the absorbance in the x-axis) can be seen for each set of solutions. This plot can be exploited to map the living cells results presented in the following sections: it is possible[245], in theory, to estimate the viscosity of the imaged areas of the cells and the concentration of dye in such regions at the same time. The figure in-set shows the relationship between the gradient of each line and the lifetime, and the behaviour appears to be linear. In practice, the gradient of the line is given by the lifetime, and the intensity value on that

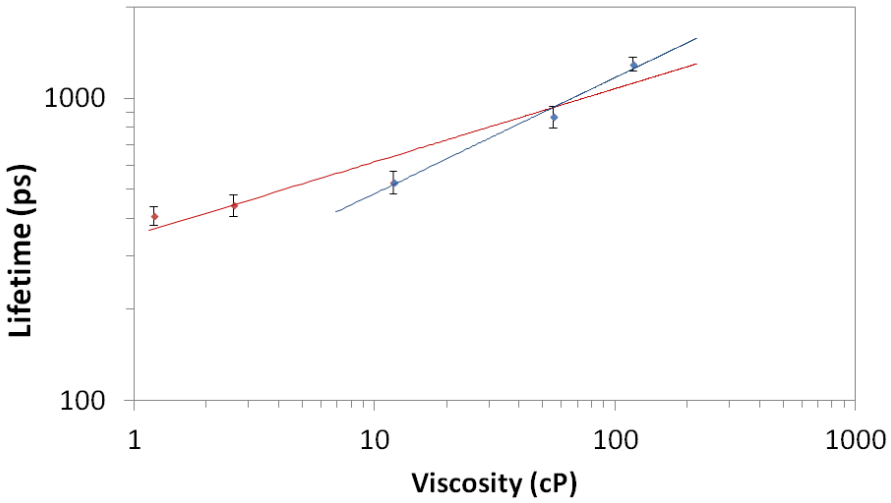

Figure 3.6: Relationship between lifetime, on the y axis, and viscosity, on the x axis, on a logarithmic plot. The best fit seems to be achieved a linear interpolations of the high viscosities only, rather than all the values. The gradient for the high viscosity values is 0.39 $\pm$0.05 (blue), and 0.24 $\pm$0.01 for all the viscosities (red).

curve identifies the concentration, according to:

$$I = m(\tau)[c] + b, \tag{3.3}$$

where I is the measured intensity, $[c]$ the concentration, b the intercept value (average value 5.6 $\pm$2.8 counts), and $m(\tau)$ the gradient of the curve, the latter being a function of the lifetime τ.
By accepting a linear approximation between the lifetime and the gradient, the equation 3.3 can be rewritten as:

$$[c] = \frac{I - b}{z\tau}, \tag{3.4}$$

where $m(\tau) = z * \tau$, and z is the slope of the linear regression between the lifetime and the gradient as shown in the inset in Figure 3.8. If the value of $m(\tau)$ varies non linearly with the lifetime, the denominator of the equation will be a function of τ and it may assume a different value in each point of the image.

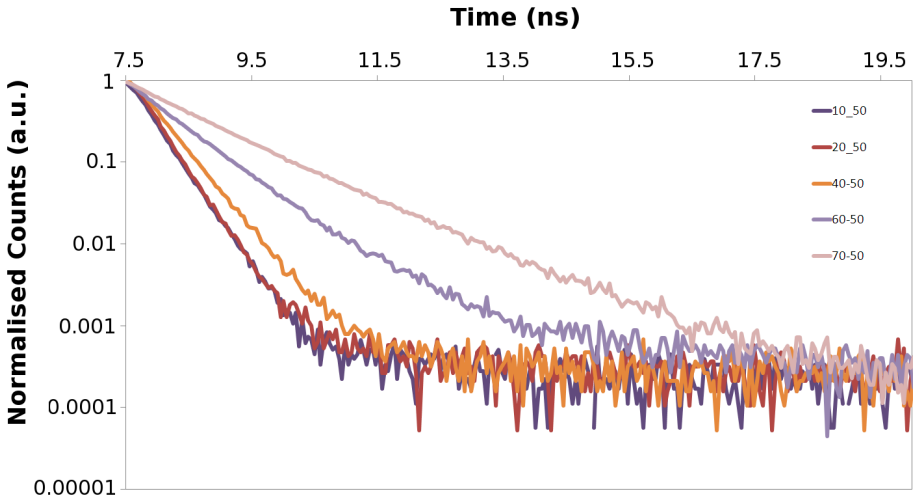

Figure 3.7: The figure shows the normalised fluorescence decays measured for the BODIPY mixtures at 5.5μM concentration. For a given viscosity (or glycerol volume fraction) the lifetime is constant: 0.43 ns for 10%, 0.45 ns for 20%, 0.53 ns for 40%, 0.88 ns for 60%, and 1.33 ns for 70%. In the graph, the values for 10% and 20% overlaps showing substantially the same lifetime.

3.4 BODIPY in Living Cells

3.4.1 Cells Preparation

As described in the introduction (see Sec. 2.6), among the several cell available for research, HeLa cells are a widely used cell line.In fact, HeLa cells are an immortalised line: they can be easily divided and further cultured for an indefinite time, reducing or removing the need of cryopreservation, thus making this line suitable for this experimental study. The used specimens were Human cervix carcinoma (HeLa) Cells from ATCC. They were cultured on a 75 cm^2 culture flask (Greiner) in DMEM with 10% FBS, 1% 1x non essential amino acid, 1 mM sodium-pyruvate and 0.1% penicillin/streptomycin at 37°C in an incubator with 95% air/5% CO_2. For harvesting the cells, 2 ml of 1x trypsin were used and diluted with culture medium. About 24 hours before imaging, 2 ml of cell solution were deposited in a 6-well glass bottom plate (WaferGen smartslide-6TM micro-incubator) and incubated overnight.

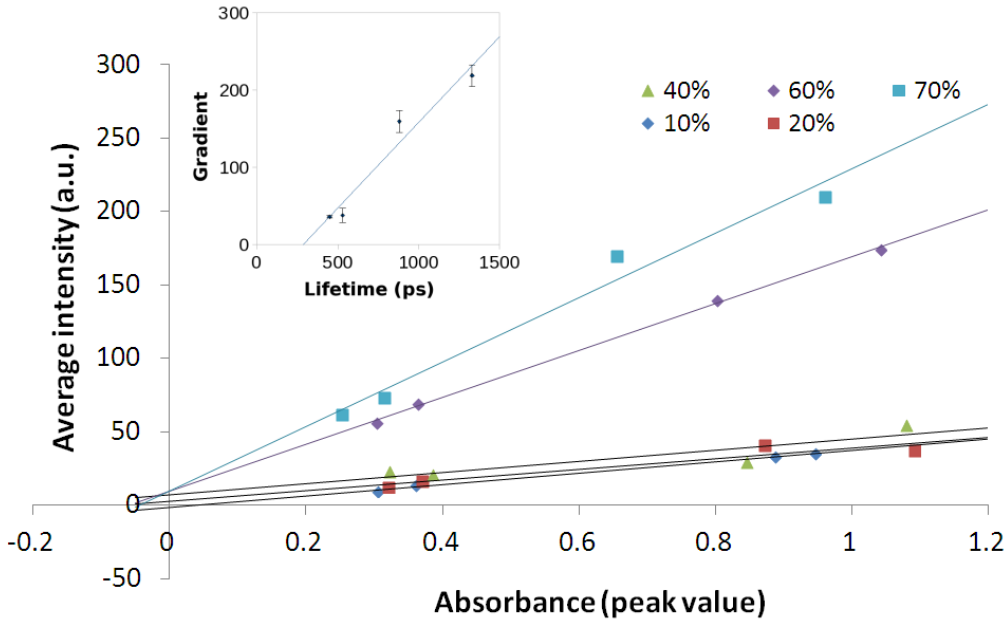

Figure 3.8: Calibration graph for BODIPY solutions at different viscosities and concentrations. The graph presents the absorbance in the x-axis and the average emission intensity in the y-axis. The viscosity, obtained from the lifetimes, identifies each set of samples. The inset shows the relationship between the lifetime and the gradient of the curves in the main graph: a linear regression gives a value for the slope z of 0.22 $\pm$ 0.03 ps^{-1} (considering the error on the linear fitting only).

For staining the cells, 20 μl of BODIPY stock solution (1.1 mM) was added to the well, lightly shaken, and incubated again for 30 minutes. After that, the solution was removed and the cells washed with clear DMEM (Opti-MEM) fives times. Finally, Opti-MEM was added to the well to be imaged and placed to the microscope stage. The temperature for the micro-incubator plate was set at 37°C with 5% CO_2. Its variation between 32 and 37°C was obtained by varying the temperature of incubator and of the imaging objective (x63 water, N.A. 1.2, Leica).

3.4.2 Living Cells Imaging

The living cells have been imaged using the FLIM system described in the previous Section 3.2 (Leica). The experiments were repeated in two different days at the two different temperatures 32° and 37°C. The images analysed in this section were obtained using the confocal microscope described in the experimental section: the pinhole size was 1 Airy (22μm), the exciting pulse at 467 nm, the resulting imaging volume 1.4μm^3; the total image size is 238×238 μm^2. In Figure 3.9 are shown the resulting intensity and FLIM images for the cells at 37°C. From the FLIM images (on the left), it can be seen that the dye is taken up by the cell: previous studies[112; 246; 247] show that BODIPY-C_{12} main locations in HeLa cell are the endoplasmic reticulum (ER) and the lipid droplets, the latter appearing as bright puncta all around the image. The false colour scale of the lifetimes indicates that the puncta have a higher lifetime (thus higher viscosity) compared to the other part of the cells. The intensity images on the right are used to measure the emission intensity. In the same way, Figure 3.10 shows the results at 32°C. The different values of the lifetime confirm a variation of the viscosity with the temperature.

3.4.3 Dye Concentration Estimation

As shown in the previous Section 3.3.1, a reference graph (Fig. 3.8) can be used to map the concentration of BODIPY-C_{12} in various parts of the living samples. A region of interest (ROI) comprising several bright puncta was used to obtain a reliable fluorescence decay and fitted to a monoexponential decay: the measured

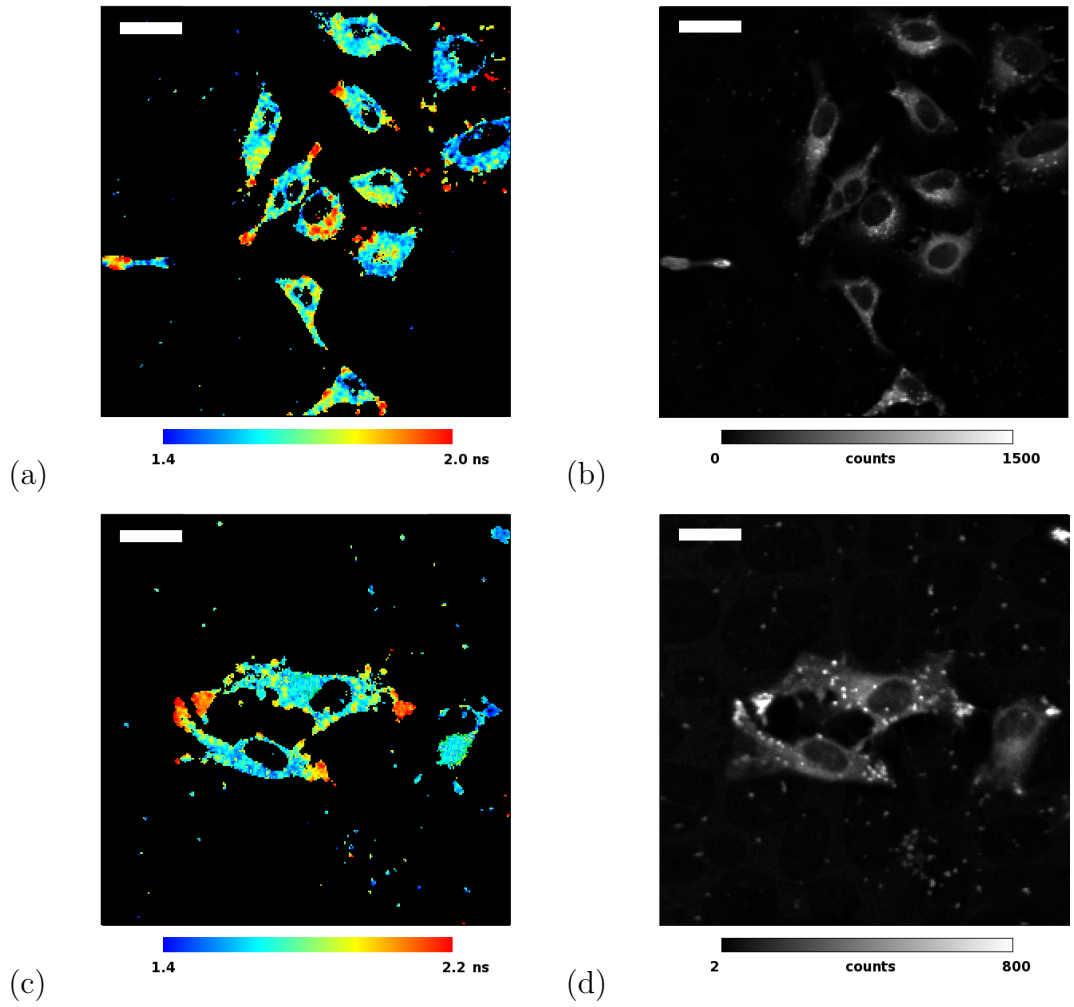

(a) (b) (c) (d)

Figure 3.9: FLIM (left) and Intensity (right) images for BODIPY-C12 in HeLa cells at 37°C. The measured cell lifetime is 1.67 ns for image (a) and 1.70 ns for (c), corresponding to a viscosity value of 101.0 cP and 104,7 cP respectively (± 30 cP). These values are in agreement with literature values for intracellular viscosity of organelles[121; 190]. The lifetime for the high viscosity puncta regions was 1.97 ns (141.5 cP) for image (a) and 2.01 ns (147.0 cP) for (c), whereas for the low viscosity regions 1.54 ns (85.6 cP) for image (a) and 1.49 ns (80.0 cP) for (b). The false-colour scale bar goes from 1.5 to 2.0 ns for (a) and from 1.4 to 2.2 ns for (c). The scale bar corresponds to 35 μm.

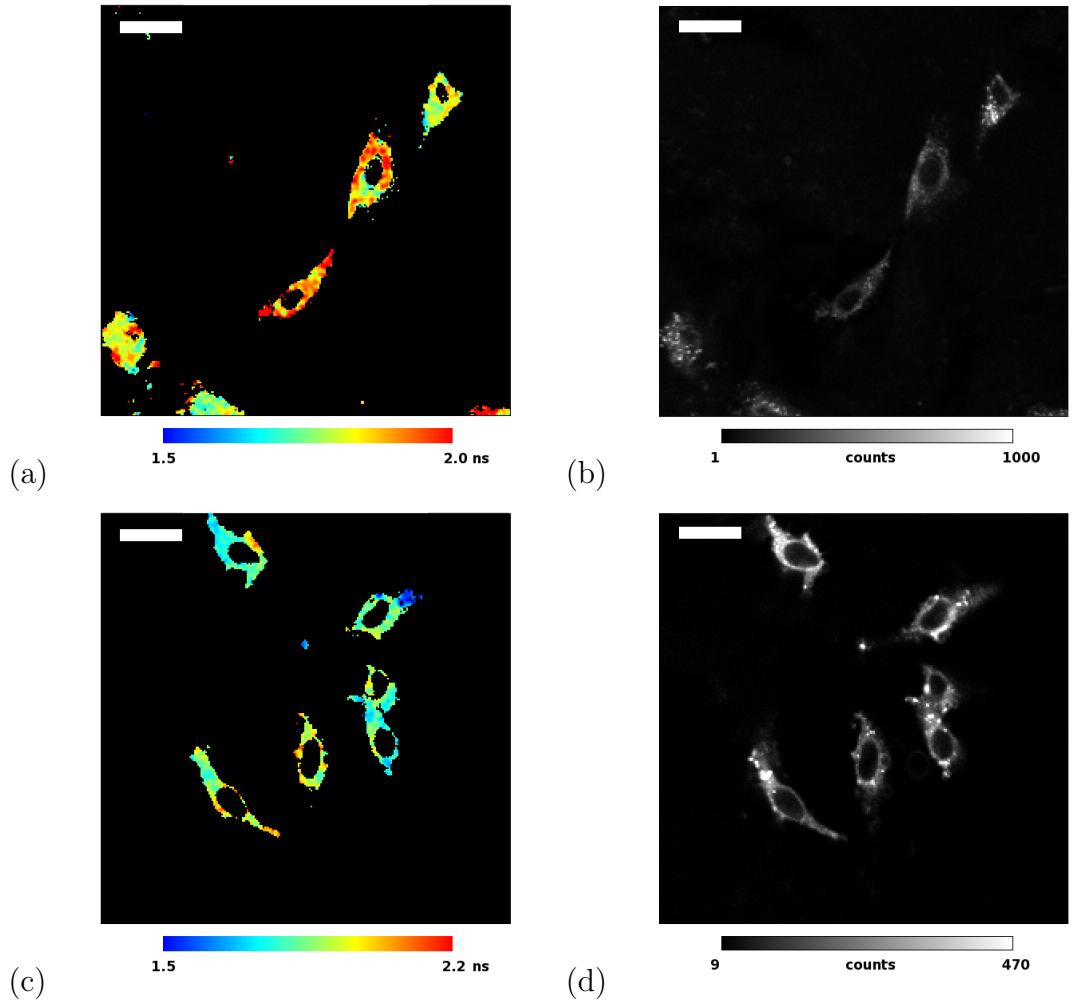

Figure 3.10: FLIM (left) and Intensity (right) images for BODIPY-C12 in HeLa cells at 32°C. The measured cell lifetime is about 1.98 ns for image (a) and 2.05 ns for (c), corresponding to a viscosity value of 142.9 cP and 153.5 cP respectively. The lifetime for the puncta regions was 1.79 ns (116.4 cP) for image (a) and 1.87 ns (127.2 cP) for (c). The false-colour scale bar goes from 1.5 to 2.0 ns for (a) and from 1.5 to 2.2 ns for (c). The scale bar corresponds to 35 μm.

lifetime corresponded to a viscosity of $141.5-147.0$ cP for the samples at 37°C. In an analogous way, a ROI for bright puncta with different viscosity and a ROI for the remaining areas of the cell stained by the dye were considered and a viscosity of $80.0-85.6$ cP for the puncta and $101.0-104.5$ cP for the cells was calculated at 37°C. Likewise, the same analysis was performed for the images at 32°C. The selection method for these areas of interest is presented in Figure 3.11. From the histogram of the lifetimes, two (or more) main components are identified; by applying a double thresholding to the FLIM image, it is possible to obtain a resulting image showing an interval of lifetimes only; the size of the interval should be evaluated according the lifetime histogram, but in practice it should clearly separate each main lifetime component. By repeating the procedure for the different components, each generated image uniquely identify the structures having the same viscosity (lifetime), and it can be used to produce a mask and apply it to the intensity image. Likewise, by performing a double thresholding on the intensity image, a selection of the areas having the same intensity can be obtained: the final image, obtained by the overlapping areas, will only show ROI with the same intensity and lifetime (or viscosity). This algorithm was performed step by step using a suitable software (Tri2), but can be automated by writing the appropriate processing code.
This procedure was repeated for each area of interest and for all the images, and the results are presented in Table 3.2. In addition to these results, by combining the linear dependence of the quantum yield on the lifetime and on the concentration[6], it is possible to map the relative concentration of dye as the ratio between the intensity and the lifetime, as shown in Figures 3.12 and 3.13 and according to equation 3.5:

$$[c] \propto \frac{I}{\tau}, \tag{3.5}$$

where I the measured intensity, $[c]$ the dye concentration and τ the fluorescence lifetime. By using the concentration values calculated from the calibration graph and equation 3.4, it is possible to rescale the false-colour bar in Figures 3.12 and 3.13 to represent the dye concentration in the various regions of the cell directly.

Intensity (counts)	τ (ns)	Viscosity (cP)	Concentration (μM)	Temp. (°C)	ROI
610	1.54	85.6	16.31	37	Puncta 1
330	1.97	141.5	6.47	37	Puntca 2
220	1.67	101.0	5.2	37	Cell
494	1.49	80.0	13.65	37	Puncta 1
527	2.01	147.0	10.19	37	Puncta 2
136	1.70	104.7	3.1	37	Cell
270	1.79	116.4	5.91	32	Puncta
97	1.98	142.9	1.81	32	Cell
297	1.87	127.2	6.19	32	Puncta
116	1.55	86.8	2.95	32	Other
85	2.05	153.5	1.51	32	Cell

Table 3.2: The average intensity, viscosity and concentration for HeLa cell various domains at different temperatures. The table shows the analysis of the sub domains for each image in Figures 3.9 and 3.10 (in the same order). The regions of interest (ROI) called *Puncta* represent the lipid droplets, whereas *Cell* identifies the other areas of the cell excluding the puncta; the values measured for all the areas were averaged within each region of interest. The further ROI subdivision in *Puncta 1* and *Puncta 2* arises from the identification of two lifetime (viscosity) regimes for the point-shaped structures in Figures 3.9. Similarly, in Figure 3.10-(b) it was identified a very low viscosity and low intensity area (*Other* in table).

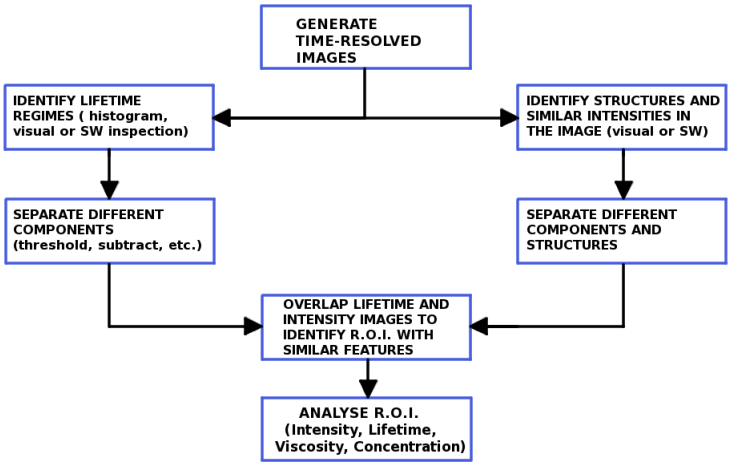

Figure 3.11: Schematic of the selection method for the areas of the cells. FLIM and Intensity image are separately analysed and thresholded to identify intervals with similar lifetime (viscosity) and similar intensity. The overlapping subregions are used to define the ROI in the cells.

3.5 Discussion

The previous sections described the method and presented the results for measuring viscosity and concentration using a molecular rotor. In the final results, the main source of error on the concentration lies in the reliability of both intensity and lifetime measurements: by calculating the error propagation on the final value of the concentration, it was found that an uncertainty of 10% on the intensity ($\frac{\Delta(I)}{I}$=0.1) and the lifetime ($\frac{\Delta(\tau)}{\tau}$=0.1) led to a final error on the concentration of about 14% ($\frac{\Delta([c])}{[c]}$=0.14), whilst an uncertainty of 5% led to an error on the concentration of about 7%. Due to the averaging on several pixels of the images, the results presented in Table 3.2 are subjected to a large error on the concentration. On the other hand, since the values on Figures 3.12 and 3.13 are calculated pixel by pixel, only the experimental error should be taken into account (reasonably around 5%) and thus an uncertainty of ∼7% can be estimated. The different viscosity regimes for the two temperatures need to be further investigated. At 37°C, the small areas with very low viscosity may suggest a different kind of lipid droplet (having a different viscosity) or may be associated to some

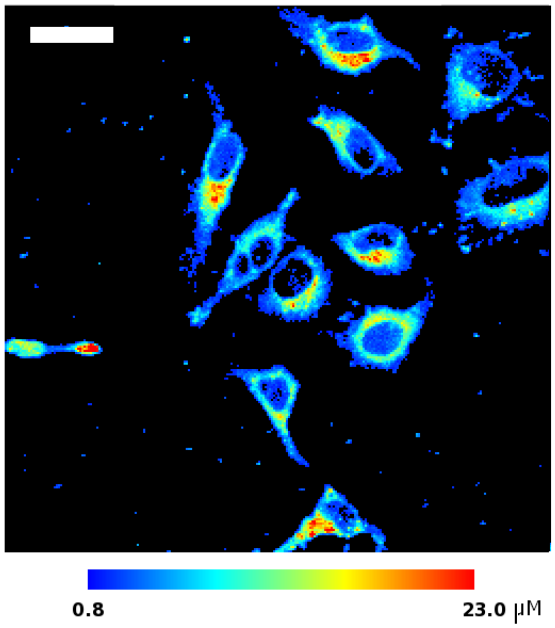

(a)

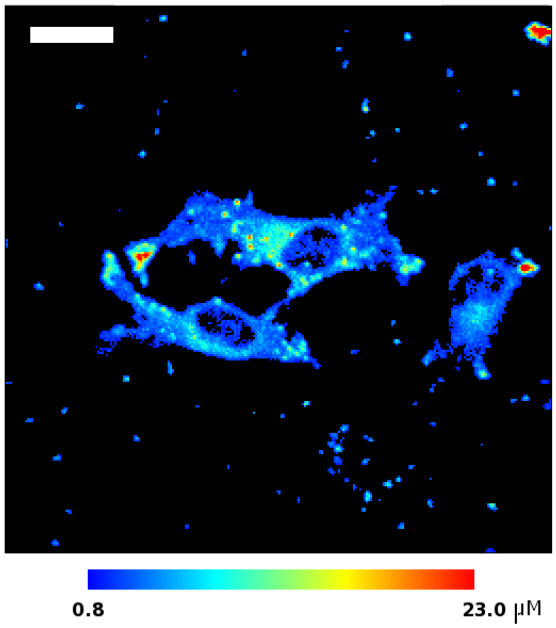

(b)

Figure 3.12: Concentration mapping for HeLa cells at 37°C. The maps are obtained as the ratio between the Intensity and the FLIM images: the colour bar ranges from 0.8 to ∼23 μM concentration. The scale bar corresponds to 35 μm.

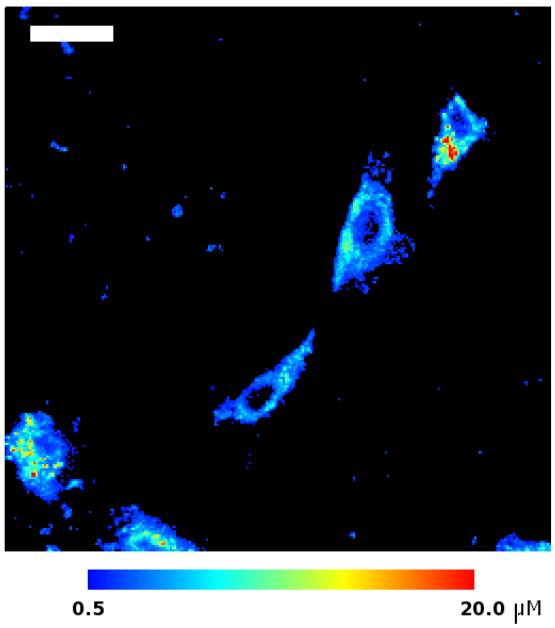

(a)

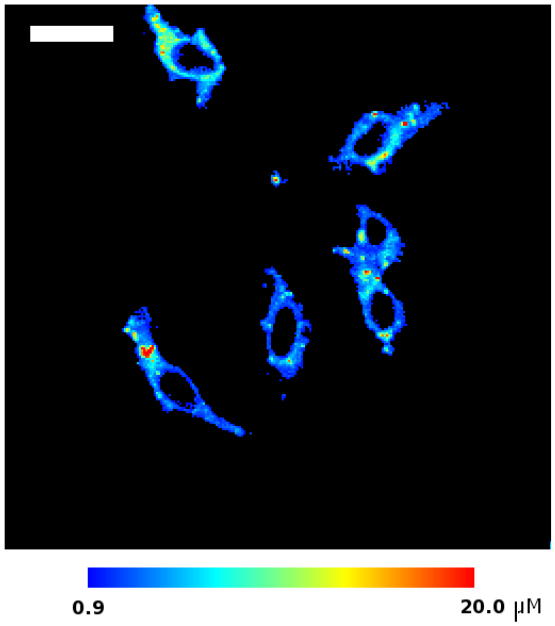

(b)

Figure 3.13: Concentration mapping for HeLa cells at 32°C. The maps are obtained as the ratio between the Intensity and the FLIM images: the colour bar ranges from 0.5 for (a) and from 0.9 for (b) to ∼20.0 μM concentration. The scale bar corresponds to 35 μm.

processes within the cell or with its environment, or be related to some changes in the structure of the droplet, or also to a change due to the droplet being at a different point in its lifespan. At 32°C, the general viscosity of the cell increases of about 50% to ∼142.9-153.5 cP, from 101.0-104.7 cP at 37°C, as expected with a decrease of the temperature; however, the lipid droplets do not undergo the same increase and their viscosity decreased instead: the viscosity for the puncta diminished by about 15% (from 147-141 at 37°C to 116-127 at 32°C). This counterintuitive effect may depend on several factors linked to the change in temperature: since the lipids are involved in the cell metabolism, reasons such as the health of the cell, its internal processes[248], and the stability of the vesicles themselves at different temperatures, may all be accounted for this change of viscosity[249].

In addition, the correct calculation of α is fundamental, as small variations in its value lead to large variation in viscosity. During the review of this thesis, the viscosity was re-calculated also using the previously obtained value of $\alpha = 0.36$, leading to viscosity measurements of above 280 cP for the cells and above 400 cP for the lipid droplets, in total disagreement with literature value for both regions. In practice, a variation of 30% on the accepted α produced a change of about 150-200% with respect to the previously measured viscosity.

The average concentrations calculated for several cell domains at the different temperatures are presented in Table 3.2 and are mapped in Figures 3.12 and 3.13. The table indicates concentration values of $13 - 16$ and $6 - 10$ μM for the two different lipid droplets, and $3.1 - 5.2$ μM for the other regions of the cell at 37°C. At lower temperature (32°C), the viscosity variation between the cell and the droplets is reduced, but a concentration difference can still be identified $1.5 - 1.8$ μM in the cell and $5.9 - 6.2$ μM in the puncta. An other area of the cell presents a low viscosity and a concentration of ~ 3 μM The concentration decreases by $\sim 50\%$ between the two temperatures: the reason for this variation may be again either a change in the cell health or its interaction with the dye, or an other effect associated with the modifications the cell undergoes at lower temperatures.

3.6 Conclusions

The presented results confirm the possibility to estimate the concentration of the BODIPY-C_{12} in cells through a combination of fluorescence lifetime and intensity images. The obtained values are in the μM range, from $\sim$4 to $\sim$14 μM for the different regions of the cell at 37°C.

The viscosities obtained for the domains of HeLa cells at 37°C and 32°C show average values of 103 cP and 147 cP respectively, in agreement with previous works[246] and in the same order of magnitude with reported values for the intracellular viscosity of SK-OV-3 of about 160 cP[95; 125]. These viscosity values are associated with cell's organelles rather than membrane as the latter has higher viscosity ($\sim$600 cP), nor with cytoplasm as this presents a very low viscosity ($\sim$1-2 cP). The localisation of the BODIPY$-C_{12}$ is then confirmed to be in the endoplasmic reticulum and its organelles. A viscosity increase with decreasing temperature (from 37 to 32°C) it is normally expected, but this particular effect may also be connected with the health of the cell. In fact the ideal temperature for HeLa cells culture is about 37°C, and it has been reported that dying cells increase largely their viscosity (up to 300$\pm$50 cP)[126]. The puncta in the images are reported to be lipid droplets[246] and their localisation around the ER-organelles supports this conclusion. The measured viscosity of the puncta is higher than the reported values of 50 cP[247] for droplets in HeLa cells, but of the same order of magnitude. The viscosity change of the puncta at lower temperature may be connected to the variation in their structure[249], as previously mentioned.

As for the validity of the results, further lifetime and intensity measurements at higher viscosities are required to obtain a more reliable value for α. In addition, the calibration graph (see Fig. 3.8) for the concentration discussed in this chapter used only 5 sets of samples at 4 different concentrations but expanding the datasets, both for higher viscosities and for different dye concentrations, it would lead to more reliable and easy-to-map results.

3.7 Chapter Summary

This chapter presented the first attempt to simultaneously estimate the concentration of BODIPY-C_{12} in cells and the viscosity of the cell itself using a combination of lifetime and intensity fluorescence measurements. The use of a single type of fluorophore (in contrast with ratiometric approach, that normally requires two) simplifies the measurement procedures and reduces the amount of extraneous substances interfering with the normal processes of the cell, but requires a longer calibration of the instruments and characterisation of the dye. Variation of viscosity and concentration with the temperature was observed, but the exact nature of this change, especially with respect to the lipid droplets, it is unclear and needs further investigation.
These results are of interest to better understand BODIPY-C_{12} interactions and distribution within the cell. Furthermore, a similar approach may be applied to measure other molecular rotors concentration and help to evaluate if their concentration plays any role in the cell health or in its internal processes.

Chapter 4

Molecular Rotors: ET Compound

In this section we present our findings in the use of the recently synthesised compound *ET* as a molecular rotor. Its spectroscopic properties and the possibility to use it to stain living HeLa cells are evaluated.

4.1 Introduction

As described in the previous Section 3.1, viscosity is fundamental in many molecular processes of the cells and the development and study of new techniques and compounds, and their analysis is then of great interest for biology and biomedical fields. The use of molecular rotors to measure intracellular viscosity has been reviewed[112], but the number of dyes having spectral properties suitable for cell imaging (such as non-UV excitation wavelength and high quantum yield) is limited.

This chapter focuses on the testing of a recently developed compound "ET", and evaluate its properties as molecular rotor. "ET" molecular structure is shown in Fig. 4.1, featuring a system of benzene rings and double bonds surrounded by tertiary amines and cyano groups. Its molecular weight is 490.6 g/mole, and it was developed by Dr Weihong Zhu group in Shanghai in 2012. From their first laboratory results (unpublished), this dye exhibited moderate fluorescence intensity, excitation and emission wavelengths in the visible spectrum, and its lifetime appeared to be sensitive to viscosity variation, thus the interest of this project

to further investigate its possible applications. Firstly its fluorescence behaviour at different viscosity is analysed along with its lifetime in order to produce a viscosity map for the dye, and these results are used as a reference in the following experiments. In the second part of the chapter the rotor performances in cells are considered via FLIM and time resolved anisotropy. Finally the results and the findings are discussed.

4.2 Fluorescence Properties of ET Rotor at Different Viscosity

4.2.1 Experimental setup

In order to test the fluorescence characteristics of the ET compound, we prepared several samples at different viscosity: each probe consist in 10 ml methanol/glycerol solution with different volume fraction of glycerol. A stock solution of 3 mg of ET compound in 6 ml was prepared (1.01 mM concentration) and dissolved in every tube so that the concentration was made approximately 20 μM.
For each sample were then collected emission and absorption spectra using a spectrophotometer and a luminescence spectrometer (Hitachi, U4100 for absorption; Perkin-Elmer, LS-50B for emission). Clear quartz cuvette (Starna) with 2 ml of solution were used for all the measurements. Then in order to calculate the correction factor (G) and the steady-state anisotropy, two polarizers were inserted in the spectrometer before the excitation source and the sensor, respectively (as described in Chapter 2.1). In addition to this correction parameter, it was important to consider the refractive index of the different solutions: its value changes depending on the ratio of glycerol and methanol in the sample. Since the refractive index affects the amount of collected light, in order to have a consistent evaluation of the intensity measurements, we have to scale the collected values by taking it into account. The refractive index values were obtained using a refractometer. We multiplied then all our measurements by a factor N^2, where N is the ratio between the refractive index of the mixture and the reference refractive index of the methanol alone ($n = 1.331$) for each sample, as described

in Section 3.2 in eq. 3.2[244]; this correction is required to discriminate the fluorescence emission due to the change in refractive index, from the emission due to the change of solution viscosity for the investigating compound.
The same samples were then used to collect the time-resolved fluorescence decay with a TCSPC acquisition board (Becker&Hickl SPC 830) connected to an inverted confocal scanning microscope (Leica), as previously described in Section 3.2. For this measurement, 10 μl of each dye solution was placed in each well of a 96-wells glass-bottom microplate (Whatman). The pulsed diode laser used for the samples excitation has a wavelength of 467 nm, pulse duration of 90 ps, and was set to a repetition rate of 20 MHz. The fluorescence signal passed through a chromatic reflector, a pinhole, and a 624 nm band pass filter (Semrock) for ET solutions and was then detected by a hybrid PMT detector. The experimental setup for the microscope was maintained the same as in the previous chapter, shown in Figure 3.2. For the anisotropy measurements, a second PMT was used to measure the perpendicular component of the polarised signal.

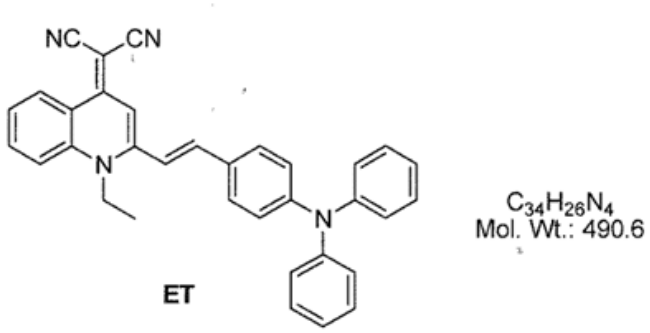

Figure 4.1: Molecular structure of ET compound. The molecule features an aromatic conjugated π system of benzene rings and double bonds, surrounded by tertiary amines and cyano groups.

4.2.2 Viscosity and Refractive Index

As previously described in Sec. 3.2, in order to characterise solutions viscosity, a model for binary liquids was used. The Table 4.1 expands the values previously

Glycerol volume fraction	Viscosity (cP)	Refractive index
10%	1.20	1.3835
15%	1.76	1.3855
20%	2.59	1.3930
25%	3.79	1.3985
30%	5.56	1.3995
35%	8.14	1.4010
40%	11.94	1.4170
45%	17.50	1.4260
50%	25.65	1.4335
55%	37.60	1.4360
60%	55.12	1.4430
70%	118.44	1.4470
75%	173.61	1.4515
80%	254.49	1.4545
85%	373.04	1.4570
90%	546.83	1.4620

Table 4.1: Relationship between glycerol volume fraction, viscosity, and measured refractive index for the solutions of ET compound in glycerol and methanol. A binary solutions model was used for the viscosity calculation.

presented (see Tab. 3.1) and displays the measured values of the refractive index for the mixtures at 22°C.

4.2.3 Absorption and Emission Spectra of ET compound

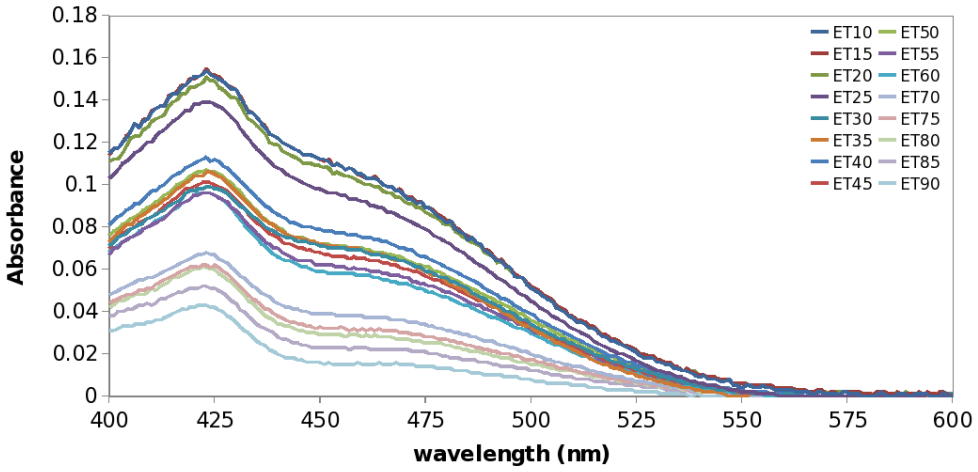

Figure 4.2: Absorption spectra for ET solutions at different viscosities. The experiments were performed with a 10 mm optical path quartz cuvette, on a Hitachi U-4100 spectrometer.

Here we present the measured absorption and emission spectra of ET in methanol and glycerol mixtures. From these spectra, absorption and emission peaks can be analysed: the absorption peak is at 423 ±0.5 nm and the emission peak at 615 ±2 nm, depending on the sample. The emission spectra were collected then using an excitation source at 423 nm on the spectrometer (Perkin-Elmer, LS-50B). According to the theory, the Stokes shift of the mixtures is almost constant and independent of the viscosity.
We also assume the ET extinction coefficient α is constant for all the mixtures. Albeit all preparation of each sample was the same, as shown in Figure 4.2 the absorbance is not constant among all the mixtures. Thus, according to Beer-Lambert's law (see eq. 1.3), the concentration is not constant: in order to make consistent the fluorescence intensity measurements, a linear correction to scale the collected emission spectra was used. The corrected emission spectra can be

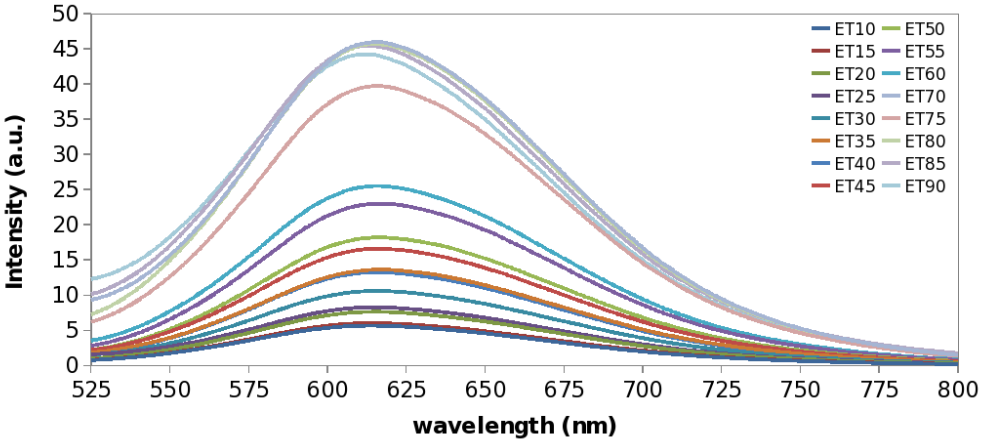

Figure 4.3: Corrected emission spectra for ET solutions of methanol and glycerol at different viscosities. The experiments were performed with a 10 mm optical path quartz cuvette, on a Perkin-Elmer LS-50B spectrometer.

seen in Figure 4.3.

4.3 Fluorescence Intensity

In this work we did not measure the quantum yield directly but the intensity of fluorescence emission only. Since the amount of light emitted is proportional to the quantum yield, we integrate the collected light in the wavelength interval 550 − 700 nm for each mixture and use these values instead. The spectra from the previous section were used for this calculation.

We considered then the corrected emission spectra and produced a plot of intensity versus viscosity as shown in Figure (4.4): it is evident the increase of intensity with the viscosity. Using a double logarithmic plot for intensity and viscosity (Figure 4.5) we can see the linear trend in accordance with Förster-Hoffmann equation, thus being the slope of the the plot equal to α, the exponent in Förster-Hoffmann equation (see eq. 1.25). From the line of best fit, for ET compound the value of α is 0.38±0.02 ($R^2 = 0.97$).

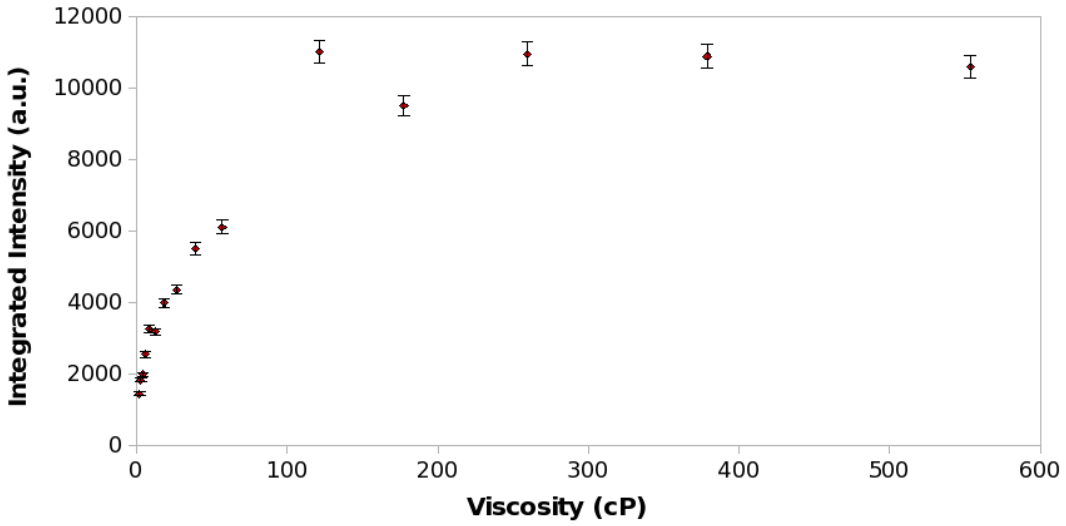

Figure 4.4: Relationship between the intensity I and the viscosity η for measured ET solutions. Since the integrated intensity was used, it was not possible to produce statistics for the error: the only error considered was the instrumental error (about 2%).

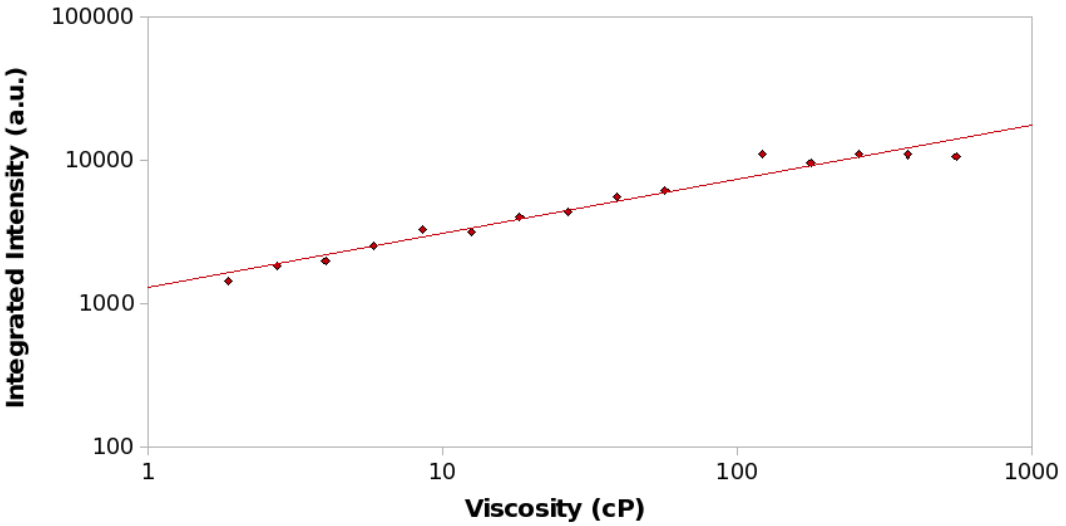

Figure 4.5: Relationship between intensity I and viscosity η on a logarithmic plot. In agreement with the Förster-Hoffmann equation, the trend can be fitted with a straight line ($R^2 = 0.97$) with slope α=0.38±0.02.

4.4 Fluorescence Lifetime Measurements

As shown, the emission intensity of ET-rotor increases with the viscosity of the solution. From the Förster-Hoffmann equation it is known that a plot of the emission intensity versus the viscosity on a double-logarithmic scale is a straight line for a given (constant) concentration of the dye. Especially when working with biological samples, however, it is difficult to control the dye concentration within complicated systems such as cells and cell environments. Thus, it is not trivial to distinguish, using the integrated emission intensity alone, the effect of viscosity from the effect of concentration. Fluorescence lifetime of molecular rotors, on the contrary, is mostly independent of the dye concentration and can be easily and accurately measured compared to the fluorescence intensity and quantum yield.
The proposed molecular rotor shows a bi-exponential behaviour, this making the fitting and lifetime estimation more complex than in monoexponential systems but nevertheless advantageous comparing to the intensity only measurement. Fluorescence decays were collected for all the samples at different viscosity and presented in Table 4.2 and Figure 4.6. The values A1 and A2 in the table represent the weight (as a percentage) of the two lifetime components $\tau 1$ and $\tau 2$. The graph in Figure 4.7 shows the distribution of the lifetimes in respect to the weight A1 (A2 value depends on A1, so it can be omitted): from the graph it is difficult to identify a definite trend, although statistical analysis indicates a small positive correlation. It is more significant instead the correlation between $\tau 1$ and $\tau 2$, presented in Figure 4.8: the regression line shows that the lifetimes tend to vary proportionally, with a gradient of 1.27 ± 0.25 (intercept 33 ± 145, $R^2 = 0.70$). This linear relationship can also be seen by analysing the variation of each lifetime with the viscosity in Figure 4.9: on a double logarithmic plot, both the lifetimes show a linear trend in respect to the viscosity, with substantially the same gradient: $\alpha_1 = 0.202 \pm 0.031$ ($R^2 = 0.78$) and $\alpha_2 = 0.198 \pm 0.031$ ($R^2 = 0.79$), for $\tau 1$ and $\tau 2$ respectively. It can be noticed that the values for α_1 and α_2 are far smaller than the previously found value for α obtained from the intensity measurements.
In order to further investigate the lifetime relationship with viscosity, the average lifetime τ can be used: the relationship is presented in Figure 4.10. The value of

Glycerol vol. fraction	Viscosity (cP)	A1 %	τ1 (ps)	τ2 %	t2 (ps)	τ (ps)
20%	2.59	14.0	430	86.0	456	451.97
30%	5.56	3.2	319	96.8	506	500.00
35%	8.14	1.6	281	98.4	445	442.44
40%	11.94	95.0	446	5.0	519	449.77
45%	17.50	77.2	388	22.8	725	464.85
50%	25.65	22.5	500	77.5	574	557.55
55%	37.60	78.4	478	21.6	752	537.10
60%	55.12	11.2	665	88.8	687	684.03
65%	83.09	10.8	677	89.2	711	707.30
70%	118.44	94.6	661	5.4	1017	680.10
75%	173.61	5.0	620	95.0	773.7	766.05
80%	254.49	10.1	792	89.9	887	849.00
85%	373.04	99.9	926	0.1	1507	925.00

Table 4.2: Lifetime measurements at different viscosities. The first two columns display the glycerol volume fraction and the viscosity for each measured solution. The following columns show the coefficients and lifetimes of a bi-exponential fitting of the decays. The last column shows the average lifetime at each viscosity.

the gradient found from a linear best fit is 0.167 ± 0.02; this value should be equal to α found from the intensity measurements experiment but it is less than half ($\alpha = 0.38$). Apparently, this is a feature of ET compound as this behaviour was reported in ethanol/glycerol solutions[250] where the values for α were found to be 0.5 and 0.23 for intensity and lifetime measurements respectively. This particular phenomenon shows that this rotor does not behave completely in accordance with Förster-Hoffmann theory, nevertheless its linear relationship between the logarithmic values of lifetime and viscosity make it a still valuable instrument for microviscosity estimation using fluorescence lifetime measurements as shown in the following sections.

4.5 ET in Living Cells via FLIM

This section describes the findings using the ET compound in living cervix cancer cells. The dye demonstrates uptake in HeLa cells, showing a diffuse distribution

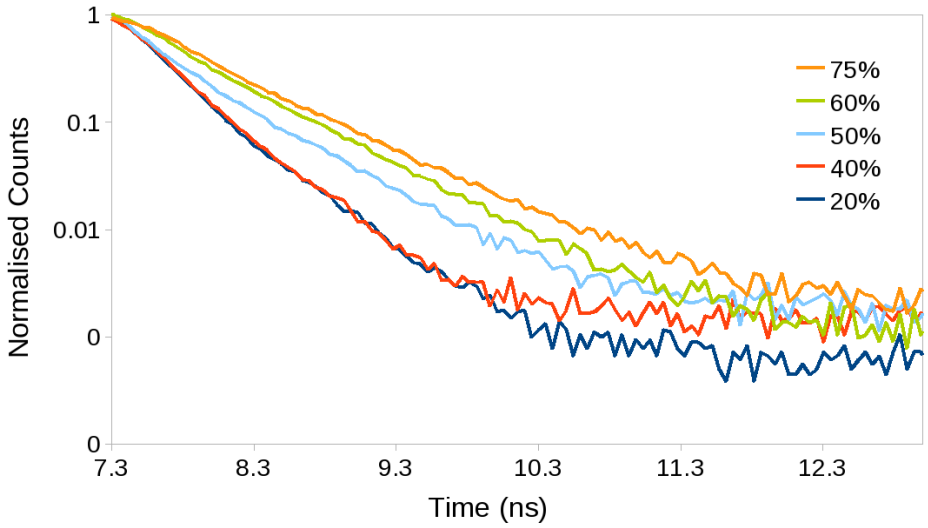

Figure 4.6: Measured fluorescence decay for a set of samples at different glycerol volume fractions. The measured average lifetimes are 452 ps (20%), 450 ps (40%), 558 ps (50%), 684 ps (60%), 766 ps (75%).

within the specimen structures. However, the precise location and structures to which the compound gets attached still need to be investigated. The presented results with living cells are obtained via FLIM techniques.

4.5.1 Experiment Setup

For the living cell experiments, human cervix carcinoma (HeLa) Cells (ATCC) were used. They were cultured on a 75 cm^2 culture flask (Greiner) in DMEM with 10% FBS, 1% 1x non essential amino acid, 1 mM sodium-pyruvate and 0.1% penicillin/streptomycin at 37°C in an incubator with 95% air/5% CO_2. The cells were then harvested by 2 ml of 1x trypsin and diluted with culture medium. The day before imaging, 2 ml of cell solution were deposited in a 6-well glass bottom plate (WaferGen smartslide-6TM micro-incubator) and incubated overnight.
For staining the cells, 20 μl of ET stock solution (1.01 mM) was added to the well, lightly shaken, and incubated again for 60 minutes. After that, the solution was removed and the cells washed with clear DMEM (Opti-MEM) fives times. Finally, clear DMEM was added to the well to be imaged and placed to the microscope

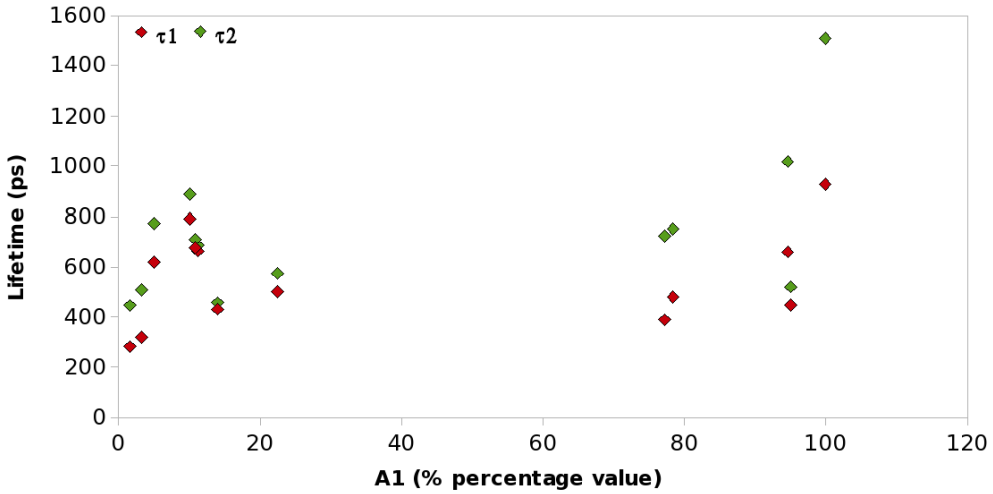

Figure 4.7: Distribution of the two lifetimes $\tau 1$ and $\tau 2$ in respect to the value of A1. The Spearman's rank values $\rho_1 = 0.297$ and $\rho_2 = 0.440$, for $\tau 1$ and $\tau 2$ respectively, suggest a weak positive correlation for both the lifetimes. The standard error on ρ_i depends on the number of points considered and equals $\sigma = 0.18$. The number of points appear to be too small to obtain reliable statistics, but the positive correlation indicates that A1, representing the weight of $\tau 1$, slightly increases for longer lifetimes (opposed to A2 that decreases instead).

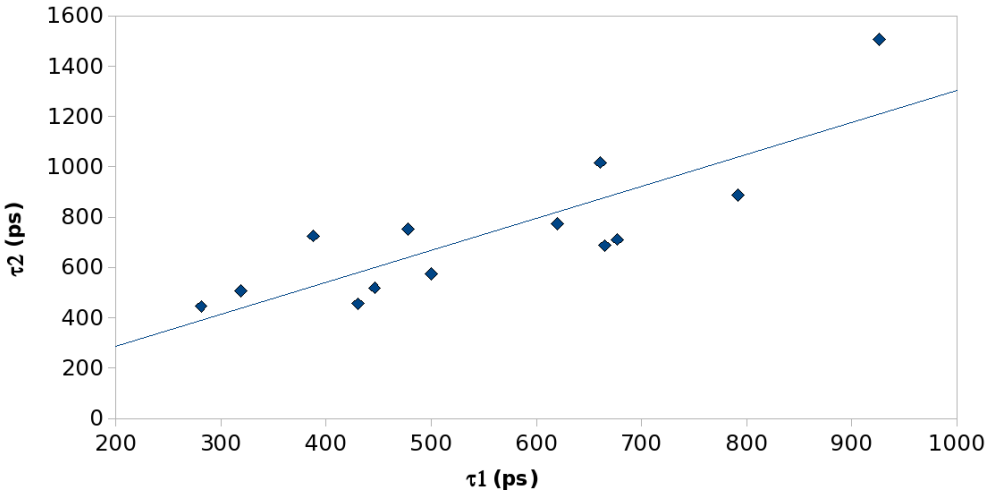

Figure 4.8: Relationship between the two lifetimes $\tau 1$ and $\tau 2$. The Spearman's rank value $\rho = 0.753$ with $\sigma = 0.18$ suggests a strong positive correlation. The linear fitting in figure has the equation $\tau 2 = 1.27\tau 1 + 33$ and $R^2 = 0.7$.

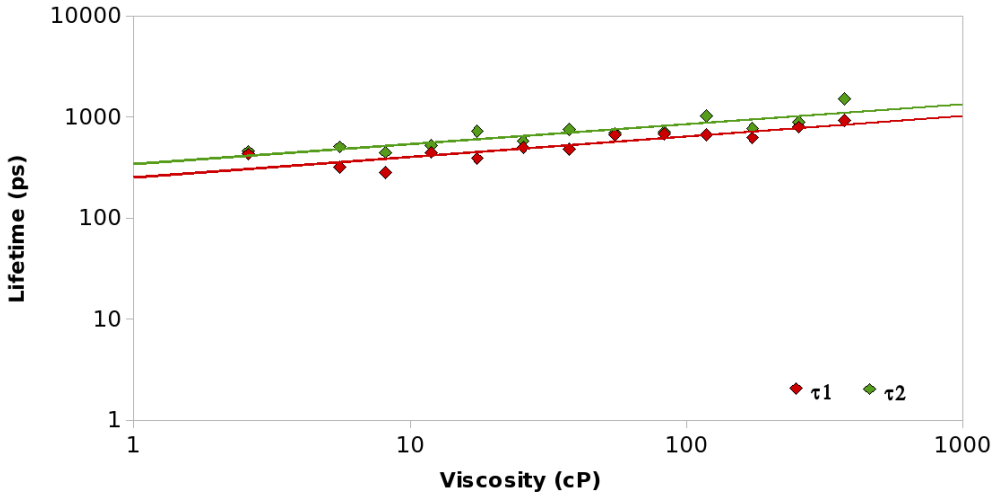

Figure 4.9: Relationship between the two lifetimes $\tau 1$ and $\tau 2$ and the viscosity. On a log-log scale, both the lifetimes exhibit a linear dependence on the viscosity: the gradient was found to be $\alpha_1 = 0.202 \pm 0.031$ ($R^2 = 0.78$) and $\alpha_2 = 0.198 \pm 0.032$ ($R^2 = 0.79$) for $\tau 1$ and $\tau 2$ respectively.

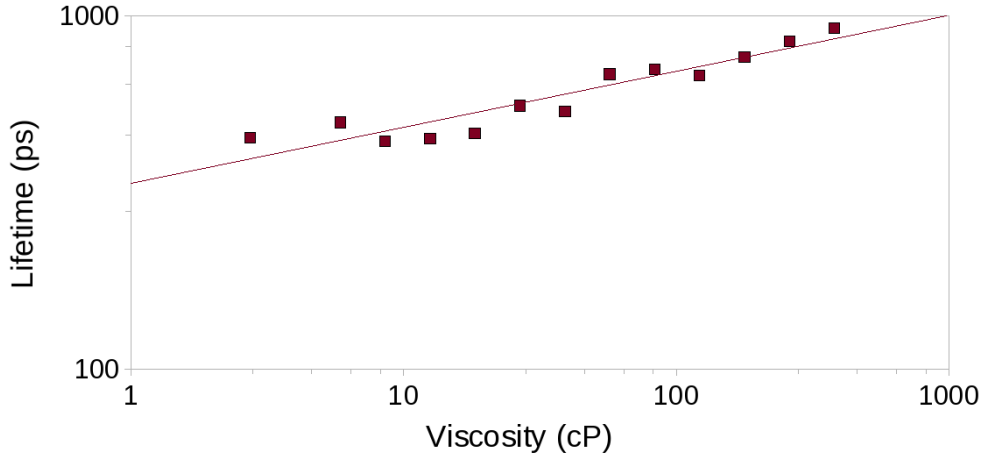

Figure 4.10: Relationship between lifetime and viscosity on a logarithmic plot. The gradient of the line of best fit is α, obtained from lifetime measurement. The measured value is 0.167 ± 0.02, in disagreement with the previous calculated value of 0.38 ± 0.02, from the intensity measurements. This difference suggests a behaviour for the ET compound in contrast with Förster-Hoffmann theory.

stage. The micro-incubator plate was set at 37°C with 5% CO_2. The temperature variation between 32 and 37°C was obtained by varying the temperature of the imaging objective (63x water, N.A. 1.2, Leica) and of the incubator.

4.5.2 Results

By comparing the measured fluorescence lifetime of ET in live samples with the calibration graph (Figure 4.10), it is possible to estimate the viscosity of the environment where the dye is attached in cells. The experiments were carried out at two different temperatures: 32°C and 37°C.
The intensity images in Figure 4.11-(a, b) show the uptake and the general localisation of the dye in the cells. The stained parts of cells demonstrate uniform intensity, thus indicating equally distributed concentration of the dye or homogeneous viscosity. In fact, the fluorescence intensity depends on both the concentration of the fluorescent molecular rotor and the viscosity of the solution, in accordance with Förster-Hoffmann equation (eq. 1.25). By using fluorescence lifetime measurements, it is possible to differentiate among these two effects. For the fitting of the fluorescence decay a bi-exponential function was used and applied to each pixel. The coloured scale bar indicated a fluorescence lifetime interval between 450 (blue) and 1500 (red) ps for all the images as shown in Figure 4.11-(c, d). The measured lifetime for ET in HeLa cells was shorter for cells imaged at 37°C than the one for cells at 32°C and the lifetime histograms show an asymmetric distribution. The average fluorescence lifetime of ET measured at 32°C was found to be 850 ps, and 647 ps at 37°C, as shown in Figure 4.11-(e, f). An example of the fluorescence decay in a single pixel is presented in Figure 4.11-(g, h), and an example of the multiexponential fitting using B&H SPCImage is shown in Figure 4.12. The intracellular viscosity corresponding to the measured lifetimes is 258±80 cP at lower temperature and 50.35 ±20 cP at 37°C. These results indicate that an increase in temperature gives place to a decrease of viscosity. Furthermore, they are in good agreement with previous results for intracellular viscosity of cells[112; 190], and such a high value suggests that ET is not located in the cell cytoplasm because the viscosity is known to be lower there (1-2 cP)(see Sec. 1.5.1).

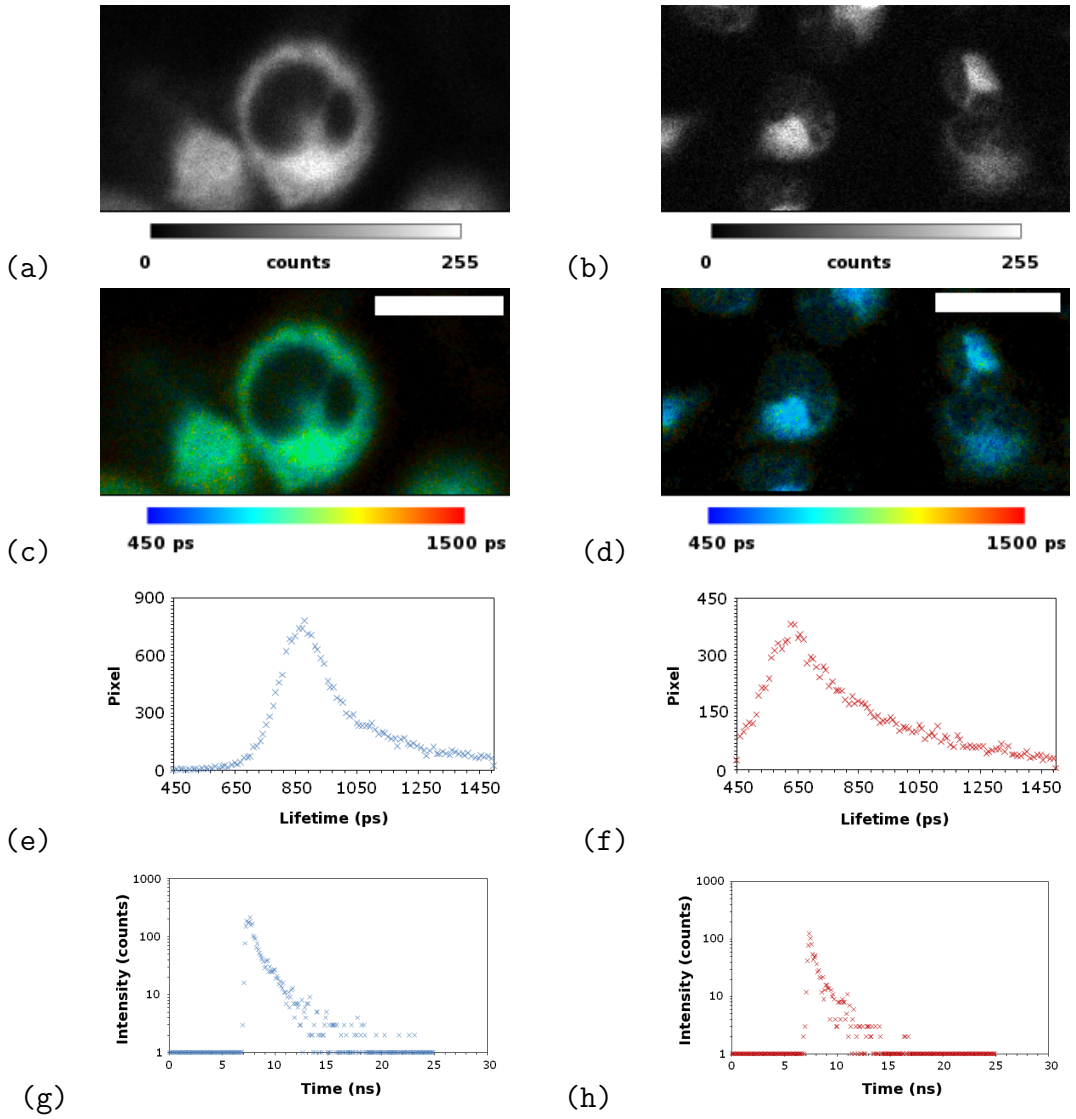

Figure 4.11: FLIM and intensity images for ET compound in HeLa cells at 32°C (a,c) and 37°C (b, d). Graphs (e) and (f) show the distribution of the lifetimes, whereas (g) and (h) present an example of the decay in a single pixel for the FLIM images at 32°C and 37°C respectively. The lifetime at 32°C is around 850ps, corresponding to a viscosity value of about 260 ±80 cP, whereas at 37°C the lifetime 647 ps corresponds to a viscosity of 50.35 ±20 cP. These values are in agreement with literature values for intracellular viscosity[190]. The scale bar corresponds to 25μm.

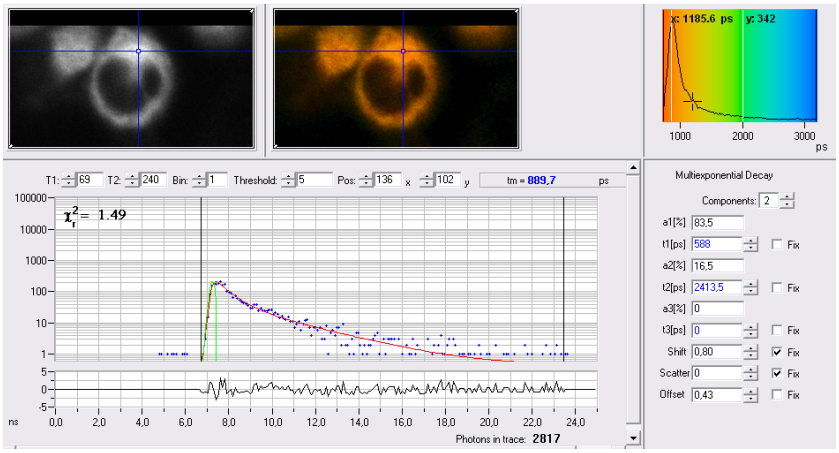

Figure 4.12: Example of decay fitting for ET compound in HeLa cells at 37°C, obtained using SPCImage software. The upper part of the figure shows the intensity and lifetime images, whilst the graph in the lower part show how the fluorescence decay is fitted with a two-exponential approximation. On the right side are presented the histogram of the lifetimes (top) and the parameters of the fitting. The calculated average lifetime is 889.7 ps, and the multiexponential decay components are a1=83.5%, t1=588 ps, a2=16.5%, t2=2413.5 ps.

4.6 Polarisation Resolved Fluorescence Measurements

In this section we present the characterisation of ET using polarisation resolved techniques. The investigation of the anisotropy can be considered an extension of the fluorescence mapping for molecular rotors: in fact, according to the theory, the value of the anisotropy is also dependent on the viscosity of the probe medium (see eq. 4.2). In addition to the information provided by the fluorescence, the anisotropy measurements may be useful to avoid false readings. For example, fluorescence-based viscosity measurements in cells with molecular rotors suffer from the potential drawback of the binding of the rotor to structures or macromolecules within the intracellular environment: this binding would hinder the rotation of the rotor, thus the measured fluorescence (intensity and/or lifetime) would not provide a reliable viscosity reading[112].

In addition, for these measurements evaluation, a modified version of Perrin equation (see equation 1.19) is used. This has been developed[98] from a combination of Förster-Hoffman (see eq. 1.25) and Debye-Stokes-Einstein (see eq. 1.20) equations, and it is designed to describe molecular rotors specifically.

4.6.1 Steady State Anisotropy in Solution

For measuring the steady-state anisotropy, the set of glycerol/methanol mixtures previously described was used. As described in the Section 2.1, in order to measure the steady state anisotropy of ET we used a spectrometer (Perkin-Elmer, LS-50B) and a set of polarizers to be introduced in the light path for excitation and emission. Each polarizer was placed in two different positions, horizontal (H) or vertical (V), for each measurement for a total of four measurements.

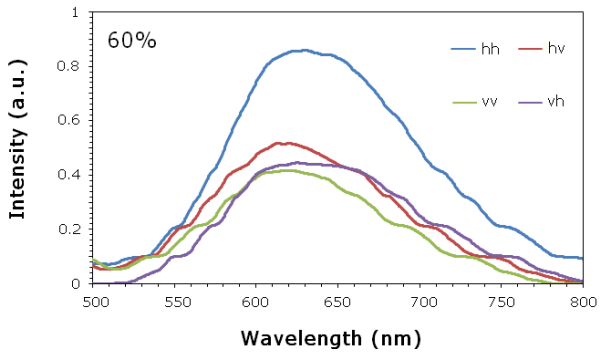

Figure 4.13: Example for 60% glycerol solution: polarised emission spectra used for G-factor and anisotropy calculation.

In Figure 4.13, an example for a 60% glycerol volume fraction sample shows the four measurements performed for each solution: the notation *VH* indicates that the polarizer between the source and the sample was oriented vertically, whereas the other one between the sample and the detector horizontally. In the same way, the notation describes the other combinations. In the figure, it can be noticed that the peaks for the *HH* and *VH* curves are slightly flatter and shifted to the right (∼5nm) in respect to the measured peak of 615 nm. In addition to that, all the curves present a sort of oscillating trend, more defined for the lower intensity

images. The reason for this effect is unclear and the fact that it appears in all the analysed samples suggest a bias in the measurements, possibly due to some effect of the polarizers: it can be noticed that the curves have similar shapes for the same polarised emission measurement (HH similar to VH, HV similar to VV). In addition, the geometry of the detector and its intrinsic characteristics may change the way the light is collected at different polarisations, thus it is necessary to introduce a correction factor G to take these effects into account. The G-factor was previously defined as the ratio between perpendicular and parallel emission intensity in respect to the polarizer orientation: in this configuration (L-shape) the measurements HV (perpendicular) and HH (parallel) were used for its calculation due to symmetry as previously described in Section 1.2.5. The polarised emission spectra were collected for each combination of polarisation and each viscosity. The G factor and the anisotropy r were calculated for each mixture using the intensity measurements at the wavelengths around the emission peak.To consider this range of wavelengths, the final value for the G-factor value was averaged between 600 and 630 nm for each solution, and the average value of 0.63 $\pm$0.04 was applied to all the following calculations. The emission intensities were integrated in the same wavelengths interval. The equation 1.8 can then be rewritten for these measurements as:

$$r = \frac{I_{VV} - G \cdot I_{VH}}{I_{VV} + 2G \cdot I_{VH}}, \tag{4.1}$$

where V and H indicate the orientation of the polarizer, I the integrated intensity, and G= 0.63 the correction factor. It has been reported[98] that by combining the Perrin equation with the Förster-Hoffmann and Stokes-Einstein-Debye equations, it is possible to write a convenient equation to describe molecular rotors behaviours, showing a direct relationship between α, the viscosity and the anisotropy:

$$\frac{1}{r} = \frac{1}{r_0} + A\eta^{\alpha-1} \tag{4.2}$$

Where A is a parameter depending on the temperature and on other intrinsic characteristics of the molecule, r_0 is the initial anisotropy, η the viscosity, and

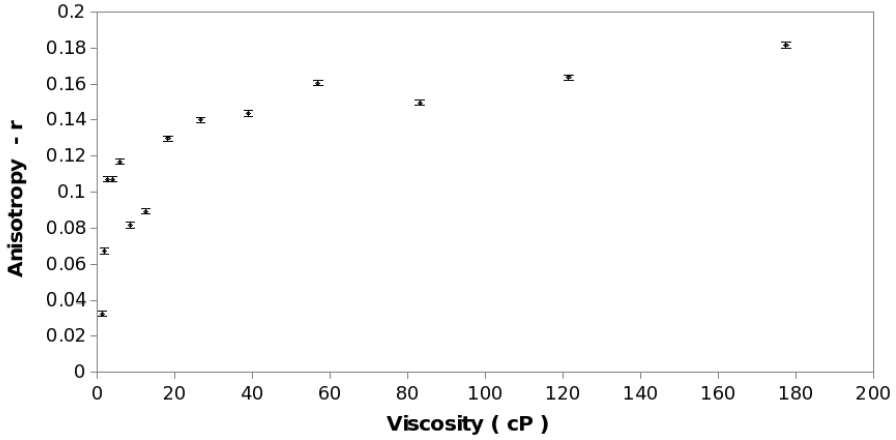

Figure 4.14: The graph describes the relationship between the anisotropy r, on the ordinate axis, and the viscosity η, on the abscissa axis, for the ET mixtures. The experiments were performed on a spectrometer (Perkin-Elmer, LS-50B) using two polarizers along the light path. For the error calculation, the propagation of the error on the G factor was used.

α the constant obtained from Förster-Hoffmann equation. The anisotropy val-

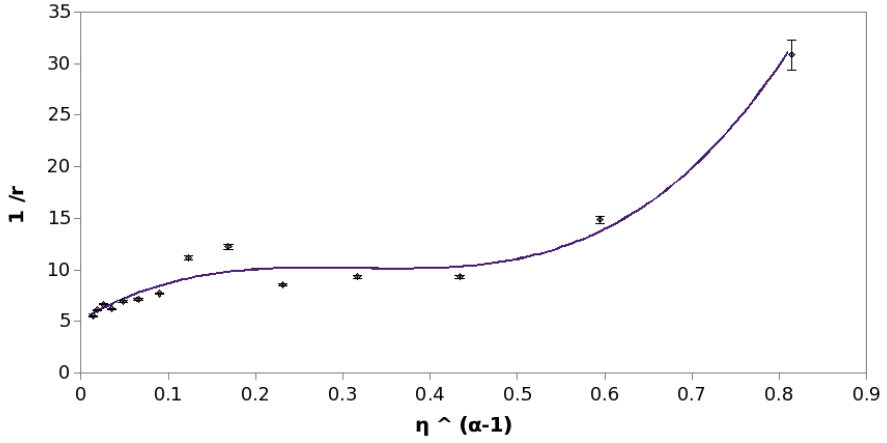

Figure 4.15: Perrin plot for molecular rotors: the relationship between the inverse of the anisotropy $\frac{1}{r}$ and $\eta^{\alpha-1}$ should be linear, and the intercept of the line of best fit equal to $\frac{1}{r_0}$. The value α=0.167 was used for plotting the graph. The regression curve in the graph was calculated using ImageJ with a third-order polynomial fitting (R^2=0.96). For the error bars calculation, the propagation of the error on the G factor was used.

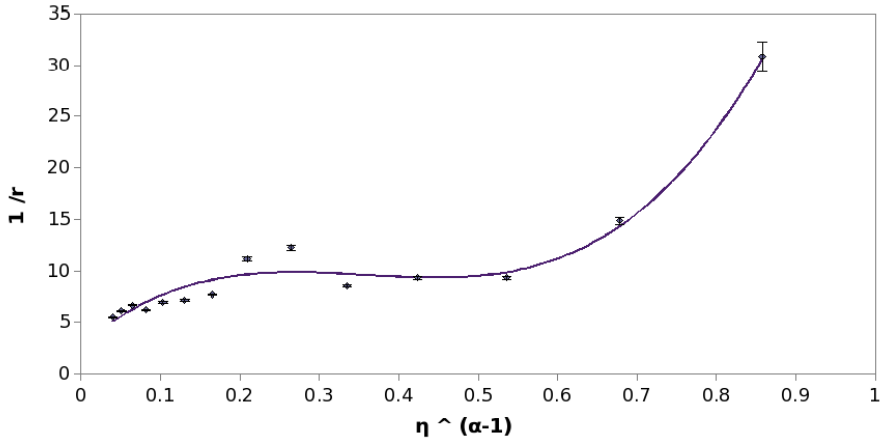

Figure 4.16: Perrin plot for molecular rotors: the relationship between the inverse of the anisotropy $\frac{1}{r}$ and $\eta^{\alpha-1}$ should be linear, and the intercept of the line of best fit equal to $\frac{1}{r_0}$. The value α=0.38 was used for plotting the graph. The regression curve in the graph was calculated using ImageJ with a third-order polynomial fitting (R^2=0.97). For the error bars calculation, the propagation of the error on the G factor was used.

ues obtained were then plotted versus viscosity in Figure 4.14 where the limiting value of r for high viscosity represents r_0. In order to better estimate the value for r_0, by exploiting the eq. 4.2, a plot of the inverse of anisotropy versus $\eta^{\alpha-1}$ was produced (see Fig. 4.15). From the intercept of a linear fit of the data, equal to $\frac{1}{r_0}$ it is then possible to calculate r_0. For the graph in Figure 4.15, the value $\alpha = 0.167$ from the lifetime measurements was used: the third-order polynomial regression curve in figure approximates the trend rather than a linear fitting. The value of the intercept for the polynomial function was 5.14 (R^2=0.96), and was 5.31 ($\pm$1.20, error on the fitting of the intercept. R^2=0.76) for a linear fitting, leading for both cases to an initial anisotropy $r_0 = 0.19 \pm 0.06$ (error obtained from the confidence interval on the intercept) for $\alpha = 0.167$.
The same graph, plotted using the value for α obtained from the intensity measurements ($\alpha = 0.38$), is presented in Figure 4.16: a good fitting is obtained using a third-order polynomial function rather than a linear fitting. The values for the intercept were 3.07 (polynomial, R^2=0.97) and 4.22 (linear, $\pm$1.49, R^2=0.77), leading to r_0 values of 0.237$\pm$0.06 (linear fitting) and 0.326 (polynomial).
However, since the tendency is not linear in opposition to what predicted, the

calculation of the value r_0 from the intercept have to be considered just a rough estimation. All the obtained values are low compared to other molecular rotors where the initial anisotropy is about 0.4, thus reducing the dynamic range of application of anisotropy measurements for the ET compound. Besides, in order to assess the uncertainty on the value of α, the line of best fit was also calculated for all its values between 0 and 0.5. The best linear fitting (R^2=0.79) was found for α=0, this contradicting the applied model and indicating an unclear behaviour in the ET compound.

4.7 Conclusions

The investigated ET complex was found to be suitable for fluorescence lifetime and intensity measurements, exhibiting average lifetimes in the hundreds of picoseconds range. The sensitivity of the complex to the environmental viscosity was confirmed via fluorescence measurements in solution, although the results for the calculated α coefficient were different for the lifetime (α=0.167) and the intensity (α=0.38) experiments. The polarisation resolved measurements show a low fluorescence intensity and a small initial anisotropy (its value is fixed, but measured values ranged from 0.19 to 0.32, depending on the value of α), reducing ET compound applications due to the small dynamic range, compared with the rotors previously used in this field[112]. The possibility to stain living cells with this compound is promising, and the calculation of intracellular viscosity lead to values (50-250 cP) in agreement with the literature[112; 190]. However, the exact location of the dye within the cells needs to be investigated (e.g. with counterstaining technique).
The contradicting results for α and the non-linear approximation for r_0 may depend on several factors: in particular, although the sample preparation routine was identical for each solution, different absorbance values were measured, leading to uncertainty in the concentration-dependent measurement (e.g. intensity). The reason for this behaviour is unclear: it may be related for example to a change in the molecular extinction coefficient ϵ (see eq. 1.3) for the different solutions, or depend on other factors, thus requiring further investigation. On the other hand, lifetime measurements are independent of concentration and thus may be

considered more reliable in this case.
In conclusion, the measurements of the compound do not follow completely the Förster-Hoffmann theory (see eq. 1.25): the value for α changes depending on the method used (lifetime or intensity measurements), and the polarisation resolved measurements lead to uncertainty in the calculation of the initial anisotropy. Among the reasons for this behaviour, there may be impurities in the analysed solutions or some isomerisation effect, as reported for other rotors[251]. Hence, It is not straightforward to confirm the molecular rotor nature of the ET compound and further analysis is required. Nevertheless, the viscosity sensing was proved and its uptake to living cells confirmed: these facts suggest that the use of ET as a viscosity sensor is possible, although the emission intensity was found to be low, compared to other rotors[112; 125; 190], and it therefore requires higher illumination levels.

4.8 Chapter Summary

The aim of this chapter was to evaluate the features of a newly developed compound, ET, as a molecular rotor, and its possible application to measure viscosity in living samples. The investigation of the compound did not entirely confirm its nature as a molecular rotor, but the possibility to sense viscosity via fluorescence intensity and lifetime was proved. However, further analyses are required to identify the exact nature of this dependence on the viscosity.
The uptake of the dye in living cells was confirmed, but due to its moderate-low fluorescent emission, high sensitivity instrumentation, long acquisition time and/or high excitation light levels are required. In addition, other drawbacks such as the difficulties in analysing the multi-exponential decay and the low polarised emission were noticed. In conclusion, the investigated compound can be used as a viscosity sensor, but the mentioned limitations reduce its possible fields of application.

Chapter 5

EBCCD and Centroiding

The main aim of this chapter was to use an EBCCD camera in a way similar to a time to amplitude converter (TAC) for SPC timing applications. With this approach, the theoretical possibility to achieve sub exposure time resolution with this class of devices was investigated. The use of centroiding algorithms may lead to a recovery of the spatial resolution loss due to the electron-acceleration process of this detector.
This chapter describes the EBCCD camera characterisation, and two main experiments. In order to characterise the device, a large dataset of images was collected with the aim to obtain a reliable statistics of the photon events. In the first experiment photon events were imaged at different gain voltages in order to investigate the use of an EBCCD device as TAC device. In the last experiment, collected EBCCD data are processed with commercially available software (QuickPALM, RapidSTORM) used for particle localisation and tracking; likewise, PALM data are given to a processing software developed during this project and the results compared.

5.1 EBCCD Data Collection

Several datasets were collected in order to characterise the photon events of the EBCCD detector and to investigate its Pulse Height Distribution at different acquisition settings.

5.1.1 Experimental Setup

For our experiments, we coupled the EBCCD detector to a Nikon inverted microscope via a C-mount. The test sample was the U.S. Air Force (USAF) test pattern (see Sec. 2.5.4) imaged on the microscope with a Nikon 10× objective and with a green bandpass filter (Comar). The light source used was the default white halogen lamp installed in the Nikon microscope, set to the minimum, working then under low light level illumination. In case of real fluorescent samples, excitation and emission are normally well separated and filters are used at the detector side to prevent unwanted wavelengths; by using a broad white light on a test sample instead, the bandpass filter is placed especially to cut out the UV part of the spectrum, as this is known to generate ghost images on EBCCD devices[252].
As previously mentioned (see Sec. 2.4.3) the settings of the camera allow to change the sensitivity (voltage) and the readout gain across the photocathode and the sensor.
For generating the dataset for the characterisation, the camera was set to Photon Counting Mode with the maximum sensitivity (value 16, equivalent to $\sim$ 8kV) and gain (named "Super-High Gain" in the manual) and used to collect thousands of frames (about $10,000$ per collection, in 9 collections); these settings were constant for all the datasets collected. One of the greatest drawbacks of this particular camera is its speed (max 3Hz in SPC mode) so in order to collect enough photon events it should run for several hours. Increasing the light intensity in order to get more events is not feasible as it would drastically increase the occurrence of double events: these arise due to photons arriving at overlapping positions in the same time window, making it difficult to resolve them as two (or more) separate events. In order to avoid this phenomenon, in addition to setting the light to the minimum, a neutral density filter was inserted along the light path to further reduce its intensity on the detector and thus the number of photon events imaged. Safety issues at the time of the experiments and the low frame rate of the camera prevented us to collect a whole and continuous data set (e.g. by leaving the camera running several days), and we had to split the collection among 9 days; we took great care that the test pattern and all the

instruments were stable in their positions and that the environment parameters were as constant as possible.

For every collection the camera was cooled down for at least 5 hours until the temperature of $-20°C$ was reached and maintained; the halogen light was then switched on and 10,000 frames collected in the following hour. At the end of each experiment day, the lights were switched off and the camera let warming up until room temperature; finally the EBCCD could be switched off and the procedure repeated the next day for the new collection. For the whole experiment the same lighting conditions were maintained and the camera set in Single Photon Counting ("Super-High Gain") mode at the maximum rate allowed (3Hz). The exposure time for each acquisition was 20 μs. The way the experiment was conducted is inconvenient: indeed, a continuous acquisition would have introduced less variations in the settings, and reduced the drawbacks of a multi-day experiment (e.g. temperature variations, light condition stability, vibration of the stage, etc.). The limitations of our laboratory at the time of the experiment prevented to use this approach, and for this reason only one continuous sub-dataset (10,000 images) was used for the imaging reconstruction (see Sec. 5.4.4). In fact, the division of the experiment in several parts, even when all the efforts were put to prevent changes in the settings, it is expected to produce a drift between the images collected in different days and then in the reconstructed image (obtained by processing all the datasets together). In order to evaluate this effect, the images of each days were summed and the results compared. Besides, since the main objective of the experiment is the evaluation of the centroiding algorithms, the drift may affect the reconstructed images but not the statistics of the collected events.

The other experiment was aiming to demonstrate the theoretical possibility to use the variation of the Pulse Height Distribution (PHD) at different applied voltages for obtaining sub-exposure time temporal resolution. For this task, we used the same settings of the previous experiment (Super High Gain mode, 20μs exposure time, low-light level) but varying the acceleration voltage, performing the measurements for all the possible voltage settings allowed by the camera: 16 step values, corresponding to a high voltage applied between 4kV and 8kV. Eight datasets, corresponding to the highest eight out of sixteen acceleration values

(6.1kV-8.0kV), are presented in this work as the lower acceleration settings did not allow to resolve single photons in these particular light conditions.
The PHD for each dataset was plotted and compared with the others in order to define the relationship between acceleration voltage and number of electron generated.

5.1.2 In-House Software

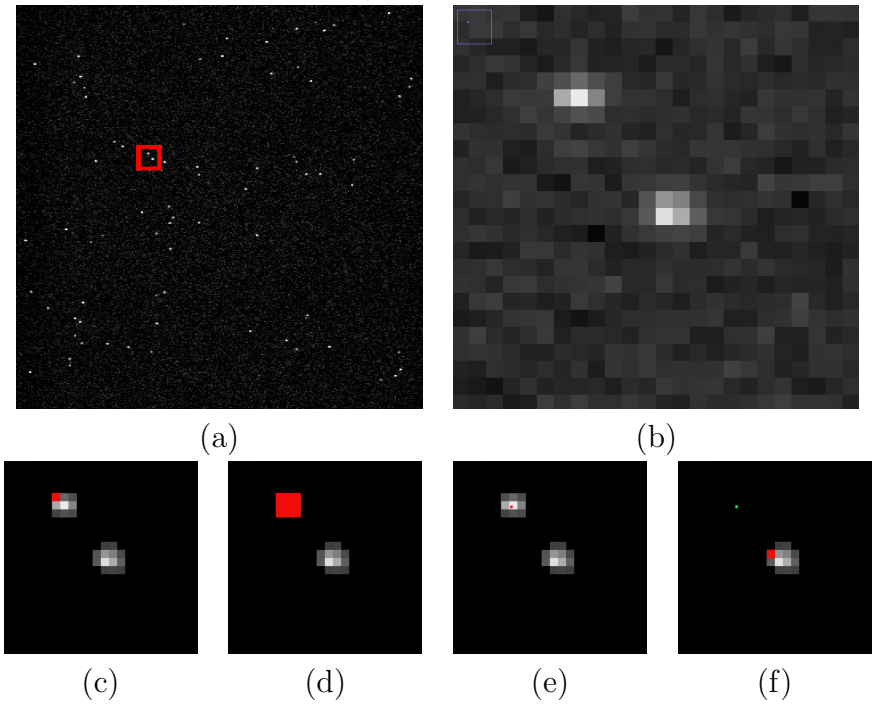

Figure 5.1: Processing example for the code developed in this project: the code reads each frame *(a)* in order to evaluate the average background and find the photon events, zoomed in *(b)* and following images; it subtracts the background value from the image, and when a pixel above the threshold is found, it scans the area around searching for the other pixels associated to the event *(c,d)*; the red pixels in figure represents the scanning steps of each event. When an event has been identified, the code calculate the sub-pixel position of is centre and "trims" its edges *(e,f)*, then continues to scan the image until it finds the next event, and start the identification again *(f)*.

The software used for the images reconstruction was originally developed[253]

in C by Dr. Nicolas Sergent, former member of our group, during his PhD at King's College. In this work, this code has been modified and expanded in order to simultaneously use different centroiding algorithms, evaluate the background noise, and generate a reconstructed image for each one. In addition, the software was changed to evaluate also the distribution of the sub-pixel centre for different centroiding algorithms. The shift from the centre of the pixel is then called x-bar (or y-bar) and it has a value between -0.5 and $+0.5$.
The Electron Bombarded CCD is designed as a back illuminated device, so the accelerated electrons hitting the silicon layer diffuse from the back to the front of the sensor causing the charge to spill to adjacent pixels. The code, aimed to recover the loss in resolution, can then be used to centroid, and also for thresholding the background noise and to discriminate the ion events. Residual gas molecules are present in the non perfect vacuum of the sensor; they can be ionised and accelerated through the electric field and interfere with the measurements. These events are much bigger in size (since they carry higher energy) than standard photelectron events, thus they can be easily excluded either by a simple size-threshold or through the analysis of their PHD. The programme calculates the average background level of each image and subtracts it, then applies a threshold to each frame and scans it pixel by pixel to find the photon events. When a pixel value above the threshold is found, it recursively scans the area around it in order do identify all the pixels associated with this event and, if the size is within a given range, accepted. Then the programme moves forward and keep on scanning the rest of the frame. Each valid event found is recorded, centroided (in x and y directions) and the count for the same position of the reconstructed image is increased by one. Its integrated intensity instead is used to produce the PHD. When sub-pixel resolution of the event position is not required, the applied centroiding algorithms consist only in the finding of the highest peak for each event and in the "trimming" of its edges. However, the subpixel centre of each event is calculated and x-bars for each centroiding algorithm produced. A schematic of the working principle of the programme is shown in Figure(s) 5.1.

5.2 EBCCD Characterisation

Each collected frame consists in a noisy background with several sparse bright spots representing the photon events. In order to reconstruct the original image it would be possible to sum a large series of frames but in this way also the background noise would be taken into account. The use of a threshold/background

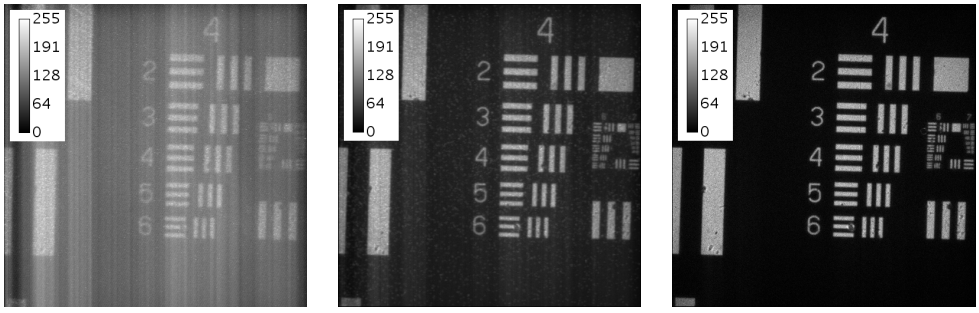

(a) (b) (c)

Figure 5.2: Image reconstruction: (*a*) sum of all the frames unprocessed; (*b*) a threshold is applied and subtracted from each frame before adding them; (*c*) only the pixel with the higher value is selected for each event and the non relevant pixels set to 0 before the addition of the frames. The reconstructed images (*a, b, c*) are obtained from a set of $5,000$ frames, collected under the settings described in Sec. 5.1.1.

to be subtracted from each frame before adding them up, would be a first improvement in the reconstruction process. As previously mentioned, the hit of a photoelectron onto the rear of the detector, frees several electron through the silicon that diffuse to the adjacent pixels and decrease the detector resolution: identifying and considering the peak pixel only for each event is expected to reduce this effect.

An example of the different techniques is shown in Fig. 5.2: the sum of all frames produces a very bright image, with a relevant background noise (*a*); by applying a thresholding, the noise effect is reduced (*b*); the reconstructed image obtained by thresholding and finding the peak pixel, shows better results (*c*). The whole datasets used consist in a total of $95,000$ frames. For each dataset the background value was measured and an example can be seen in Figure 5.3; the same datasets were used for showing the events count rates in Figure 5.4. The grey

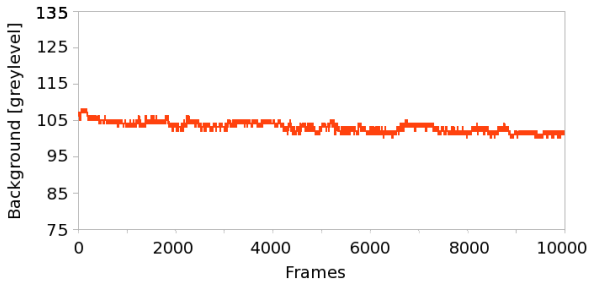

(a)

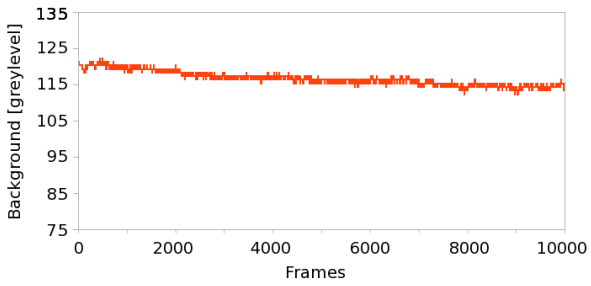

(b)

Figure 5.3: Variation in time of background noise calculated in each frame, for two different sets (a) and (b) of 10,000 frames each.

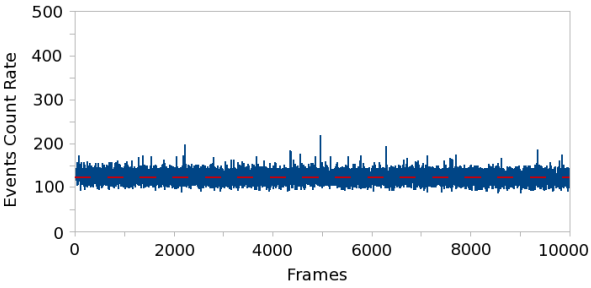

(a)

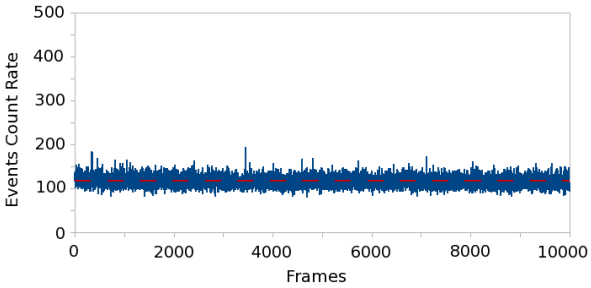

(b)

Figure 5.4: Variation in time of number of events counted in each frame, for two different sets (a) and (b) of 10,000 frames each.

level of the background changes between different collection and also during each single acquisition cycle, this indicating that the temperature may not be constant as expected. Furthermore, this means that the value subtracted from the each pixel differs from frame to frame, affecting the distribution of pulse heights. However, the event count-rate is independent on the background noise as can be seen from a comparison of Figures 5.3 and 5.4: at a variation in the background measured values, does not correspond a variation in the counted events. The distribution of the count rate can be evaluated and is shown in Figure 5.5: the bell shaped histogram can be fitted to a Gaussian function with a good approximation ($R^2 = 0.9985$), having as a result a mean value $\mu = 102.5$ and FWHM $= 25.4$.

The pulse height distribution for $95,000$ frames is shown in Figure 5.6. The intensity of each event collected along the processing is calculated as the sum of the pixel values comprised in that particular spot; the number of occurrences of each given intensity is then represented in the y axis of the graph. The mean value of the distribution is 334.1 greylevels and the full width at half maximum 102.3 greylevels.

These results are not completely in agreement with the expected Poisson statistics, as this distribution requires the mean value μ to be equal to the variance according to the equation[254]:

$$\mu \;=\; \sigma^2 \tag{5.1}$$

where σ is the standard deviation and σ^2 the variance. Since Poisson distribution can be approximated with a Gaussian for high values of μ[254], the condition on eq. 5.1 can be verified after considering the FWHM and the standard deviation relationship for a normal distribution:

$$\text{FWHM} = \;\; 2\sqrt{2\ln 2}\sigma \;\; \approx 2.355\sigma. \tag{5.2}$$

For the event count-rate distribution, the values are in good agreement with Poisson distribution as $\sigma = 10.8$ and $\sigma^2 = 116.3 \approx \mu$. On the other hand, the pulse height distribution shows a broader shape than expected, being $\sigma = 43.5$

and thus $\sigma^2 = 1894.4 \neq \mu$.
The total effect on the FWHM, in electrons, can be considered as the contribution from the variance of the Poisson distribution, from the readout noise ($15e^-$), and from the dark noise ($8e^-$) at the given temperature (-20°C), according to the equation:

$$\begin{aligned} \Delta^2 &\cong \sigma^2_{PHD} + \Delta^2_{Dark} + \Delta^2_{Readout} \\ \Delta &\cong 40e^- \end{aligned} \tag{5.3}$$

where Δ is the total noise affecting the measurements, σ^2_{PHD} the variance depending only on the PHD ($=\mu$), and Δ_{Dark} and $\Delta_{Readout}$ the dark and readout noise respectively. The results indicate that the real noise ($\sigma \cong 174e^-$) is much larger than the predicted one. The main cause is probably the temperature, as the value of the dark noise changes greatly with small temperature variations ($8e^-$ at -20°C to $50e^-$ at -15°C). This suggests that the real temperature on the chip is higher than the measured one. In addition to that, the back-scattering effect can contribute to broaden the distribution: electrons reaching the detector can be back scattered towards the photocathode but, due to the applied potential, they are forced again onto the CCD with a lower energy.
On the other hand, the good results for the events count rate distribution indicate that the thresholding process is sufficient to reduce the effect of the noise.

5.2.1 X-bars characterisation

The centroiding algorithms were described in detail in the previous Section 2.5.1, and their application to the EBCCD will be further discussed in Section 5.4. A short analysis of their application to the whole dataset (∼95,000 frames) is presented here to further investigate the EBCCD characteristics. In this section, the distribution of the subpixel peak for each event has been evaluated. Centroiding with different algorithms was performed and the results are shown in Figure 5.7: the processing considered the peak value (brightest pixel) of the event and centroided it in horizontal and vertical directions, producing the $x-$ and $y-$bar representing the "shift" (between -0.5 and $+0.5$) of the so calculated new-centre

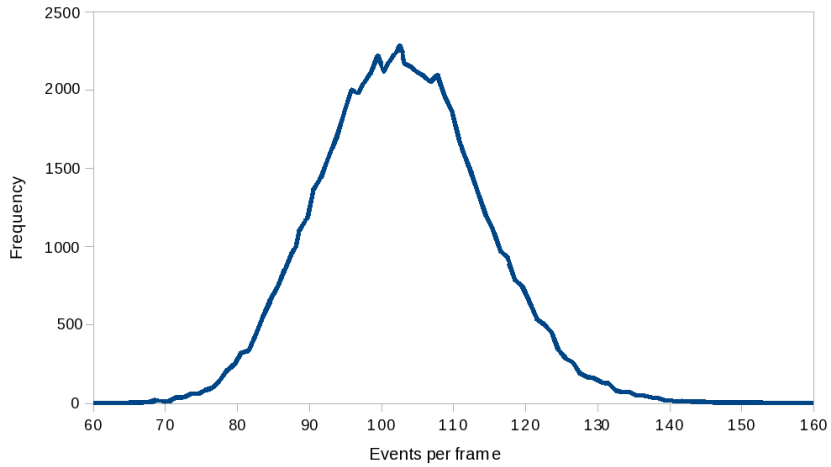

Figure 5.5: Distribution of the count rate for 60, 000 frames. The number of events counted per each frame is shown on the x axis, whereas on the y axis is indicated their frequencies. The histogram can be fitted to a normal distribution with a $R^2 = 0.9985$; the mean value μ is 102.5 and the FWHM 25.4, corresponding to a $\sigma = 10.8$, in good agreement with the Poisson distribution of the events where $\sqrt{\mu} = \sigma$.

from the original centre of the pixel (assumed to be 0). It is evident a shift in the x direction for all the applied algorithms: this is probably due to a readout effect of the EBCCD; in fact, also in Figure 5.2-(a) it is possible to see vertical bright lines affecting the image quality.

5.3 EBCCD as a Parallel Time to Amplitude Converter

As previously mentioned (see Sec. 2.3.1) the TAC is a device that allows to obtain time information from an amplitude measurement. By increasing the amplitude gain of the detector with time, when the input signal is processed, the converted output value will be proportional to the input arrival time. In particular, if the value of all input signals is the same , it is possible to determine the arrival time of each signal within a given time window.
In fluorescence measurements there are different ways to achieve temporal reso-

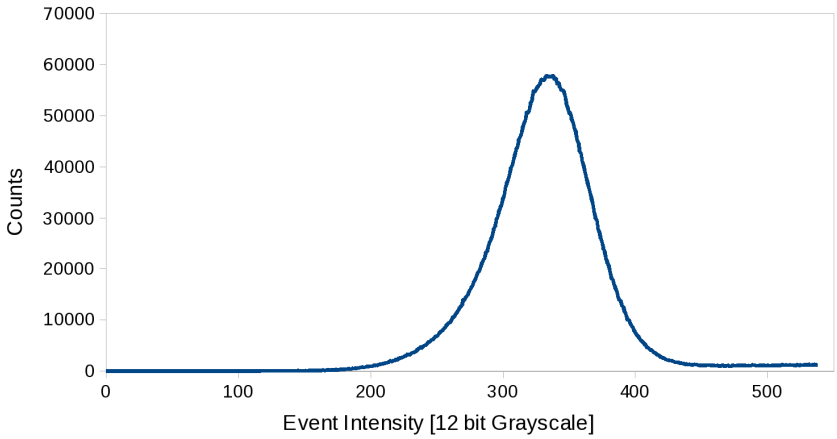

Figure 5.6: Pulse height distribution for 95,000 frames, collected at 8.0kV acceleration voltage and Super High Gain (value 2 in the Hi-Pic software) settings. With this configuration, each measured greyscale level corresponds to 4 generated electrons. The x axis represents the integrated intensity (expressed as 12-bit greyscale values) of the detected events; the y axis shows the occurrences of a given intensity value. Mean value is 334.1 and FWHM 102.3 greylevels.

lution, such as time-gating or precise and direct measurement of photon arrival time; the former has the disadvantage of losing all of the light emitted "outside" the gating window, and the latter needs either the scanning of the sample or multiple detectors for timing each pixel in wide-field imaging. Among the widefield techniques, the coupling of an intensifier with a wedge and strip anode, delay line anode or quadrant anode has been proposed[13]. Although this method achieves picosecond resolution, its timing capability is limited to one single photon per excitation cycle. In addition to these techniques, the possibility to perform wide-field TCSPC with single photon avalanche diode (SPAD) arrays and picosecond resolution has been reported[255].

In the case of EBCCDs, where the photons are accelerated from the photocathode to the detecting stage by a potential difference, in theory it is possible to vary this difference with time, thus creating a relationship between the acceleration voltage and the photons arrival times. Conceptually, the amplitude of a signal is modulated with time to carry extra information, and with this technique the

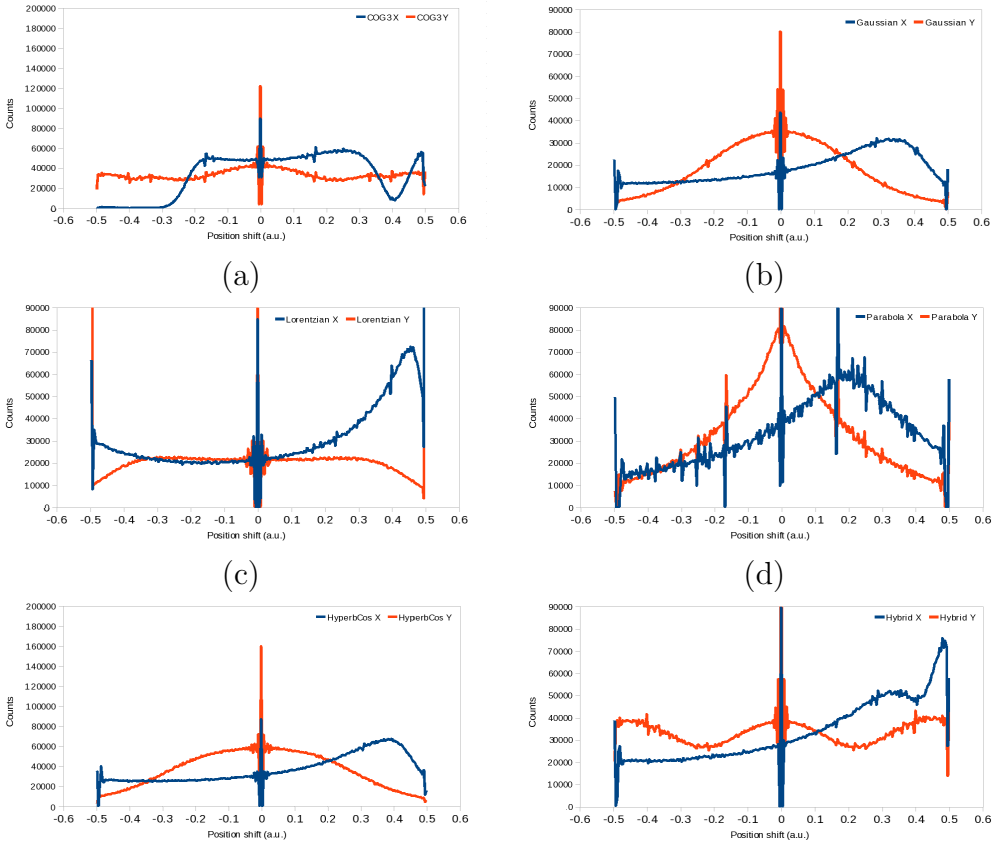

Figure 5.7: X-bars for different centroiding algorithms and associated reconstructed images. (a) Centre of gravity (COG); (b) Gaussian; (c) Lorentzian; (d) Parabola; (e) Hyperbolic cosine; (f) Hybrid algorithm: COG/Gaussian.

arrival time of the photons on the photocathode is proportional to the energy of the photoelectrons it generates. The schematic working principle of the proposed device is shown in Figure 5.8: the events 1, 2 and 3 shown in (a) have different heights, so they are timed according to the acceleration voltage increase within the camera exposure time T. The main advantage of this technique is the possi-

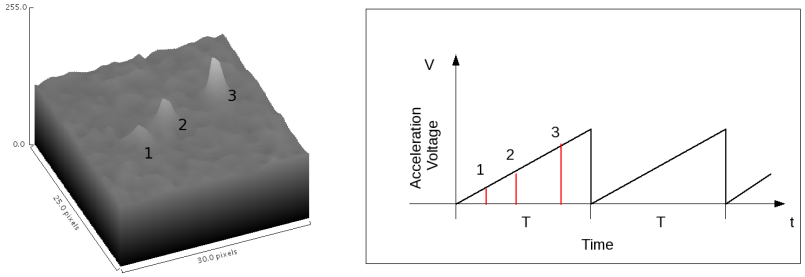

(a) (b)

Figure 5.8: Working principle of TAC-EBCCD. During the exposure time T, the acceleration voltage of the EBCCD is increased (b). Events 1, 2 and 3 (a) are thus identified by their height, and timed according to the variation of the total gain.

bility to parallel process all the pixels in the field of view simultaneously, if care is taken to avoid double events. The correct timing of each event requires a proper calibration of Pulse Height Distribution during the voltage sweep. Furthermore, a well defined PHD allows to easily identify the time-tag for each photon, and a large variation in the voltage during the sweep increases the dynamic range of the TAC. In addition, for fluorescence decay measurements, the gain variation has to occur in a temporal window about five times bigger than the lifetime to be measured[11]. Similar devices such as image intensifiers previously described (see Sec. 2.4.2) cannot take advantage of this technique because of their generally broad PHD, depending on the non linear multiplication stages of the MCPs.
The total gain of the system is influenced by a thin aluminium layer deposited on the CCD to protect the active area of the device. In fact, this layer reduces the photoelectron energy: it has been determined by the manufacturer that it introduces a threshold voltage. Thus, being V the acceleration voltage between the CCD and the photocathode, V_{thresh} the threshold voltage and $W$the required

energy for one electron-hole pair generation in silicon, we can define the gain as:

$$EBCCD_{Gain} = \frac{V - V_{thresh}}{W} \tag{5.4}$$

The maximum voltage this particular device can be set to is 8kV due the imperfect vacuum in the tube between the photocathode and the actual detector. In fact, according to the manufacturer, applying a higher acceleration voltage would cause a dielectric breakdown and damage the device.

5.3.1 Results and Discussion

Figure 5.9 shows the distributions for several applied acceleration voltages and in the following Figure 5.10 the linear relationship between the pixel values and the applied high voltage. The intensities of the events for each acquisition (voltages $6.1 - 8.0$kV) have been plotted and it is possible to see how the distributions positions shift accordingly the increase of the difference of potential. In order to evaluate the linear dependence on the acceleration gain, according to equation 5.4, the mean intensity of the PHD at each voltage was considered; these values were then converted into electrons (each grey level corresponds to 4 generated electrons). The total numbers of generated electrons were finally plotted versus the applied voltages, demonstrating the linearity of the relationship as shown in Figure 5.10. Exploiting the equation 5.4, from the gradient of the trendline should be possible to retrieve the electron-hole pair generation voltage (W), whereas from the intercept with the y axis the value of the thresholding voltage (see Sec. 5.3). The linear fit obtained by experimental data shows a gradient of $238.8e^{-}/kV$ and an intercept of -618.9 ($R^2 = 0.97$), thus, in agreement with equation 5.4, the values for the electron-hole pair generation energy and for the threshold voltage are $W = 4.19 \pm 0.09$eV and $V_{thresh} = 2.59 \pm 0.11$kV. The generation of the electron-hole pairs in silicon is dependent on the temperature, the purity of the silicon, the depth within the medium at which the pairs are generated, and the type of ionising particle impacting the silicon. The electron-hole pair generation process using x-rays has been studied previously on silicon[212; 213; 215; 217] and

specifically on CCD sensors[214], leading to a range of values for W of $3.60-3.81$ eV and x-rays' energies from 50 eV to 60 keV. Although the obtained results are relevant for electron-hole pairs generated by photoelectrons, rather than x-rays, the value for W is close to this range. While this value is of interest for the study of the generation process, the aim of this project is rather to demonstrate the linear relationship between the brightness of the photon-events and the acceleration voltage, as confirmed by the results. The bell-shaped distributions allow

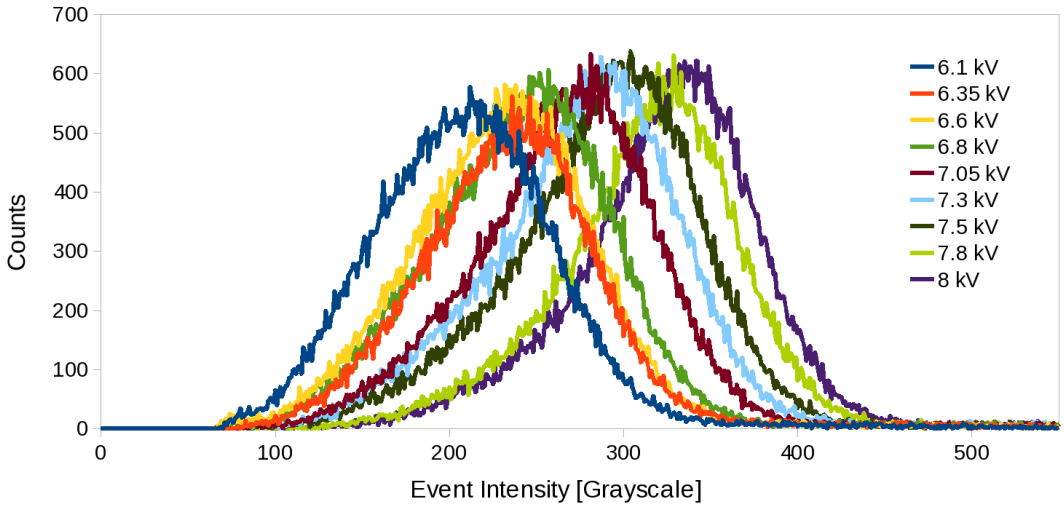

Figure 5.9: Pulse Height Distribution obtained from each dataset. The graphs represent the distribution of 9 different acceleration voltage values, with a gain setting of "2" (equivalent to 4 electrons per greyscale value). These voltages range from 6.1kV to 8.0kV: the average number of events per frame in the datasets varies slightly between 61.2 for 6.35 kV and 76.6 for 7.5 kV. The x axis represents the integrated intensity (expressed as greyscale values) of the detected events; the y axis shows the occurrences of a given intensity value for each dataset.

to identify each acceleration voltage, but for close values of the settings they overlap, making difficult to resolve between adjacent curves. It is also possible to notice that for high gain-voltages the curves are asymmetric, with a "tail" at lower intensities. The proposed explanation for this effect is the backscattering of the electrons: as previously mentioned (see Sec. 5.2), the accelerated photoelectrons can be first scattered and then re-accelerated towards the detector, yielding

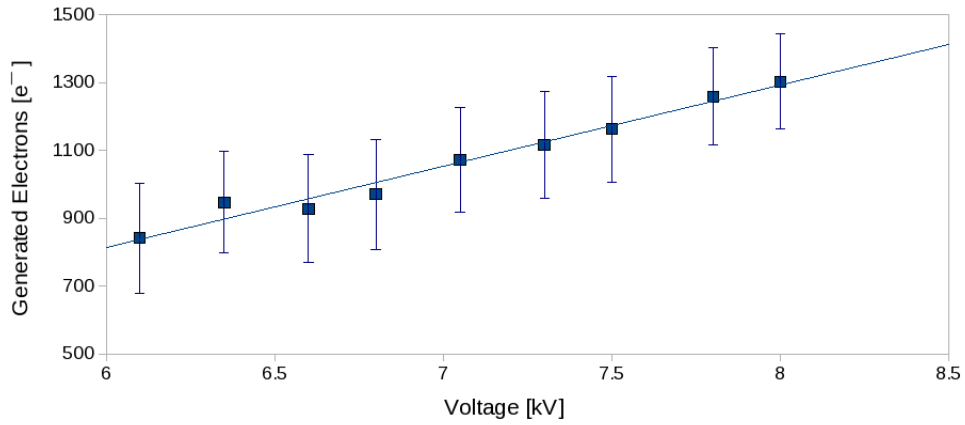

Figure 5.10: Relationship between pixel counts and potential difference applied. The x axis represents the applied voltage; the y axis shows the mean value of the PHD, expressed as the number of generated electrons. The trendline presents a gradient of $238.8e^{-}/kV$ and an intercept of -618.9 ($R^2 = 0.97$).

to detected events with lower energy/brightness. This particular effect may be present also for lower applied voltages, but the low-energy events are thresholded with the background, thus showing symmetric curves in Figure 5.9. In Figure 5.10 it is possible to better evaluate the standard deviation of the distributions and discuss the accuracy of the method. Also in this case, the standard deviation for each point is larger than the square root of the average, as discussed in Section 5.2.For this reason, it is very difficult to accurately tag-time each collected event due to the error bars overlapping for many values, and allowing a reliable timing only for the extreme voltages (very low and very high). Besides, since this camera does not allow to sweep the gain within the exposure time, it was not possible to experimentally test its timing capability on a real dataset. To overcome this limitations and test the method, a simulation was used in [1]. Frames of real experimental data, acquired at different voltages, were combined in different proportion to mimic exponential decays; the simulated arrival time was derived from the pulse height of each photon, by converting the voltage axis to time, according to the linear relationship in Figure 5.10 and equation 5.4. A sweep time of 50 ns, between the high (8.0 kV, 0 ns) and the low voltage (6.1 kV, 50 ns), and three simulated decays of 5, 8, and 20 ns were used: the results can

be seen in Figure 5.11, where the decay times fitted to a single exponential were 20.27 ns (χ^2=1.03), 8.78 ns (χ^2=1.08), and 4.72 ns (χ^2=1.31) respectively, and the 8 kV pulse height distribution was used as the instrument response function (IRF). These results indicate that the method can be used to time the arrival of photons, but also that a higher maximum voltage for the sweep is needed to achieve more precise timing. This last condition in particular requires the vacuum between the high voltage plates to be nearly perfect, as impurities may be accelerated and damage the device[256].

The average number of events per frame was not exactly the same for each accel-

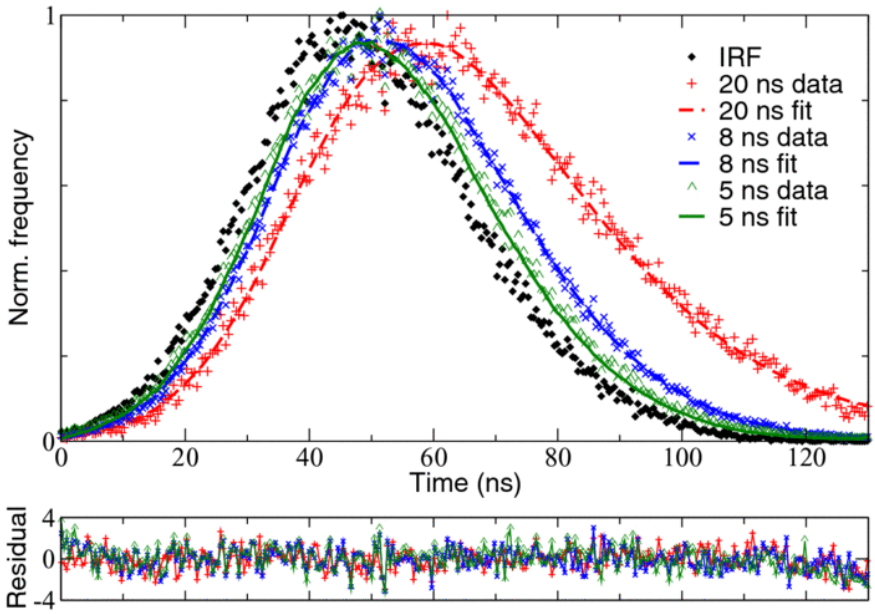

Figure 5.11: Simulated fluorescence decays generated from frames acquired at different acceleration voltages. The instrument response function (IRF) was obtained from measurement with the highest voltage (simulated time 0). The arrival time of each event was found from its pulse height. Single-exponential fits to the decays yield decay times of 20.27 ns, 8.78 ns, and 4.72 ns for the 20 ns, 8 ns, and 5 ns simulated decays, respectively. Reproduced with permission from [1].

eration voltage: even if the lighting conditions where the same for each collected set, the measured background value for the images varied for every dataset and within each acquisition cycle as well. This made more difficult for the events at lower intensities to be resolved, and vice versa some noise may be recognised as a

Voltage (kV)	8	7.8	7.5	7.3	7.05	6.8	6.6	6.35	6.1
Events	70.3	67.4	76.6	75.6	71.0	73.0	69.4	61.2	69.0

Table 5.1: Average number of events per frame, calculated on a 10,000 frames dataset for each different acceleration voltage.

valid event. For the different applied potentials, the average events per frame are shown in Figure 5.12 and in Table 5.3.1. In addition to the integrated intensity,

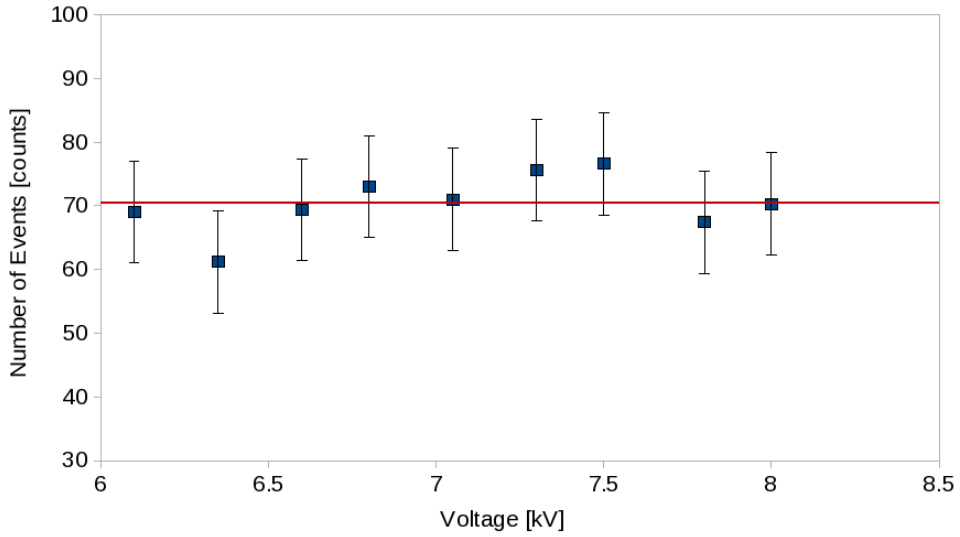

Figure 5.12: Average number of events per frame (y axis) at different acceleration voltages (x axis). The red line indicates the average value of 70.4 events (standard deviation $\sigma = 4.6$). The number of events per frame shows a weak correlation to the applied voltage, as suggested by the calculated correlation Spearman's rank $\rho = 0.37$.

the peak-pixel height distribution of each event was recorded for the datasets and the results can be seen in Figure 5.13: the gradient is 14.8 $greylevels/kV$ and the intercept -38.7. Although these values are not directly related to the electron-hole pair generation (see eq. 5.4), they show how also the peak intensity alone is directly proportional to the acceleration voltage. The small value for the gradient compared to the previous graph in Figure 5.10, in particular, suggests that for

lower voltages the largest part of the event intensity is in the peak pixel, whereas the intensity is more spread among several pixels for higher voltage settings, although further analysis of the event sizes and shape is required. This particular feature may be exploited to reduce the processing time: by considering the peak pixel only a TAC system with no need to evaluate all the pixels in each event can be designed. The small value for the gradient though, reduces the dynamic range and thus very precise an adequate calibration for the height distributions would be necessary.

For values of the voltage below 6 kV, it was not possible to clearly identify the photon events: in practice, with these settings the mean value of the event distribution was very close to the value of the background noise. The code developed thresholds every image subtracting the averaged background value: if the ratio between the event signal (proportional to the count rate) and the noise (including background, also proportional to the count rate, and the read-out noise) is too low, it is impossible to differentiate a real photon event above the threshold from a false event generated by random variation of the background. The EBCCD tested in this project has a maximum voltage of 8 kV and events can be identified for voltages not smaller than 6 kV, so the dynamic range is limited to about 2 kV in the 6-8 kV window. EBCMOS cameras with 6-10 kV range have been reported[257], and recent EBCCD developments report maximum voltages above 14 kV[207; 209; 258], allowing a larger dynamic range for this class of detectors.

Another advantage of this technique is the possible applications to both short and long lifetime measurements, by simply adjusting the voltage-sweep duration: the time window can be indefinitely extended in order to measure long lifetimes (e.g. μseconds and above). Similarly, the window can be shortened to measure short lifetimes, but technical issues limit this approach. The time each photoelectron takes to move from the photocathode to the CCD (time-of-flight) can be considered equivalent to the instrumentation response in a standard TCSPC system: this time (is in the order of tens of ps for the investigated camera) needs to be taken into account when reducing the sweep duration to avoid unwanted convolution effects with the measured decay. Also, the possibility to vary the voltage by several kV in a short time is strongly dependent on the technical advancements of the instrumentation.

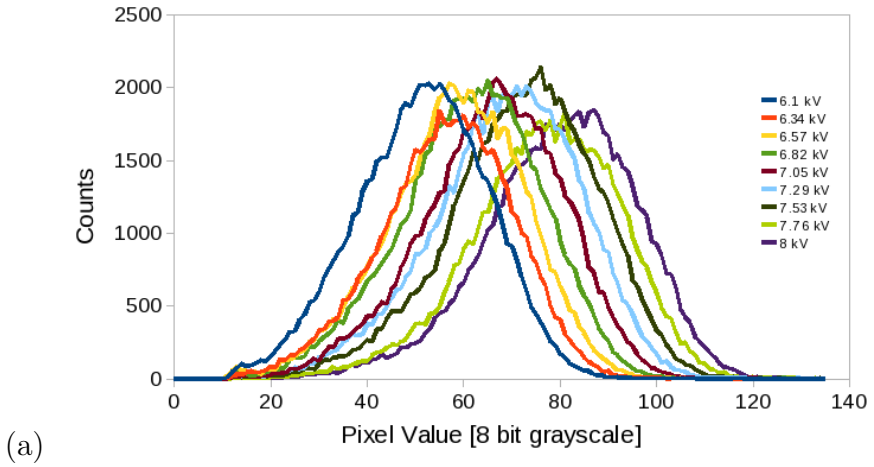

(a)

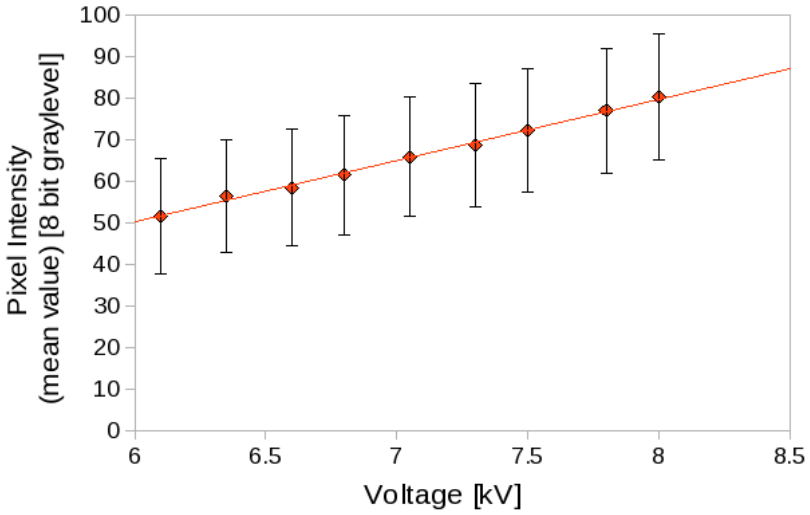

(b)

Figure 5.13: Peak Height Distribution obtained from each dataset. (a) The graphs represent the distribution of 9 different acceleration voltage values, with a gain setting of "2". The voltages ranges from 6.1kV to 8.0kV. The x axis represents the intensity (expressed as greyscale values) of the peak pixel for the detected events; the y axis shows the occurrences of that given intensity value for each dataset. (b) The mean value for each distribution was plotted versus the acceleration voltage: the x axis represents the applied voltage; the y axis shows the mean value of the peak-height distribution. The gradient and intercept for the line of best fit are 14.8 $greylevels/kV$ and -38.7.

5.4 Centroiding Algorithms Comparison

Centroiding is a widely used technique in photon counting imaging systems and in single-molecule fluorescence microscopy[13]. In this section we present a comparison between the centroiding algorithms of two freely available fluorescence microscopy super resolution software packages, QuickPALM and RapidSTORM, with those used by our in-house software. The aim of this work was to evaluate if this software could be used for centroiding in photon counting imaging. The analysis will focus on the effect of the centroiding with subpixel resolution on final reconstructed images and the related noise each method generates, and briefly compare speed and other software performances.
PALM and STORM techniques consists of imaging sequences of photoswitchable molecules aimed to achieve, through centroiding, images below the diffraction limit. In an analogous way, some single photon counting imaging techniques exploits centroiding to recover loss in resolution due to amplification methods (see Chapter 6).
In practice, this part of the thesis investigates the possibility to apply super-resolution techniques and algorithms to the SPC field.

5.4.1 Experimental Data

In this section we aim to process two different datasets with the mentioned programmes. The first dataset, more relevant for this project, is composed by 512 $\times$ 512 pixels SPC images we collected with the EBCCD camera as described in the previous sections (see Sec. 5.1.1). Due to the large amount of data and to the image drift that may arise from using different datasets, only a subset of $10,000$ frames (taken in one single experiment) was processed, instead of all the $95,000$ collected images. *ImageJ* in particular presented problems of available memory on our 32bit system, so a larger dataset could not be used.
The second dataset consists of $20,000$ (256×256 pixels) STORM images of a fixed cell with the tubulin labelled with Alexa 568 (courtesy of Dr. Susan Cox). These results are presented in Section 5.4.5, while the SPC ones in Section 5.4.4. Great care has been taken that the same settings for all the processing programmes, such as background/threshold values and size of the Point Spread Func-

tion in order to have comparable results from each software. For the evaluation of the centroiding algorithms and to estimate the introduction of Fixed Pattern Noise in the reconstructed image, a sub-pixel resolution of 3 was chosen. This means that every pixel in the original image is divided in 3×3 sub pixels in the reconstruction.

5.4.2 QuickPALM

QuickPALM has been presented as a freely available plug-in for ImageJ software[232]. This plug-in, instead of using a Gaussian fitting to detect and resolve blurs below the diffraction limit, rely on a high-speed algorithm to locate the spots and a centre of mass algorithm to identify position and relevant information. We are going to focus on this centroiding algorithm, rather than all the other programme's features.
As stated before, QuickPALM uses a centre of gravity algorithm as follows[232, supplement 1]:

$$x_c = \frac{\sum_{i,j} I_{i,j} x_{i,j}}{\sum_{i,j} I_{i,j}} \tag{5.5}$$

$$y_c = \frac{\sum_{i,j} I_{i,j} y_{i,j}}{\sum_{i,j} I_{i,j}} \tag{5.6}$$

where x_c and y_c are the resolved centre coordinates, i, j the pixel indices along x and y axes respectively, $x_{i,j}$ $y_{i,j}$ are the coordinates expressed in nanometres for the analysed pixel, and finally $I_{i,j}$ is the intensity of the associated pixel.

5.4.3 RapidSTORM

Also RapidSTORM is presented as an open-source software for localisation microscopy. This particular program relies on a Levenberg-Marquardt fitting[259] of a Gaussian PSF in addition to either a least-squares or Poissonian MLE[260] distance metrics. In practice, the software searches for local maxima, and fit

	Position parameters
x, y	position of image pixel
I	Image Intensity (in photons)
	Fluorophore parameters
x_0, y_0, z_0	fluorophore position
A	amplitude of the signal (in photons)
	Optics parameters
B	local background (in photons)
θ	fraction of detected photons
σ_x, σ_y	width of the PSF in x and y

Table 5.2: Parameters for RapidSTORM software[234, supplement 1].

them with a Gaussian point spread function; before accepting an event it verifies the consistency of the fitting with one of the proposed methods.
As reported on RapidSTORM supplementary documentation[234], the algorithm can be expressed as follows:

$$\begin{aligned} \Phi = & \quad \frac{A\theta}{2\pi\sigma_x(z)^2\sigma_y(z)^2} \exp\left[-\frac{(x-x_0)^2}{2\sigma_x(z)^2} - \frac{(y-y_0)^2}{2\sigma_y(z)^2} \right] + B \\ \chi^2_{MLE} = & \quad 2\sum_{p\in P} \Phi(p) - I(p) - I(p)\ln\frac{\Phi(p)}{I(p)} \end{aligned} \tag{5.7}$$

being p the value of the pixel, P the whole input pixels, and being the other parameters as shown in the Table 5.2.

5.4.4 SPC data processed with QuickPALM, RapidSTORM and in-house software

In this section are shown the results for the processing of EBCCD collected data with the analysing software: QuickPALM, RapidSTORM and our developed programme, labelled THRESH for brevity now on. In Figures 5.14 and 5.15 are presented the reconstructed images for RapidSTORM, QuickPALM and THRESH respectively, with a subpixel resolution of 3×3 (each pixel is divided into 9 sub-

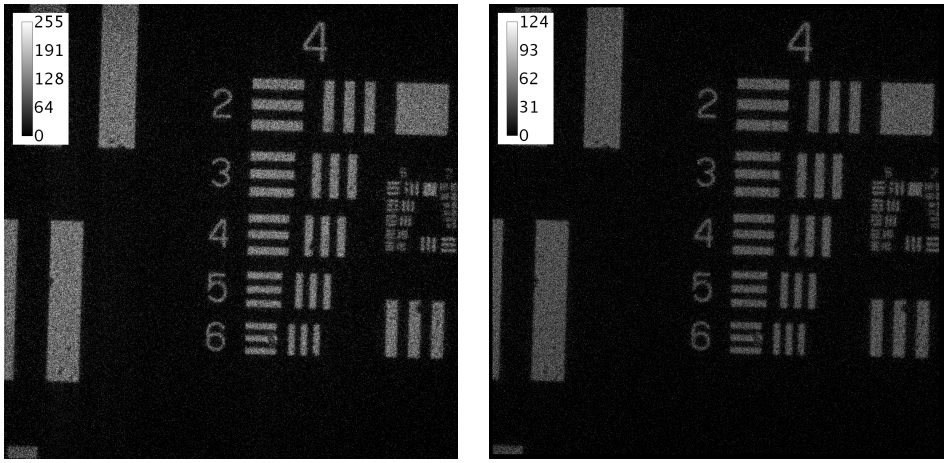

(a) (b)

Figure 5.14: EBCCD images dataset (10,000 frames) processed with RapidSTORM (*a*) and QuickPALM (*b*), converted to greyscale images for comparison. The square at the top right corner has a side of 139.3 μm

pixels). The results of the processing show already that it is possible to use these packages for single photon counting applications.

By observing the test pattern dimensions, it can be derived that the pixel size in the original images is 2.4μm and 0.8 μm in the sub-divided reconstructions. Although the optical resolution limit at 530 nm (green filter, Semrock) for this setting was $\sim 1.08\mu$m, due to the nature of the device the photo-electron charge is distributed among several pixels, thus applying a centroiding algorithm reduces this spread-effect rather than improving the optical resolution. In order to better evaluate the differences between the algorithms and the software used, also a variable N-Points centre of gravity algorithm was implemented in THRESH, equivalent to the QuickPALM's one, according to eq. 5.6. The code processes each image pixel by pixel, and when it finds values above the background level, the surrounding area is evaluated: a subprocess identifies all the pixels above the threshold associated to the event, its peak, and accepts or rejects the event, according to its size (events too small are considered background noise, and events too large overlapping events). For each accepted event, a routine calculates the centroided position by using the values of the peak and of the adjacent pixels in x and then in y. The subpixel position of the event is recorded and used to

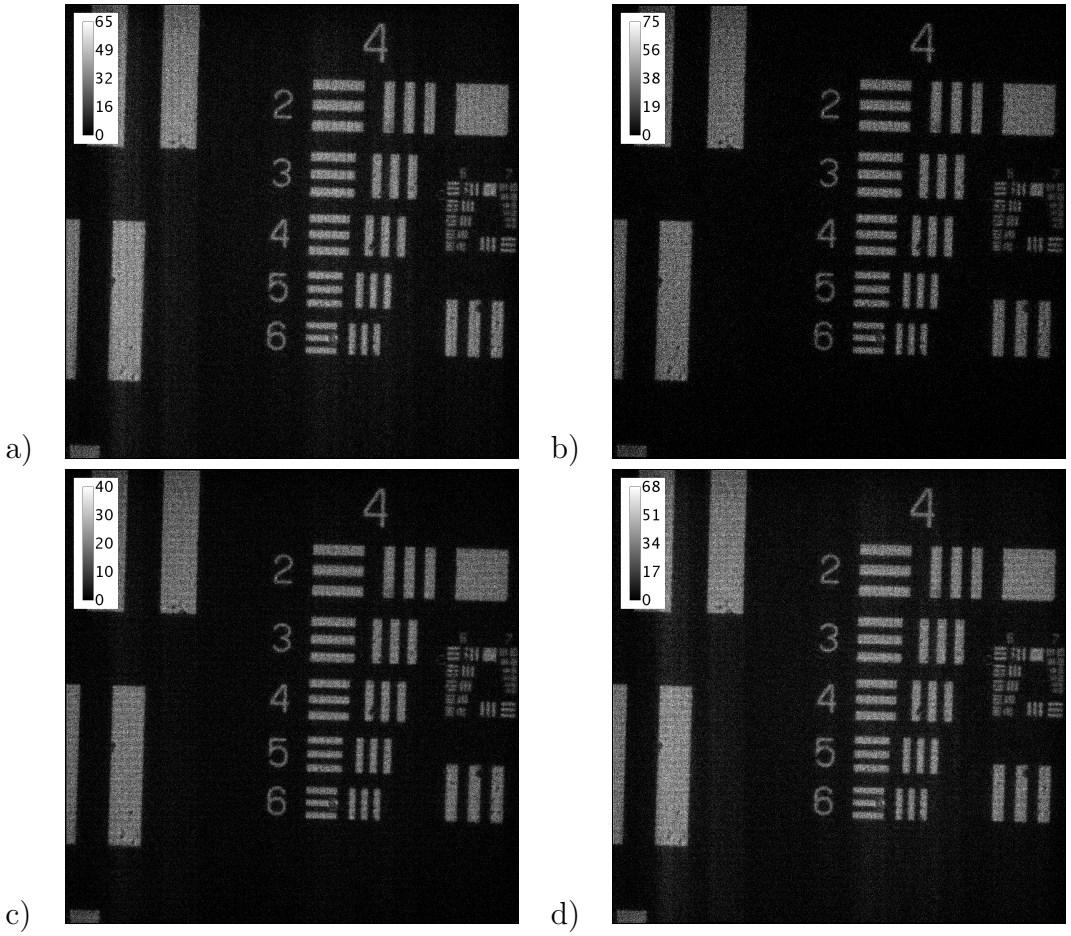

Figure 5.15: EBCCD images dataset processed with THRESH software: centre of gravity (a), Gaussian (b), Lorentzian (c), parabola (d). The square at the top right corner has a side of 139.3 μm.

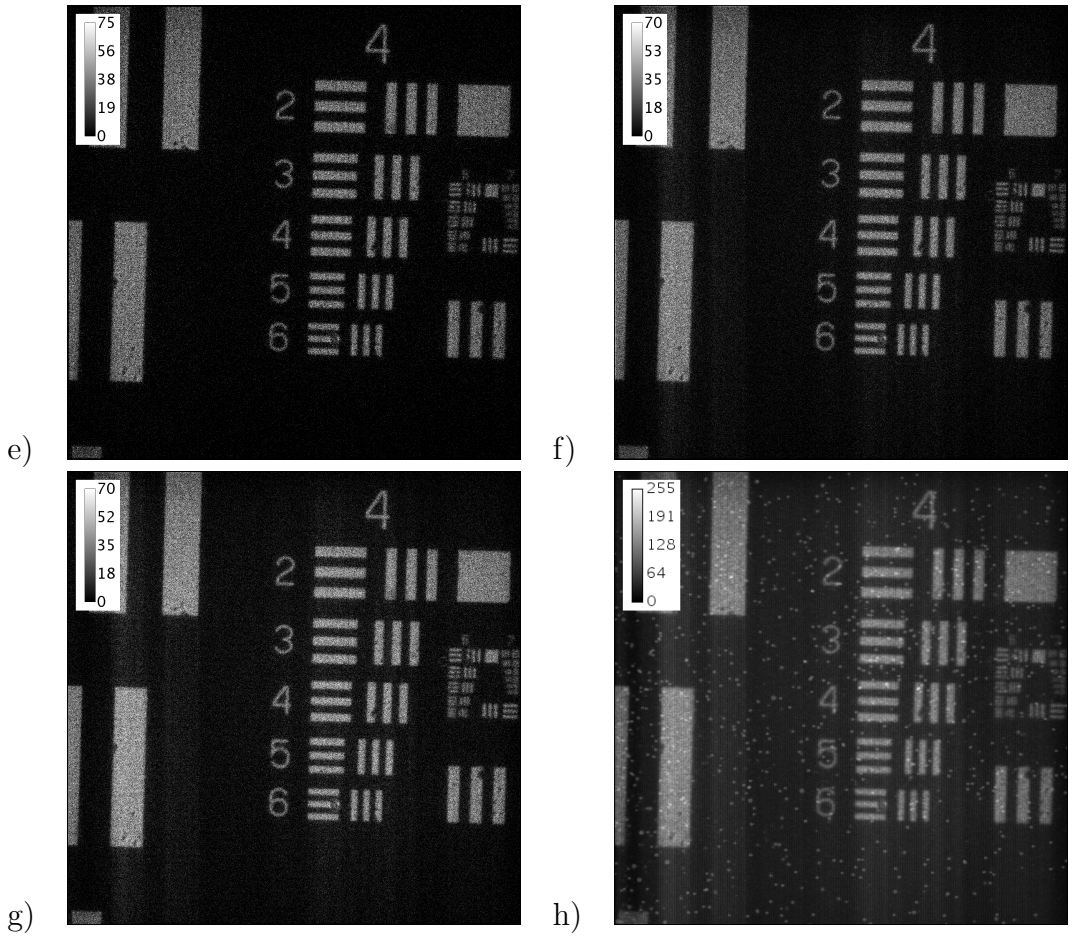

Figure 5.16: EBCCD images dataset processed with THRESH software: in addition to the hyperbolic cosine (e), the QuickPALM centre of gravity algorithm (f) was implemented on our software to allow a better comparison; an hybrid algorithm 50%Lorentzian/50%centre of gravity was found to slightly reduce the FPN (g); a sum of the $10,000$ frames, previously thresholded (h). The square at the top right corner has a side of 139.3 μm

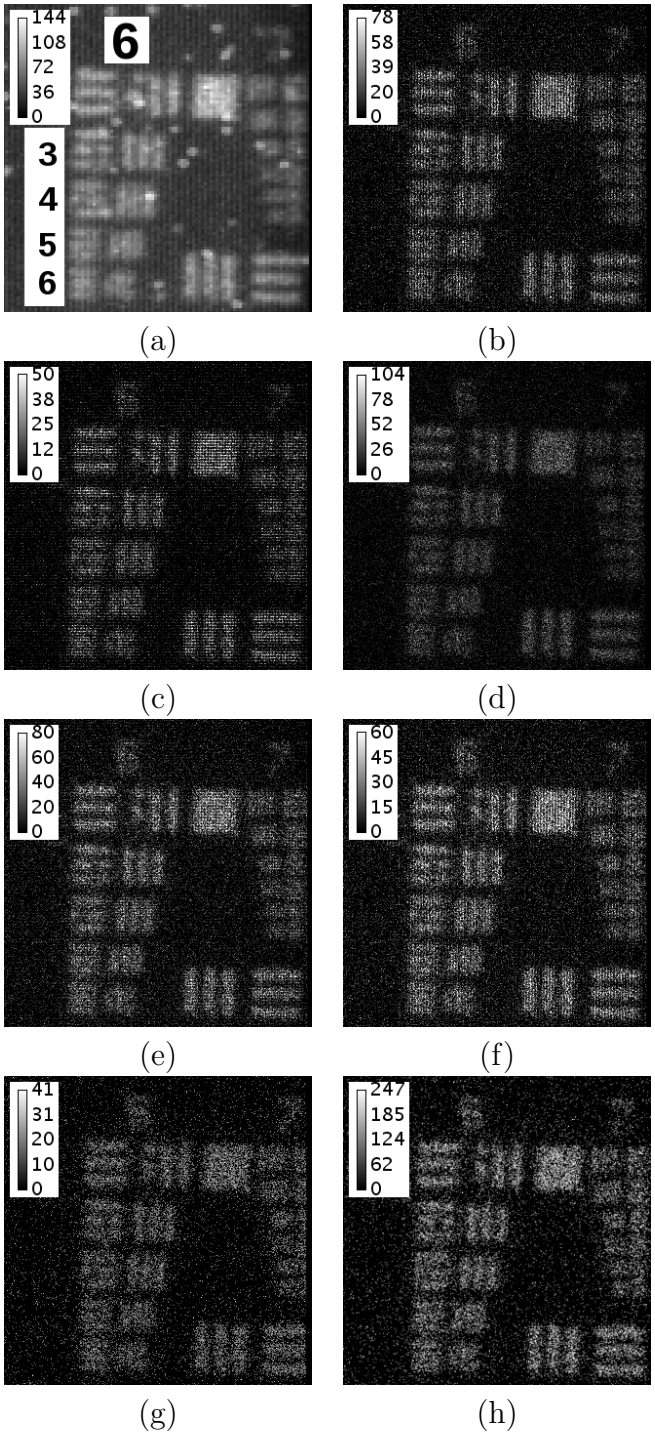

Figure 5.17: Evaluation of the methods for the different algorithms in a zoomed area: Sum of all frames (after background subtraction) *(a)*; 3-points COG *(b)*; Lorentzian *(c)*; N-points COG (equivalent to QuickPALM algorithm) *(d)*; Hybrid (50% Lorentzian / 50% COG) *(e)*; Hybrid (Gaussian/COG) (g); QuickPALM (f); RapidSTORM (h). The text in *(a)* identify the group (*6*) and the its elements (*3-6*). The square in the upper part of the figure has a side of 34.8 μm.

reconstruct the final image.

In order to compare the performances, a region of interest (a set of bars of the USAF pattern) was investigated for each reconstructed image. It is possible to define the maximum resolution of the system as the smallest set of bars that can be resolved. The limit of our system falls within the elements of the group *6* of the USAF test pattern, as can be seen in Figure(s) 5.17-(a): for the smallest elements [6;5] and [6;6], the plot of the profile of the bars shows only a blur for all the algorithms. The larger elements, group-elements [6;4] and [6;3], were investigated and an example of the profile plots for [6:3] is presented in Figure 5.18, where the x axis represents the relative position in micrometres, and the y axis the number of counts in each pixel. In addition to the algorithms previously

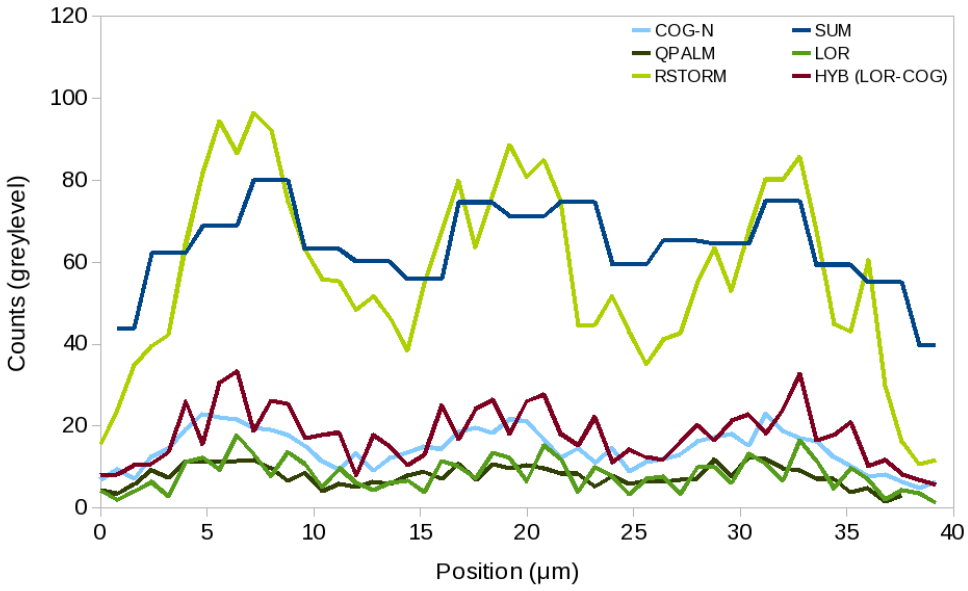

Figure 5.18: Profile of three vertical bars for the position [6;3], corresponding to a line-width of 6.2 μm. The *SUM* line identifies the reconstruction obtained by summing all the images, scaled to be compared with the other algorithm; the plateaus are an artifact due to the scaling. The RapidSTORM profile has the highest counts and less "spikes", whereas the other algorithms count rate is far lower. The spike effect is less evident for the N-point centre of gravity algorithms (*COG-N* and QuickPALM), while it is predominant for the Lorentzian and Hybrid profiles.

introduced, a combination of Gaussian and Centre of Gravity (COG), Hyperbolic Cosine and COG, and Lorentzian and COG hybrid algorithms were used. For the first two algorithms, the Gaussian or hyperbolic cosine centroiding is attempted at first and, if the conditions on the equations prevent to use them (i.e. division by zero), a three point COG is used instead. For the last hybrid algorithm, since the number of accepted events was similar for both Lorentzian and COG, a "50%" condition was added so that the code would centroid using alternatively one of the two algorithms; in the events where the conditions on Lorentzian equations were not met, again the COG algorithm was used.

As mentioned, to evaluate the resolution, the profile of the USAF bars were investigated: the elements [6;4] have a bar width of 5.5 μm, and the elements [6;3] 6.2 μm. Each of the two set of bars were fitted to three Gaussian curves for all the applied algorithms. The results can be seen in Figure 5.19: the red line identify the distance between the centres of two adjacent bars, whereas the columns represent the FWHM for each algorithm (green-[6;3]; orange-[6;4]). The bars can be resolved if the FWHM is smaller than this distance (12.4 μm for [6;3], and 11.0 μm for [6;4]): the *SUM* column shows that, for the simple averaging of the images, it is not possible to resolve the [6;3] elements, whilst some of the applied algorithms allow it. For [6;4] elements, none of the algorithms allow to resolve the bars, setting then the smallest resolvable distance to $\sim$6.2 μm. Due to the strong variations in the values for some of the algorithms, it was not possible to reliably fit all the curves (for example the COG algorithm yield a R^2=0.29): these values are presented but their validity must be treated with caution.

As shown in the previous Section 5.2, the centroiding of EBCCD data presents a shift along the x axis that affects the quality of the reconstructed image when processed with THRESH and this generating the strong variation in the plot. This behaviour is not evident in the other software tested and no evident artifacts appear in the resulting images generated by any of the programmes. In particular, it can be noticed that the shift effect is almost removed by RapidSTORM, whereas a small noise effect is present in QuickPALM results. From the analysis of the profile plots in Figure 5.18, it can be noticed that centroiding using all the pixels in each event (like QuickPALM and COG-N), on the contrary of using just 3-points, also reduces the "spikes" effect.

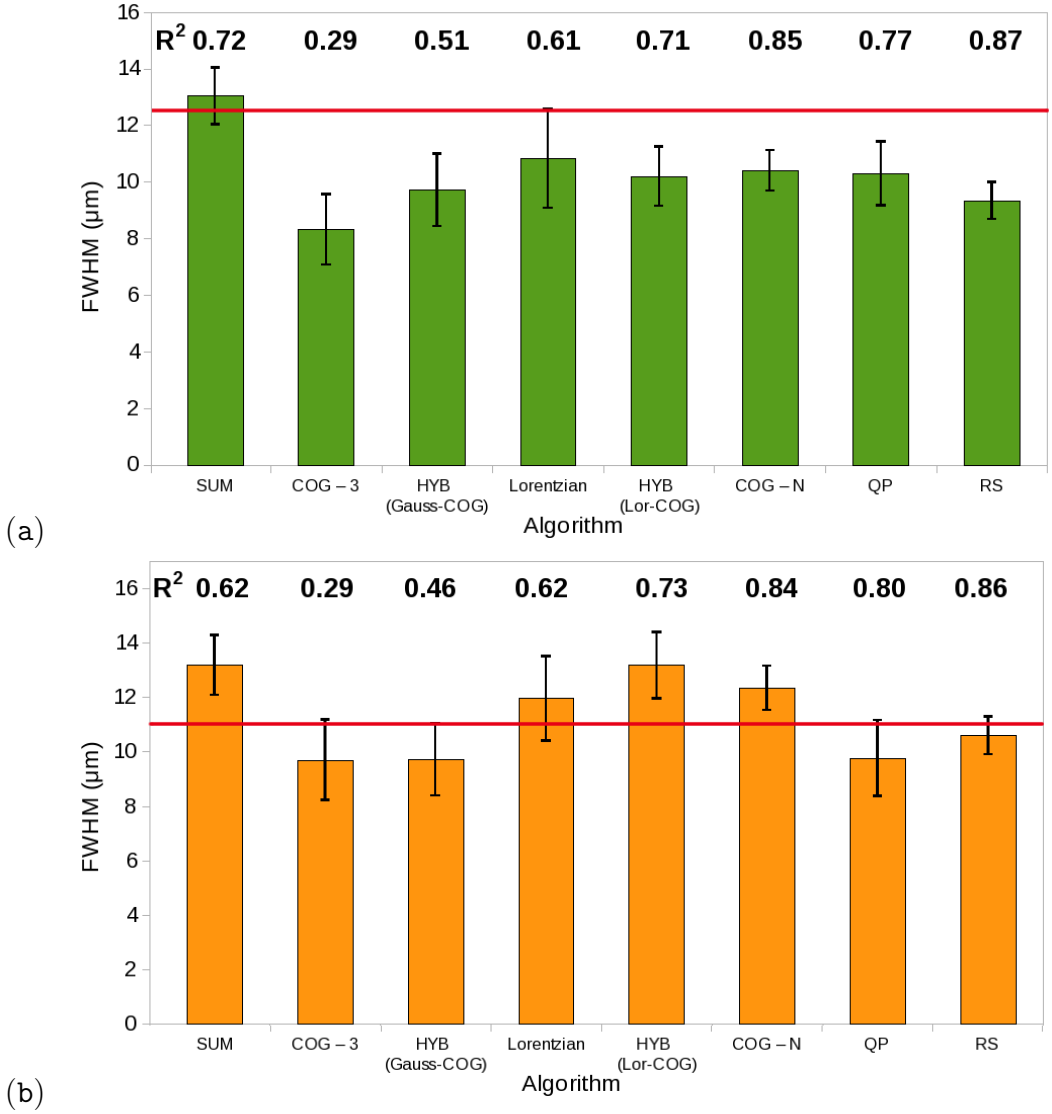

Figure 5.19: Resolution evaluation for (a) the position [6;3] (bar-width of 6.2 μm) and (b) the position [6;4] (bar-width of 5.5 μm). Each column represents the FWHM for three Gaussians fitted to the bars profiles for each algorithm. The *SUM* column identifies the reconstruction obtained by summing all the images, and it can be noticed that it is above the distance between the centres of the bars (red line) in both graphs: the elements [6;3] and [6;4] cannot be resolved with this method. The R^2 value for the fitting is shown on top of each column: it is important to notice that, although some algorithms can theoretically resolve the bars, the low quality of the fitting make them unreliable. QuickPALM, RapidSTORM, and some THRESH algorithms (having values for R^2 above 0.77) allow to resolve the bars for the [6;3], partly recovering the loss in resolution due to the charge-spread effect. For the position [6;4] (b), QuickPALM and RapidSTORM profiles present a FWHM below the distance between the bars, but the red line falls within their error bars. The Gaussian fitting and the error calculations were obtained using the software MagicPlot 2.0.5.

5.4.4.1 Fixed Pattern Noise

The Fixed Pattern Noise for all the images was calculated: for the QuickPALM image, the value was found to be 49%; for RapidSTORM, FPN was 13%. For our code the effect of fixed pattern noise appears quite larger, as shown in Table 5.3. The number of events accepted by our code ($\sim 1,050,000$) was larger than for QuickPALM ($\sim 750,000$), and again smaller than RapidSTORM ($\sim 1,200,000$). The fact that RapidSTORM collects more photons than THRESH suggests that it is taking into account some background noise, but due to the better centroiding these are not affecting the resulting image. Alternatively, it is our software that it is not accepting all the events, possibly due to the reported "shift" in the EBCCD data: this may affect the shape of the detected photon events, and because of that they are being rejected by the code.
All the results with standard algorithms are affected by the shift in the EBCCD data (leading to FPN values above 150%), and even QuickPALM seems to be slightly affected by it. The use of hybrid algorithm combinations did not significantly improve the FPN ($\sim 100\%$). On the other hand, the choice of a N-points algorithm alone gives similar results ($\sim 99\%$).

5.4.5 STORM data processed with QuickPALM, RapidSTORM and in-house software

Here are presented the results of the STORM dataset processing. RapidSTORM uses an iterative fitting algorithm, QuickPALM uses a centre-of-gravity centroiding algorithm, whereas the code presented in this thesis applies several single iteration centroiding algorithms. In order to have a complete picture of the possible applications of the discussed algorithms, and to evaluate if a single-iteration can be used for single-molecule detection, a set of STORM data were fed to all the software.
Few images of the used dataset are presented in Figure 5.20 as an example (a,b). The set shows several very bright spots that are persistent in all the frames: the brightness of the switching molecules decreases along the acquisition, so the first frames (a) are in general brighter then the last ones (b). The exact set-up of

Algorithm	**FPN total** (%)	**FPN x** (%)	**FPN y** (%)	**Accepted Events**
RapidSTORM	13	6	6.9	1,210,027
QuickPALM	49	22	27	769,831
COG3	153	96	53	1,071,169
COG-QuickPALM	102	45	58	1,071,169
Gaussian	181	77	86	388,570
Lorentzian	171	102	71	822,941
Parabola	184	60	115	1,071,047
Hyperbolic Cosine	148	80	54	235,744
Hybrid - Gauss	123	74	41	1,071,169
Hybrid - Hyp Cos	105	75	27	1,071,169
Hybrid - Lor 50%	99	77	24	1,071,169

Table 5.3: Results comparison for EBCCD data. The table summarises the fixed pattern noise for the different programmes and algorithms: the column "FPN total" shows the overall effect, whereas "FPN x" and "FPN y" the noise associated to x and y directions, respectively. In the "Hybrid - Gauss" and"- Hyp Cos" rows are presented the results for hybrid algorithms: when possible, Gaussian or Hyperbolic Cosine fitting is used, and the Centre of Gravity algorithm when the pixel values forbids to use other methods. The "Hybrid - Lor 50%" instead, alternatively uses a Lorentzian and a COG algorithms.

the data collection is unknown, so no precise scaling of the structures in the images can be given. However, since the aim of this investigation is the algorithms application, and not the actual resolution of the imaged samples, this issue will not interfere with the presented analysis. In Figure 5.21 it is possible to see

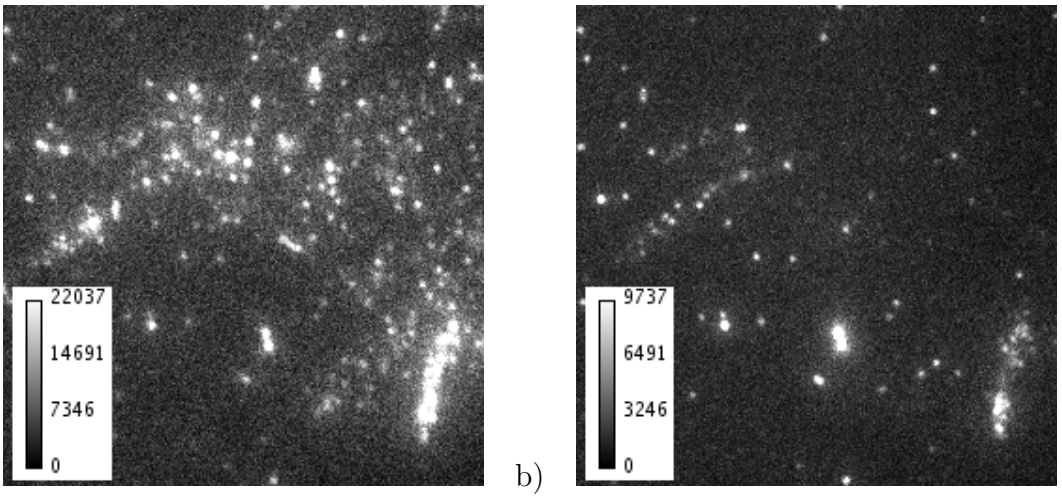

Figure 5.20: STORM data example. Single frames taken at the beginning of the dataset *(a)* and at the end of it *(b)*. It can be noticed that the switching molecule activity decreases along the acquisition.

the results for RapidSTORM (*a*) and QuickPALM (*b*); the original images were coloured but were converted to greyscale for comparison.

The data were processed with THRESH using the algorithms discussed in Section 2.5, and an example of the results are presented in Figure(s) 5.22: on the left column are shown the resulting images for 3-point Centre of Gravity (*a*), and N-Points centre of gravity (*b*) algorithms; the contrast was changed in order to better show the results of the processing. On the right column are displayed the modulo-3 images for the applied algorithms: they represent the sub pixel distribution of the events, so a uniform image indicates low fixed pattern noise and good matching between the algorithm and the centroided fluorophore. The issues encountered in the processing can clearly be seen: by adjusting the accepted/rejected size of the events, the largest spots in the centre of the picture are not considered (compare with Fig. 5.20-*c*, -*d*). This leads to the formation of artifacts around these events: the main event is rejected, but the bright area

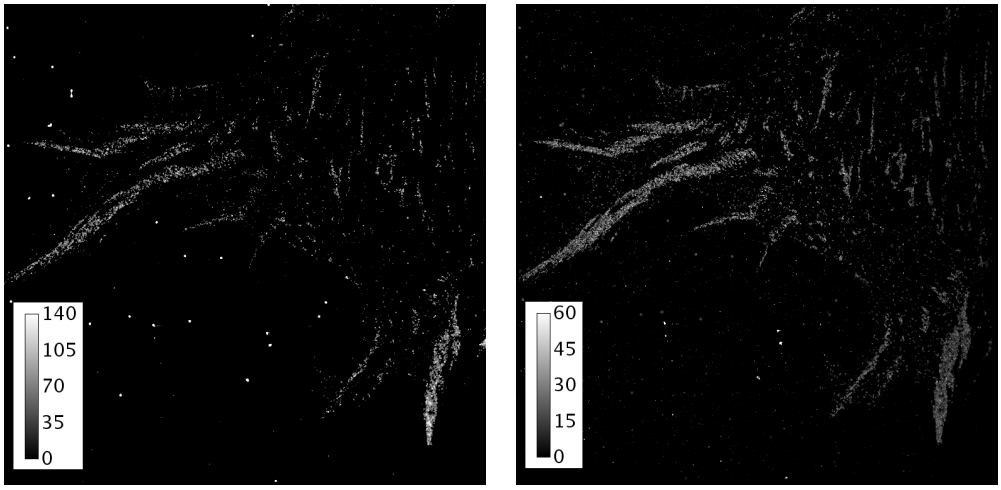

(a) (b)

Figure 5.21: RapidSTORM (a) and QuickPALM (b) processing. The results for 20,000 STORM images processed were converted to a greyscale image for comparison. The contrast has been adjusted equally in both images for clarity.

around it is considered as several small events that are erroneously taken into account. On the other hand, also the small but very bright events are processed in each frame: the number of counts corresponding to these spots is high and it drastically reduce the dynamic range of the image, making difficult to resolve other areas of interest. This is the reason the contrast adjustment is required. It is possible to note that similar artifacts do not appear in QuickPALM nor in RapidSTORM, but the bright events reduce the dynamic range of the image (to avoid saturation) for QuickPALM; this effect is not visible in RapidSTORM. By zooming in a small region of the reconstructed images, it is possible to compare the different techniques. The region of interest (in yellow) for each image is shown in Figure(s) 5.23, and a profile plot for the more relevant reconstructed image is presented in (j). The profile graph present the pixel distance in the x axis and the number of counts in the y axis. It can be seen that AVG (averaged sum of all frames) image is affected by the bright spots like our code and QuickPALM: to avoid saturation of the pixels, the scaling of the pixel values make it difficult to resolve the patterns of the structure. Since there are not reference information for the exact dimensions of the cell structures, a precise resolution evaluation

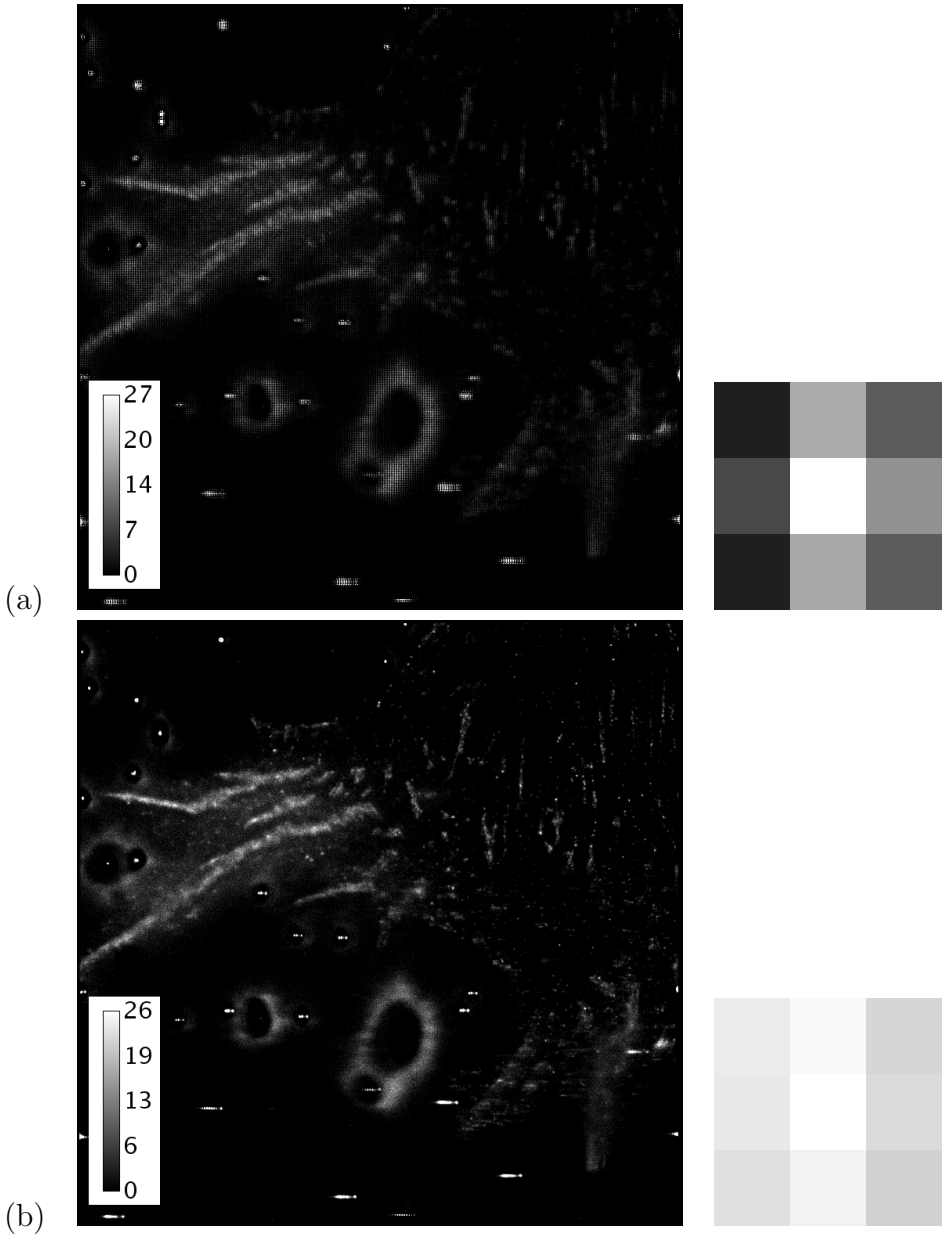

Figure 5.22: Processing of the STORM dataset (20,000 frames) with different centroiding algorithms. The left column shows the output images of the processing code; the contrast of the images were adjusted in order to better show the details; the right column presents the "modulo 3" images associated with each algorithm, representing the distribution of the sub-pixels after the centroiding. (a) 3-Points Centre of Gravity; (b) N-Points Centre of Gravity. The short "lines", appearing at the bright spots locations, seem to be artifacts due to the way THRESH scans each frame: instead of a single large event, several sequential events (scanned from left to right) are identified.

cannot be performed. However, from the qualitative analysis of the profiles, it can be seen how RapidSTORM allows a better distinction between the two cell structures, and how the 3-point centroiding produces noisy profiles without any visible improvements. A summary is presented at the end of the next section in Table 5.4.

5.4.5.1 Fixed Pattern Noise

The Fixed Pattern Noise for all the images was calculated: for the QuickPALM image, the value was found to be 20.1%; for RapidSTORM, FPN was 14.9%. For the code developed, the effect of fixed pattern noise appears quite larger: for the Gaussian fitting, it is 60.5%; for Lorentzian fitting $FPN = 150\%$; whereas for COG and parabola it is above 200%. A better result was obtained with the N-point COG algorithm, where FPN= 42.3%.
The number of accepted events for our code were in the same range of QuickPALM ($\sim 650,000 - 692,000$), but RapidSTORM had the highest number counts ($\sim 1,019,000$). The different number of events accepted for each algorithm depends on the possibility to apply the relative equation or not: for example, if the value of a considered pixel is zero, the use of a certain algorithm may lead to a division by zero or similar forbidden operation. The count of emitters (molecules) identified by each software seems to be independent of the algorithm used but rather depends on the way each code identifies and accepts the events: scanning, background thresholding, and event size selection for THRESH; filtering, spot identification, and event size selection for QuickPALM; spot identification and iterative Gaussian fit for RapidSTORM.
The high FPN values found for THRESH code are probably due to the difficulties in dealing with the background noise and in resolving very close or overlapping events. As previously described (see Sec. 2.5), our programme processes each event with different 3-points centroiding algorithms (the peak pixel and two "wings" in x and y): for large bright blurs very close to each other as in the processed dataset, using a single-iteration algorithm is not sufficient to obtain a reliable centroiding. In principle, by increasing the threshold level for the presented code, it would be possible to separate two partly overlapping emitters.

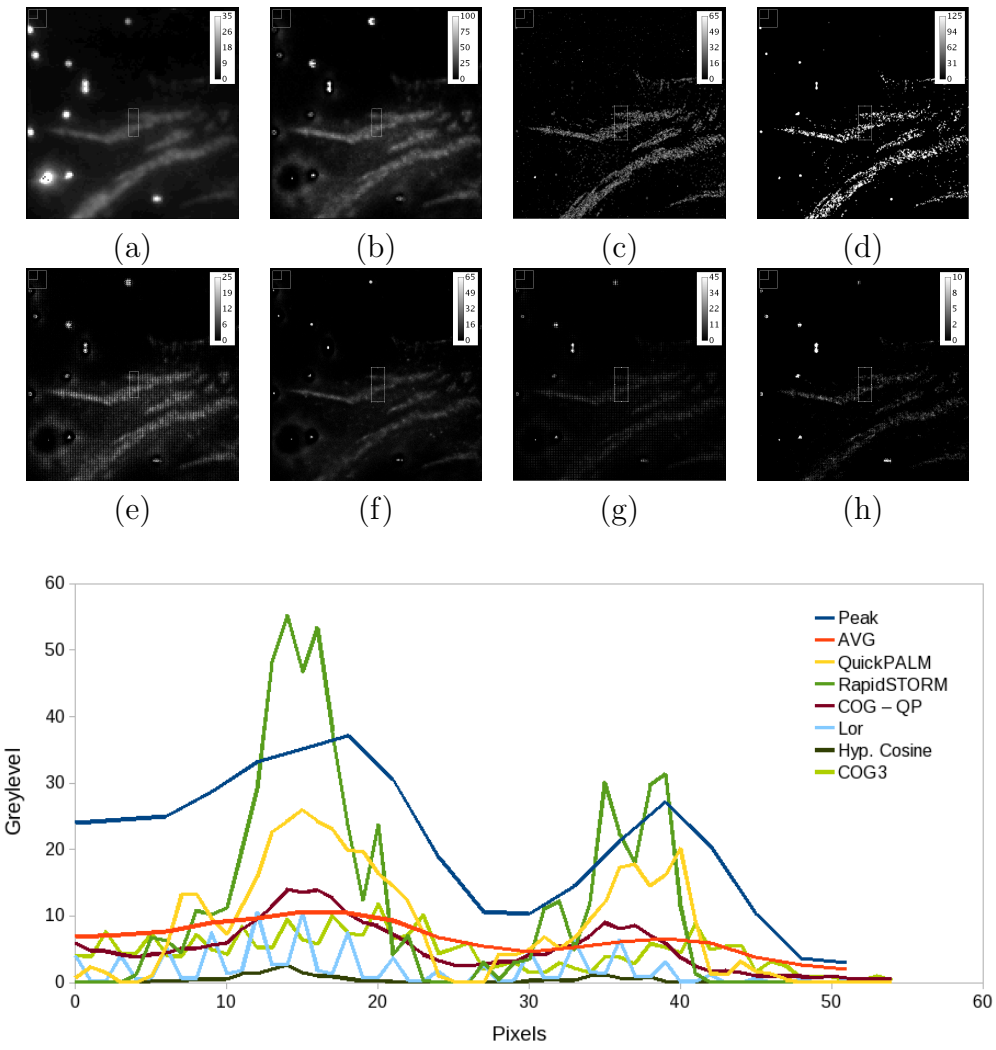

Figure 5.23: Sub-pixel resolution for STORM data: a zoomed area of the reconstructed images are analysed and the profile plot of a region of interest (j) measured for: a reconstruction via the sum of all frames, where the background has been subtracted (a); a centroided image where only the highest pixel is taken into account (b); QuickPALM (c); RapidSTORM (d); 3-Points COG (e); N-Points COG (f); Lorentzian (g); Hyperbolic Cosine (h).

Algorithm	FPN (%)	Events accepted
RapidSTORM	20.1	1,018,291
QuickPALM	14.9	692,483
COG-3	209.2	648,730
Gaussian	60.5	387,281
Lorentzian	150.0	617,142
Parabola	202.5	648,730
COG-N (QuickPALM)	42.3	648,730

Table 5.4: Results comparison for STORM data. The table summarises the fixed pattern noise for the different programmes and algorithms: the column "FPN" shows the overall effect of the fixed pattern noise expressed as a percentage, whereas the last column "Events accepted" states the number of valid events processed.

However, with this approach only the very bright events would be processed, thus losing the information carried by the dimmer spots. Furthermore, even by using an optimal threshold value, the presence of several morphological structures in the cell may be identified by the software either as a dim event, or as background noise, making difficult to resolve the real emitting spots from the artifacts.

5.5 Conclusions

In this chapter we investigated the application of an EBCCD camera as a multichannel-TAC and the effect of event-fitting on the fixed pattern noise.
Presented results confirm the potential of Electron Bombarded detectors for this task. This would be an advancement for all the applications that require photon timing as it allows temporal resolution below the camera exposure time. Techniques such as TIRF and light-sheet microscopy, where scanning is difficult or impossible, may benefit of this wide-field technique, whereas FLIM may take advantage of the high signal-to-noise ratio of this TCSPC approach, in addition to an effective use of the limited photonic budget available[1]. The case presented had a maximum frame rate of 3 Hz for 512×512 pixels (not editable) and even by increasing the number of photons per frame to 1000, the effective event count

rate would be only 3 kHz. This is far too low compared to commercially available TCSPC devices (in the order of MHz)[13], but recently developed[210] EBCMOS photon counting devices achieve 500 Hz already. The proposed application for EBCCD, or for the analogous EBCMOS, detectors would then require the possibility to vary the total gain during each frame acquisition; the frame rate should be comparable with available techniques; the amplitude of the acceleration voltage has to be high enough to clearly resolve the pulse height distribution, and thus the sub-frame temporal resolution.
The comparison of our SPC code with PALM/STORM software showed that it is possible to use them to process data obtained with both the techniques. QuickPALM and RapidSTORM performed effectively in the processing of EBCCD data, presenting a smaller FPN effect: the Gaussian fitting used by RapidSTORM in particular seems to completely cancel the "shifting" effect in x direction shown in Figure 5.7.
THRESH presented limitations in the analysis of large structures and in dealing with very bright events in the processing of STORM data. It would be possible to improve the code in order to address these issues, however the application of single-iteration algorithms does not produce appreciable results compared to multiple-iteration fittings.

5.6 Chapter Summary

The investigation confirmed the theoretical possibility to use an electron-bombarded device as a parallel time-to-amplitude converter, achieving sub-exposure time resolution. It was confirmed that single-molecule localisation algorithms can be used to process single-photon counting data. The application of centroiding algorithms led to an improvement of the maximum resolving capabilities on a test pattern, but a strong fixed-pattern noise was introduced by both the applied algorithm and the device inherent read-out process. The fixed pattern noise was reduced for iterative fitting and N-points centroiding approaches.
Wide-field techniques requiring photon timing may benefit of the temporal resolution below the exposure time, and when the events are spread above several pixels the use of centroiding can improve the resolution.

Chapter 6

High speed cameras

6.1 Introduction

Here we propose a technique exploiting the high-frame rate of novel complementary metal-oxide semiconductor (CMOS) cameras for SPC imaging. By coupling the camera with an image intensifier, it is possible to achieve single-photon sensitivity.

For this class of devices, all pixels can be processed simultaneously at high rate, because each one has its own dedicated electronics. This is an advantage compared to CCD devices where charge transfer limits the maximum speed achievable and introduces noise effects (see Sec. 5.2.1). On the other end, the high frame rate these cameras can achieve ($\sim$1 MHz[261]) and the resulting reduction of the exposure time, increase the effect of thermal and read-out noise on the measured luminescence signal. The coupling of the CMOS camera with a photon counting image intensifier can solve this problem, creating a wide-field single photon imaging system with a very high frame rate[165; 171; 261]. The main drawback of this approach is the loss in quantum efficiency of the photocathode: whereas CMOS sensors have a high quantum efficiency (QE), very important for exploiting the limited photon budget of the fluorophores, a photocathode QE ranges from 25% to 50%[13; 195]. In addition, this method presents a loss in the resolution due to the second multiplication effect of the MCP in the intensifier, this generating a large electron cloud hitting the phosphor screen, but we propose to reduce this

effect by applying a centroiding algorithm. Furthermore, since phosphor screens may present a long afterglow effect, we propose to take advantage of this feature to obtain sub exposure time resolution. The final aim is to achieve the best possible tradeoff among spatial and temporal resolution, and the need for low level light conditions in biological samples. During this project two different cameras (Phantom v7.3, Photron SA1) were used; this section will focus on the results with the SA1 model and briefly mention other camera's features.

6.1.1 Phosphorescence Lifetime Imaging (PLIM) and Long Lifetime Probes

Fluorescence lifetime imaging microscopy is a very powerful tool and widely used in biology, medicine and research[134; 262]. This technique is restricted though by the nanoseconds range of the available probes, this limiting its contrast and sensitivity. This is true in particular in biology and medical diagnosis procedure[263], as autofluorescence increases with the complexity of the cells and tissues involved, greatly reducing the contrast in fluorescence imaging[42; 264]. Moreover, the timescale of some biological processes[144; 149; 265] can vary between the subsecond range to several hours[14], well above the nanoseconds scale achievable by FLIM. Phosphorescence lifetime imaging (PLIM) of long lifetimes probes, such as transition metals, can then be exploited as a versatile research tool[140].
For some of the results presented later on, a long lifetime complex based on the transition metal Ruthenium was used: tris(4,7-dyphenyl-1,10-phenanthronline) ruthenium(II) dichloride, $[Ru(dpp)_3]^{2+}$, Molecular weight: 1169.17 g/l (76886, Sigma Aldrich, UK). In this dye, the central chemical component is the metal, ruthenium, surrounded by six ligands attached to nitrogen, composed by a phenanthroline and a phenyl, as shown in the compound structure in Figure 6.1.
The luminescence decay of the sensor is affected by the quenching of phosphorescence due to the oxygen, thus lifetime measurements allow to map the partial oxygen pressure in tissues or thick biological samples. By increasing the viscosity, the oxygen diffusion rate is smaller, this leading to longer lifetimes[139]. An other candidate to be analysed in this work was Europium, a Lanthanide: these elements tend to have very long lifetimes, thus excluding autofluorescence effects

during live-sample measurements, and are commonly used in FRET techniques [149; 151]. This measurements can then be exploited to obtain quantitative information on several cells, and cancer cells in particular like: tumour growth, metabolism, prognosis, and effectiveness of therapies[151; 263].
Previous results with Europium-polyoxometalate (Eu-POM)[172], having an average lifetime of 2.9 ms, show that fast cameras can be used to perform luminescence lifetime imaging for this particular dye (see Fig. 6.2). The sensitivity of the sensor and the noise limit the maximum frame rate at which the camera can be used for lifetime measurements: in fact, at high rates the information carried by each frame is very small as shown in Figure 6.3. The figure shows an image of a Convallaria majalis (Lily of the valley sample) at 500 fps *(a)* and an image at 10 kfps *(b)* collected with an inverted microscope and the fast camera Phantom V7.3. It is evident how the active sensor of the camera alone cannot be used at frame rates above 10 kfps, as no light can actually be measured. This shows the need of a different approach, as the proposed one exploiting an image intensifier to take advantage of the technical possibilities of these devices.

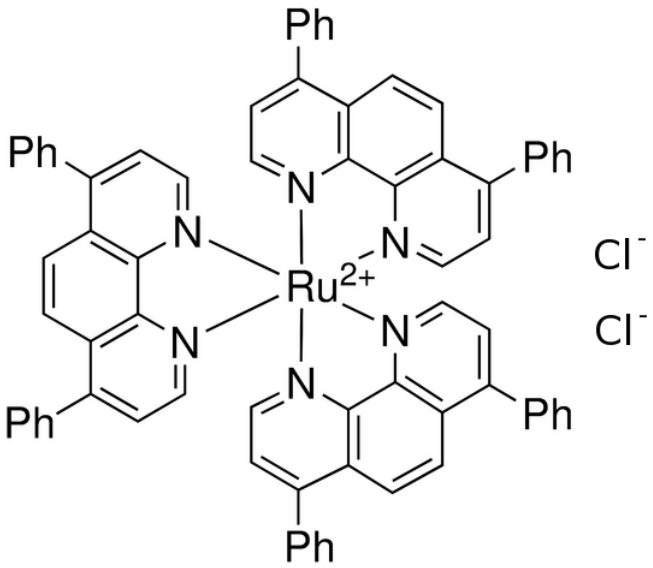

Figure 6.1: Schematic diagram of the chemical structure of the ruthenium(II) complex: $[Ru(dpp)_3]2+$. **Ru** - ruthenium, **N** - nitrogen, **Ph** - phenyl, **Cl** - chloride. Image reused with permission from [266]

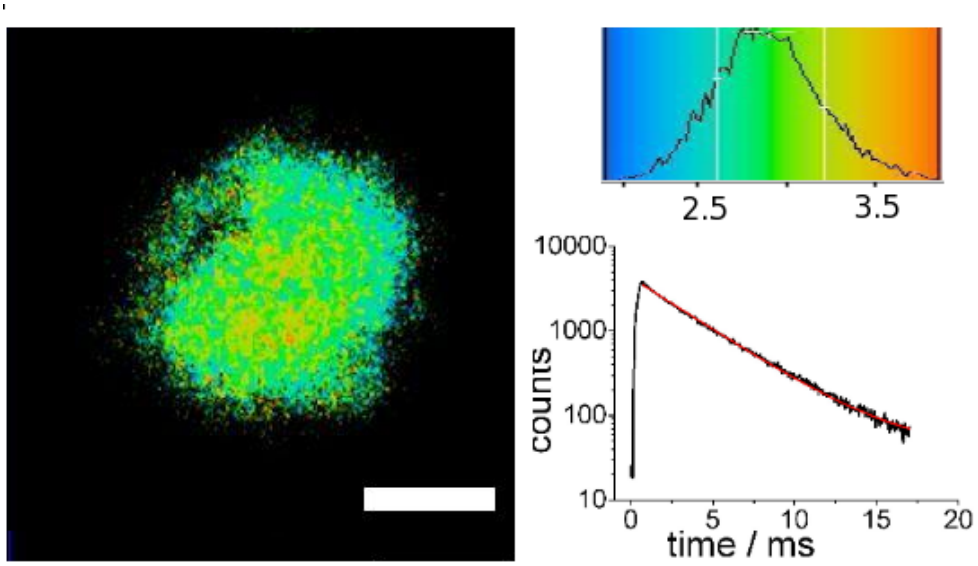

Figure 6.2: A FLIM image of a cluster of Europium-containing polyoxometalate (POM) nanoparticles *(left)* and lifetime histogram *(top right)* with an average lifetime of 2.9 ms. The monoexponential decay *(right)* was collected via 256 excitation pulses averaged over the whole field of view with a time channel width of 25 s. The scale-bar is 100 μm. Reproduced with permission from [172]

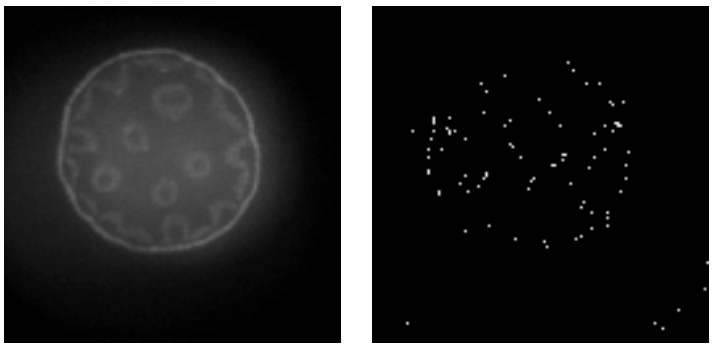

(a) (b)

Figure 6.3: Imaging of a Convallaria majalis (Lily of the valley) sample with Phantom V7.3 FastCamera. *(a)* The sample at 500 fps, using the built-in halogen lamp as light source. *(b)* The same sample at 10 kfps, in the same light conditions: the contrast in this image has been increased to present the amount of information carried by each frame.

6.2 Experimental Setup

The standard setup used for this experiment is shown in Figure 6.4. The image intensifier was mounted on the side port of the Nikon Eclipse TE2000 inverted microscope; a Canon photographic lenses (F=1.2) with 50 mm focal length was used to image the phosphor with a fast CMOS camera. The camera was set to image the entire phosphor screen (40mm diameter) but for high frame rates, only a subsection of the CMOS active area is used, thus imaging only a relevant section of the screen. The used intensifier was a P20 photon counting intensifier, and its voltage settings were as described in Section 2.4.2: from the photocathode to the phosphor screen, 150V, 800V, 2.35kV, and 4.50kV. A second analogue intensifier, equipped with a P47 phosphor, was tested to investigate its afterglow; no photon counting was possible on it due to its particular design. The FastCamera (SA1.1, Photron) was coupled with a pulsed diode laser (Hamamatsu) in order to trigger the acquisition. Most of the camera settings were varied according to the specific sample and task. For all the experiments, the "shading" command was used, this subtracting a dark value from each individual CMOS pixel in order to have a uniform image (see Sect.2.4.4); the acquisition was split in several partitions to speed up the download of the data after the experiment. The area of the CMOS chip is 20.5×20.5 mm^2 for the camera used, with pixel size 20×20 μm^2. The P20 and P47 phosphor screens have 40 mm diameter.

In order to investigate the possibility of achieving sub-exposure time resolution, the camera was set at 100 kfps and the laser at 500 kHz repetition rate. Thus, in each 10 μs exposure time window, we have 5 laser pulses. The sample used was the USAF pattern (see Sect. 2.5.4) for testing and calibration, and a Ruthenium compound for the actual experiments.

The lifetime measurements were also performed using a TCSPC board (B&H, SPC830) on a confocal microscope (Leica TCS SP2), in order to compare the results with the post processing of the FastCam acquired data. A stock solutions having 0.5 mg Ru(dpp) dissolved in 2 ml Ethanol ($\sim$0.4 mM) was prepared. Ruthenium fluorescence decay was firstly measured using a TCSPC board (B&H SPC-830) on a Leica confocal microscope, and the lifetime calculated using the associated fitting software (B&H SPCimage). The $[Ru(dpp)_3]^{2+}$ probe was then

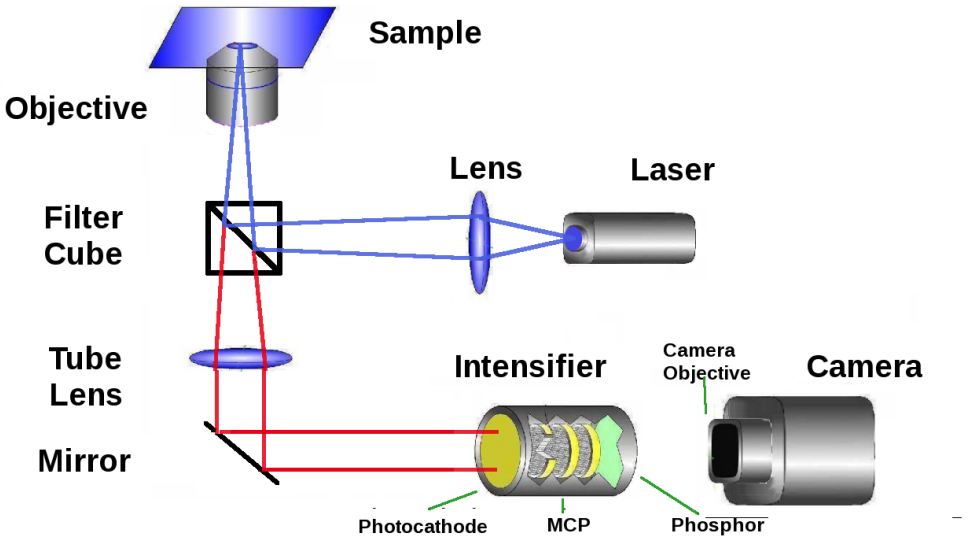

Figure 6.4: Schematic of the imaging system. The laser pulses excite the sample, and the emitted photons are routed to the intensifier; the photons are converted into photoelectrons from the photocathode and multiplied through the MCPs stages; the electrons are re-converted into photons at the phosphor screen and imaged by the fast camera.

placed on the inverted microscope (Nikon) and imaged with the coupled FastCam, then the results processed with in-house software.

6.2.1 Sub-exposure time resolution

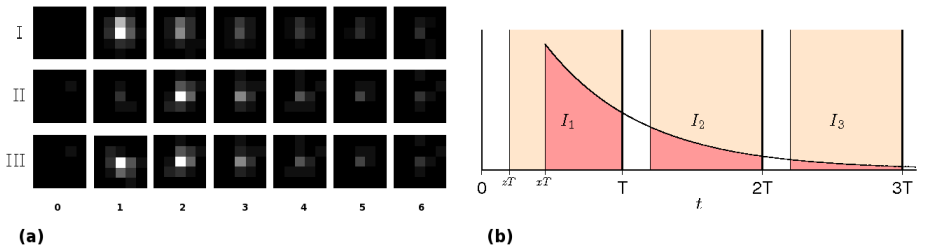

Figure 6.5: Phosphor decay: (a) Afterglow effect on collected events in several frames; (b) Schematic of phosphor decay and how it spreads among several frames: the coloured areas indicate the exposure window in each frame, whereas the blank gaps between each frame represent the dark time of the camera. Reused with permission from [267]

The invariant phosphor decay of the image intensifiers phosphor screen can be exploited in order to achieve sub-exposure time resolution [267]. The ratio of the intensities in consecutive frames due to the phosphor decay after the photon detection can be used to uniquely determine the photon arrival time. These arrival times can be determined with sub exposure time resolution, similar to a double exposure scheme proposed by studies in the field of ion velocity mapping [268; 269]. Fast luminescence decays in parallel in many pixels can then be measured using this method.
Figure 6.5 shows three typical events and associated decays. Note that in the two sequences I and II the events reach their maximum in two different frames although the detection threshold is exceeded in frame 1 in both sequences. This difference is because the photon in sequence II arrives near the end of the exposure time of the frame 1 whereas the other arrives at the beginning of the exposure. In sequence III instead the maximum value is the same in both frames 1 and 2: this happens when the event arrives at such a time inside the frame, the amount

of light collected in the two frames is the same. The phosphor screen decay can be approximated with a sum of exponential decays as follows:

$$I(t) = \sum_i a_i e^{-\frac{t}{\tau_i}} \tag{6.1}$$

where $I(t)$ is the intensity value for the phosphor at the given time t.
Assuming a monoexponential phosphor decay, it is possible to calculate the intensity in the first and second frames, and thus their ratio. The event intensity on the first frame can be expressed as the integral between the photon arrival time and the end of the frame as follows:

$$I_1 = \int_{xT}^{T} I(t - xT)dt = a\tau e^{\frac{xT}{\tau}} \left(e^{-\frac{xT}{\tau}} - e^{-\frac{T}{\tau}} \right) \tag{6.2}$$

and the intensity of the following frame can be expressed as:

$$I_2 = \int_{T}^{2T} I(t - xT)dt = a\tau e^{\frac{xT}{\tau}} \left(e^{-\frac{T}{\tau}} - e^{-\frac{2T}{\tau}} \right) \tag{6.3}$$

where T is the exposure time period, τ the decay constant of the phosphor, and $x \in (0, 1)$ the relative arrival time in respect to T. We can then estimate the arrival time xT from the ratio of the two first frames:

$$\frac{I_2}{I_1} = \frac{\left(e^{-\frac{T}{\tau}} - e^{-\frac{2T}{\tau}} \right)}{\left(e^{-\frac{xT}{\tau}} - e^{-\frac{T}{\tau}} \right)} = \frac{1 - e^{-\frac{T}{\tau}}}{e^{\frac{(1-x)T}{\tau}} - 1} \tag{6.4}$$

Thus, being the arrival time:

$$xT = T - \tau \ln \left(1 + \frac{1 - e^{-\frac{T}{\tau}}}{\frac{I_2}{I_1}} \right) \tag{6.5}$$

The procedure just described assumes it is possible to resolve single events in the image, that is, there are no overlapping events in the same frame. Thus, a limitation to the photon density needs to be set in order to avoid this phenomenon. If this particular limitation cannot be set, it will theoretically be possible to separate spatially overlapping events by increasing the frame rate: in this way

the events will be "separated" in different frames, but the frame rate should be high enough to avoid the overlapping of the afterglow decay as well.

6.3 Phosphor Screen Characterisation

During this project two phosphor screens were used, a P20 and a P47. The former being capable of single photon counting, whereas the latter (on loan from Photek) could just be used for analogue imaging. A phosphor is generally a material that exhibits luminescence: this feature is used to design materials that emit photons when hit by an accelerated electron. The most common application of phosphor screens were in old cathode ray tube (CRT) displays (such as monitors and TVs). They are normally inorganic alloys, classified with the letter "P" followed by a number to identify their composition and emission wavelength. They also vary in colour and exhibit a lifetime (afterglow) that depends on the material and on the phosphor production method.

6.3.1 P20

The P20 phosphor is composed by a mix of zinc cadmium sulfide and silver, emitting in green-yellow range (550 nm) as shown in the emission spectrum (Figure 6.6). In order to characterise the afterglow effect and to apply the proposed method for sub exposure time calculation, equation 6.1 was considered in the case of a single exponential ($i = 1$) and applied to fit the P20 phosphor decay. By using the SA1 camera at 500 kfps, a series of events timely-spread among several frames were collected, as shown in Figure 6.5-*(a)*. The greylevel values for the first frames was summed, then for the second ones and so on. By doing that, we obtained a decay plot as shown in Figure 6.7 and fit it to a single exponential so that we obtained a decay time of 6.09μs. The actual decay of the phosphor is known to have several components, and reported to have a falling time (time from 90% to 10% of the emitting light intensity) of 250μs [270], so it would be best fitted with a multi-exponential or a stretched exponential method [271; 272], but at this high frame rate the long components of the decay are not detected. In addition, for the purpose of applying the equation 6.5 and testing the model, only

a single exponential was used. This lifetime value has been used for the following calculations of the photons arrival time. The fact that the decay time is in the order of several microseconds prevented us to use the TCSPC board for measuring it, as the maximum time window allowed is 5μs. In fact, it is reported[11] that in order obtain a reliable value, a measuring time window about five times bigger than the expected lifetime is needed.

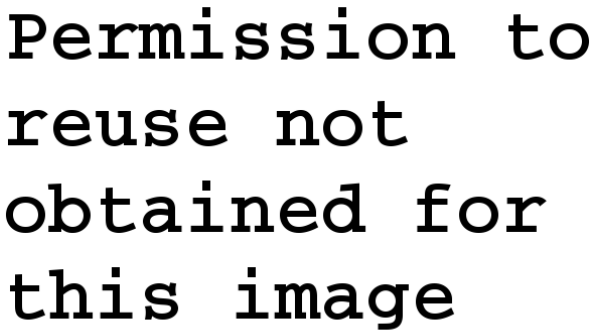

Figure 6.6: Fluorescence emission of P20 phosphor screen, the maximum intensity is at 550 nm [273].

6.3.2 P47

The P47 is an alloy of yttrium silicate and cerium, and emits in the blue range (410 nm). As our P47 is an analogue device, we could not measure the decay of single photon events as for the P20. Instead, we placed the phosphor on the confocal microscope's (Leica) stage and excited with a low power pulsed laser (Picoquant) coupled with the TCSPC board (B&H). The phosphor decay was measured for different applied currents (154 mA, 164 mA, and 181 mA) and

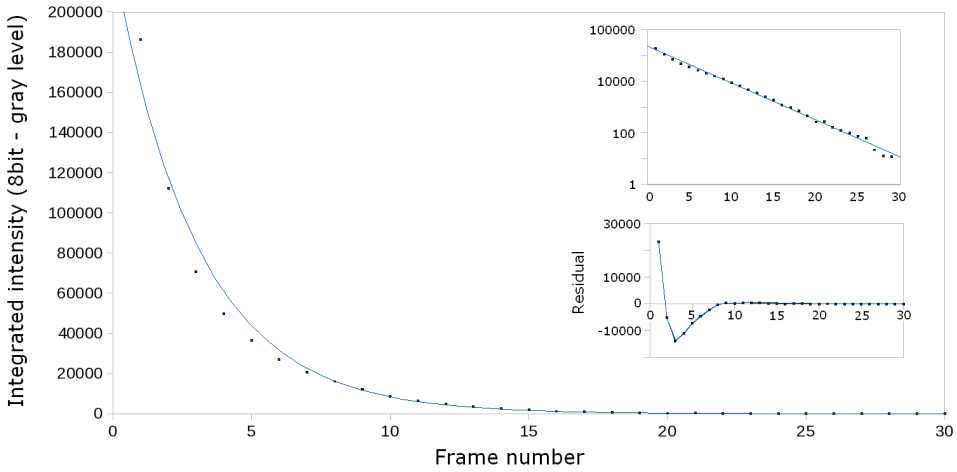

Figure 6.7: Fluorescence decay of P20 phosphor screen, obtained by integrating the decay of all collected events.

the results are shown in Figure 6.8. The normalised values show a faster decay time for higher currents. The behaviour is multi exponential and the calculated average lifetimes (2-exponential fitting) are 58.98 ns for 154 mA, 59.67 ns for 164 mA, and 59.94 for 181 mA, in agreement with the falling time of 80ns (from 90% to 10% of the maximum intensity) reported for this device [274]. Also for the P47 we report the measured emission spectrum in Figure 6.9, obtained using the Leica confocal microscope and its associated software. Due to the settings of the microscope, it was possible to obtain only the part of the spectrum above 500 nm, whereas the real emission peak is expected to be at 410 nm[274].

6.4 Results and Discussion

Here are presented the results for the different experiments. In the first part are described the achievements in increasing the temporal resolution with the proposed method. In the second section are shown the results with a Ruthenium probe and the possible applications in live-samples.

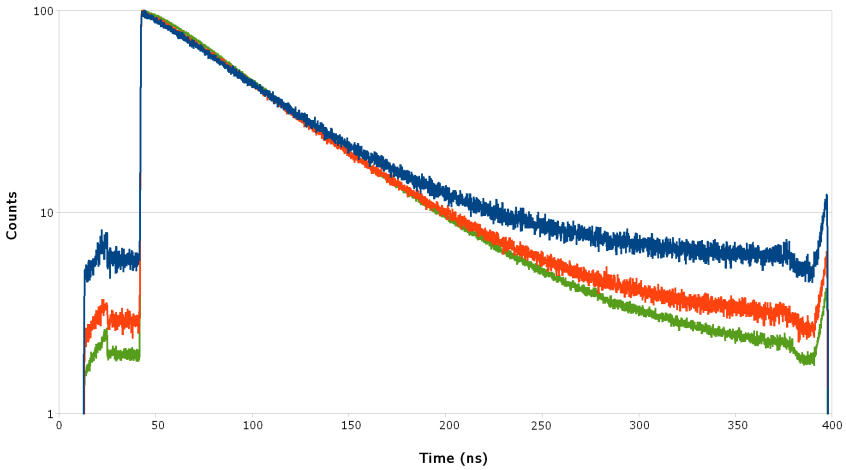

Figure 6.8: Fluorescence decay of P47 phosphor screen. Normalised to 100 for three different current values: 58.98 ns for 154 mA (green), 59.67 ns for 164 mA (orange), and 59.94 for 181 mA (blue).

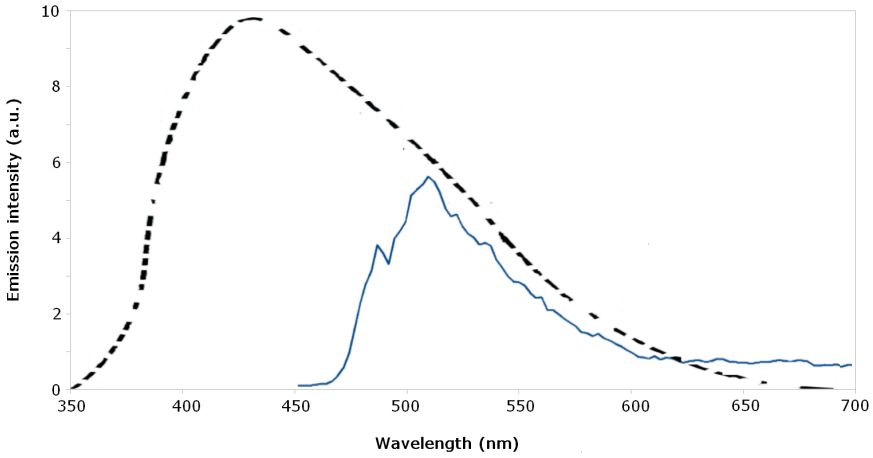

Figure 6.9: Fluorescence emission spectrum of P47 phosphor screen. The emission peak is centred at 410 nm[274] (dashed black line), but due to the limitation of the dichroic mirror, only the part of the signal above 500 nm could be imaged (blue line).

6.4.1 Preliminary Results on Sub-exposure Time Resolution

We investigated the possibility of achieving sub exposure time resolution: the rates of the camera and the laser were set so that in a 10μ exposure time frame, the laser pulsed 5 times. Each event in every frame was identified and the afterglow decay in the following frames considered, then processed to exploit this feature of the phosphor screen as described in Section 6.2.1.
In Figure 6.10 it is possible to see the result for 5 laser pulses in a 10μs window frame: the first image shows the timing for our proposed method *(a)*; the second image shows the same data processed by our collaborator with a different method[267] *(b)*. For applying the proposed method, the ratio between the first two frames was calculated and then converted into time by using eq. 6.5. The laser and the camera where running at a 500 kHz and 100 kfps respectively and were not coupled, so the ratio between the frame rates is expected to be 0.20. In Figure 6.10 it is evident how the pulses do not arrive always at the same time within the frame (due to the not coupling of the devices) and so generating a "drift" of the arrival times in the plot. By calculating the shift in the arrival

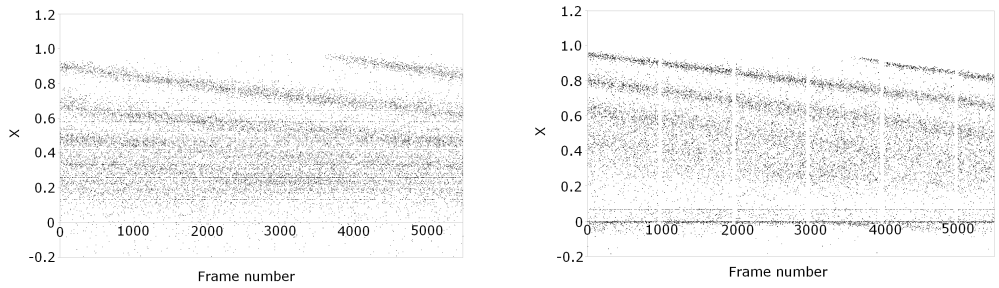

(a) (b)

Figure 6.10: Achieving sub-exposure time resolution. X axis represents the frame number and Y axis the arrival time of each event, expressed as the fraction x in respect to the exposure time T, then being xT the actual arrival time within the frame window (1 is the end of the frame and 0 the beginning of it). The deadtime is reported to be 600ns by the manufacturer [275]. (a) Dataset processed with two-frame-ratio method. (b) Dataset processed with alternative method on Matlab as described by[267].

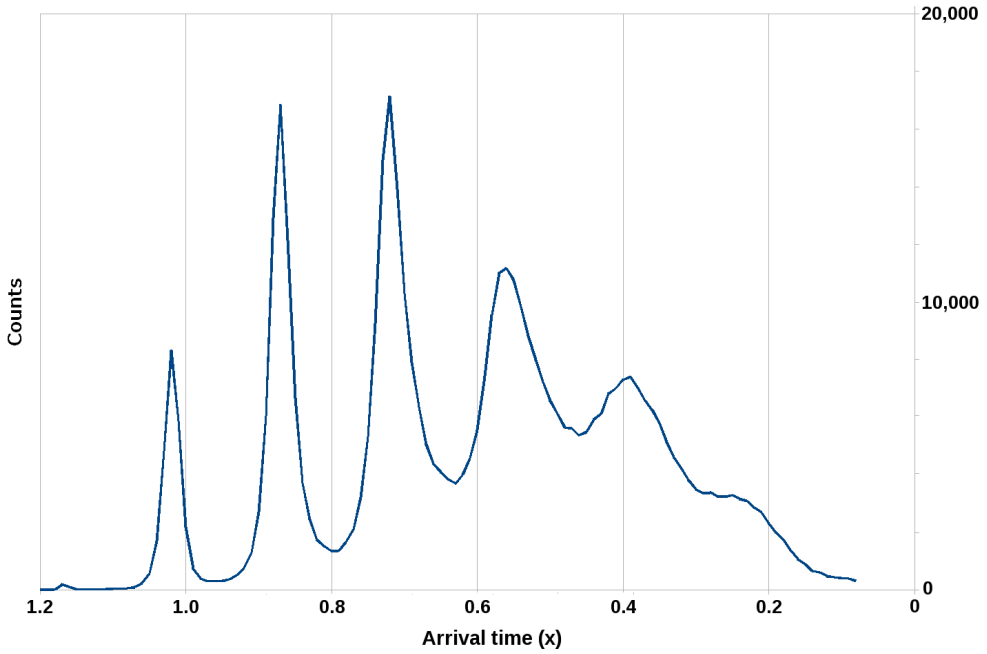

Figure 6.11: The laser pulses arrival times for the data in Fig. 6.10-(a) were drift-corrected and an histogram of counted photon was produced. The ordinates axis is the arrival time of each event, expressed as the fraction x in respect to the exposure time T, then being xT the actual arrival time within the frame window (1 is the end of the frame and 0 the beginning of it). The value of the axis goes up to 1.2 as the events above 1 represents the extra laser pulse appearing after $25,000$ frames as can be seen in the previous images.

times for the measured events, it is possible to correct the drift effect and resolve more clearly several pulses in each frame: each event's arrival time is calculated from the ratio of the intensities, corrected, and the number of events for a given time integrated as presented in Figure 6.11. This plot shows the correction applied to the data in Figure 6.10: the pulses arriving at the beginning of the frame are more difficult to resolve; the timing of the events arriving at the end of frame's exposure time is narrow and well defined. This happens because the former are close to end of the camera exposure, and the arrival time estimation is obtained via the ratio of the first two frames only: a large part of the event signal happens outside of the actual acquisition window, this leading to uncertainty in the calculated value.
The proposed method uses a single exponential fitting, this being a simple model, whereas the alternative method uses a three exponential one. From the comparison of the results, it can be seen a small "shift" in the timing of the pulses on the y axis of Figure 6.10, but both methods show the same drift in the results, as expected due to the mismatch of of the rates of the camera and the laser. Both techniques allow to resolve quite easily the first 2-3 pulses, but the closer the event to the beginning of the frame, the more uncertain the arrival calculation is, as can be seen by the larger shape of the event distributions in Figure 6.11. The decay-fitting method leads to neater separation of the laser pulses, but the two-frame-ratio method shows comparable timing with less computational efforts. These results indicates that it is possible to obtain temporal information below the exposure time of the camera using this approach.

6.4.2 Ruthenium Results

The lifetime of $[Ru(dpp)_3]^{2+}$ compound was measured using both a TCSPC board on a confocal microscope, and the FastCamera plus intensifier on an inverted microscope. The arrival time calculation for the FastCamera was performed as described in Section 6.2.1. For the TCSPC system on the confocal, the measured lifetime was 1.46μs. The measuring time window was set to 5μs, the maximum available for the acquisition board, and the laser pulse rate to 100 kHz; the acquisition time lasted several minutes in order to achieve at least 1000 counts in

the peak of the decay.
In order to exploit the P20 afterglow, the camera was set to 300 kfps and the laser repetition rate to 100 kHz, so having an exposure time of 3.3 μs. The counts of the events arriving at a given time within each frame have been integrated (within intervals of 0.1 μs) in order to build the decay, then a single exponential fitting was used to obtain the lifetime. The calculated phosphorescence lifetime with the ratio-to-time method was 1.65±0.09 μs, close to the result obtained with the TCSPC system. A plot of the decay fittings for SPC830 board (a), and a comparison of the calculated arrival times (green) with the measured decay (blue) (b) are shown in Figure 6.12. In the same figure-(c), the graph shows the relationship between the 2-frame-ratio and the arrival time obtained by applying eq. 6.5. The photons arriving during the first frame are timed in respect to the ratio with the second frame; the photons in the second frame in respect to the third and so on.

6.4.3 PLIM: Wide-field and Scanning Techniques Comparison

The previous results demonstrated the possibility to use the FastCamera coupled with the P20 intensifier to achieve sub-exposure time resolution and to calculate the luminescence (i.e. phosphorescence) decay. In this section are presented the PLIM results of Ruthenium for various viscosity: four solutions of $[Ru(dpp)_3]^{2+}$ in ethanol and different volume fractions of glycerol (5, 20, 50, 60 %) were placed in different wells of a glass-bottom multiwell plate (Whatman) and imaged. The resulting PLIM image is shown in Fig. 6.14-(a), and the total acquisition time required to create it was about 4 hours. It is possible to see that lifetime varies according to the viscosity: 1.524 μs for 5% glycerol, 1.716 μs for 20%, 2.399 μs for 50%, and 2.786 μs for 60%. The particular disposition of the wells reduce the effective speed of the scanning, as also "dark" areas need to be scanned in order to generate the lifetime images, and this should be taken into account. The camera, on the other hand, allows to collect ∼700,000 frames (for the used 8GB model) at 300 kfps, with a limited 128×64 size, in less than 3 seconds: even considering the reduced size of the image and the limitation on the number of

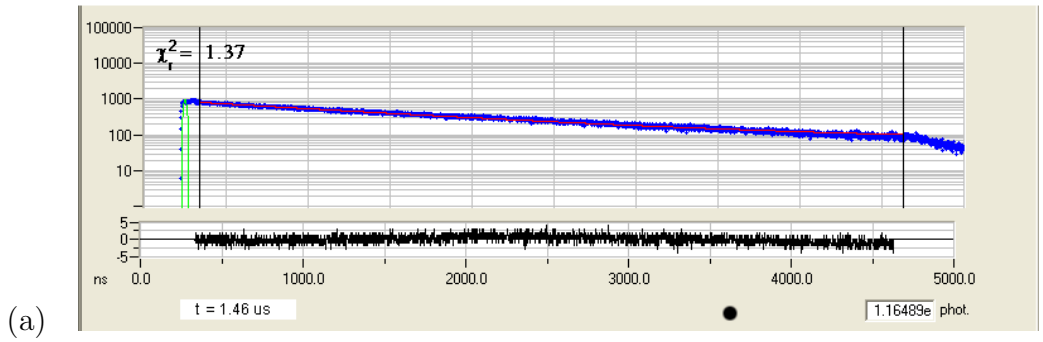

(a)

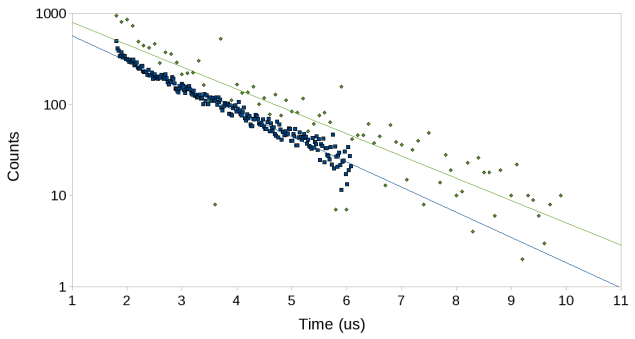

(b)

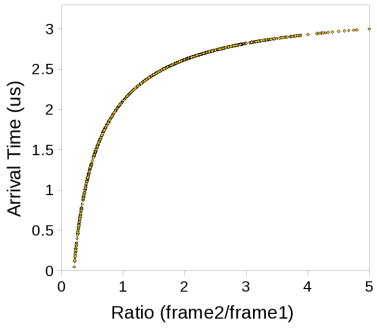

(c)

Figure 6.12: Ruthenium lifetime. x axis is the time and y axis represents the counts of the events. *(a)* TCSPC measured value for $[Ru(dpp)_3]^{2+}$ on a confocal microscope. The calculated lifetime is 1.46 μs. *(b)* A comparison of the phosphorescence decay with two-frame-ratio calculation (green) and TCSPC on confocal (blue). The peaks have been aligned and the decays normalised to 1000 and 500 respectively. The calculated lifetime for the two-frame-ratio is 1.65$\pm$0.09 μs. *(c)* A graph of the relationship between calculated frame ratio and photon arrival time. These results confirm the possibility to use this novel approach to measure the lifetime, as an alternative to standard scanning techniques.

photons simultaneously detected (to prevent overlapping), the technique allows to collect tens of photons per pulse. By comparing it with the few photons per pulse collected with the TCSPC, this approach presents a great advantage when live samples are involved as it reduces both the acquisition time and the amount of light the sample has to suffer.
The use of transient metal complexes as microenvironment probes (for example as oxygen sensors) it is known[6], and recent results with Ruthenium-based dye ($[Ru(bipy)_3]^{2+}$ complex) have been reported[139]. To investigate its possible applications, the proposed Ruthenium complex ($[Ru(dpp)_3]^{2+}$) was used to stain HeLa cells as shown in Figure 6.14-*(a, b)*. The images, obtained with the experimental setup presented in Section 3.2 for cell imaging, confirm the uptake of the dye to the cell. The long acquisition time, required by Ruthenium on a scanning system, prevented to obtain a FLIM image for the living samples. The results with similar metal complexes[139] and the confirmed uptake suggest the possibility to use this dye and exploit the proposed technique for living cells measurements.

6.5 Chapter Summary

The experiments proved the possibility to exploit phosphor decay time to achieve temporal resolution below the frame exposure time. The application of this technique to ruthenium solutions showed close results to the ones achieved with TCSPC standards, confirming the reliability of the method, albeit with a single exponential fitting of the phosphor screen. The possibility to use $[Ru(dpp)_3]^{2+}$ complex to stain live cells needs further investigation and the use of counterstaining techniques can show the exact localisation of the compound within the cell. The theoretical comparison of a scanning TCSPC system on confocal with the FastCAM and intensifier approach demonstrated the great advantages of this technique, especially on living samples: shorter time of analysis reduces the amount of phototoxicity the cells have to suffer, improving the quality of the results. Albeit wide-field microscopy achieves a lower spatial resolution than confocal microscopy due to the out-of-focus fluorescence, techniques where the

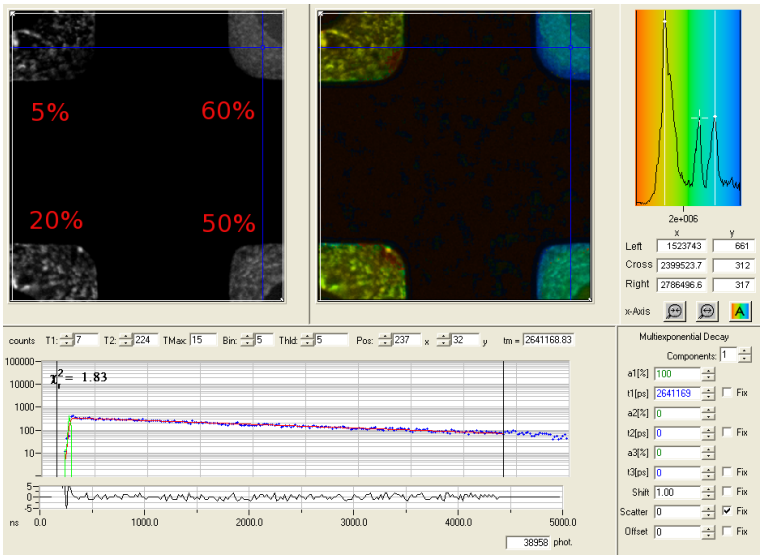

(a)

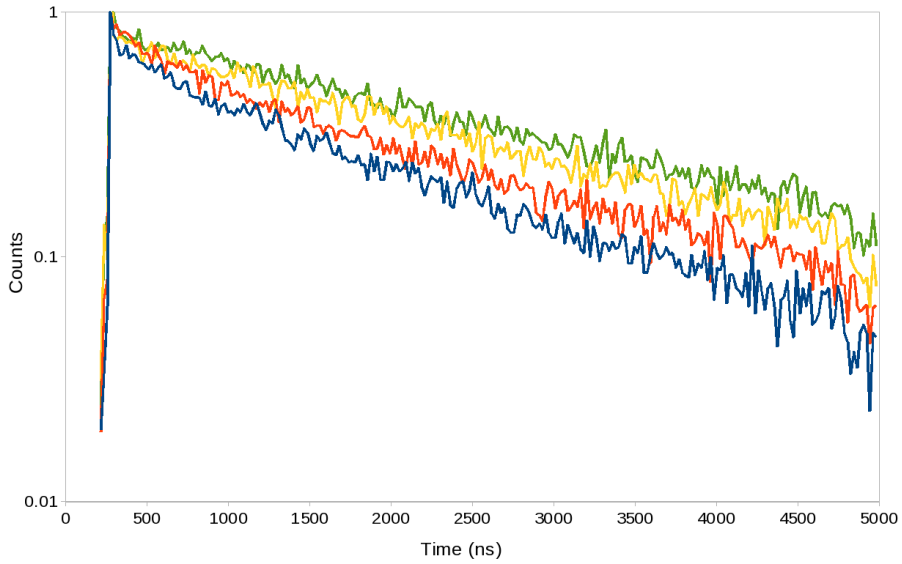

(b)

Figure 6.13: $[Ru(dpp)_3]^{2+}$ solutions in 4 wells. *(a)*: PLIM image for mixtures of 5, 20, 50 and 60 % volume fraction of glycerol and ethanol. *(a)*: Normalised luminescence decay for mixtures of 5 (blue), 20 (red), 50 (green), and 60% (yellow) volume fraction of glycerol and ethanol.

(a)

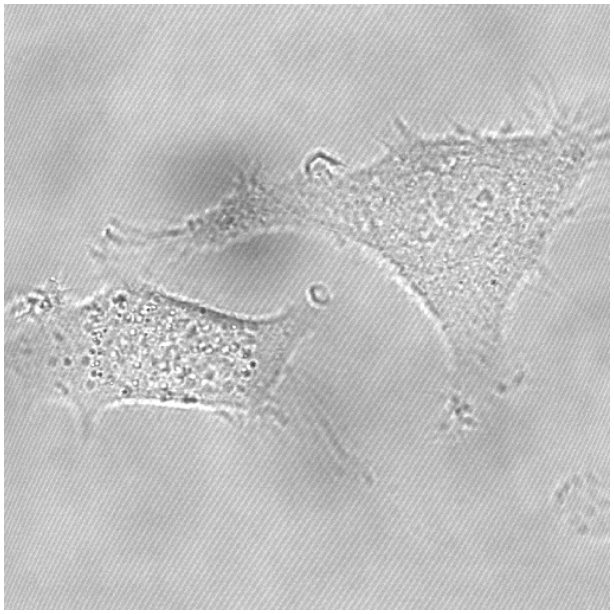

(b)

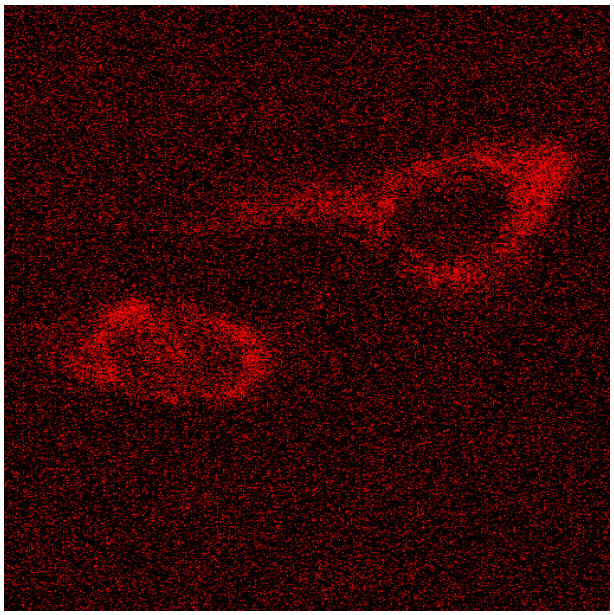

Figure 6.14: Ruthenium in HeLa cells: *(a)* transmitted light image and *(b)* PMT image in 590nm - 620nm wavelength range, at 37°C.

scanning cannot be applied or is difficult to implement can benefit from the proposed wide-field imaging system: techniques such as lightsheet microscopy, TIRF, and supercritical angle fluorescence (SAF) may take advantage of this approach.

Chapter 7

Conclusions and Future Work

7.1 Molecular Rotors

The fluorescence lifetime measurements on BODIPY-C_{12} molecular rotor confirmed the reported values for the intracellular viscosity of HeLa cells. The main advantages of using molecular rotors rather than anisotropy for viscosity mapping are the lower number of counts needed for a correct measurement, the simpler equipment, and the possibility to obtain dynamic measurements (e.g. movie). In addition to the possibility to map the viscosity of whole cell, rather than in a small region (like in FRAP or FCS), also a concentration mapping within the cell was performed. The measured values are promising and suggest a homogeneous concentration of the dye in the endoplasmic reticulum, albeit quite low, and a higher concentration in the lipid droplets in the range of micromolar. This is the first quantitative result on a reported[95] qualitative effect for the concentration of dye in lipid droplets. These measured values have also been found to vary slightly with the temperatures.
Further investigations in order to confirm the value of the concentration in cells and puncta are needed, but the obtained results are promising: it may be possible to observe over time variations in the measured concentration and obtain dynamic information on lipid droplets.

The use of ET compound as a molecular rotor led to unclear results. This complex behaves only partially in agreement with the Förster-Hoffmann theory and two

different extinction coefficients were obtained from lifetime and intensity based measurements. Nevertheless, the measured viscosity is close to the reported values for endoplasmic reticulum in HeLa cells, indicating a possible localisation of the dye. The polarisation resolved measurements, led to a low value for the initial anisotropy, thus reducing the dynamic range of this approach. The uncertainty in the results indicates that further investigation and verification are needed.

7.2 Electron-Bombarded CCD and Centroiding

Although it was not possible, due to hardware limitations, to implement the proposed technique on the EBCCD used, the experiments proved a linear dependence of an EBCCD pulse height distribution on the applied gain voltage. These results and simulated data[1] confirm the possibility to exploit this feature to design a parallel-processing photoelectronic time-to-amplitude converter. In addition, also the peak height distribution was found to increase proportionally to the applied voltage.
Recently designed electron-bombarded detectors achieving faster frame rates[210] are promising candidate for the implementation of this approach.
For some microscopy techniques, scanning cannot be applied or is difficult to implement: techniques such as lightsheet microscopy, TIRF, and supercritical angle fluorescence (SAF) in particular may benefit from this wide-field development.

The comparison of our code with PALM/STORM software showed that it is possible to use single-molecule localisation programmes to process single photon counting data. In addition, our code was capable to process a STORM dataset, albeit with some unwanted effect in the results. The EBCCD characterisation showed a "shift" in the centroiding plots along the x direction, possibly associated with the charge transfer during the readout. This effect generated high fixed pattern noise for all the reconstructed images. The results with RapidSTORM software though, were not affected by this "shift": this suggests the possibility to use its centroiding algorithm to overcome this issue.

7.3 FastCamera

A wide-field TCSPC imaging system exploiting the phosphor afterglow on an image intensifier achieved to measure the phosphorescence decay of a Ruthenium based sample. The fitting of the decay led to results comparable with confocal scanning TCSPC, in the range of microseconds. The theoretical comparison of a scanning system with the proposed wide-field design for long lifetime probes demonstrates the advantages of this technique on living samples measurements: the shorter time required reduces the amount of phototoxicity the cells have to suffer, and the ability to time tens of photons per excitation cycle fully exploit the available photon budget.
The uptake of Ru(dpp) complex in HeLa cells confirms the possibility to use this sensor on living specimens, and previous results[139] suggest its application to map the oxygen pressure on biological samples.

Although wide-field microscopy achieves a lower spatial resolution than confocal microscopy, the previously mentioned techniques (see Sec. 7.2) where scanning is difficult may take advantage of this approach. In addition to these techniques, also time resolved anisotropy may benefit of this method to identify interactions of large proteins, normally taking place in the microsecond region.

7.4 Future Work - Centroiding

The correct application of centroiding algorithms is fundamental in both single-molecule localisation techniques and the described imaging systems, where the charge diffuses among several pixels (EBCCD) or the electron multiplication generates an electronic cloud (Intensifier). It is then interesting to better understand why the centroiding routine applied by RapidSTORM provides better results also on SPC data. For this software, after a bright spot (local maximum) is found in the image, the candidate is fitted with a two-dimentional Gaussian function[234].

The function is expressed as:

$$\exp -\frac{1}{2}\overrightarrow{X}^T \mathbf{V}^{-1} \overrightarrow{X} \tag{7.1}$$

where $\overrightarrow{X}$ is the point on which the fitting is applied and $\mathbf{V}$ is a covariance matrix that defines the Gaussian function parameters. This matrix is iteratively adjusted to find the best fit for the analysed spot, that can then be accepted or rejected in respect to the fitting results. The covariance matrix $\mathbf{V}$ can be expressed as:

$$\begin{pmatrix} \sigma_x^2 & \rho\sigma_x\sigma_y \\ \rho\sigma_x\sigma_y & \sigma_y^2 \end{pmatrix} \tag{7.2}$$

where σ_x and σ_y are the standard deviations in x and y directions, and ρ the correlation between x and y axes.
Previously to this fitting process, the identification of the local maxima is performed with a non-maximum suppression (NMS) algorithm.
Either the fitting or the spot identification process are a possible reason for the better results of RapidSTORM. Thus, an improvement in our processing code may be to implement the relevant part of this routine, or a variant of it, to reduce FPN and achieve sub-pixel resolution in SPC data processing.

Bibliography

[1] LM Hirvonen, S Jiggins, N Sergent, G Zanda, and K Suhling. Photon counting imaging with an electron-bombarded ccd: Towards a parallel-processing photoelectronic time-to-amplitude converter. *REVIEW OF SCIENTIFIC INSTRUMENTS*, **85**[12]:–, 2014. 19, 152, 153, 174, 198

[2] Masters, BR. Abbe Theory of Image Formation. In *Confocal Microscopy and Multiphoton Excitation Microscopy: The Genesis of Live Cell Imaging*, SPIE. Springer, 2006. 25, 47, 51

[3] WE Moerner and L Kador. Optical-detection and spectroscopy of single molecules in a solid. *PHYSICAL REVIEW LETTERS*, **62**[21]:2535–2538, MAY 22 1989. 31, 53

[4] E Betzig, GH Patterson, R Sougrat, OW Lindwasser, S Olenych, JS Bonifacino, MW Davidson, J Lippincott-Schwartz, and HF Hess. Imaging intracellular fluorescent proteins at nanometer resolution. *SCIENCE*, **313**[5793]:1642–1645, SEP 15 2006. 31, 53

[5] TA Klar, S Jakobs, M Dyba, A Egner, and SW Hell. Fluorescence microscopy with diffraction resolution barrier broken by stimulated emission. *PROCEEDINGS OF THE NATIONAL ACADEMY OF SCIENCES OF THE UNITED STATES OF AMERICA*, **97**[15]:8206–8210, JUL 18 2000. 31, 53

[6] JR Lakowicz. *Principles of fluorescence spectroscopy*. Springer Science, New York, 2006. 31, 35, 38, 41, 42, 44, 45, 46, 47, 108, 193

[7] E Gratton, S Breusegem, J Sutin, and QQ Ruan. Fluorescence lifetime imaging for the two-photon microscope: time-domain and frequency-domain methods. *JOURNAL OF BIOMEDICAL OPTICS*, **8**[3]:381–390, JUL 2003. 31, 32

[8] A Esposito, HC Gerritsen, and FS Wouters. Optimizing frequency-domain fluorescence lifetime sensing for high-throughput applications: photon economy and acquisition speed. *JOURNAL OF THE OPTICAL SOCIETY OF AMERICA A-OPTICS IMAGE SCIENCE AND VISION*, **24**[10]:3261–3273, OCT 2007. 31

[9] J Philip and K Carlsson. Theoretical investigation of the signal-to-noise ratio in fluorescence lifetime imaging. *JOURNAL OF THE OPTICAL SOCIETY OF AMERICA A-OPTICS IMAGE SCIENCE AND VISION*, **20**[2]:368–379, FEB 2003. 31

[10] Q Zhao, IT Young, and JGS de Jong. Photon budget analysis for fluorescence lifetime imaging microscopy. *JOURNAL OF BIOMEDICAL OPTICS*, **16**[8], AUG 2011. 31

[11] K Suhling, PMW French, and D Phillips. Time-resolved fluorescence microscopy. *PHOTOCHEM. PHOTOBIOL. SCI.*, **4**:13–22, 2005. 32, 44, 149, 185

[12] JW Lichtman and JA Conchello. Fluorescence microscopy. *NATURE METHODS*, **2**[12]:910–919, DEC 2005. 32, 40, 41

[13] X Michalet, RA Colyer, G Scalia, A Ingargiola, R Lin, JE Millaud, S Weiss, OHW Siegmund, AS Tremsin, JV Vallerga, A Cheng, M Levi, D Aharoni, K Arisaka, F Villa, F Guerrieri, F Panzeri, I Rech, A Gulinatti, F Zappa, M Ghioni, and S Cova. Development of new photon-counting detectors for single-molecule fluorescence microscopy. *PHILOSOPHICAL TRANSACTIONS OF THE ROYAL SOCIETY B-BIOLOGICAL SCIENCES*, **368**[1611, SI], FEB 5 2013. 33, 64, 65, 66, 71, 79, 147, 157, 175, 176

[14] DG Spiller, CD Wood, DA Rand, and MRH White. Measurement of single-cell dynamics. *Nature*, **465**[7299]:736–745, 2010. 33, 177

[15] A Fontes, ML Barjas Castro, MM Brandao, HP Fernandes, AA Thomaz, RR Huruta, LY Pozzo, LC Barbosa, FF Costa, STO Saad, and CL Cesar. Mechanical and electrical properties of red blood cells using optical tweezers. *JOURNAL OF OPTICS*, **13**[4, SI], APR 2011. 33, 34, 60

[16] M Shinitzky. Membrane fluidity in malignancy. Adversative and recuperative. *BIOCHIMICA ET BIOPHYSICA ACTA*, **738**[4]:251–261, FEB 1984. 34, 60

[17] SJ SINGER and GL NICOLSON. FLUID MOSAIC MODEL OF STRUCTURE OF CELL-MEMBRANES. *SCIENCE*, **175**[4023]:720–&, 1972. 34

[18] G DELICONSTANTINOS, V VILLIOTOU, and JC STAVRIDES. MODULATION OF PARTICULATE NITRIC-OXIDE SYNTHASE ACTIVITY AND PEROXYNITRITE SYNTHESIS IN CHOLESTEROL-ENRICHED ENDOTHELIAL-CELL MEMBRANES. *BIOCHEMICAL PHARMACOLOGY*, **49**[11]:1589–1600, MAY 26 1995. 34

[19] GS Zubenko, U Kopp, T Seto, and LL Firestone. Platelet membrane fluidity individuals at risk for Alzheimer's disease: a comparison of results from fluorescence spectroscopy and electron spin resonance spectroscopy. *PSYCHOPHARMACOLOGY*, **145**[2]:175–180, JUL 1999. 34

[20] O NADIV, M SHINITZKY, H MANU, D HECHT, CT ROBERTS, D LEROITH, and Y ZICK. ELEVATED PROTEIN-TYROSINE-PHOSPHATASE ACTIVITY AND INCREASED MEMBRANE VISCOSITY ARE ASSOCIATED WITH IMPAIRED ACTIVATION OF THE INSULIN-RECEPTOR KINASE IN OLD RATS. *BIOCHEMICAL JOURNAL*, **298**[2]:443–450, MAR 1 1994. 34

[21] W Osterode, C Holler, and F Ulberth. Nutritional antioxidants, red cell membrane fluidity and blood viscosity in Type 1 (insulin dependent)

diabetes mellitus. *DIABETIC MEDICINE*, **13**[12]:1044–1050, DEC 1996. 34

[22] MM GLEASON, MS MEDOW, AND TN TULENKO. EXCESS MEMBRANE CHOLESTEROL ALTERS CALCIUM MOVEMENTS, CYTOSOLIC CALCIUM LEVELS, AND MEMBRANE FLUIDITY IN ARTERIAL SMOOTH-MUSCLE CELLS. *CIRCULATION RESEARCH*, **69**[1]:216–227, JUL 1991. 34

[23] J KORLACH, P SCHWILLE, WW WEBB, AND GW FEIGENSON. Characterization of lipid bilayer phases by confocal microscopy and fluorescence correlation spectroscopy (vol 96, pg 8461, 1999). *PROCEEDINGS OF THE NATIONAL ACADEMY OF SCIENCES OF THE UNITED STATES OF AMERICA*, **96**[17]:9966, AUG 17 1999. 34

[24] NL THOMPSON, AM LIETO, AND NW ALLEN. Recent advances in fluorescence correlation spectroscopy. *CURRENT OPINION IN STRUCTURAL BIOLOGY*, **12**[5]:634–641, OCT 2002. 34

[25] PETER KAPUSTA, MICHAEL WAHL, ALES BENDA, MARTIN HOF, AND JORG ENDERLEIN. Fluorescence lifetime correlation spectroscopy. *JOURNAL OF FLUORESCENCE*, **17**[1]:43–48, JAN 2007. 34

[26] MJ DAYEL, EFY HOM, AND AS VERKMAN. Diffusion of green fluorescent protein in the aqueous-phase lumen of endoplasmic reticulum. *BIOPHYSICAL JOURNAL*, **76**[5]:2843–2851, MAY 1999. 34

[27] J SIEGEL, K SUHLING, S LEVEQUE-FORT, SED WEBB, DM DAVIS, D PHILLIPS, Y SABHARWAL, AND PMW FRENCH. Wide-field time-resolved fluorescence anisotropy imaging (TR-FAIM): Imaging the rotational mobility of a fluorophore. *REVIEW OF SCIENTIFIC INSTRUMENTS*, **74**[1, 1]:182–192, JAN 2003. 34, 45

[28] K FUSHIMI AND AS VERKMAN. Low viscosity in the aqueous domain of cell cytoplasm measured by picosecond polarization microfluorimetry. *JOURNAL OF CELL BIOLOGY*, **112**[4]:719–725, FEB 1991. 34, 61

[29] JA DIX AND AS VERKMAN. MAPPING OF FLUORESCENCE ANISOTROPY IN LIVING CELLS BY RATIO IMAGING - APPLICATION TO CYTOPLASMIC VISCOSITY. *BIOPHYSICAL JOURNAL*, **57**[2]:231–240, FEB 1990. 34

[30] R IINO AND A KUSUMI. Single-fluorophore dynamic imaging in living cells. *JOURNAL OF FLUORESCENCE*, **11**[3]:187–195, SEP 2001. 34

[31] THOMAS BREITENBACH, MARINA K. KUIMOVA, PETER GBUR, SONJA HATZ, NICKOLASS BITSCH SCHACK, BRIAN WETT PEDERSEN, JOHN D. C. LAMBERT, LARS POULSEN, AND PETER R. OGILBY. Photosensitized production of singlet oxygen: spatially-resolved optical studies in single cells. *PHOTOCHEMICAL & PHOTOBIOLOGICAL SCIENCES*, **8**[4]:442–452, 2009. 34

[32] ELSA F. F. DA SILVA, BRIAN W. PEDERSEN, THOMAS BREITENBACH, RASMUS TOFTEGAARD, MARINA K. KUIMOVA, LUIS G. ARNAUT, AND PETER R. OGILBY. Irradiation- and Sensitizer-Dependent Changes in the Lifetime of Intracellular Singlet Oxygen Produced in a Photosensitized Process. *JOURNAL OF PHYSICAL CHEMISTRY B*, **116**[1]:445–461, JAN 12 2012. 34

[33] MARINA K. KUIMOVA, GOKHAN YAHIOGLU, AND PETER R. OGILBY. Singlet Oxygen in a Cell: Spatially Dependent Lifetimes and Quenching Rate Constants. *JOURNAL OF THE AMERICAN CHEMICAL SOCIETY*, **131**[1]:332–340, JAN 14 2009. 34

[34] CT LIM, M DAO, S SURESH, CH SOW, AND KT CHEW. Large deformation of living cells using laser traps. *ACTA MATERIALIA*, **52**[7]:1837–1845, APR 2004. 34, 60

[35] GG STOKES. On the change of refrangibility of light. *PHILOSOPHICAL TRANSACTIONS OF THE ROYAL SOCIETY OF LONDON*, **142**:463–562, 1852. 35

[36] A JABLONSKI. Efficiency of anti-stokes fluorescence in dyes. *NATURE*, **131**:839–840, JAN-JUN 1933. 35

[37] N Boens, W Qin, N Basaric, J Hofkens, M Ameloot, J Pouget, JP Lefevre, B Valeur, E Gratton, M Van De Ven, J Silva, D Norberto, Y Engelborghs, K Willaert, A Sillen, G Rumbles, D Phillips, AJWG Visser, A van Hoek, JR Lakowicz, H Malak, I Gryczynski, AG Szabo, DT Krajcarski, N Tamai, and A Miura. Fluorescence lifetime standards for time and frequency domain fluorescence spectroscopy. *ANALYTICAL CHEMISTRY*, **79**[5]:2137–2149, MAR 1 2007. 35

[38] RF Chen. Fluorescence lifetime reference standards for range 0.189 to 115 nanoseconds. *ANALYTICAL BIOCHEMISTRY*, **57**[2]:593–604, 1974. 35

[39] RF Chen, GG Vurek, and N Alexande. Fluorescence decay times - Proteins coenzymes and other compounds in water. *SCIENCE*, **156**[3777]:949–&, 1967. 35

[40] DJS Birch. Fluorescence detections and directions. *MEASUREMENT SCIENCE & TECHNOLOGY*, **22**[5], MAY 2011. 36

[41] B Valeur. *Molecular Fluorescence*. Wiley-VCH, Weinheim, 2003. 39, 42, 57

[42] Mikhail Y. Berezin and Samuel Achilefu. Fluorescence Lifetime Measurements and Biological Imaging. *CHEMICAL REVIEWS*, **110**[5]:2641–2684, MAY 2010. 40, 41, 62, 63, 64, 177

[43] Becker, W. *The bh TCPSC Handbook*. Becker & Hickl GmbH, Berlin, Germany, 2005. 42, 75, 76

[44] P Wahl. Analysis of fluorescence anisotropy decays by a least-square method. *BIOPHYSICAL CHEMISTRY*, **10**[1]:91–104, 1979. 42

[45] EL Rachofsky, B Wolf, CN Bialik, JBA Ross, and WR Laws. A general method for constrained analysis of fluorescence anisotropy decay: Application of the steady-state anisotropy. *JOURNAL OF FLUORESCENCE*, **9**[4]:379–390, DEC 1999. 42

[46] K.A. Lidke, B. Rieger, D.S. Lidke, and T.M. Jovin. The role of photon statistics in fluorescence anisotropy imaging. *Image Processing, IEEE Transactions on*, **14**[9]:1237–1245, Sept 2005. 43, 44

[47] I Gryczynski, H Malak, and JR Lakowicz. 3-photon induced fluorescence of 2,5-diphenyloxazole with a femtosecond ti-sapphire laser. *CHEMICAL PHYSICS LETTERS*, **245**[1]:30–35, 1995. 45

[48] D Axelrod. Carbocyanine dye orientation in red-cell membrane studied by microscopic fluorescence polarization. *BIOPHYSICAL JOURNAL*, **26**[3]:557–573, 1979. 45

[49] D Axelrod. Fluorescence polarization microscopy. *METHODS IN CELL BIOLOGY*, **30**:333–352, 1989. 45

[50] T Ha, TA Laurence, DS Chemla, and S Weiss. Polarization spectroscopy of single fluorescent molecules. *JOURNAL OF PHYSICAL CHEMISTRY B*, **103**[33]:6839–6850, AUG 19 1999. 45

[51] K Bahlmann and SW Hell. Depolarization by high aperture focusing. *APPLIED PHYSICS LETTERS*, **77**[5]:612–614, JUL 31 2000. 45

[52] JJ Fisz. Fluorescence polarization spectroscopy at combined high-aperture excitation and detection: application to one-photon-excitation fluorescence microscopy. *JOURNAL OF PHYSICAL CHEMISTRY A*, **111**[35]:8606–8621, SEP 6 2007. 45

[53] JJ Fisz. Another Treatment of Fluorescence Polarization Microspectroscopy and Imaging. *JOURNAL OF PHYSICAL CHEMISTRY A*, **113**[15]:3505–3516, APR 16 2009. 45

[54] DJS Birch. Multiphoton excited fluorescence spectroscopy of biomolecular systems. *SPECTROCHIMICA ACTA PART A-MOLECULAR AND BIOMOLECULAR SPECTROSCOPY*, **57**[11]:2313–2336, SEP 14 2001. 45

[55] Rosenthal, CK. *Invention of the microscope*. Milestone. 2009. 47

[56] R Hooke. *Micrographia: or some physiological descriptions of minute bodies made by magnifying glasses with observations and inquiries thereupon.* Martin and Allestry, London, England, 1664. 47

[57] E Abbe. Beitriege zur Theorie des Mikroskops und der mikroskopischen Wahrnehmung. *ARCHIV FÜR MIKROSKOPISCHE ANATOMIE*, **9**[1]:413–418, 1873. 47

[58] Nikon website, `http://www.microscopyu.com/articles/`; Last visited, Aug 2014. 48, 49

[59] F Helmchen and W Denk. Deep tissue two-photon microscopy. *NATURE METHODS*, **2**[12]:932–940, 2005. 50

[60] Winfried Denk, James H. Strickler, and Watt W. Webb. Two-photon laser scanning fluorescence microscopy. *Science*, **248**[4951]:pp. 73–76, 1990. 50

[61] Inoue, S. *Foundations of confocal scanned imaging in light microscopy.* HANDBOOK OF BIOLOGICAL CONFOCAL MICROSCOPY. Springer, New York, USA, 2006. 50, 55

[62] PJ Shaw. Comparison of widefield/deconvolution and confocal microscopy for three-dimensional imaging. In JB Pawley, editor, *Handbook of Biological Confocal Microscopy*. Springer Verlag, New York, 2006. 51

[63] SW Hell. Toward fluorescence nanoscopy. *NATURE BIOTECHNOLOGY*, **21**[11]:1347–1355, NOV 2003. 53, 54

[64] J Lippincott-Schwartz and GH Patterson. Photoactivatable fluorescent proteins for diffraction-limited and super-resolution imaging. *TRENDS IN CELL BIOLOGY*, **19**[11]:555–565, NOV 2009. 53, 56

[65] GH Patterson. Fluorescence microscopy below the diffraction limit. *SEMINARS IN CELL & DEVELOPMENTAL BIOLOGY*, **20**[8]:886–893, OCT 2009. 53, 55

[66] Huang, B and Bates, M and Zhuang, X. Super-Resolution Fluorescence Microscopy. *ANNUAL REVIEW OF BIOCHEMISTRY*, **78**:993–1016, 2009. 53, 55

[67] MJ Rust, M Bates, and X Zhuang. Sub-diffraction-limit imaging by stochastic optical reconstruction microscopy (STORM). *NATURE METHODS*, **3**[10]:793–795, OCT 2006. 53

[68] ST Hess, TPK Girirajan, and MD Mason. Ultra-high resolution imaging by fluorescence photoactivation localization microscopy. *BIOPHYSICAL JOURNAL*, **91**[11]:4258–4272, DEC 2006. 53

[69] V Westphal and SW Hell. Nanoscale resolution in the focal plane of an optical microscope. *PHYSICAL REVIEW LETTERS*, **94**[14], APR 15 2005. 53, 55, 56

[70] E Rittweger, KY Han, SE Irvine, C Eggeling, and SW Hell. STED microscopy reveals crystal colour centres with nanometric resolution. *NATURE PHOTONICS*, **3**[3]:144–147, MAR 2009. 53

[71] MGL Gustafsson. Surpassing the lateral resolution limit by a factor of two using structured illumination microscopy. *JOURNAL OF MICROSCOPY-OXFORD*, **198**[2]:82–87, MAY 2000. 54, 56

[72] MAA Neil, R Juskaitis, and T Wilson. Method Of Obtaining Optical Sectioning By Using Structured Light In A Conventional Microscope. *OPTICS LETTERS*, **22**[24]:1905–1907, DEC 15 1997. 54

[73] B Bailey, DL Farkas, DL Taylor, and F Lanni. Enhancement of axial resolution in fluorescence microscopy by standing-wave excitation. *NATURE*, **366**[6450]:44–48, NOV 4 1993. 54, 56

[74] PA TEMPLE. Total Internal-Reflection Microscopy - A Surface Inspection Technique. *APPLIED OPTICS*, **20**[15]:2656–2664, 1981. 54

[75] MGL Gustafsson, L Shao, PM Carlton, CJR Wang, IN Golubovskaya, WZ Cande, DA Agard, and JW Sedat. Three-dimensional resolution doubling in wide-field fluorescence microscopy by

structured illumination. *BIOPHYSICAL JOURNAL*, **94**[12]:4957–4970, JUN 15 2008. 54, 56

[76] A Stemmer, M Beck, and R Fiolka. Widefield fluorescence microscopy with extended resolution. *HISTOCHEMISTRY AND CELL BIOLOGY*, **130**[5]:807–817, NOV 2008. 54

[77] Gustafsson, MGL. Nonlinear structured-illumination microscopy: Wide-field fluorescence imaging with theoretically unlimited resolution. *PROCEEDINGS OF THE NATIONAL ACADEMY OF SCIENCES OF THE UNITED STATES OF AMERICA*, **102**[37]:13081–13086, SEP 13 2005. 54

[78] B Bailey, DL Farkas, DL Taylor, and F Lanni. Enhancement of axial resolution in fluorescence microscopy by standing-wave excitation. *NATURE*, **366**[6450]:44–48, NOV 4 1993. 54

[79] F Lanni and B Bailey. Standing-wave excitation for fluorescence microscopy. *TRENDS IN CELL BIOLOGY*, **4**:262–265, 1994. 54

[80] SK Pierce and W Liu. The tipping points in the initiation of B cell signalling: how small changes make big differences. *NATURE REVIEWS IMMUNOLOGY*, **10**[11]:767–777, NOV 2010. 54

[81] L Schermelleh, R Heintzmann, and H Leonhardt. A guide to super-resolution fluorescence microscopy. *JOURNAL OF CELL BIOLOGY*, **190**[2]:165–175, JUL 26 2010. 54, 55

[82] SA Jones, SH Shim, J He, and X Zhuang. Fast, three-dimensional super-resolution imaging of live cells. *NATURE METHODS*, **8**[6]:499–U96, JUN 2011. 55

[83] L Schermelleh, PM Carlton, S Haase, L Shao, L Winoto, P Kner, B Burke, MC Cardoso, DA Agard, MGL Gustafsson, H Leonhardt, and JW Sedat. Subdiffraction multicolor imaging of the nuclear periphery with 3D structured illumination microscopy. *SCIENCE*, **320**[5881]:1332–1336, JUN 6 2008. 55, 56

[84] WE Moerner and L Kador. Optical-detection and spectroscopy of single molecules in a solid. *PHYSICAL REVIEW LETTERS*, **62**[21]:2535–2538, MAY 22 1989. 54

[85] E Betzig and RJ Chichester. Single molecules observed by near-field scanning optical microscopy. *SCIENCE*, **262**[5138]:1422–1425, NOV 26 1993. 54

[86] RE Thompson, DR Larson, and WW Webb. Precise nanometer localization analysis for individual fluorescent probes. *BIOPHYSICAL JOURNAL*, **82**[5]:2775–2783, MAY 2002. 54

[87] GH Patterson and J Lippincott-Schwartz. A photoactivatable GFP for selective photolabeling of proteins and cells. *SCIENCE*, **297**[5588]:1873–1877, SEP 13 2002. 56

[88] MGL Gustafsson, DA Agard, and JW Sedat. (IM)-M-5: 3D wide-field light microscopy with better than 100 nm axial resolution. *JOURNAL OF MICROSCOPY-OXFORD*, **195**[1]:10–16, JUL 1999. 56

[89] WR Zipfel, RM Williams, and WW Webb. Nonlinear magic: multiphoton microscopy in the biosciences. *NATURE BIOTECHNOLOGY*, **21**[11]:1368–1376, NOV 2003. 56

[90] L Shao, B Isaac, S Uzawa, DA Agard, JW Sedat, and MGL Gustafsson. I(5)S: Wide-field light microscopy with 100-nm-scale resolution in three dimensions. *BIOPHYSICAL JOURNAL*, **94**[12]:4971–4983, JUN 15 2008. 56

[91] M Heilemann, S van de Linde, M Schuttpelz, R Kasper, B Seefeldt, A Mukherjee, P Tinnefeld, and M Sauer. Subdiffraction-resolution fluorescence imaging with conventional fluorescent probes. *ANGEWANDTE CHEMIE-INTERNATIONAL EDITION*, **47**[33]:6172–6176, 2008. 56

[92] M Dyba and SW Hell. Focal spots of size lambda/23 open up far-field florescence microscopy at 33 nm axial resolution. *PHYSICAL REVIEW LETTERS*, **88**[16], APR 22 2002. 56

[93] MA Haidekker and EA Theodorakis. Molecular rotors - fluorescent biosensors for viscosity and flow. *ORGANIC & BIOMOLECULAR CHEMISTRY*, **5**[11]:1669–1678, 2007. 58, 93

[94] WJ Akers and MA Haidekker. Precision assessment of biofluid viscosity measurements using molecular rotors. *JOURNAL OF BIOMECHANICAL ENGINEERING-TRANSACTIONS OF THE ASME*, **127**[3]:450–454, JUN 2005. 58, 93

[95] JA Levitt, MK Kuimova, G Yahioglu, PH Chung, K Suhling, and D Phillips. Membrane-Bound Molecular Rotors Measure Viscosity in Live Cells via Fluorescence Lifetime Imaging. *JOURNAL OF PHYSICAL CHEMISTRY C*, **113**[27]:11634–11642, JUL 9 2009. 58, 62, 93, 96, 100, 101, 114, 197

[96] F Zhou, J Shao, Y Yang, J Zhao, H Guo, X Li, S Ji, and Z Zhang. Molecular rotors as fluorescent viscosity sensors: Molecular design, polarity sensitivity, dipole moments changes, screening solvents, and deactivation channel of the excited states. *European Journal of Organic Chemistry*, **2011**[25]:4773–4787, 2011. 58, 93

[97] J Sutharsan, D Lichlyter, NE Wright, M Dakanali, MA Haidekker, and EA Theodorakis. Molecular rotors: synthesis and evaluation as viscosity sensors. *TETRAHEDRON*, **66**[14]:2582–2588, APR 3 2010. 58, 93

[98] JA Levitt, PH Chung, MK Kuimova, G Yahioglu, Y Wang, J Qu, and K Suhling. Fluorescence Anisotropy of Molecular Rotors. *CHEMPHYSCHEM*, **12**[3, SI]:662–672, FEB 25 2011. 58, 59, 62, 131, 132

[99] T Forster and G Hoffman. Die Viskositätsabhängigkeit der Fluoreszenzquantenausbeuten einiger Farbstoffsysteme. *Z. PHYS. CHEM.*, **75**:63–76, 1971. 59

[100] Kung, CE and Reed, JK. Microviscosity measurements of phospholipid-bilayers using fluorescent dyes that undergo torsional relaxation. *BIOCHEMISTRY*, **25**[20]:6114–6121, OCT 7 1986. 59

[101] MA Haidekker, N L'Heureux, and JA Frangos. Fluid shear stress increases membrane fluidity in endothelial cells: a study with DCVJ fluorescence. *AMERICAN JOURNAL OF PHYSIOLOGY-HEART AND CIRCULATORY PHYSIOLOGY*, **278**[4]:1401–1406, APR 2000. 59

[102] MA Haidekker, TT Ling, M Anglo, HY Stevens, JA Frangos, and EA Theodorakis. New fluorescent probes for the measurement of cell membrane viscosity. *CHEMISTRY & BIOLOGY*, **8**[2]:123–131, FEB 2001. 59

[103] Aniruddha, P and Anunay, S. Free Volume Dependence of the Internal Rotation of a Molecular Rotor Probe in Room Temperature Ionic Liquids. *JOURNAL OF PHYSICAL CHEMISTRY B*, **112**[51]:16626–16632, DEC 25 2008. 59

[104] Howell, S and Dakanali, M and Theodorakis, EA and Haidekker, MA. Intrinsic and Extrinsic Temperature-Dependency of Viscosity-Sensitive Fluorescent Molecular Rotors. *JOURNAL OF FLUORESCENCE*, **22**[1]:457–465, JAN 2012. 59

[105] ZA Dreger, JO White, and HG Drickamer. High pressure-controlled intramolecular-twist of flexible molecules in solid polymers. *CHEMICAL PHYSICS LETTERS*, **290**[4-6]:399–404, JUL 3 1998. 59

[106] JM Lang, ZA Dreger, and HG Drickamer. A high-pressure study of the effect of viscosity on the light-induced isomerization of dmabn in 3 linear alcohols, iso-butanol and glycerol. *CHEMICAL PHYSICS LETTERS*, **243**[1-2]:78–84, SEP 8 1995. 59

[107] A Zhu, B Wang, JO White, and HG Drickamer. The effect of high pressure on the twisted intramolecular charge transfer of 2-(4-dimethylaminonaphthalen-1-ylmethylene) malononitrile. *JOURNAL OF PHYSICAL CHEMISTRY A*, **107**[36]:6932–6935, SEP 11 2003. 59

[108] WJ Akers, JM Cupps, and MA Haidekker. Interaction of fluorescent molecular rotors with blood plasma proteins. *BIORHEOLOGY*, **42**[5]:335–344, 2005. 59

[109] SL Laporte, A Harianawala, and RH Bogner. The application of malononitriles as microviscosity probes in pharmaceutical systems. *PHARMACEUTICAL RESEARCH*, **12**[3]:380–386, MAR 1995. 59

[110] NA Hosny, G Mohamedi, Rademeyer, J Owen, Y Wu, MX Tang, RJ Eckersley, E Stride, and MK Kuimova. Mapping microbubble viscosity using fluorescence lifetime imaging of molecular rotors. *PROCEEDINGS OF THE NATIONAL ACADEMY OF SCIENCES OF THE UNITED STATES OF AMERICA*, **110**[23]:9225–9230, JUN 4 2013. 59, 93

[111] A Bhattacharyya, K Bhattacharyya, B Bhattacharyya, and S Roy. A study of aggregation of 9-(dicyano-vinyl)julolidine. *INDIAN JOURNAL OF BIOCHEMISTRY & BIOPHYSICS*, **32**[6]:442–446, 1995. 59

[112] MK Kuimova. Mapping viscosity in cells using molecular rotors. *PHYSICAL CHEMISTRY CHEMICAL PHYSICS*, **14**[37]:12671–12686, 2012. 59, 100, 105, 116, 128, 130, 135, 136

[113] MM Gleason, MS Medow, and TN Tulenko. Excess membrane cholesterol alters calcium movements, cytosolic calcium levels, and membrane fluidity in arterial smooth-muscle cells. *CIRCULATION RESEARCH*, **69**[1]:216–227, JUL 1991. 60

[114] O Nadiv, M Shinitzky, H Manu, D Hecht, CT Roberts, D Leroith, and Y Zick. Elevated protein-tyrosine-phosphatase activity and increased membrane viscosity are associated with impaired activation of the insulin-receptor kinase in old rats. *BIOCHEMICAL JOURNAL*, **298**[2]:443–450, MAR 1 1994. 60

[115] T Koike, G Ishida, M Taniguchi, K Higaki, Y Ayaki, M Saito, Y Sakakihara, M Iwamori, and K Ohno. Decreased membrane fluidity and unsaturated fatty acids in Niemann-Pick disease type C fibroblasts.

BIOCHIMICA ET BIOPHYSICA ACTA-MOLECULAR BASIS OF DISEASE, **1406**[3]:327–335, APR 28 1998. 60

[116] DA Fedosov, W Pan, B Caswell, G Gompper, and GE Karniadakis. Predicting human blood viscosity in silico. *PROCEEDINGS OF THE NATIONAL ACADEMY OF SCIENCES OF THE UNITED STATES OF AMERICA*, **108**[29]:11772–11777, JUL 19 2011. 60

[117] K Suhling, J Siegel, PMP Lanigan, S Leveque-Fort, SED Webb, D Phillips, DM Davis, and PMW French. Time-resolved fluorescence anisotropy imaging applied to live cells. *OPTICS LETTERS*, **29**[6]:584–586, MAR 15 2004. 60

[118] Tomasz Kalwarczyk, Natalia Ziebacz, Anna Bielejewska, Ewa Zaboklicka, Kaloian Koynov, Jedrzej Szymanski, Agnieszka Wilk, Adam Patkowski, Jacek Gapinski, Hans-Juergen Butt, and Robert Holyst. Comparative analysis of viscosity of complex liquids and cytoplasm of mammalian cells at the nanoscale. *NANO LETTERS*, **11**[5]:2157–2163, MAY 2011. 61

[119] K Lubyphelps, S Mujumdar, RB Mujumdar, LA Ernst, W Galbraith, and AS Waggoner. A novel fluorescence ratiometric method confirms the low solvent viscosity of the cytoplasm. *BIOPHYSICAL JOURNAL*, **65**[1]:236–242, JUL 1993. 61

[120] A Srivastava and G Krishnamoorthy. Cell type and spatial location dependence of cytoplasmic viscosity measured by time-resolved fluorescence microscopy. *ARCHIVES OF BIOCHEMISTRY AND BIOPHYSICS*, **340**[2]:159–167, APR 15 1997. 61

[121] X Peng, Z Yang, J Wang, J Fan, Y He, F Song, B Wang, S Sun, J Qu, J Qi, and M Yang. Fluorescence Ratiometry and Fluorescence Lifetime Imaging: Using a Single Molecular Sensor for Dual Mode Imaging of Cellular Viscosity. *JOURNAL OF THE AMERICAN CHEMICAL SOCIETY*, **133**[17]:6626–6635, MAY 4 2011. 61, 106

[122] Matthew E. Nipper, Sheereen Majd, Michael Mayer, James C. M. Lee, Emmanuel A. Theodorakis, and Mark A. Haidekker. Characterization of changes in the viscosity of lipid membranes with the molecular rotor FCVJ. *BIOCHIMICA ET BIOPHYSICA ACTA-BIOMEMBRANES*, **1778**[4]:1148–1153, APR 2008. 61

[123] CE Kung and JK Reed. Microviscosity measurements of phospholipid-bilayers using fluorescent dyes that undergo torsional relaxation. *BIOCHEMISTRY*, **25**[20]:6114–6121, OCT 7 1986. 61

[124] Matthew E. Nipper, Marianna Dakanali, Emmanuel Theodorakis, and Mark A. Haidekker. Detection of liposome membrane viscosity perturbations with ratiometric molecular rotors. *BIOCHIMIE*, **93**[6]:988–994, JUN 2011. 61, 62

[125] MK Kuimova, G Yahioglu, JA Levitt, and K Suhling. Molecular rotor measures viscosity of live cells via fluorescence lifetime imaging. *JOURNAL OF THE AMERICAN CHEMICAL SOCIETY*, **130**[21]:6672+, MAY 28 2008. 62, 93, 100, 101, 114, 136

[126] MK Kuimova, SW Botchway, AW Parker, Milan Balaz, HA Collins, HL Anderson, K Suhling, and PR Ogilby. Imaging intracellular viscosity of a single cell during photoinduced cell death. *NATURE CHEMISTRY*, **1**[1]:69–73, APR 2009. 62, 114

[127] JR Blinks, WG Wier, P Hess, and FG Prendergast. Measurement of Ca-2+ Concentrations in Living Cells. *PROGRESS IN BIOPHYSICS & MOLECULAR BIOLOGY*, **40**[1]:1–114, 1982. 62

[128] MA Haidekker, TP Brady, D Lichlyter, and EA Theodorakis. A ratiometric fluorescent viscosity sensor. *JOURNAL OF THE AMERICAN CHEMICAL SOCIETY*, **128**[2]:398–399, JAN 18 2006. 62

[129] Bethany B. Hueholt, Wenying Xu, Michal Sabat, B. A. DeGraff, and J. N. Demas. Structure and luminescence properties

of monomeric and dimeric Re(I) complexes with dicarboxylic acid-2,2'-bipyridine ligands. *JOURNAL OF FLUORESCENCE*, **17**[5]:522–527, SEP 2007. 63

[130] Lucia Flamigni, Andrea Barbieri, Cristiana Sabatini, Barbara Ventura, and Francesco Barigelletti. Photochemistry and photophysics of coordination compounds: Iridium. In Balzani, V and Campagna, S, editor, *PHOTOCHEMISTRY AND PHOTOPHYSICS OF COORDINATION COMPOUNDS II*, **281** of *Topics in Current Chemistry*, pages 143–203. 2007. 63

[131] S Campagna, F Puntoriero, F Nastasi, G Bergamini, and V Balzani. Photochemistry and photophysics of coordination compounds: Ruthenium. In *PHOTOCHEMISTRY AND PHOTOPHYSICS OF COORDINATION COMPOUNDS I*, **280** of *Topics in Current Chemistry*, page 117214. 2007. 63

[132] EA Medlycott and GS Hanan. Designing tridentate ligands for ruthenium(II) complexes with prolonged room temperature luminescence lifetimes. *CHEMICAL SOCIETY REVIEWS*, **34**[2]:133–142, 2005. 63

[133] MG SASSO, FH QUINA, and EJH BECHARA. RUTHENIUM(II) TRIS(BIPYRIDYL) ION AS A LUMINESCENT PROBE FOR OXYGEN-UPTAKE. *ANALYTICAL BIOCHEMISTRY*, **156**[1]:239–243, JUL 1986. 63

[134] Gerritsen, HC and Sanders, R and Draaijer, A and Ince, C and Levine, YK. Fluorescence lifetime imaging of oxygen in living cells. *JOURNAL OF FLUORESCENCE*, **7**[1]:11–15, 1997. 63, 177

[135] Dhruv Sud, Geeta Mehta, Khamir Mehta, Jennifer Linderman, Shuichi Takayama, and Mary-Ann Mycek. Optical imaging in microfluidic bioreactors enables oxygen monitoring for continuous cell culture. *JOURNAL OF BIOMEDICAL OPTICS*, **11**[5], SEP-OCT 2006. 63

[136] Dhruv Sud and Mary-Ann Mycek. Calibration and validation of an optical sensor for intracellular oxygen measurements. *JOURNAL OF BIOMEDICAL OPTICS*, **14**[2], MAR-APR 2009. 63

[137] Cornelia Lochmann, Thomas Hansel, Tilmann Haeupl, and Juergen Beuthan. An Oxygen Imaging System for Medical Applications: Preliminary Results. *BIOMEDIZINISCHE TECHNIK*, **51**[3]:111–115, 2006. 63

[138] Cornelia Lochmann, Tilmann Haeupl, and Juergen Beuthan. Luminescence Lifetime Determination for Oxygen Imaging in Human Tissue. *LASER PHYSICS LETTERS*, **5**[1-2]:151–155, 2008. 63

[139] NA Hosny, DA Lee, and MM Knight. Single photon counting fluorescence lifetime detection of pericellular oxygen concentrations. *JOURNAL OF BIOMEDICAL OPTICS*, **17**[1], JAN 2012. 63, 177, 193, 199

[140] H Choi, DS Tzeranis, JW Cha, P Clemenceau, SJG de Jong, LK van Geest, JH Moon, IV Yannas, and PTC So. 3D-resolved fluorescence and phosphorescence lifetime imaging using temporal focusing wide-field two-photon excitation. *OPTICS EXPRESS*, **20**[24]:26219–26235, NOV 19 2012. 63, 177

[141] A Dossing. Luminescence from lanthanide(3+) ions in solution. *EUROPEAN JOURNAL OF INORGANIC CHEMISTRY*, [8]:1425–1434, APR 22 2005. 63

[142] Aurore Thibon and Valerie C. Pierre. Principles of responsive lanthanide-based luminescent probes for cellular imaging. *ANALYTICAL AND BIOANALYTICAL CHEMISTRY*, **394**[1]:107–120, MAY 2009. 64

[143] Evan G. Moore, Amanda P. S. Samuel, and Kenneth N. Raymond. From Antenna to Assay: Lessons Learned in Lanthanide Luminescence. *ACCOUNTS OF CHEMICAL RESEARCH*, **42**[4]:542–552, APR 2009. 64

[144] B Song, CDB Vandevyver, AS Chauvin, and JCG Buenzli. Time-resolved luminescence microscopy of bimetallic lanthanide helicates in living cells. *ORGANIC & BIOMOLECULAR CHEMISTRY*, **6**[22]:4125–4133, 2008. 64, 177

[145] Jean-Claude G. Bnzli. Lanthanide luminescence for biomedical analyses and imaging. *Chemical Reviews*, **110**[5]:2729–2755, 2010. PMID: 20151630. 64

[146] D Parker. Luminescent lanthanide sensors for pH, pO(2) and selected anions. *COORDINATION CHEMISTRY REVIEWS*, **205**:109–130, AUG 2000. 64

[147] James Hynes, Tomas C. O'Riordan, Alexander V. Zhdanov, Georg Uray, Yvonne Will, and Dmitri B. Papkovsky. In vitro analysis of cell metabolism using a long-decay pH-sensitive lanthanide probe and extracellular acidification assay. *ANALYTICAL BIOCHEMISTRY*, **390**[1]:21–28, JUL 1 2009. 64

[148] Bo Song, Guilan Wang, Mingqian Tan, and Jingli Yuan. A europium(III) complex as an efficient singlet oxygen luminescence probe. *JOURNAL OF THE AMERICAN CHEMICAL SOCIETY*, **128**[41]:13442–13450, OCT 18 2006. 64

[149] LJ Charbonniere and N Hildebrandt. Lanthanide complexes and quantum dots: A bright wedding for resonance energy transfer. *EUROPEAN JOURNAL OF INORGANIC CHEMISTRY*, [21]:3241–3251, JUL 2008. 64, 177, 178

[150] Kazuki Aita, Takashi Temma, Yuji Kuge, Koh-ichi Seki, and Hideo Saji. NIR fluorescent ytterbium compound for in vivo fluorescence molecular imaging. *LUMINESCENCE*, **25**[1]:19–24, JAN-FEB 2010. 64

[151] V Fernandez-Moreira, B Song, V Sivagnanam, AS Chauvin, CDB Vandevyver, M Gijs, I Hemmila, HA Lehr, and JCG Buenzli. Bioconjugated lanthanide luminescent helicates as multilabels for lab-

on-a-chip detection of cancer biomarkers. *ANALYST*, **135**[1]:42–52, 2010. 64, 178

[152] EB SHERA, NK SEITZINGER, LM DAVIS, RA KELLER, AND SA SOPER. DETECTION OF SINGLE FLUORESCENT MOLECULES. *CHEMICAL PHYSICS LETTERS*, **174**[6]:553–557, NOV 23 1990. 64

[153] S FELEKYAN, R KUHNEMUTH, V KUDRYAVTSEV, C SANDHAGEN, W BECKER, AND CAM SEIDEL. Full correlation from picoseconds to seconds by time-resolved and time-correlated single photon detection. *REVIEW OF SCIENTIFIC INSTRUMENTS*, **76**[8], AUG 2005. 64, 65

[154] DL ROBINSON AND BD METSCHER. PHOTON DETECTION WITH COOLED AVALANCHE PHOTODIODES. *APPLIED PHYSICS LETTERS*, **51**[19]:1493–1494, NOV 9 1987. 64

[155] X. MICHALET, ADRIAN CHENG, JOSHUA ANTELMAN, MOTOHIRO SUYAMA, KATSUSHI ARISAKA, AND SHIMON WEISS. Hybrid photodetector for single-molecule spectroscopy and microscopy - art. no. 68620F. In ENDERLEIN, J AND GRYCZYNSKI, ZK AND ERDMANN, R, editor, *SINGLE MOLECULE SPECTROSCOPY AND IMAGING*, **6862** of *PROCEEDINGS OF THE SOCIETY OF PHOTO-OPTICAL INSTRUMENTATION ENGINEERS (SPIE)*, page F8620, 1000 20TH ST, PO BOX 10, BELLINGHAM, WA 98227-0010 USA, 2008. SPIE, SPIE-INT SOC OPTICAL ENGINEERING. Conference on Single Molecule Spectroscopy and Imaging, San Jose, CA, JAN 19-21, 2008. 64, 65

[156] A. FUKASAWA, A. KAMIYA, S. MURAMATSU, Y. NEGI, AND M. SUYAMA. High Performance HPD for Photon Counting. In ITZLER, MA AND CAMPBELL, JC, editor, *ADVANCED PHOTON COUNTING TECHNIQUES V*, **8033** of *Proceedings of SPIE*. SPIE, 2011. Conference on Advanced Photon Counting Techniques V, Orlando, FL, APR 27-29, 2011. 64

[157] I Rech, GB Luo, M Ghioni, H Yang, XLS Xie, and S Cova. Photon-timing detector module for single-molecule spectroscopy with 60-ps resolution. *IEEE JOURNAL OF SELECTED TOPICS IN QUANTUM ELECTRONICS*, **10**[4]:788–795, JUL-AUG 2004. 65

[158] S Cova, M Ghioni, A Lotito, I Rech, and F Zappa. Evolution and prospects for single-photon avalanche diodes and quenching circuits. *JOURNAL OF MODERN OPTICS*, **51**[9-10]:1267–1288, JUN-JUL 2004. Workshop on Single-Photon, Gaithersburg, MD, MAR 31-APR 01, 2003. 65

[159] Gerald Kell, Andreas Buelter, Michael Wahl, and Rainer Erdmann. tau-SPAD: A new red sensitive single photon counting module. In Itzler, MA and Campbell, JC, editor, *ADVANCED PHOTON COUNTING TECHNIQUES V*, **8033** of *Proceedings of SPIE*. SPIE, 2011. Conference on Advanced Photon Counting Techniques V, Orlando, FL, APR 27-29, 2011. 65

[160] Massimo Ghioni, Angelo Gulinatti, Ivan Rech, Franco Zappa, and Sergio Cova. Progress in silicon single-photon avalanche diodes. *IEEE JOURNAL OF SELECTED TOPICS IN QUANTUM ELECTRONICS*, **13**[4]:852–862, JUL-AUG 2007. 65

[161] Mattia Assanelli, Antonino Ingargiola, Ivan Rech, Angelo Gulinatti, and Massimo Ghioni. Photon-Timing Jitter Dependence on Injection Position in Single-Photon Avalanche Diodes. *IEEE JOURNAL OF QUANTUM ELECTRONICS*, **47**[2]:151–159, FEB 2011. 65

[162] Angelo Gulinatti, Ivan Rech, Piera Maccagnani, Massimo Ghioni, and Sergio Cova. Improving the performance of Silicon Single Photon Avalanche Diodes. In Itzler, MA and Campbell, JC, editor, *ADVANCED PHOTON COUNTING TECHNIQUES V*, **8033** of *Proceedings of SPIE*. SPIE, 2011. Conference on Advanced Photon Counting Techniques V, Orlando, FL, APR 27-29, 2011. 65

[163] G ANZIVINO, H ARNAUDON, P BAILLON, P BENETTI, L BOSKMA, P BURGER, A CONTIN, R DESALVO, P GORODETZKY, D GRASSI, W HAO, H HE, L LIU, M LUNDIN, MR MONDARDINI, S PAOLUCCI, M ROSSELLA, JC SANTIARD, R SCHOMAKER, K YOU, K WANG, Y WANG, X XIA, C XU, C YANG, AND M ZHAO. REVIEW OF THE HYBRID PHOTO DIODE TUBE (HPD) AN ADVANCED LIGHT DETECTOR FOR PHYSICS. *NUCLEAR INSTRUMENTS & METHODS IN PHYSICS RESEARCH SECTION A-ACCELERATORS SPECTROMETERS DETECTORS AND ASSOCIATED EQUIPMENT*, **365**[1]:76–82, NOV 1 1995. 65

[164] A FRENKEL, MA SARTOR, AND MS WLODAWSKI. Photon-noise-limited operation of intensified CCD cameras. *APPLIED OPTICS*, **36**[22]:5288–5297, AUG 1 1997. 65

[165] N SERGENT, JA LEVITT, M GREEN, AND K SUHLING. Rapid wide-field photon counting imaging with microsecond time resolution. *OPTICS EXPRESS*, **18**[24]:25292–25298, NOV 22 2010. 66, 176

[166] OHNUKI TOHRU, XAVIER MICHALET, ARUN TNPATHI, SHIMON WEISS, AND KATSUSHI ARISAKA. Development of an ultra-fast single-photon counting imager for single-molecule imaging - art. no. 60920P. In ENDERLEIN, J AND GRYCZYNSKI, ZK, editor, *Ultrasensitive and Single-Molecule Detection Technologies*, **6092** of *PROCEEDINGS OF THE SOCIETY OF PHOTO-OPTICAL INSTRUMENTATION ENGINEERS (SPIE)*, page P920. SPIE, 2006. Conference on Ultrasensitive and Single-Molecule Detection Technologies, San Jose, CA, JAN 21-24, 2006. 66

[167] S BUONTEMPO, G CHIODI, IN DALINENKO, A EREDITATO, AV EKIMOV, JP FABRE, VY FEDOROV, A FRENKEL, F GALEAZZI, F GARUFI, SV GOLOVKIN, VN GOVORUN, NN KALASHNIKOVA, VG KOSSOV, EN KOZARENKO, IE KRESLO, LY LASOVSKY, B LIBERTI, AV MALYAROV, G MARTELLOTTI, AM MEDVEDKOV, G PENSO, GI VISHNEVSKY, T WOLFF, AND A ZHUK. The Megapixel EBCCD: A high-

resolution imaging tube sensitive to single photons. *NUCLEAR INSTRUMENTS & METHODS IN PHYSICS RESEARCH SECTION A-ACCELERATORS SPECTROMETERS DETECTORS AND ASSOCIATED EQUIPMENT*, **413**[2-3]:255–262, AUG 21 1998. 66

[168] I Koyama-Honda, K Ritchie, T Fujiwara, R Iino, H Murakoshi, RS Kasai, and A Kusumi. Fluorescence imaging for monitoring the colocalization of two single molecules in living cells. *BIOPHYSICAL JOURNAL*, **88**[3]:2126–2136, MAR 2005. 66

[169] D Quang Tuyen, R Barbier, A Dominjon, T Cajgfinger, and C Guerin. Multiple-target tracking implementation in the ebCMOS camera system: the LUSIPHER prototype. In Schelkens, P and Ebrahimi, T and Cristobal, G and Truchetet, F and Saarikko, P, editor, *OPTICS, PHOTONICS, AND DIGITAL TECHNOLOGIES FOR MULTIMEDIA APPLICATIONS II*, **8436** of *Proceedings of SPIE*, 1000 20TH ST, PO BOX 10, BELLINGHAM, WA 98227-0010 USA, 2012. SPIE; Brussels Photon Team (B-PHOT); Brussels-Capital Reg; Fonds Wetenschappelijk Onderzoek (FWO); Int Commiss Opt (ICO); Ville Bruxelles, SPIE-INT SOC OPTICAL ENGINEERING. Conference on Optics, Photonics and Digital Technologies for Multimedia Applications II, Brussels, BELGIUM, APR 17-18, 2012. 66

[170] MS Robbins and BJ Hadwen. The noise performance of electron multiplying charge-coupled devices. *IEEE TRANSACTIONS ON ELECTRON DEVICES*, **50**[5]:1227–1232, MAY 2003. 66

[171] Hirvonen, LM and Petrášek, Z and Suhling, K. Wide-field time-correlated single photon counting (TCSPC) microscopy with time resolution below the frame exposure time. *NUCLEAR INSTRUMENTS AND METHODS IN PHYSICS RESEARCH SECTION A: ACCELERATORS, SPECTROMETERS, DETECTORS AND ASSOCIATED EQUIPMENT*, []:, 2014. 66, 176

[172] G Zanda, N Sergent, M Green, JA Levitt, Z Petrasek, and K Suhling. Wide-field single photon counting imaging with an ultra-

fast camera and an image intensifier. *NUCLEAR INSTRUMENTS & METHODS IN PHYSICS RESEARCH SECTION A-ACCELERATORS SPECTROMETERS DETECTORS AND ASSOCIATED EQUIPMENT*, **695**:306–308, DEC 11 2012. 66, 178, 179

[173] TCS SP2 User manual; `Leica Microsystems`, 2010. 70

[174] DV O'Connor and D Philips. *Time-correlated single photon counting.* Academic Press, 1984. 71

[175] K Suhling, G Hungerford, RW Airey, and BL Morgan. A position-sensitive photon event counting detector applied to fluorescence imaging of dyes in sol-gel matrices. *MEASUREMENT SCIENCE & TECHNOLOGY*, **12**[2]:131–141, FEB 2001. 71, 86, 89

[176] G Hungerford and DJS Birch. Single-photon timing detectors for fluorescence lifetime spectroscopy. *MEASUREMENT SCIENCE & TECHNOLOGY*, **7**[2]:121–135, FEB 1996. 71

[177] X Michalet, OHW Siegmund, JV Vallerga, P Jelinsky, JE Millaud, and S Weiss. Detectors for single-molecule fluorescence imaging and spectroscopy. *JOURNAL OF MODERN OPTICS*, **54**[2-3]:239–281, JAN 20 2007. 71, 76

[178] MD Eisaman, J Fan, A Migdall, and SV Polyakov. Invited Review Article: Single-photon sources and detectors. *REVIEW OF SCIENTIFIC INSTRUMENTS*, **82**[7], JUL 2011. 71

[179] W Becker. *Advanced time-correlated single-photon counting techniques.* Berlin, Heidelberg, New York, 2005. 71, 72, 75

[180] L Bollinger and GE Thomas. Measurement of time dependence of scintillation intensity by a delayed-coincidence method. *REVIEW OF SCIENTIFIC INSTRUMENTS*, **32**[9]:1044, 1961. 71

[181] R Paschotta. *Encyclopedia of Laser Physics and Technology.* Wiley-VCH, Berlin, 1st edition edition, 2008. 72

[182] GW Clark. Bruno Benedetto Rossi (13 April 1905 21 November 1993). *PROCEEDINGS OF THE AMERICAN PHILOSOPHICAL SOCIETY*, **144**[3]:329–341, SEP 2000. 72

[183] RKP Benninger, O Hofmann, J McGinty, J Requejo-Isidro, I Munro, MAA Neil, AJ deMello, and PMW French. Time-resolved fluorescence imaging of solvent interactions in microfluidic devices. *OPTICS EXPRESS*, **13**[16]:6275–6285, AUG 8 2005. 73

[184] PR Barber, SM Ameer-Beg, J Gilbey, RJ Edens, I Ezike, and B Vojnovic. Global and pixel kinetic data analysis for FRET detection by multi-photon time-domain FLIM. In Periasamy, A and So, PTC, editor, *MULTIPHOTON MICROSCOPY IN THE BIOMEDICAL SCIENCES V*, **5700** of *Proceedings of the society of photo-optical instrumentation engineers (SPIE)*, pages 171–181, 2005. 75

[185] PR Barber, SM Ameer-Beg, J Gilbey, LM Carlin, M Keppler, TC Ng, and B Vojnovic. Multiphoton time-domain fluorescence lifetime imaging microscopy: practical application to protein-protein interactions using global analysis. *JOURNAL OF THE ROYAL SOCIETY INTERFACE*, **6**[1]:S93–S105, FEB 6 2009. 75

[186] DK Bird, KW Eliceiri, CH Fan, and JG White. Simultaneous two-photon spectral and lifetime fluorescence microscopy. *APPLIED OPTICS*, **43**[27]:5173–5182, SEP 20 2004. 75

[187] W Becker, A Bergmann, and C Biskup. Multispectral fluorescence lifetime imaging by TCSPC. *MICROSCOPY RESEARCH AND TECHNIQUE*, **70**[5]:403–409, MAY 2007. Workshop on Advanced Multiphoton and Fluorescence Lifetime Imaging Techniques, St Ingbert, Ingbert, GERMANY, JUN 19-21, 2006. 75

[188] A Rueck, CH Huelshoff, I Kinzler, W Becker, and R Steiner. SLIM: A new method for molecular imaging. *MICROSCOPY RESEARCH AND TECHNIQUE*, **70**[5]:485–492, MAY 2007. Workshop on Advanced

Multiphoton and Fluorescence Lifetime Imaging Techniques, St Ingbert, Ingbert, GERMANY, JUN 19-21, 2006. 75

[189] C Thaler, SV Koushik, HL Puhl, III, PS Blank, and SS Vogel. Structural rearrangement of CaMKII alpha catalytic domains encodes activation. *PROCEEDINGS OF THE NATIONAL ACADEMY OF SCIENCES OF THE UNITED STATES OF AMERICA*, **106**[15]:6369–6374, APR 14 2009. 75

[190] JA Levitt, DR Matthews, SM Ameer-Beg, and K Suhling. Fluorescence lifetime and polarization-resolved imaging in cell biology. *CURRENT OPINION IN BIOTECHNOLOGY*, **20**[1]:28–36, FEB 2009. 75, 106, 128, 129, 135, 136

[191] H Iams and B Salzberg. The secondary emission phototube. *PROCEEDINGS OF THE INSTITUTE OF RADIO ENGINEERS*, **23**[1]:55–64, JAN 1935. 76

[192] RW Engstrom. Photomultiplier tube characteristics. *JOURNAL OF THE OPTICAL SOCIETY OF AMERICA*, **36**[12]:720, 1946. 76

[193] H Bruining. *Physics and applications of secondary electron emission*. New York, McGraw-Hill Book Co., 1954. 76, 78

[194] R Foord, R Jones, CJ Oliver, and ER Pike. Use of photomultiplier tubes for photon counting. *APPLIED OPTICS*, **8**[10]:1975, 1969. 76

[195] THBV3-0206EA Photomultiplier Tubes - Basics and Applications, 3rd Edition; `Hamamatsu Photonics K.K.`, 2006. 76, 78, 176

[196] A Shih, J Yater, C Hor, and R Abrams. Secondary electron emission studies. *APPLIED SURFACE SCIENCE*, **111**:251–258, FEB 1997. 78

[197] RS GAO, PS GIBNER, JH NEWMAN, KA SMITH, and RF STEBBINGS. Absolute And Angular Efficiencies Of A Microchannel-Plate Position-Sensitive Detector. *REVIEW OF SCIENTIFIC INSTRUMENTS*, **55**[11]:1756–1759, 1984. 79

[198] Microchannel Plates and MCP Detectors and Imaging Systems; `Del Mar Photonics`. 79, 80, 81, 88

[199] M Akatsu, Y Enari, K Hayasaka, T Hokuue, T Iijima, K Inami, K Itoh, Y Kawakami, N Kishimoto, T Kubota, M Kojima, Y Kozakai, Y Kuriyama, T Matsuishi, Y Miyabayashi, T Ohshima, N Sato, K Senyo, A Sugi, S Tokuda, M Tomita, H Yanase, and S Yoshino. MCP-PMT timing property for single photons. *NUCLEAR INSTRUMENTS & METHODS IN PHYSICS RESEARCH SECTION A-ACCELERATORS SPECTROMETERS DETECTORS AND ASSOCIATED EQUIPMENT*, **528**[3]:763–775, AUG 11 2004. 79

[200] AS Tremsin, JV Vallerga, OHW Siegmund, and JS Hull. Centroiding algorithms and spatial resolution of photon counting detectors with cross strip anodes. In Siegmund, OHW, editor, *UV/EUV AND VISIBLE SPACE INSTRUMENTATION FOR ASTRONOMY II*, **5164** of *PROCEEDINGS OF THE SOCIETY OF PHOTO-OPTICAL INSTRUMENTATION ENGINEERS (SPIE)*, pages 113–124, 1000 20TH ST, PO BOX 10, BELLINGHAM, WA 98227-0010 USA, 2003. SPIE, SPIE-INT SOC OPTICAL ENGINEERING. 80, 85

[201] K Suhling, RW Airey, and BL Morgan. Minimization of fixed pattern noise in photon event counting imaging. *REVIEW OF SCIENTIFIC INSTRUMENTS*, **73**[8]:2917–2922, AUG 2002. 80, 85, 86, 88, 89

[202] ML Edgar, R Kessel, JS Lapington, and DM Walton. Spatial Charge Cloud Distribution of Microchannel Plates. *REVIEW OF SCIENTIFIC INSTRUMENTS*, **60**[12]:3673–3680, DEC 1989. 80

[203] JS Lapington. High speed imaging using a capacitive division technique. *NUCLEAR INSTRUMENTS & METHODS IN PHYSICS RESEARCH SECTION A-ACCELERATORS SPECTROMETERS DETECTORS AND ASSOCIATED EQUIPMENT*, **695**:410–414, DEC 11 2012. 80

[204] JG Cuby, JC Richard, and M Pemonier. Electron-bombarded ccd: first results with a prototype tube. *INSTRUMENTATION IN ASTRONOMY VII*, [5]:294–304, 2007. 80

[205] G Auriemma, L Errico, C Satriano, and AA Vittone. EBCCD applications in astronomy. Memorie della Società Astronomica Italiana. **73**[1]:433–438, 2002. 80

[206] SB Sobottka, T Meyer, M Kirsch, E Koch, R Steinmeier, U Morgenstern, and G Schackert. Evaluation of the clinical practicability of intraoperative optical imaging comparing three different camera setups. *BIOMEDICAL ENGINEERING-BIOMEDIZINISCHE TECHNIK*, **58**[3, SI]:237–248, 2013. 81

[207] M Rossi, F Casali, SV Golovkin, and VN Covorun. Digital radiography using an EBCCD-based imaging device. *APPLIED RADIATION AND ISOTOPES*, **53**[4-5]:699–709, OCT-NOV 2000. 4th Topical Meeting on the Industrial Radiation and Radioisotope Measurement Applications (IRRMA 99), RALEIGH, NORTH CAROLINA, OCT 03-07, 1999. 81, 155

[208] J Baudot, W Dulinski, M Winter, R Barbier, E Chabanat, P Depasse, and N Estre. Photon detection with CMOS sensors for fast imaging. *NUCLEAR INSTRUMENTS & METHODS IN PHYSICS RESEARCH SECTION A-ACCELERATORS SPECTROMETERS DETECTORS AND ASSOCIATED EQUIPMENT*, **604**[1-2]:111–114, JUN 1 2009. 8th International Conference on Position Sensitive Detectors, Univ Glasgow, Glasgow, SCOTLAND, SEP 01-05, 2008. 81

[209] L Benussi, V Fanti, D Frekers, A Frenkel, G Giannini, SV Golovkin, EN Kozarenko, IE Kreslo, B Liberti, G Martellotti, AM Medvedkov, MR Mondardini, G Penso, A Polizzi, R Santacesaria, G Santini, M Spinetti, P Vilain, L Votano, G Wilquet, and K Winter. A multichannel single-photon sensitive detector for high-energy physics: the megapixel EBCCD. *NUCLEAR INSTRUMENTS & METHODS IN PHYSICS RESEARCH SECTION*

A-ACCELERATORS SPECTROMETERS DETECTORS AND ASSOCIATED EQUIPMENT, **442**[1-3]:154–158, MAR 11 2000. 2nd International Conference on New Developments in Photodetection, BEAUNE, FRANCE, JUN 21-25, 1999. 81, 155

[210] R Barbier, T Cajgfinger, P Calabria, E Chabanat, D Chaize, P Depasse, QT Doan, A Dominjon, C Guerin, J Houles, L Vagneron, J Baudot, A Dorokhov, W Dulinski, M Winter, and CT Kaiser. A single-photon sensitive ebCMOS camera: The LUSIPHER prototype. *NUCLEAR INSTRUMENTS & METHODS IN PHYSICS RESEARCH SECTION A-ACCELERATORS SPECTROMETERS DETECTORS AND ASSOCIATED EQUIPMENT*, **648**[1]:266–274, AUG 21 2011. 81, 82, 175, 198

[211] JR Fiebiger and RS Muller. Pair-production energies in silicon and germanium bombarded with low-energy electrons. *JOURNAL OF APPLIED PHYSICS*, **43**[7]:3202, 1972. 81

[212] GW Fraser, AF Abbey, A Holland, K Mccarthy, A Owens, and A Wells. The x-ray-energy response of silicon .a. theory. *NUCLEAR INSTRUMENTS & METHODS IN PHYSICS RESEARCH SECTION A-ACCELERATORS SPECTROMETERS DETECTORS AND ASSOCIATED EQUIPMENT*, **350**[1-2]:368–378, OCT 15 1994. 81, 150

[213] P Lechner and L Struder. Ionization statistics in silicon x-ray-detectors - new experimental results. *NUCLEAR INSTRUMENTS & METHODS IN PHYSICS RESEARCH SECTION A-ACCELERATORS SPECTROMETERS DETECTORS AND ASSOCIATED EQUIPMENT*, **354**[2-3]:464–474, JAN 30 1995. 81, 150

[214] RP Kraft, DN Burrows, GP Garmire, JA Nousek, JR Janesick, and PN Vu. Soft-x-ray spectroscopy with subelectron readnoise charge-coupled-devices. *NUCLEAR INSTRUMENTS & METHODS IN PHYSICS RESEARCH SECTION A-ACCELERATORS SPECTROMETERS DETECTORS AND ASSOCIATED EQUIPMENT*, **361**[1-2]:372–383, JUL 1 1995. 81, 151

[215] P Lechner, R Hartmann, H Soltau, and L Struder. Pair creation energy and Fano factor of silicon in the energy range of soft X-rays. *NUCLEAR INSTRUMENTS & METHODS IN PHYSICS RESEARCH SECTION A-ACCELERATORS SPECTROMETERS DETECTORS AND ASSOCIATED EQUIPMENT*, **377**[2-3]:206–208, AUG 1 1996. 7th European Symposium on Semiconductor Detectors, SCHLOSS ELMAU, GERMANY, MAY 07-JUL 10, 1995. 81, 150

[216] A Owens, GW Fraser, AF Abbey, A Holland, K McCarthy, A Keay, and A Wells. The X-ray energy response of silicon .B. Measurements. *NUCLEAR INSTRUMENTS & METHODS IN PHYSICS RESEARCH SECTION A-ACCELERATORS SPECTROMETERS DETECTORS AND ASSOCIATED EQUIPMENT*, **382**[3]:503–510, NOV 21 1996. 81

[217] F Scholze, H Rabus, and G Ulm. Mean energy required to produce an electron-hole pair in silicon for photons of energies between 50 and 1500 eV. *JOURNAL OF APPLIED PHYSICS*, **84**[5]:2926–2939, SEP 1 1998. 81, 150

[218] Springer, KR, Davidson, MW. Concepts in Digital Imaging Technology: Electron-Bombarded Charge-Coupled Devices (EBCCDs); . Online document from: `http://micro.magnet.fsu.edu/primer/digitalimaging/concepts/ebccd.html`. 82

[219] KR Spring. Cameras for Digital Microscopy. In Sluder, G and Wolf, DE, editor, *DIGITAL MICROSCOPY, 4TH EDITION*, **114** of *Methods in Cell Biology*, pages 163–178. ELSEVIER ACADEMIC PRESS INC, 2013. 82

[220] C7190-13w instruction manual, ver. 2.1; `Hamamatsu Photonics K.K.` 82

[221] A Rabner and Y Shacham-Diamand. Electron-Bombarded CMOS Image Sensor in Single Photon Imaging Mode. *IEEE SENSORS JOURNAL*, **11**[1]:1–8, JAN 2011. 82

[222] ER Fossum. *Active pixel sensors: are CCDs dinosaurs?*, **1900** of *Proceedings of SPIE*. San Jose, CA, USA, 1993. 83

[223] R Turchetta, N Guerrini, and I Sedgwick. Large area CMOS image sensors. *JOURNAL OF INSTRUMENTATION*, **6**, JAN 2011. 84

[224] OHW Siegmund, M Lampton, J Bixler, S Chakrabarti, J Vallerga, S Bowyer, and RF Malina. Wedge and strip image readout systems for photon-counting detectors in space astronomy. *JOURNAL OF THE OPTICAL SOCIETY OF AMERICA A-OPTICS IMAGE SCIENCE AND VISION*, **3**[12]:2139–2145, DEC 1986. 85

[225] H Inaba, Y Shimizu, Y Tsuji, and A Yamagishi. Photon-counting spectral analyzing system of extra-weak chemiluminescence and bioluminescence for biochemical applications. *PHOTOCHEMISTRY AND PHOTOBIOLOGY*, **30**[1]:169–175, 1979. 85

[226] DA Chesler, SJ Riederer, and NJ Pelc. Noise due to photon-counting statistics in computed x-ray tomography. *JOURNAL OF COMPUTER ASSISTED TOMOGRAPHY*, **1**[1]:64–74, 1977. 85

[227] Tpho9001e04 - photon counting using photomultiplier tubes; `Hamamatsu Photonics K.K.`, 2005. 85

[228] JS Lapington. Developments in imaging devices for microchannel plate detectors. In Blades, JC and Siegmund, OHW, editor, *FUTURE EUV/UV AND VISIBLE SPACE ASTROPHYSICS MISSIONS AND INSTRUMENTATION*, **4854** of *PROCEEDINGS OF THE SOCIETY OF PHOTO-OPTICAL INSTRUMENTATION ENGINEERS (SPIE)*, pages 191–202. SPIE, SPIE-INT SOC OPTICAL ENGINEERING, 2003. 85

[229] K Suhling, RW Airey, and BL Morgan. Optimisation of centroiding algorithms for photon event counting imaging. *NUCLEAR INSTRUMENTS & METHODS IN PHYSICS RESEARCH SECTION A-ACCELERATORS SPECTROMETERS DETECTORS AND ASSOCIATED EQUIPMENT*, **437**[2-3]:393–418, NOV 21 1999. 86, 87, 88, 89

[230] K Lau and J Pyrlik. Optimization of centroid-finding algorithms for cathode strip chambers. *NUCLEAR INSTRUMENTS & METHODS IN PHYSICS RESEARCH SECTION A-ACCELERATORS SPECTROMETERS DETECTORS AND ASSOCIATED EQUIPMENT*, **366**[2-3]:298–309, DEC 1 1995. 86

[231] TJ Collins. ImageJ for microscopy. *BIOTECHNIQUES*, **43**[1, S]:25+, JUL 2007. 89

[232] R Henriques, M Lelek, EF Fornasiero, F Valtorta, C Zimmer, and MM Mhlanga. QuickPALM: 3D real-time photoactivation nanoscopy image processing in ImageJ. *NATURE METHODS*, **7**[5]:339–340, MAY 2010. 89, 158

[233] JA Högbom. Aperture Synthesis with a Non-Regular Distribution of Interferometer Baselines. *ASTRONOMY AND ASTROPHYSICS SUPPLEMENT SERIES*, **15**:417–426, June 1974. 89

[234] S Wolter, A Loeschberger, T Holm, S Aufmkolk, MC Dabauvalle, S van de Linde, and M Sauer. rapidSTORM: accurate, fast open-source software for localization microscopy. *NATURE METHODS*, **9**[11]:1040–1041, NOV 2012. 89, 159, 199

[235] USAF 1951 target, datasheet; `Thornlabs`. 90

[236] R Ian Freshney. *Culture Of Animal Cells: A Manual Of Basic Technique, Third Edition*. Wiley-Liss, New York, 3rd edition edition, 1994. 91

[237] A Loudet and K Burgess. BODIPY dyes and their derivatives: Syntheses and spectroscopic properties. *CHEMICAL REVIEWS*, **107**[11]:4891–4932, NOV 2007. 93

[238] G Ulrich, R Ziessel, and A Harriman. The chemistry of fluorescent bodipy dyes: Versatility unsurpassed. *ANGEWANDTE CHEMIE-INTERNATIONAL EDITION*, **47**[7]:1184–1201, 2008. 93

[239] Y Gabe, T Ueno, Y Urano, H Kojima, and Te Nagano. Tunable design strategy for fluorescence probes based on 4-substituted bodipy chromophore: improvement of highly sensitive fluorescence probe for nitric oxide. *ANALYTICAL AND BIOANALYTICAL CHEMISTRY*, **386**[3]:621–626, 2006. 93

[240] H Xingxing, Z Jing, L Xungao, D Lin, L Di, Q Huayu, and Y Shouchun. A novel bodipy-based colorimetric and fluorometric dual-mode chemosensor for hg2+ and cu2+. *SENSORS AND ACTUATORS B: CHEMICAL*, **192**[0]:29 – 35, 2014. 93

[241] P Loison, NA Hosny, P Gervais, D Champion, MK Kuimova, and JM Perrier-Cornet. Direct investigation of viscosity of an atypical inner membrane of Bacillus spores: A molecular rotor/FLIM study. *BIOCHIMICA ET BIOPHYSICA ACTA-BIOMEMBRANES*, **1828**[11]:2436–2443, NOV 2013. 93

[242] HL Kee, C Kirmaier, LH Yu, P Thamyongkit, WJ Youngblood, ME Calder, L Ramos, BC Noll, DF Bocian, WR Scheidt, RR Birge, JS Lindsey, and D Holten. Structural control of the photodynamics of boron-dipyrrin complexes. *JOURNAL OF PHYSICAL CHEMISTRY B*, **109**[43]:20433–20443, NOV 3 2005. 95

[243] AA Newman. *Physical Properties of Glycerol*. Leonard Hill, London, 1968. 96

[244] JV Morris, MA Mahaney, and JR Huber. Fluorescence Quantum Yield Determinations - 9,10-Diphenylanthracene as a Reference-Standard In Different Solvents. *JOURNAL OF PHYSICAL CHEMISTRY*, **80**[9]:969–974, 1976. 100, 118

[245] RH Bisby, SW Botchway, JA Hadfield, AT McGown, AW Parker, and KM Scherer. Fluorescence lifetime imaging of E-combretastatin uptake and distribution in live mammalian cells. *EUROPEAN JOURNAL OF CANCER*, **48**[12]:1896–1903, AUG 2012. 101

[246] Chung, PH. *Advanced Fluorescence Lifetime Imaging and Spectroscopy Techniques for Biological Samples*. PhD thesis, Kings College London, 2012. 105, 114

[247] C Juengst, M Klein, and A Zumbusch. Long-term live cell microscopy studies of lipid droplet fusion dynamics in adipocytes. *JOURNAL OF LIPID RESEARCH*, **54**[12]:3419–3429, DEC 2013. 105, 114

[248] M Suzuki, Y Shinohara, Y Ohsaki, and T Fujimoto. Lipid droplets: size matters. *JOURNAL OF ELECTRON MICROSCOPY*, **60**[1]:S101–S116, AUG 2011. 113

[249] Y Guo, KR Cordes, Jr Farese, V Robert, and TC Walther. Lipid droplets at a glance. *JOURNAL OF CELL SCIENCE*, **122**[6]:749–752, MAR 15 2009. 113, 114

[250] Private communication with Dr Weihong Zhu and ET preliminary study, University of Shanghai. 124

[251] Christopher Rumble, Kacie Rich, Gang He, and Mark Maroncelli. CCVJ is Not a Simple Rotor Probe. *JOURNAL OF PHYSICAL CHEMISTRY A*, **116**[44]:10786–10792, NOV 8 2012. 136

[252] C Haisch and H Becker-Ross. An electron bombardment CCD-camera as detection system for an echelle spectrometer. *SPECTROCHIMICA ACTA PART B-ATOMIC SPECTROSCOPY*, **58**[7]:1351–1357, JUL 18 2003. 138

[253] Sergent, N. *A Novel Wide-Field Time-Correlated Single Photon Counting Technique for Luminescence Lifetime Imaging*. PhD thesis, Kings College London, 2009. 140

[254] Bevington, PR, Robinson, DK. *Data reduction and error analysis for the physical sciences*. McGraw Hill, New York, 2003. 144

[255] DDU Li, J Arlt, D Tyndall, R Walker, J Richardson, D Stoppa, E Charbon, and RK Henderson. Video-rate fluorescence

lifetime imaging camera with CMOS single-photon avalanche diode arrays and high-speed imaging algorithm. *JOURNAL OF BIOMEDICAL OPTICS*, **16**[9], SEP 2011. 147

[256] Private communication with Mr Masahiko Shirai; `Hamamatsu Photonics K.K.` , 2011. 153

[257] J Baudot, W Dulinski, M Winter, R Barbier, E Chabanat, P Depasse, and N Estre. Photon detection with CMOS sensors for fast imaging. *NUCLEAR INSTRUMENTS & METHODS IN PHYSICS RESEARCH SECTION A-ACCELERATORS SPECTROMETERS DETECTORS AND ASSOCIATED EQUIPMENT*, **604**[1-2]:111–114, JUN 1 2009. 8th International Conference on Position Sensitive Detectors, Univ Glasgow, Glasgow, SCOTLAND, SEP 01-05, 2008. 155

[258] S Buontempo, G Chiodi, IN Dalinenko, A Ereditato, AV Ekimov, JP Fabre, VY Fedorov, A Frenkel, F Galeazzi, F Garufi, SV Golovkin, VN Govorun, NN Kalashnikova, VG Kossov, EN Kozarenko, IE Kreslo, LY Lasovsky, B Liberti, AV Malyarov, G Martellotti, AM Medvedkov, G Penso, GI Vishnevsky, T Wolff, and A Zhuk. The Megapixel EBCCD: A high-resolution imaging tube sensitive to single photons. *NUCLEAR INSTRUMENTS & METHODS IN PHYSICS RESEARCH SECTION A-ACCELERATORS SPECTROMETERS DETECTORS AND ASSOCIATED EQUIPMENT*, **413**[2-3]:255–262, AUG 21 1998. 155

[259] DW MARQUARDT. An Algorithm for Least-Squares Estimation of Nonlinear Parameters. *JOURNAL OF THE SOCIETY FOR INDUSTRIAL AND APPLIED MATHEMATICS*, **11**[2]:431–441, 1963. 158

[260] RA Fisher. On the mathematical foundations of theoretical statistics. *Philosophical Transactions of the Royal Society of London A: Mathematical, Physical and Engineering Sciences*, **222**[594-604]:309–368, 1922. 158

[261] Hirvonen, LM and Festy, F and Suhling, K. Wide-field time-

correlated single-photon counting (TCSPC) lifetime microscopy with microsecond time resolution. *OPT. LETT.*, **39**[19]:5602–5605, Oct 2014. 176

[262] D Elson, J Requejo-Isidro, I Munro, F Reavell, J Siegel, K Suhling, P Tadrous, R Benninger, P Lanigan, J McGinty, C Talbot, B Treanor, S Webb, A Sandison, A Wallace, D Davis, J Lever, M Neil, D Phillips, G Stamp, and P French. Time-domain fluorescence lifetime imaging applied to biological tissue. *PHOTOCHEMICAL & PHOTOBIOLOGICAL SCIENCES*, **3**[8]:795–801, 2004. 10th Congress of the European-Society-for-Photobiology, Vienna, AUSTRIA, SEP 06-11, 2003. 177

[263] KJ Morris, MS Roach, W Xu, JN Demas, and BA DeGraff. Luminescence lifetime standards for the nanosecond to microsecond range and oxygen quenching of ruthenium(ii) complexes. *ANALYTICAL CHEMISTRY*, **79**[24]:9310–9314, 2007. 177, 178

[264] RM Levenson, DT Lynch, H Kobayashi, JM Backer, and MV Backer. Multiplexing with multispectral imaging: From mice to microscopy. *ILAR JOURNAL*, **49**[1]:78–88, 2008. 177

[265] AE Soini, A Kuusisto, NJ Meltola, E Soini, and L Seveus. A new technique for multiparameter imaging microscopy: Use of long decay time photoluminescent labels enables multiple color immunocytochemistry with low channel-to-channel crosstalk. *MICROSCOPY RESEARCH AND TECHNIQUE*, **62**[5]:396–407, DEC 1 2003. 177

[266] Sigma-aldrich and fluka, `Tris(4,7-Diphenyl-1,10-Phenanthroline) Ruthenium(Ii) Dichloride Complex`, 2008. 178

[267] Z Petrášek and K Suhling. Photon arrival timing with sub-camera exposure time resolution in wide-field time-resolved photon counting imaging. *OPTICS EXPRESS*, **18**[24]:24888–24901, 2010. 182, 188

[268] D Strasser, X Urbain, HB Pedersen, N Altstein, O Heber, R Wester, KG Bhushan, and D Zajfman. An innovative approach

to multiparticle three-dimensional imaging. *REVIEW OF SCIENTIFIC INSTRUMENTS*, **71**[8]:3092–3098, 2000. 182

[269] L Dinu, ATJB Eppink, F Rosca-Pruna, HL Offerhaus, WJ van der Zande, and MJJ Vrakking. Application of a time-resolved event counting technique in velocity map imaging. *REVIEW OF SCIENTIFIC INSTRUMENTS*, **73**[12]:4206–4213, 2002. 182

[270] P20 Phosphor screen datasheet; `Photek Ltd`. 184

[271] JE Martin and LE Shea-Rohwer. A 1-D model of the photoluminescent decay of ZnS phosphors as a function of excitation conditions. *JOURNAL OF LUMINESCENCE*, **128**[9]:1407–1420, SEP 2008. 184

[272] KCB Lee, J Siegel, SED Webb, S Leveque-Fort, MJ Cole, R Jones, K Dowling, MJ Lever, and PMW French. Application of the stretched exponential function to fluorescence lifetime imaging. *BIOPHYSICAL JOURNAL*, **81**[3]:1265–1274, SEP 2001. 184

[273] TII 1004E03 - X-ray image intensifiers; `Hamamatsu Photonics K.K.`, 1998. 185

[274] MCP140 P47 Phosphor screen datasheet; `Photek Ltd`, 2012. 186, 187

[275] Private communication with Mr Russell Brown; `Photron (Europe) Ltd.`, 2012. 188